University of Southampton Research Repository

THE INTERACTION BETWEEN THE THERMOSPHERE AND IONOSPHERE AT HIGH LATITUDES

by

Christopher John Davis
B.Sc. Hons., (Aberystwyth)

Thesis submitted for the degree of
Doctor of Philosophy

Department of Physics
University of Southampton
April, 1993

To my mother, Monica Davis,
whose enquiring mind is an inspiration.

UNIVERSITY OF SOUTHAMPTON

ABSTRACT

FACULTY OF SCIENCE

PHYSICS

Doctor of Philosophy

THE INTERACTION BETWEEN THE THERMOSPHERE AND IONOSPHERE AT HIGH LATITUDES.

by Christopher John Davis

A study has been made of the interaction between the thermosphere and the ionosphere at high latitudes, with particular attention to the value of the O^+-O collision parameter. The European Incoherent SCATter facility (EISCAT) based at Tromsø was used to make tristatic measurements of plasma parameters at F region altitudes while simultaneous independent measurements of the neutral wind were made by a Fabry-Perot Interferometer (FPI). The radar data were used to derive values of the meridional neutral wind. The accuracy of this technique at high latitudes is reduced by the dynamic nature of the auroral ionosphere and the presence of significant vertical winds. The derived winds were compared with the meridional winds measured by the FPI. For each night, the value of the O^+-O collision parameter was found which produced the best agreement between the two data sets. The precision of the collision frequency obtained in this way depends on the accuracy of the data. The statistical method was critically examined in an attempt to account for the variability in the data sets. The results indicate that the most probable value of the O^+-O collision parameter is a factor of between 1.2 and 1.7 greater than Banks' theoretical value (Banks, 1966).

The contribution of ion drag to the acceleration of the neutral air was also considered. During times of enhanced ion drift, ion drag dominates all other forces acting on the neutral air. A method for determining the neutral ion collision frequency during such an event is described. It was not possible to calculate the neutral ion collision frequency for the two examples in this thesis due to limitations in the radar data.

Acknowledgements

Throughout the course of my research, I have received much support and encouragement from the people with whom I have worked.

I wish to thank my supervisor, Professor Henry Rishbeth, for his advice and help throughout my time at Southampton.

I am grateful to Dr. Rees from UCL, for allowing me to use the Fabry-Perot data, which was supplied by Anasuya Aruliah.

The EISCAT data was analyzed with a great deal of help from the EISCAT group at the Rutherford Appleton Laboratory. In particular I wish to thank Alan Farmer for spending a considerable amount of time analyzing data on my behalf.

The Upper Atmosphere group at the University of Southampton provided me with a wonderful working environment. I wish to thank everyone who was part of the group throughout the course of my work for their friendship as well as for their professional help. Particular thanks must go to Rachel Edwards, Betty Lanchester, Fred Rees and Mihail Codrescu. I am also grateful to Dr G. J. Daniell for his advice on the statistics used in chapter 4 of this thesis.

TABLE OF CONTENTS

CHAPTER 3

CHAPTER 4

CHAPTER 5

CHAPTER 6

APPENDIX A

APPENDIX B

APPENDIX C

List of figures

Introduction

This thesis is concerned with the collisional interaction between the ionosphere and the neutral atmosphere at high latitudes and in particular, the estimation of the O^+-O collision parameter. The European Incoherent SCATter radar (EISCAT) was used to study the ionosphere, while simultaneous independent measurements were made of the neutral atmosphere by a Fabry Perot Interferometer (FPI). Studies of this nature have been made before by Burnside et al (1987) using the incoherent scatter radar at Arecibo and by Sipler et al (1991) at Millstone Hill. Neither of these radars is able to make direct measurements of the full vector velocity of the plasma. They have to rely on beam swinging techniques which assume that the ionosphere is constant within the observed area for the duration of the scan. EISCAT is unique in being able to measure three components of plasma vector velocity in one scattering volume.

Initial attempts to compare EISCAT and FPI data (D. Rees et al, 1984) led to the design of the Ion Neutral Dynamics Investigation (INDI) by Winser et al, (1988). Since then, the experiment has been run regularly, producing many hours of data (e.g Farmer et al, 1990). In this thesis, a study has been made of all INDI data, and the method of analysis for determining the O^+-O collision frequency refined. A series of programs was developed using the interactive mathematical package MATLAB to provide a comprehensive analysis of the FPI data following the methods of Burnside et al (1981). As a result of this analysis, it was possible to include in the study FPI data collected during EISCAT common program time.

It is possible to observe the effect of ion drag by studying the acceleration of the zonal neutral wind. Where data are available, some other terms in the neutral wind momentum equation can be estimated to provide a comparison between ion drag and the other forces. If the ion velocities are large relative to the neutral wind then ion drag will dominate the acceleration of the neutral atmosphere. Initially it was thought possible to obtain an estimate of the neutral-ion collision frequency from such an event. This proved not to be possible for the observed events because of changes in ion composition and electron density.

The forces controlling the neutral atmosphere and the ionosphere are described below and the collision frequency discussed in detail, including a summary of the work done by others in determining theoretical and experimental values for the most elusive collision frequency, that of the O^+ ion with the O neutral.

The derivation of neutral winds from radar data is described in chapter 3. Use of this derivation to estimate the O^+-O collision parameter is explained in section 3.3, including a discussion of the results of Burnside et al and previous INDI analyses. Chapter 4 contains a detailed discussion of the method used in this thesis to estimate the O^+-O collision parameter. The main part of the chapter (section 4.5) contains a full description of the data and derivation of the O^+-O collision parameter.

Chapter 5 Discusses the effect of enhanced ion drifts on the acceleration of the neutral air and the behaviour of the collision frequency during such an enhancement.

Details of how the INDI experiment could be altered to improve the quality of the data are given in Chapter 6. An experiment to study the neutral-ion collision frequency during an ion heating event is also discussed.

A description of EISCAT and the technique of incoherent scatter can be found in Appendix A, whilst Appendix B contains details of the FPI instrument and data collection. The combination of these two instruments in the INDI programme is discussed in Chapter 2. Details of the FPI analysis are given in Appendix C.

All the data used in section 4.5 to derive the O^+-O collision parameter are plotted in the last two appendices, D and E. The data in appendix D was analysed without vertical wind data, whilst the data in Appendix E was analysed with vertical wind data.

Chapter 1

The dynamics of the neutral atmosphere and ionosphere at high latitudes.

1.1 The interplanetary environment.

The upper atmosphere is very dynamic at high latitudes. The plasma moves under the influence of large electric fields and the atmosphere is heated by precipitating particles. A study of the interaction between the ionosphere and the neutral atmosphere at high latitudes must be conducted in this context. The energy source for these processes is the sun.

At the surface of the sun, the outward plasma pressure exceeds gravity. The resulting outflow of plasma, at approximately 400 km s^{-1}, is known as the solar wind. The sun's magnetic field extends into interplanetary space, where it becomes the Interplanetary Magnetic Field (IMF). As the plasma moves outward, the IMF is drawn out into interplanetary space and becomes very elongated. Since the orbit of the Earth is inclined to the rotational axis of the sun, the polarity of the IMF at the Earth changes throughout the Earth's orbit. Distortions in the IMF cause deviations from this simplistic model and many sectors can be formed. Figure 1.1.1 includes a definition of the IMF coordinates, B_x, B_y and B_z. B_x and B_y are in the ecliptic plane, where B_x is the component pointing away from the sun. B_z is the perpendicular to the ecliptic plane, positive to the north.

On reaching the Earth, the interaction between the IMF and the geomagnetic field forms a bow shock on the dayside. Some of the energy of the IMF is transferred through the bow shock to the region beyond - the magnetosphere, where some of the energy is converted into heat, and some of the momentum causes the magnetospheric plasma to move away from the sun over the poles. This interaction between the IMF and the geomagnetic field is controlled by two processes; viscous interaction and magnetic reconnection (where the IMF and the geomagnetic field join). The direction of the IMF at the Earth is very important in determining the effect each

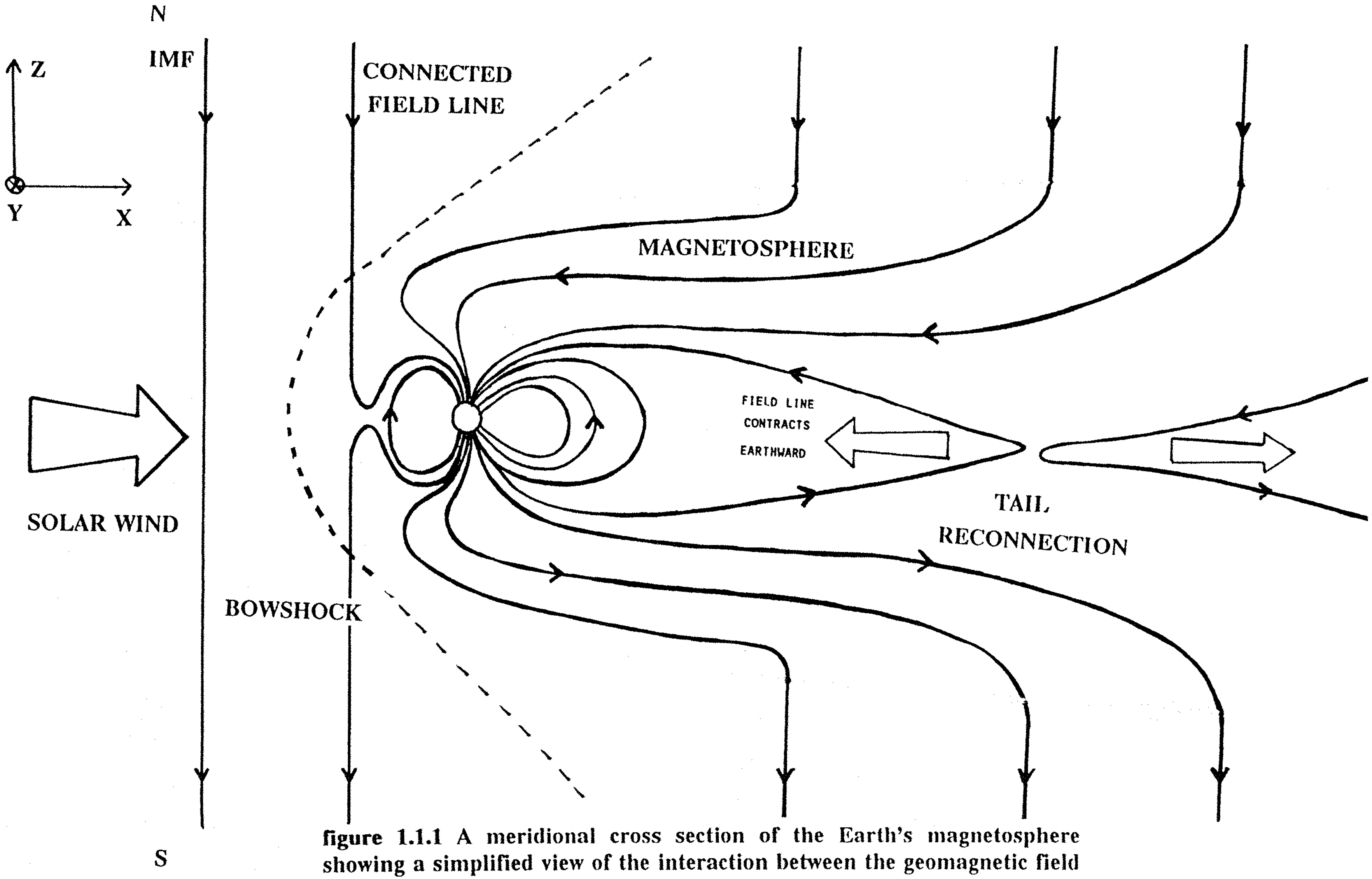

figure 1.1.1 A meridional cross section of the Earth's magnetosphere showing a simplified view of the interaction between the geomagnetic field and a southward IMF.

process has on the interaction between the two fields. The geometry for magnetic reconnection is most favourable when B_z is southward as shown in figure 1.1.1. Under such circumstances, the two fields reconnect on the sunward side of the planet. As the IMF moves away from the sun, the connected geomagnetic field lines and their associated plasma are dragged with it, over the poles. On the nightside of the planet, the movement of the IMF stretches the geomagnetic field out into a long tail, many Earth radii in length. Eventually, the combined field becomes so distorted that field lines of opposite polarity meet and magnetic reconnection occurs, separating the two fields. The distorted geomagnetic field contracts earthward, and in doing so, accelerates the plasma with it. These return flows of plasma occur at lower latitudes to complete the cycle. This cycle is mapped down in to the atmosphere, where it causes the ionospheric plasma to follow a two celled convection pattern. Figure 1.1.2 demonstrates, in a simplified form, the relation between magnetospheric plasma flows and the circulation of the ionospheric plasma. If Bz is northward, magnetic reconnection can still occur, but the process is much more complicated.

A geomagnetic field line is said to be 'closed' if it is not connected to the IMF. An 'open' field line is one that is joined to the IMF. Plasma can flow into the atmosphere along open field lines, where it excites the neutral gas to produce diffuse aurora. Along the boundary between open and closed field lines, plasma is accelerated into the atmosphere and this enhanced energy input causes the bright, discrete aurora. This region is the auroral oval and it marks the boundary between open and closed field lines. If dayside reconnection is exactly balanced by reconnection in the tail, the size of the auroral oval remains constant. Magnetic reconnection is not a steady process however, but occurs in bursts. If dayside reconnection exceeds nightside reconnection, more field lines are being opened than closed, and the auroral oval expands. Conversely, if nightside reconnection exceeds dayside reconnection, the auroral oval contracts. Because reconnection occurs in bursts, a steady

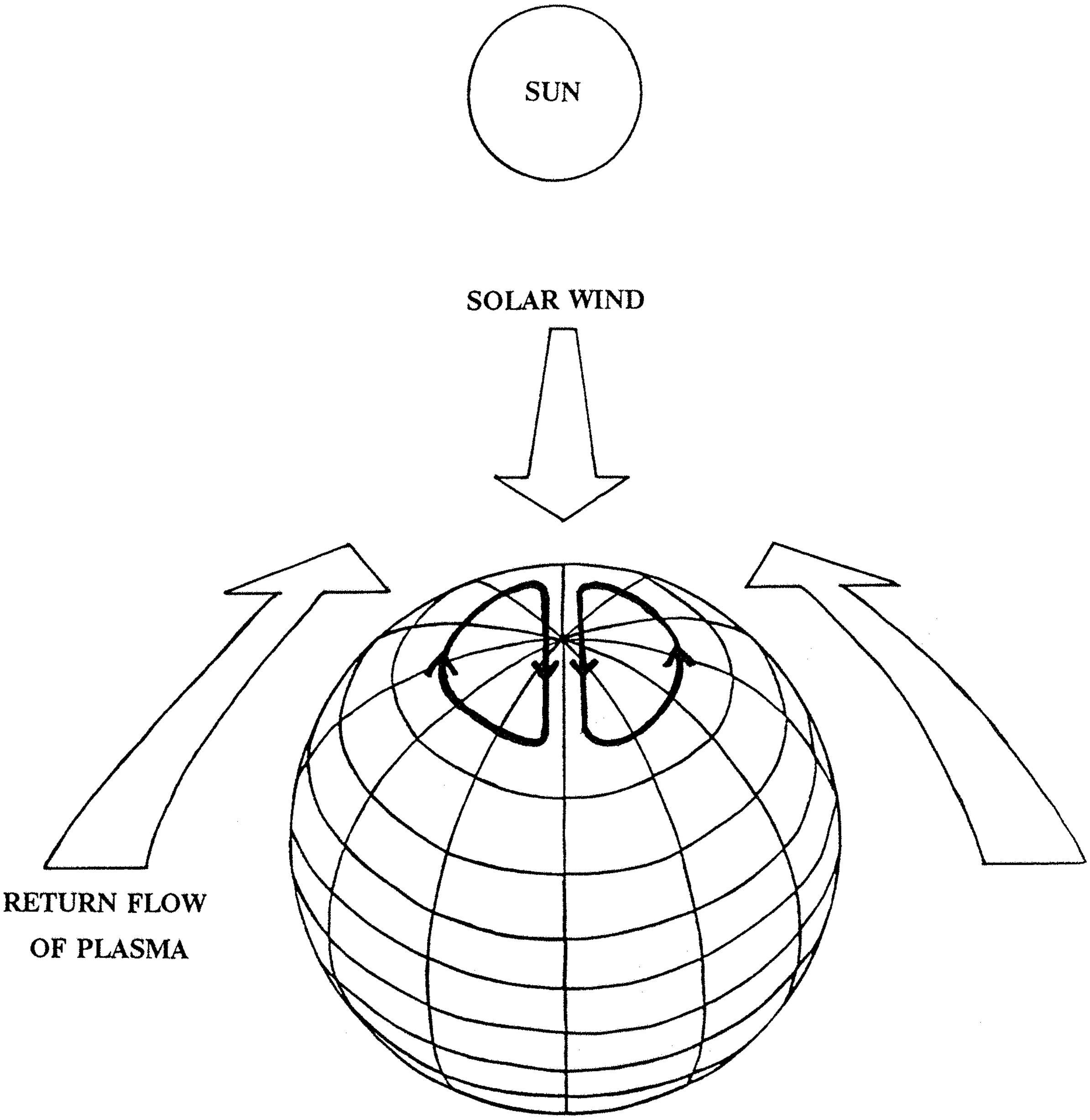

figure 1.1.2 A simplified diagram demonstrating how the motion of the magnetospheric plasma generates a two celled convection pattern in the high latitude ionosphere.

convection pattern is only a statistical average. The movement of the magnetic field determines the flow of the ionospheric plasma, which also follows the convection pattern. At the latitude of EISCAT (~ 69°), the direction of the plasma drift is determined by the return flow of the convection cell, and is therefore largest in the east-west (zonal) direction. Bursts of reconnection can cause short lived enhancements in the plasma flow of several kilometres per second. Dayside reconnection is responsible for most enhancements around noon and nightside reconnection causes enhancements around midnight (Lockwood et al, 1990).

In the atmosphere, momentum is transferred between the ionosphere and the neutral atmosphere by collisions. The greater the difference in velocity between the plasma and the neutral atmosphere, the greater the amount of momentum transferred per collision. At times of enhanced ion drift, the relative velocity between the species is several kilometres per second. On collision, frictional heating enhances the temperature of the ions. For this reason, such velocity enhancements are also termed 'ion heating events'. The neutral atmosphere is 10^4 times more dense than the plasma (at the F2 peak) and its large thermal capacity means that more energy is required to raise the neutral temperature than the ion temperature. The composition of the ionosphere is determined by many reactions. The rates of these reactions are temperature dependent and so a change in temperature causes a change in composition. The size and duration of the burst of reconnection determines the size and duration of the ion heating event.

The discussion of the forces controlling the neutral atmosphere and the ionosphere which follows is applicable to the auroral zone.

1.2 The neutral air momentum equation.

The movement of the neutral atmosphere is controlled by the sum of many different forces. Each of these forces varies in a characteristic way, determined by the process which leads to it. Equation 1.2.1 is the neutral air momentum equation, which represents the acceleration due to the most important of these forces.

$$\begin{array}{ccccccccccc} \frac{D\underline{U}}{Dt} & = & -\frac{1}{\rho}\nabla P & + & \frac{\mu}{\rho}\nabla^2\underline{U} & + & 2\underline{\Omega}\wedge\underline{U} & + & \nu_{ni}(\underline{V}-\underline{U}) & + & \underline{g} \\ acc^n & = & \begin{array}{c}\textit{pressure}\\ \textit{gradient}\end{array} & + & \textit{viscosity} & + & \begin{array}{c}\textit{coriolis}\\ \textit{acceleration}\end{array} & + & \begin{array}{c}\textit{ion}\\ \textit{drag}\end{array} & + & \textit{gravity} \end{array}$$

(1.2.1)

Here, and throughout this thesis, $\underline{U}$ is the neutral wind velocity, $\underline{V}$ is the ion drift velocity, ρ is the neutral density, P is pressure, μ is the coefficient of viscosity, ν_{ni} is the neutral-ion collision frequency, $\underline{\Omega}$ is the angular velocity of the Earth and g is the acceleration due to gravity. $D\underline{U}/Dt$ is the rate of change due to temporal and spatial variations in the wind field. These can be written separately as;

$$\frac{D\underline{U}}{Dt} = \frac{\partial \underline{U}}{\partial t} + \underline{U}.\nabla\underline{U} \qquad \textbf{(1.2.2)}$$

The spatial term, $\underline{U}.\nabla\underline{U}$, is known as the advection and contributes to the overall acceleration of the atmosphere. The terms on the right hand side of equation 1.2.1 represent the forces due to pressure gradients, viscosity, coriolis acceleration, ion drag and gravity, respectively. The size and direction of each of these forces varies throughout the day and the acceleration of the atmosphere is determined by the dominant force at any one time. In order to understand the variation of the wind, it is necessary to study how the relative size of these forces changes with time.

Owing to the dominance of gravity in the vertical direction, it is convenient to consider the vertical and horizontal components of the momentum equation separately.

1) The vertical component.

In the vertical direction, the neutral air is controlled by the pressure gradient and by gravity. The centripetal force, caused by the rotation of the Earth, and the vertical component of the coriolis acceleration are much smaller than the gravitational acceleration and can be ignored. At a height of 240 km, $g=9.1\ \mathrm{ms}^{-2}$.

Above 100 km, the neutral density drops to a level where diffusion of the gas is no longer limited by turbulence. Each species within the gas assumes its own height distribution governed by the mass and temperature of the particles. This vertical pressure gradient opposes gravitational acceleration. The rate of diffusion of a gas is governed by the resultant of these two forces. At equilibrium,

$$-\frac{dp}{dh}=nmg \qquad \textbf{(1.2.3)}$$

where p represents the partial pressure, h, height, n, the neutral concentration and m_n, the neutral particle mass. By considering each species of gas to be ideal, $p=nkT_n$, where k is Boltzmann's constant and T_n is the neutral temperature, this equation can be solved for any height above a reference level, h_o, at pressure p_o.

$$p=p_o\exp\left(-\int_{h_o}^{h}\frac{dh}{H}\right) \qquad \textbf{(1.2.4)}$$

where $H = kT_n/m_n g$ is the scale height of the gas. This is the height range over which the pressure changes by 1/e. The greater the particle mass, m_n, the smaller the scale height. The total pressure, P, at a given height, is the sum of the partial pressures, $P=\Sigma p$. Energy is required to move air vertically. In the absence of auroral heating, vertical winds are usually small and the steady state approximation is a good one. If the atmosphere is heated however, it expands and the complete vertical momentum equation must be invoked.

2) The horizontal component.

The horizontal momentum of the neutral air is governed by a complex balance of the components. The nature of each of these will be considered separately.

a) Advection

$$\frac{\partial \underline{U}}{\partial t} = -\underline{U}.\nabla_H \underline{U} = -\left(U_E \frac{\partial \underline{U}}{\partial x} + U_N \frac{\partial \underline{U}}{\partial y}\right) \qquad \textbf{(1.2.5)}$$

This is the force due to the spatial variation of the wind field as it moves through the point of observation. E and N refer to the east and the north respectively. In the absence of information about the wind gradients, $\partial \underline{U}/\partial x$ and $\partial \underline{U}/\partial y$, this term is often assumed to be zero. The comprehensive FPI analysis discussed in Appendix C estimates these gradients from the data, enabling advection to be modelled. The acceleration is usually small and slowly varying, rarely exceeding 0.05 ms^{-2} (Nkg^{-1}). With the inclusion of this term, the neutral wind momentum equation becomes non-linear.

b) Ion Drag

$$\frac{\partial \underline{U}}{\partial t} = \nu_{ni}(\underline{V}-\underline{U}) \qquad \textbf{(1.2.6)}$$

The ion drag force is very important in the transfer of momentum. It is this process that couples the momentum of the ionosphere with that of the neutral atmosphere. When the ionospheric plasma moves relative to the neutral atmosphere, momentum is transferred by collision. Since the mass of an electron is insignificant in comparison with the mass of an ion, it is the neutral-ion collisions which are important. The rate at which ions collide with neutrals, the neutral-ion collision frequency, is determined by the collision parameter for the reaction and the number of ions providing the momentum. The collision parameter depends on the species involved in the collision, and so ν_{ni} depends on the composition of both the ionosphere and the neutral atmosphere. A detailed explanation of the collision frequency and how it varies with composition is given in section 1.2.5.

Ion drag acts in a direction determined by the velocities of the plasma and the neutral atmosphere. Ion velocities can reach several kms^{-1}. For such large plasma flows, the velocity of the neutrals becomes insignificant and ion drag acts in the direction of the ion velocities. Section 1.1 discussed the convective flow of plasma in the high latitude ionosphere. The EISCAT radar lies at a latitude where the ion velocities are generally part of the return flow. These are seen as eastward flows in the morning and westward flows in the afternoon. For large ion flows therefore, ion drag acts almost exclusively in a zonal direction. For an ion drift of 2 kms^{-1} and a typical neutral-ion collision frequency of $7\mathrm{x}10^{-5}$ s^{-1}, the acceleration of the neutrals by the ions is 0.1 ms^{-2}. Since ν_{ni} is in units of s^{-1}, the inverse of this, τ_{ni}, is a measure of the response time of the neutrals to forcing by the ions. For the values given above, it would take the ionosphere over five hours to accelerate the neutral atmosphere to the velocity of the plasma. A given parcel of air will not remain in contact with the fast moving plasma for that length of time.

c) Pressure gradient

$$\frac{\partial \underline{U}}{\partial t} = -\frac{1}{\rho}\nabla_H P \qquad \textbf{(1.2.7)}$$

The equilibrium set up between gravity and pressure in the vertical direction, as described in section 1.2.1, leads to a horizontally stratified atmosphere. If the temperature varies horizontally, two columns of air at different temperatures have different density distributions. If two such columns are adjacent, there is a difference in pressure between them at a given height. Gas particles will move against the gradient, from high to low pressure. The horizontal pressure gradient therefore represents a force. By dividing the pressure gradient by the density, ρ, this force can be expressed as an acceleration.

The atmosphere is heated by the sun on the dayside of the planet and gradually cools as it is moved into the nightside by the rotation of the Earth. This temperature difference results in a pressure gradient between the sunlit and night time hemispheres. In the absence of any other forces, air will flow from the dayside to the nightside, against this gradient. From the ground, this force varies sinusoidally in a given direction as the Earth rotates. Superimposed on the global flow, is the effect of pressure gradients set up during localised heating. At high latitudes, such heating is caused by precipitation of energetic plasma into the atmosphere, or frictional heating between ions and neutrals moving at different velocities. The neutral atmosphere has a large thermal capacity, however, and the energy from such events is soon dissipated. In order to increase the neutral temperature significantly, such heating must be prolonged. In the absence of local heating, the force can be assumed to be dominated by the day-night pressure gradient. The magnitude of such an acceleration depends on the temperature gradient, and is typically 0.05 ms^{-2}.

d) Coriolis acceleration.

Coriolis acceleration is the apparent force due to the conservation of angular momentum as air moves on a rotating planet. For a parcel of air moving northward, between latitudes ψ and $\psi+\delta\psi$, the distance from the rotational axis decreases from $R.\cos(\psi)$ to $R.\cos(\psi+\delta\psi)$. Since momentum is conserved, the velocity of the air parcel increases and it accelerates eastward. The value of this acceleration is obtained by equating the angular momentum at the two latitudes, and is given by

$$\frac{\partial U_E}{\partial t}=2\Omega U_N\sin\psi \qquad \textbf{(1.2.8)}$$

where Ω is the Earth's angular velocity, and ψ is the latitude. Similarly, a parcel of air moving eastward, faster than the Earth's rotational velocity, experiences a southward force. This moves the parcel to a latitude where the distance

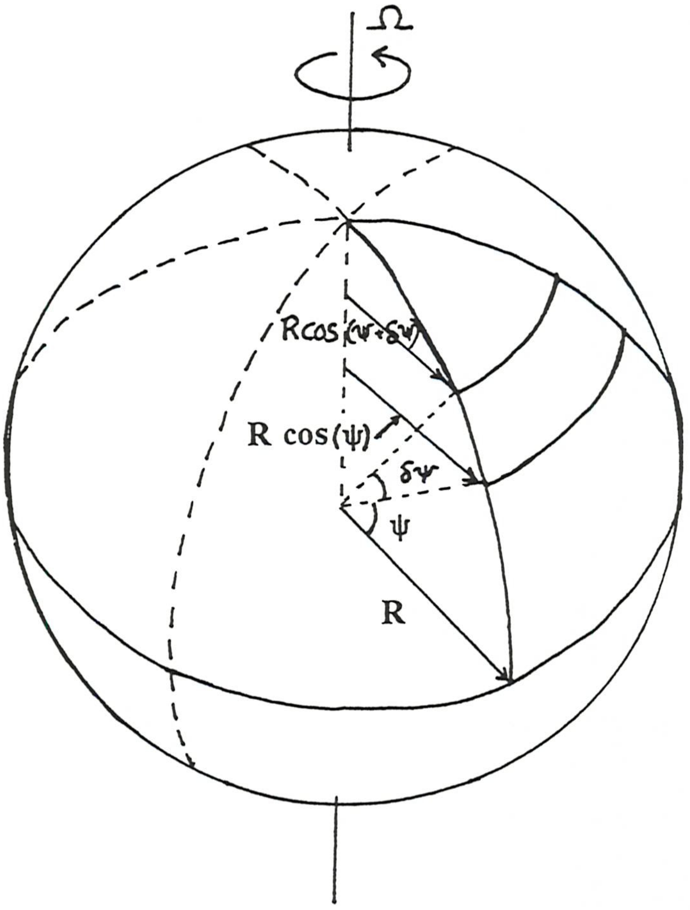

figure 1.2.1 A diagram showing the terms required in the derivation of the coriolis force.

from the rotational axis is greater:

$$\frac{\partial U_N}{\partial t} = -2\Omega U_E \sin\psi \qquad (1.2.9)$$

The acceleration is perpendicular to both the original wind direction and the angular velocity of the Earth. This can be represented for the entire wind field, $\underline{U}$, by the cross product $2\Omega\wedge\underline{U}$. Generally, the northward wind, U_N, has a well defined diurnal trend, due to the dominance of the day-night pressure gradient force in this direction. In the zonal direction the resultant coriolis acceleration is a slowly varying, diurnal function. In contrast, the zonal wind can be dominated by ion drag, since ion drifts are largely zonal. The variation of the wind pattern will be determined by the size and duration of the ion drift. As a result, the meridional coriolis acceleration can be highly variable.

The coriolis acceleration perpendicular to a wind of 200 ms^{-1} is 0.027 ms^{-2} at the latitude of Kiruna (67.9°).

e) Viscosity

$$\frac{\mu}{\rho}\nabla^2\underline{U} \qquad (1.2.10)$$

Viscosity is the force by which momentum is transferred throughout a fluid. In the case of the neutral atmosphere, this is by neutral-neutral collisions. If a velocity shear exists within a fluid, particles moving across the shear, take with them the horizontal velocity characteristic of the layer from which they came, and momentum transfer takes place by collision. It is in this way that viscosity limits such a shear. The most important velocity shear in a horizontally stratified atmosphere is the vertical shear. The force per unit area for a linear shear, t, is

$$t=\mu\frac{\partial\underline{U}}{\partial z} \qquad (1.2.11)$$

where μ is the coefficient of viscosity. For a cubic volume element, the stress exerted across the bottom face by the fluid element on the fluid below is t_{zy}. For an infinitesimally small cube (figure 1.2.2), the stress exerted by the fluid above on the top surface of the cube is

$$t_{zy}+\frac{\partial t_{zy}}{\partial z}dz \qquad (1.2.12)$$

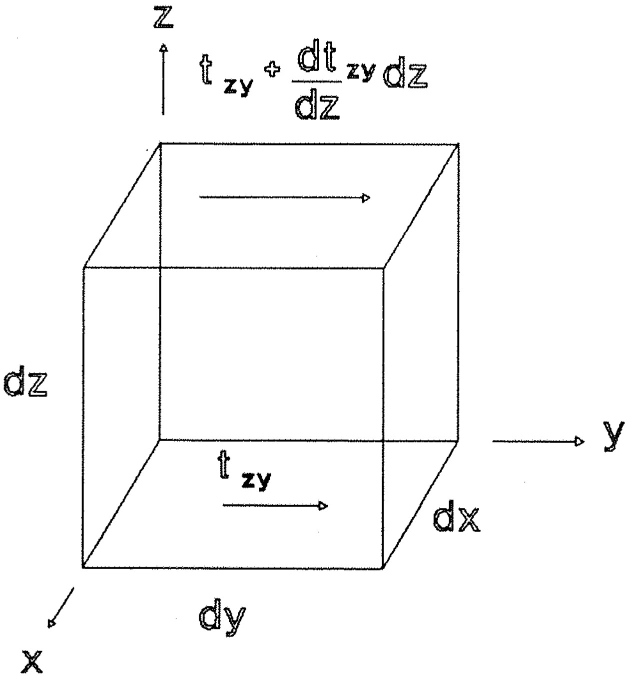

Figure 1.2.2

as a linear shear approximation can be used. The total force on the cube is the difference between these two;

$$\left(t_{zy}+\frac{\partial t_{zy}}{\partial z}dz\right)dxdy - t_{zy}dxdy = \frac{\partial t_{zy}}{\partial z}dxdydz \qquad (1.2.13)$$

This gives an acceleration of

$$\frac{1}{\rho}\frac{\partial t_{zy}}{\partial z} = \frac{1}{\rho}\frac{\partial}{\partial z}\left(\mu\frac{\partial \underline{U}}{\partial z}\right) \qquad (1.2.14)$$

The coefficient of viscosity, μ, is determined for the fluid in question by its density and temperature. Empirically, μ, can be represented by the formula

$$\mu=AT^{B} \qquad (1.2.15)$$

where B=0.69 for all major atmospheric constituents and A is a constant for a particular gas. For N_2, $A=3.43\times10^{-5}$ kg $m^{-1}s^{-1}$ and for O, $A=3.90\times10^{-5}$ kg $m^{-1}s^{-1}$.

The FPI used in this study cannot measure vertical gradients and so viscosity cannot be measured directly. The effect of viscosity is to smooth out any wind shear.

Summary

Since the diurnal pressure gradient force varies consistently with local time, it is this which determines the wind pattern. In the upper atmosphere, the other forces are either small in comparison (eg the coriolis force) or can be impulsive (eg ion drag), and these are superimposed on the general trend. Clearly, ion drag can be dominant if large ion drifts occur and so it is necessary to understand the nature of these drifts.

The movement of the interplanetary magnetic field and its interaction with the Earth's own magnetic field causes magnetospheric plasma to flow away from the sun over the poles. The return flow of plasma is at lower latitudes. The movement of this plasma is mapped down into the ionosphere as a two cell convection pattern. The return flows tend to be impulsive and as a result, the largest ion drifts are generally in this region.

Heating on the sunward side of the planet produces a global flow of air to the nightside. Over the poles, therefore, both ions and neutrals flow away from the sun. Here, however, ion drag effects may be important as $\underline{V}$ is sometimes very large. The return flow of plasma opposes the neutral flow so although $\underline{V}$ is smaller $(\underline{V}-\underline{U})$ may be large, and ion drag can have a significant effect on the neutral wind.

An instrument looking meridionally measures the velocity component over the pole. Zonally, the same instrument views the component parallel to the return flow of ions. As the Earth turns, the observer rotates, whilst the terminator remains fixed in the solar reference frame. The convection cell, controlled by the geomagnetic field, precesses about the Earth's rotational axis, but retains the same orientation with respect to the terminator. For a constant solar heating rate, the observer looking meridionally (where the effects of ion drag are reduced) sees a diurnal variation in wind velocity. Zonally however, ion drag and the pressure gradient force oppose each other, ion drag is large and any sudden variation in plasma velocity dominates the zonal wind pattern. Such a situation has been observed in satellite data (Killeen et al 1984) and in radar data (Nagy et al 1974). Two such events seen in the INDI data are discussed in chapter 5.

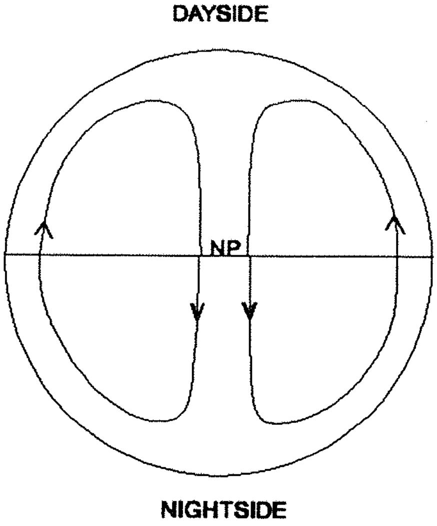

Figure 1.2.3 Plan view of the auroral region, showing a simplified two celled convection pattern.

1.3 The ion and electron momentum equations.

In addition to the forces controlling the neutral air, the charged particles of the ionospheric plasma are influenced by the presence of electric and magnetic fields. Plasma is accelerated by an electric field, and any component of this movement perpendicular to the magnetic field induces Lorentz forcing, $\underline{V}\wedge\underline{B}$. Hence the momentum equations for the ions and electrons are;

$$\frac{\mathcal{D}\underline{V}_i}{\mathcal{D}t}=\frac{N_i e}{\rho_i}(\underline{E}+\underline{V}_i\wedge\underline{B})-\frac{1}{\rho_i}\nabla P_i+\frac{\mu}{\rho_i}\nabla^2\underline{V}_i+2\Omega\wedge\underline{V}_i+\nu_{in}(\underline{U}-\underline{V}_i)+\underline{g} \tag{1.3.1}$$

$$\frac{\mathcal{D}\underline{V}_e}{\mathcal{D}t}=-\frac{N_e e}{\rho_e}(\underline{E}+\underline{V}_e\wedge\underline{B})-\frac{1}{\rho_e}\nabla P_e+\frac{\mu}{\rho_e}\nabla^2\underline{V}_e+2\Omega\wedge\underline{V}_e+\nu_{en}(\underline{U}-\underline{V}_e)+\underline{g} \tag{1.3.2}$$

where $\underline{E}$ is the electric field strength, $\underline{B}$ is the magnetic field strength, ν_{in} is the ion neutral collision frequency, ν_{en} is the electron-neutral collision frequency and the subscripts i and e refer to ions and electrons respectively.

An electric field perpendicular to the magnetic field, typically of the order of 10 mV m^{-1}, results in an acceleration on the ions of the order of 6×10^4 ms^{-2}. Ions moving perpendicular to the magnetic field at 100 ms^{-1} will experience an $\underline{E}\wedge\underline{B}$ acceleration of the order of 6×10^4 ms^{-2}. In the F-region, under such conditions, these two forces so completely dominate the movement of the plasma perpendicular to the magnetic field that collision with neutral particles can be ignored. If the electric field is small however, ion-neutral collisions are a significant source of plasma acceleration.

Owing to their high mobility parallel to the magnetic field, the electrons can move easily, minimizing any component of the electric field in this direction. The only parallel electric field remaining is the small polarisation field due to the vertical imbalance between plasma diffusion and gravity, causing a small charge separation.

Because of the major difference between the parallel and perpendicular components, it is useful to consider them separately. Perpendicular to the magnetic field the momentum equations are;

$$\frac{\mathcal{D}V_{i\perp}}{\mathcal{D}t}=\frac{N_i e}{\rho_i}\left(E_\perp+V_{i\perp}\wedge\underline{B}\right)+\nu_{in}\left(U_\perp-V_{i\perp}\right) \qquad \mathbf{(1.3.3)}$$

$$\frac{\mathcal{D}V_{e\perp}}{\mathcal{D}t}=\frac{N_e e}{\rho_e}\left(E_\perp+V_{e\perp}\wedge\underline{B}\right) \qquad \mathbf{(1.3.4)}$$

Parallel to the magnetic field, coriolis and viscous forces are insignificant and for the purposes of this discussion therefore, they are not considered. The momentum equations parallel to the magnetic field can then be written as;

$$\frac{dV_{i\parallel}}{dt} = \frac{N_i e E_\parallel}{\rho_i}+\nu_{in}\left(U_\parallel-V_{i\parallel}\right)-\sin I\left(\frac{1}{\rho_i}\frac{\partial P_i}{\partial h}-g\right) \qquad \mathbf{(1.3.5)}$$

$$\frac{dV_{e\parallel}}{dt} = -\frac{N_e e E_\parallel}{\rho_e}+\nu_{en}\left(U_\parallel-V_{e\parallel}\right)-\sin I\left(\frac{1}{\rho_e}\frac{\partial P_e}{\partial h}-g\right) \qquad \mathbf{(1.3.6)}$$

where I is the inclination angle of the magnetic field. For typical values of the vertical temperature gradient, vertical wind and ion density, the acceleration of the ions due to the pressure gradient and ion drag are both approximately 50 ms^{-2}

The ion-neutral collision frequency, ν_{in}, is the rate of transfer of momentum from the neutrals to the ions. Electrons contribute little to the transfer of momentum because of their much smaller mass.

Ion drag is the mechanism by which momentum is exchanged between the ionosphere and the neutral atmosphere. The collision frequency determines the rate of momentum transfer and so it is important to understand the nature of this parameter.

1.4 The Collision Frequency.

Momentum is transferred by collisions. For particles of species b transferring momentum to particles of species a, this change of momentum, a force, is written;

$$F_{ab}=m_a[a]\nu_{ab}(V_b-V_a) \tag{1.4.1}$$

where V is velocity, m is the mass of a particle, [] denotes the number density of a species and the subscripts a and b refer to the species of particle. ν_{ab}, the collision frequency, is defined as the rate of momentum transfer from species b to species a and is expressed in units of s^{-1}. Similarly, the rate of momentum transfer from a to b can be defined.

$$F_{ba}=m_b[b]\nu_{ba}(V_a-V_b) \tag{1.4.2}$$

For any reaction, $F_{ab}=-F_{ba}$. By equating 1.4.1 and 1.4.2, and cancelling terms, the collision frequencies are related by the expression;

$$\nu_{ab}=\nu_{ba}\frac{[b]}{[a]}\frac{m_b}{m_a} \tag{1.4.3}$$

ν_{ab} is the product of the collision parameter, K_{ab} (also known as the collision rate coefficient) and the number density of the particles imparting the momentum, [b]. K_{ab} is determined by the species involved in the reaction. Similarly, ν_{ba} is the product of K_{ba} and [a]. If $m_a=m_b$, from equation 1.4.3;

$$\nu_{ab}=\nu_{ba}\frac{[b]}{[a]} \tag{1.4.4}$$

and therefore;

$$K_{ab}=K_{ba} \tag{1.4.5}$$

In order to determine the rate of momentum transfer for a reaction, a value of K must be determined. This can either be done theoretically or experimentally.

This thesis is concerned with the collisional processes between the ionospheric plasma and the particles of the neutral atmosphere. Since the mass of an electron is negligible in comparison with the mass of an ion, it is the collisions between ions and neutral particles which contribute most to the transfer of momentum between the two.

The magnitude of the collision parameter depends on the species involved. If more than one species of neutral particle is present, the total ion-neutral collision frequency for a single ion species is the sum of the individual collisional terms. In the F-region, the dominant neutral species are O, N_2 and O_2. The dominant ion is O^+, with the proportion of NO^+ increasing with the level of auroral activity. So, for example, the total ion-neutral collision frequency for O^+ ions is written;

$$\nu_{in}^{(O^+)} = [N_2] \,.\, K_{in}^{(O^+-N_2)} + [O] \,.\, K_{in}^{(O^+-O)} + [O_2] \,.\, K_{in}^{(O^+-O_2)} \tag{1.4.6}$$

Such an expression can also be formed for the NO^+ ions. The total momentum transfer to the plasma from the neutrals is therefore proportional to the sum of the two ion-neutral collision frequencies weighted by their relative abundances (equation 1.4.7).

$$\nu_{in}^{TOT} = \frac{[O^+]}{[O^+]+[NO^+]} \,.\, \nu_{in}^{(O^+)} + \frac{[NO^+]}{[O^+]+[NO^+]} \,.\, \nu_{in}^{(NO^+)} \tag{1.4.7}$$

Similarly, the corresponding transfer of momentum from the ions to the neutrals, the neutral-ion collision frequency, is written;

$$\nu_{ni}^{TOT} = \frac{[N_2]}{[N_2]+[O]+[O_2]} \,.\, \nu_{ni}^{(N_2)} + \frac{[O]}{[N_2]+[O]+[O_2]} \,.\, \nu_{ni}^{(O)} + \frac{[O_2]}{[N_2]+[O]+[O_2]} \,.\, \nu_{ni}^{(O_2)} \tag{1.4.8}$$

Table 1.4.1 summarises the relevant collision parameters taken from Schunk and Nagy (1980). It can be seen that the collision parameters for O^+ ions are on average twice the size of the equivalent NO^+ collision parameters. The total collision frequency is therefore sensitive to the ionospheric composition. The change in the total neutral ion collision frequency for a range of compositions is shown in figure 1.4.1. This plot was produced by assuming neutral densities of $2x10^{15}$, $1x10^{15}$ and $7.5x10^{13}$ m^{-3} for O, N_2 and O_2 respectively and an electron density of $1x10^{11}$ m^{-3}. The O^+-O collision parameter was calculated using Banks' value at a reduced temperature of 1000 K (detailed in section 1.5). The collision parameters for the rest of the reactions are given in table 1.4.1.

Since the composition of the ionosphere and neutral atmosphere change with height, the total collision frequencies are height dependent. In the E-region, NO^+ is the dominant ion, and the neutral composition is dominated by N_2 and O_2. To illustrate this height dependence, an arbitrary thermospheric composition profile taken from MSIS86 (figure 1.4.2 (a)), the EISCAT ionospheric composition profile (figure 1.4.2 (c)) and a typical electron density profile (shown in figure 1.4.2 (c)) were used to calculate the total collision frequency for a range of heights. The resulting ion-neutral and neutral-ion collision frequency profiles are shown in figures 1.4.2 (d) and (e). Table 1.4.1 contains all the relevant collision parameters (in m^3s^{-1}). The expression for the resonant O^+-O parameter, derived by Banks, is given in equation 1.5.2.

$x10^{-16}$ $m^3 s^{-1}$	O	N_2	O_2
O^+	7.5*	6.82	6.64
NO^+	2.44	4.34	4.27
O_2^+	2.31	4.13	
N_2^+	2.58		4.49

Table (1.4.1)

* Calculated at a reduced temperature of 1000 K.

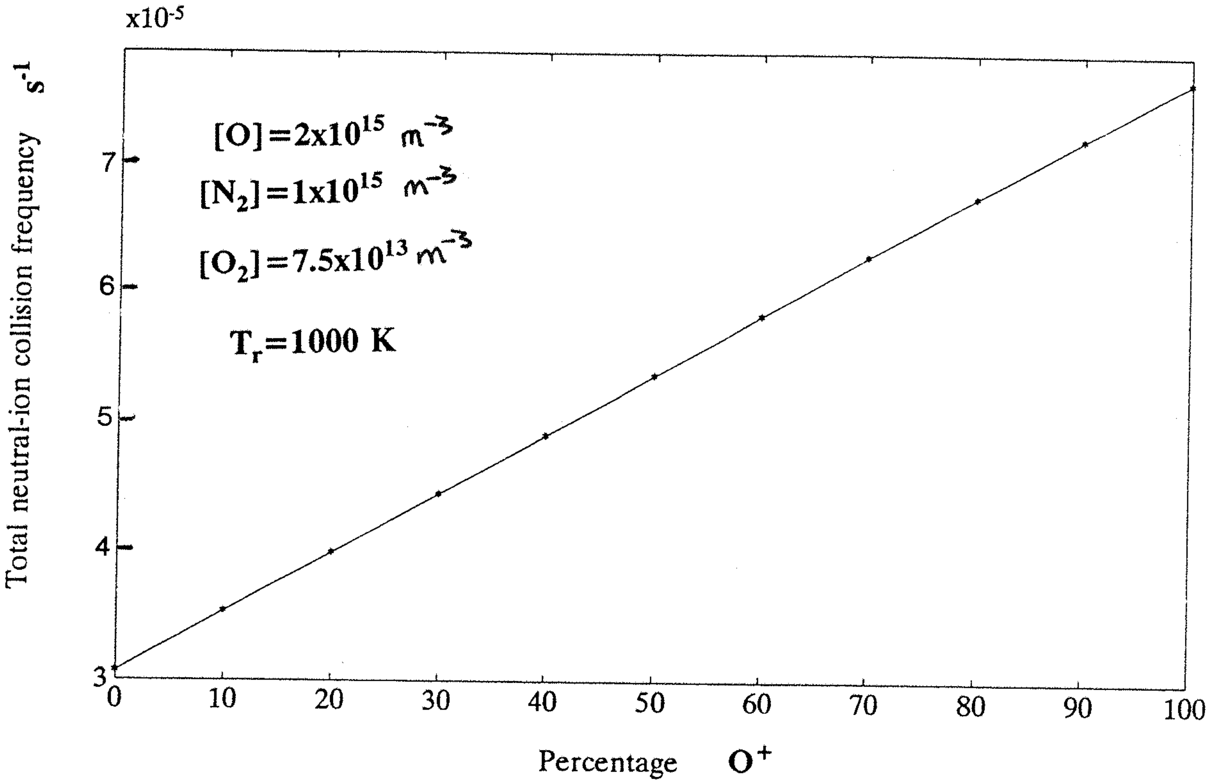

figure 1.4.1 The total neutral ion collision frequency for a range of ionospheric compositions, assuming constant neutral densities, electron density and temperature. ((Collision parameters from Schunk and Nagy, 1980)

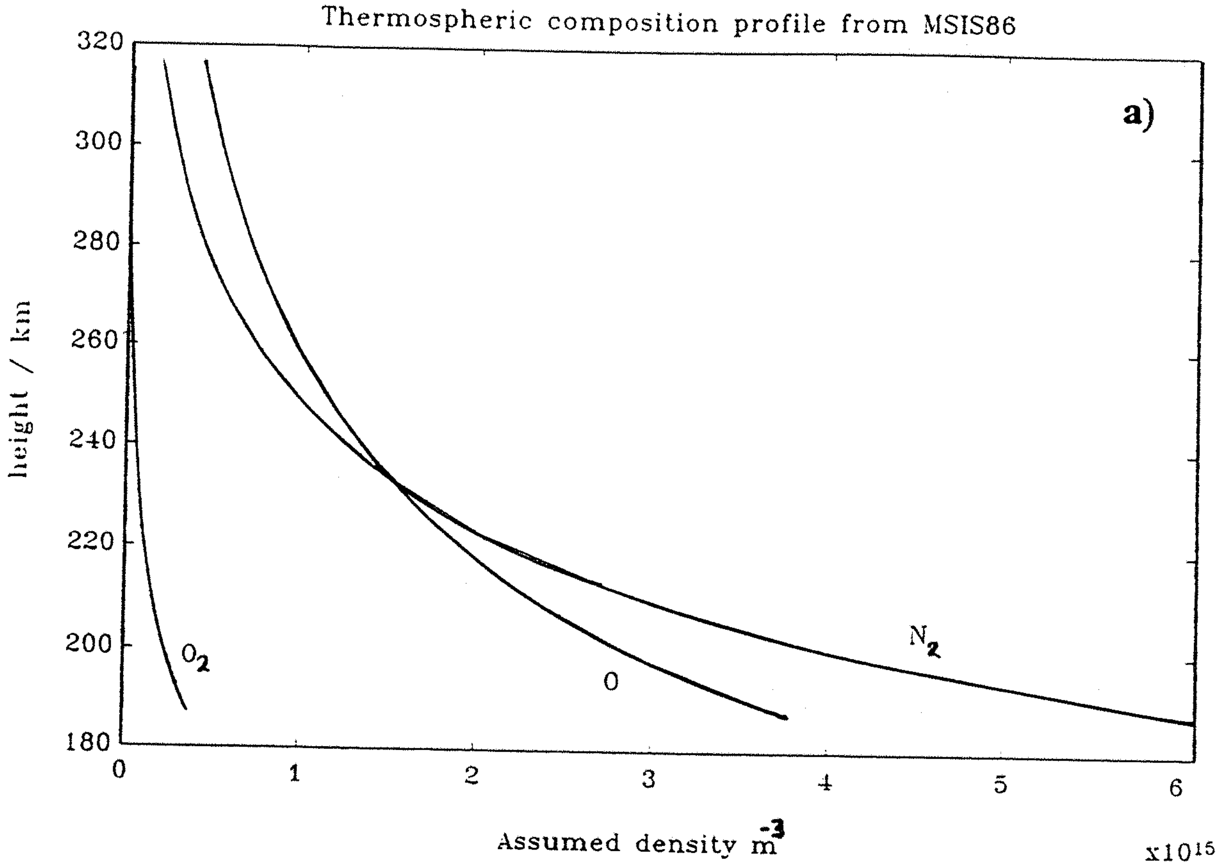

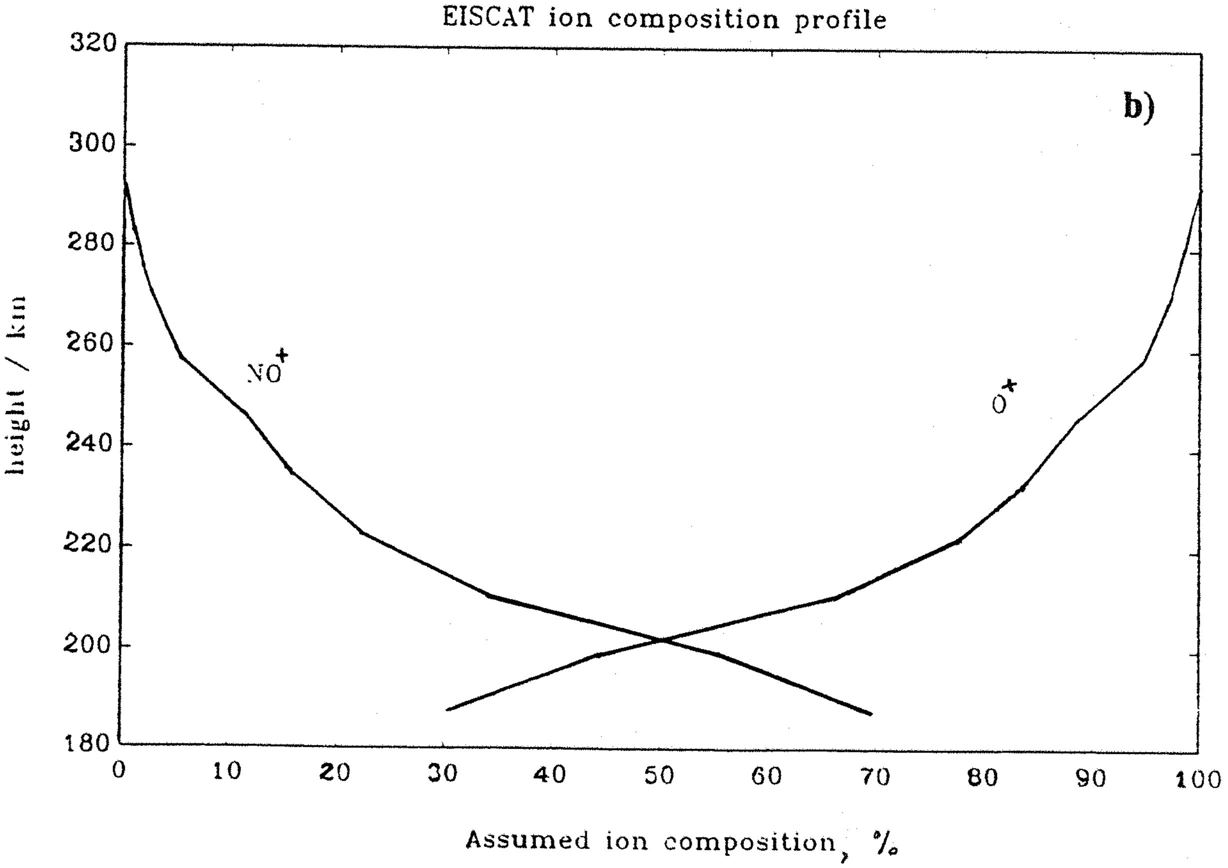

figure 1.4.2 The height dependence of both neutral-ion, (d), and ion-neutral, (e), collision frequencies using the composition profile given in (a), (b) and (c).

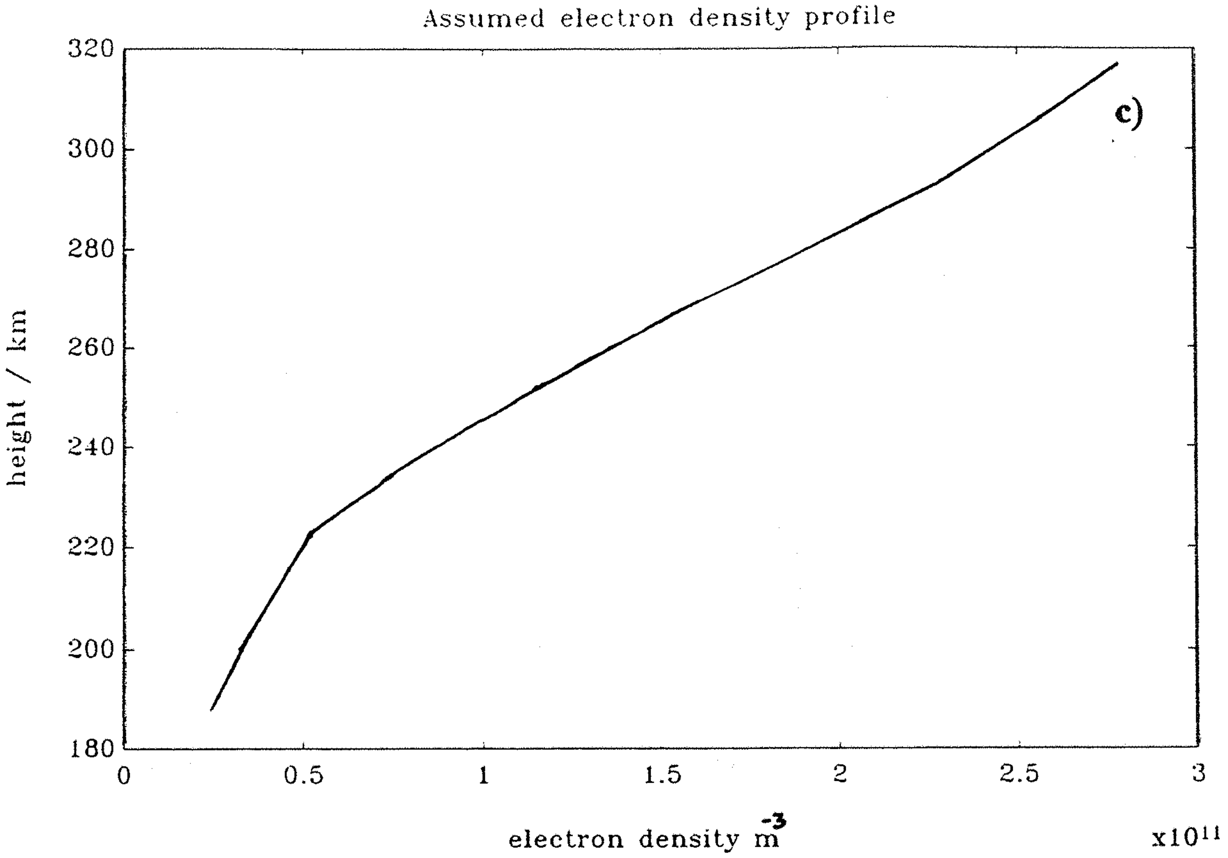
Assumed electron density profile
c)
height / km
320
300
280
260
240
220
200
180
0
0.5
1
1.5
2
2.5
3
electron density m⁻³
x10¹¹

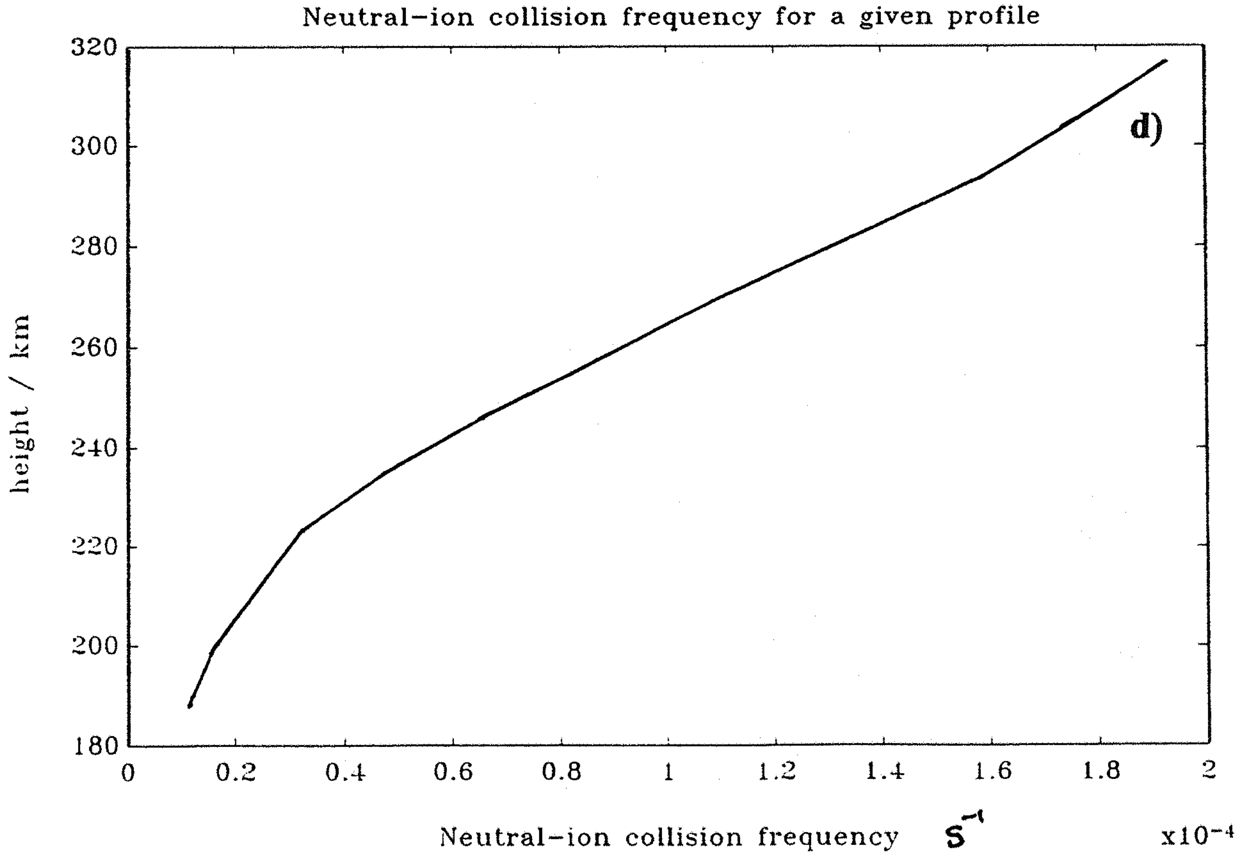
Neutral-ion collision frequency for a given profile
d)
height / km
320
300
280
260
240
220
200
180
0
0.2
0.4
0.6
0.8
1
1.2
1.4
1.6
1.8
2
Neutral-ion collision frequency s⁻¹
x10⁻⁴

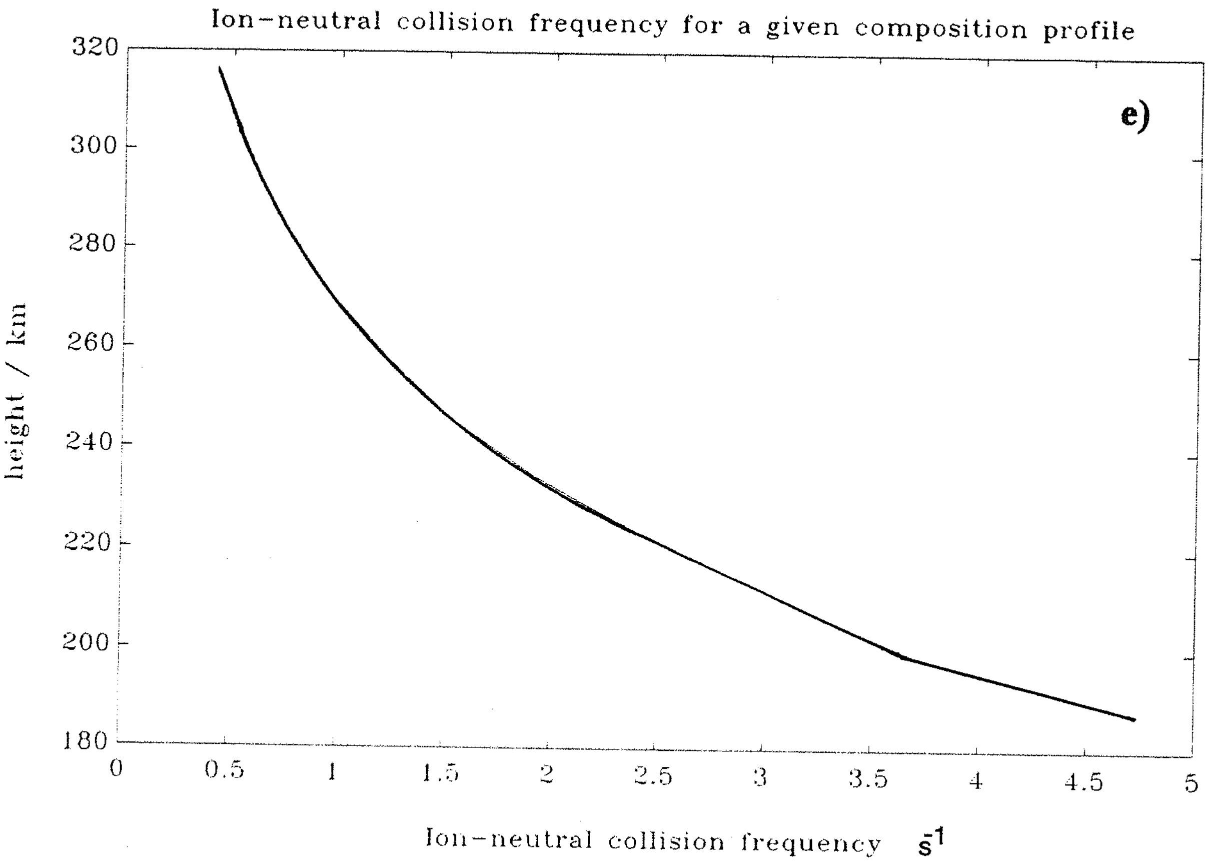

1.5 Resonant charge transfer and the O^+-O collision parameter

There have been many studies of the collisional properties of atmospheric gases (Dalgarno 1958, Banks 1966) and the collision parameters for reactions between unlike species are well defined. Complications arise when collision occurs between an ion and its parent neutral. Under such circumstances, charge can be transferred from the ion to the neutral and the two particles swap identities. This process, known as resonant charge transfer or charge exchange, enhances the collision cross section. A glancing collision between two particles transfers little momentum. If however charge exchange occurs, the reaction can be interpreted as a direct impact with backscatter. Because of the uncertainty in the past identity of a particle, it is very difficult to determine the collision parameter for such a reaction. The only significant resonant reaction occurring in the upper atmosphere is between O and O^+. In the F-region, O^+ is the dominant ion and so the total collision frequency, and thus the amount of momentum transfer, depends critically on the value of the O^+-O collision parameter. As a result, determining the value of this collision parameter has been the subject of much work.

Stebbings et al (1964) used a cross beam flow tube experiment to estimate the O^+-O collision cross-section. Oxygen atoms were formed from O_2 in an electrodeless radio frequency discharge. The resulting gas, consisting of O and O_2, was divided into two beams, one of which was ionised using an electron gun. The two beams were then crossed and the O^+-O collision cross-section was determined from their interaction. The accuracy of this experiment was limited by uncertainties in the molecular collision cross-sections, the existence of neutrals in excited states and the fact that the experiment was performed in a temperature regime well outside the thermal range. The temperature range considered (40-10,000 ev) compares with a typical thermal energy of ~0.5 ev in the F-region and so the results had to be extrapolated through a considerable temperature.

Charge transfer is dependent on the temperature of the system and so resonant collision parameters are not constant, but vary with temperature. According to Dalgarno (1958) this temperature relation can be represented by;

$$K_{in}=(A-B\log E)^2 \tag{1.5.1}$$

where A and B are constants for a given gas and E is the kinetic energy of the relative motion between the ions and the neutrals.

Banks (1966) stated that at the temperatures found in the F-region (>470 K), the effect of charge transfer dominated any polarisation forces between the particles. Using the experimental results of Stebbings et al (1964) and the theoretical predictions of Knoff et al (1964), Banks derived a value for the O^+-O collision parameter of

$$K_{in}^{(O^+-O)}=3.67x10^{-17}T_r^{\frac{1}{2}}(1-0.064\log_{10}T_r)^2\ m^3s^{-1}$$

(1.5.2)

where $T_r=(T_i+T_n)/2$ is the reduced temperature. Stubbe (1968) added to the work of Banks by including the effects of curved particle trajectories. He concluded that polarisation was significant and this increased the collision frequency under F-region conditions by about 30 per cent.

Strictly speaking, the O^+-O collision frequency is also dependent on the relative velocity of the ion and neutral particles. Stubbe (1968) studied this velocity relation and concluded that the collision frequency could be considered constant for velocities below 300 ms^{-1}. The velocity dependence only becomes significant for velocities of the order of kms^{-1}.

Since resonant reactions are the least accurately known any uncertainty in the total collision frequency lies mainly in the value of the O^+-O collision parameter. In order to determine the amount of momentum transfer between the ionosphere and the neutral atmosphere, it is important to determine this parameter accurately.

1.6 The O^+-O collision parameter from aeronomical experiments.

Laboratory work requires the extrapolation of results to the relevant pressure and temperature regimes for comparison with atmospheric conditions. It is desirable therefore for an experiment to be carried out using direct measurements from the F-region. Thomas and Williams (1975) used the Malvern radar to detect any time lag between ion velocity components parallel and perpendicular to the geomagnetic field. This phenomenon, described by Rishbeth et al (1978) and Walker (1980), is caused by an applied electric field moving ions perpendicular to B which in turn accelerates the neutral air. The poleward meridional component of this wind would cause the ion velocity parallel to B to move downwards, anticorrelated with the $B_\perp$ component of the ion velocity. For the value predicted by Banks, the components would be anticorrelated with a time delay of the order of an hour. With a time resolution of 20 minutes, Thomas and Williams saw no time delay, and this suggested that the collision frequency must be much larger than expected by theory. Since then, Breen and Williams (1993) have shown that any tristatic radar will produce spurious anticorrelations in $V_{//}$ and $V_{\perp}$ due to error mixing between the look directions. These spurious anticorrelations occur at zero time lag and for EISCAT they swamp any authentic correlation. This problem can be overcome by using monostatic $V_{//}$ measurements which results in a marked drop in the anticorrelation.

Another technique, used by Burnside et al (1987), Winser et al (1988), Farmer et al (1990), Titheridge (1991) and Sipler et al (1992) uses the assumption that a state of diffusive equilibrium exists parallel to the geomagnetic field. This method is studied in more detail in Section 3.3. Burnside et al concluded that $\nu_{in}^{(O+-O)}$ should be increased to $1.7^{+0.7}_{-0.3}$ times Banks' value, whilst the results of Winser et al and Farmer et al indicated that $\nu_{in}^{(O+-O)}$ should be reduced to 30 per cent of Banks' value. Winser et al state that in their calculation (from one data set), only O^+-O collisions were considered, not the collisions between O^+ and N_2 and O^+ and O_2. This would make a considerable difference to the result. Sipler et al, using a method similar to Burnside et al, with the Millstone Hill radar, derived a value of 1.9 ± 0.15 Banks' value, from 22 days of data. Titheridge obtained a value of 1.7 times Banks' value with data from the field aligned EISCAT Common Program, CP1. He derived meridional winds at three different altitudes and varied the O^+-O collision parameter to minimise the vertical wind shear in his results. Moffett et al (1990) summarise the effects of the proposed values of the O^+-O collision parameter on thermosphere-ionosphere coupling.

The springboard for this thesis was the work of Winser et al (1988) and Farmer et al (1990). Using all the INDI data and other simultaneous EISCAT and FPI measurements, a value of the O^+-O collision parameter has been obtained. A careful assessment of the statistical accuracy of the method has been included.

Chapter 2.

The ion neutral dynamics investigation.

The interaction between the neutral atmosphere and the ionosphere can best be studied if simultaneous independent measurements of both neutral and ionised particles are made. This study uses the EISCAT radar to obtain information about the ionospheric plasma and an FPI to observe the neutral atmosphere.

2.1 Measurement of ionospheric parameters with EISCAT

EISCAT uses incoherent scatter to observe the plasma. A powerful radio signal is transmitted into the ionosphere where it is scattered by the electrons. The movement of the electrons is controlled by the ions and so information about the plasma as a whole is obtained. A small fraction of the signal is returned to the receiving antennas. The strength of the returned signal indicates the density of the plasma. The single transmitted frequency is returned as a characteristic spectrum. From the shape of such a spectrum, the temperature of the plasma can be obtained, whilst the plasma velocity can be inferred from its Doppler shift. By measuring the returned signal at three locations, a full vector velocity can be obtained from a single scattering volume. This is known as a tristatic measurement. The process of incoherent scatter is discussed in detail in Appendix A, along with a description of the EISCAT radar itself.

2.2 Measurement of the neutral wind with an FPI

The neutral thermosphere is invisible to radar. Fabry Perot Interferometers (FPI) exploit the phenomenon of airglow to observe the neutral atmosphere. In the F-region, excited oxygen atoms can remain in metastable energy states without being collisionally quenched, due to the paucity of the atmosphere. These excited atoms, therefore move with the bulk velocity of the background gas. A proportion of excited atoms survive collisional deactivation and eventually decay to stable energetic levels by photon emission. The FPI detects one of the brightest of these lines, the 630 nm emission as the $O(^1D)$ state decays. The spectrum of this radiation is broadened by the temperature of the gas and is Doppler shifted by its bulk motion. In order to compare FPI data with EISCAT, it is necessary to study the $O(^1D)$ emission profile to determine the height at which it is most intense.

In the absence of auroral activity, the major mechanism at night for the production of the 630 nm emission is the dissociative recombination of O_2^+ (Hays et al, 1978) in the reaction

$$O_2^+ + e \rightarrow O(^1D) + O \qquad \textbf{(2.2.1)}$$

The alternative, the dissociative recombination of NO^+, violates the conservation of spin (Torr and Torr, 1979). The emission is quenched by molecular nitrogen and atomic oxygen in the reactions

$$O(^1D) + N_2 \rightarrow O(^3P) + N_2 \qquad \textbf{(2.2.2)}$$

$$O(^1D) + O(^3P) \rightarrow O(^3P) + O(^3P) \qquad \textbf{(2.2.3)}$$

which are especially important at lower altitudes, because of the density of O and N_2 there. Quenching by electrons also occurs, but is not as important.

At high latitudes, energy input from the aurora produces other sources of $O(^1D)$. The most important of these is excitation by auroral electron impact in the reaction

$$O + e^* \rightarrow O(^1D) + e^{*\prime} \qquad \textbf{(2.2.4)}$$

where e^* represents the auroral electron. The effect this has on the shape of the emission profile and the height of the emission peak depends on the energy spectrum of the precipitating electrons. The greater the energy of the electron, the further it can penetrate into the atmosphere before its energy is dissipated. This determines the height at which the airglow is enhanced. The higher energy electrons reach the E-region, where the $O(^1D)$ emission is quenched by the high density of N_2. The lower energy tail of this type of precipitation will alter the shape of the $O(^1D)$ emission profile in the F region and will lower the height of the emission peak. Rees and Roble (1986) modelled the $O(^1D)$ emission profile for 'reasonably intense' auroral conditions. The resulting profile was broad, with a peak emission at around 200 km. With more airglow occurring above the peak than below, the line of sight integration of such a profile is weighted towards the greater altitudes. Since energy inputs at the high latitude of Kiruna are complex and varied, it is simply assumed that the combination of production and loss results in a broad emission profile which peaks at 200-240 km, (Rees et al, 1984). In the thermosphere, velocity differences are limited by viscosity (as discussed in section 1.2 e) and the neutral wind is unlikely to change significantly over a scale height (Rishbeth and Garriott, 1967). As a result, the wind is insensitive to absolute height at which it is measured. For comparison with the radar, the height of the airglow emission is assumed to be 240 km. The neutral velocity measured by the FPI is integrated over the line of sight of the instrument. The final measurement will be weighted by the intensity of the airglow at each height. If a wind shear does exist, any difference between the assumed and actual height of the peak emission will result in a systematic error in the measurement of the neutral wind.

Unlike EISCAT, the FPI must take measurements in several directions in order to obtain vector velocities. The FPI used in this study is run by University College London, and is housed at the Kiruna Geophysical Institute. A detailed description of the instrument is given in Appendix B. The FPI rotates at a zenith angle of 60° through six positions, north, north-east, east, south, west and north-west. Instead of the south-east and south-west positions, a zenith measurement is made, and the instrument is calibrated against a reference lamp. The total scan time depends on the integration time at each of the positions. Initially this was 100 seconds and the scan time was 15 minutes. Winser et al (1988) and Farmer et al (1990) simply combined the north and south measurements to obtain an average meridional wind, and east and west measurements for an average zonal wind. These values were used for the whole scan area, despite evidence of significant wind gradients. A more comprehensive analysis of FPI data was detailed by Burnside et al (1981) and a similar technique was adopted for INDI data. The analysis assumes a linear velocity field across the FPI scan area. Fourier analysis of the measurements from the perimeter of the scan enables zonal and meridional gradients to be fitted to the data. In this way, the value of the wind can be modelled at the position of the radar. This procedure is described in detail in Appendix C.

2.3 The development of the Ion Neutral Dynamics Investigation

The earliest attempt to compare EISCAT data with that of the FPI, by Rees et al (1984), was complicated by the lack of coordination between the two instruments. An EISCAT experiment was therefore designed to compliment the FPI. The resulting experiment was named the Ion Neutral Dynamics Investigation, (INDI). Early versions of the INDI experiment attempted to scan the radar through 360° every 15 minutes, observing the same volumes as the FPI. This was not possible as the radar had to return through 360° after each scan, which took too long. As well as this, the west position had a very poor tristatic geometry as the Kiruna and Sodankyla receivers look in almost the same direction and the SNR at the north and south of the FPI scan was poor because of the large distances of the scattering volume from the receivers. As a result, it was decided that the radar need scan only through the meridian, which allows the determination of the meridional component of the neutral wind, the main object of the comparative study. A modified version of the EISCAT CP-3 experiment was used, with only the seven central positions of the original scan from above Kiruna to the north of Tromsø. In this way, the scan time was reduced to fifteen minutes, each of the seven measurements taking approximately two minutes. In the CP-3 experiment, the radar takes tristatic measurements in a line of points perpendicular to the L shell in the F-region. This corresponds to a line 15° from the geomagnetic meridian on the ground. Fortuitously, the FPI is also aligned 15° from the local meridian, due to a local magnetic anomaly, so the two instruments are aligned. The error in the assumption that this is north is negligible (cos(15°) = 0.9659). The tristatic measurements were made at 240 km to correspond to the assumed centroid of the O(^{1}D) airglow emission.

Figure 2.3.1 is a plan of the INDI experiment geometry. This shows the relation between the FPI and EISCAT scattering volumes. Figure 2.3.2 is a section from Tromsø to Kiruna showing the direction of the radar in relation to the geomagnetic field. Of the seven EISCAT measurement volumes, each has its own advantages with respect to the derivation of neutral winds. The northernmost position (e1) was chosen so that it coincided with the northern viewing volume of the FPI, providing a direct comparison between the two instruments. Unfortunately, as the EISCAT receiving sites are south of Tromsø, the signal to noise ratio in this position is poor (Appendix A). Position e4 is vertically above Tromsø and provides vertical profiles of electron density, ion, and electron temperatures, which are required for the derivation of the meridional wind, as detailed in chapter 3. The field aligned position (e5) is useful for a more detailed study of field parallel plasma movement at a range of heights, by again using monostatic information. Finally, position e7 is near the centre of the FPI scan, where the zenith measurement is made. This is required for the best estimate of the meridional neutral wind.

Before the winter campaign of 89/90 the FPI was adjusted from a 100 seconds dwell per position to 120 seconds, as the increased integration time produced better results. The total scan time of the FPI was increased to 19 minutes. This resulted in the EISCAT measurements becoming unsynchronised with the FPI over the course of a night. The problem can be overcome by linearly interpolating between the results, but this is inaccurate. The solution was to consider a scan as one complete rotation of the FPI irrespective of starting position. e.g north to north, north-east to north-east, east to east etc. In this way, a measurement can be output every two minutes (the difference in time between adjacent scan positions) integrated over the scan time (now 19 minutes). By doing this, there is always an FPI scan whose

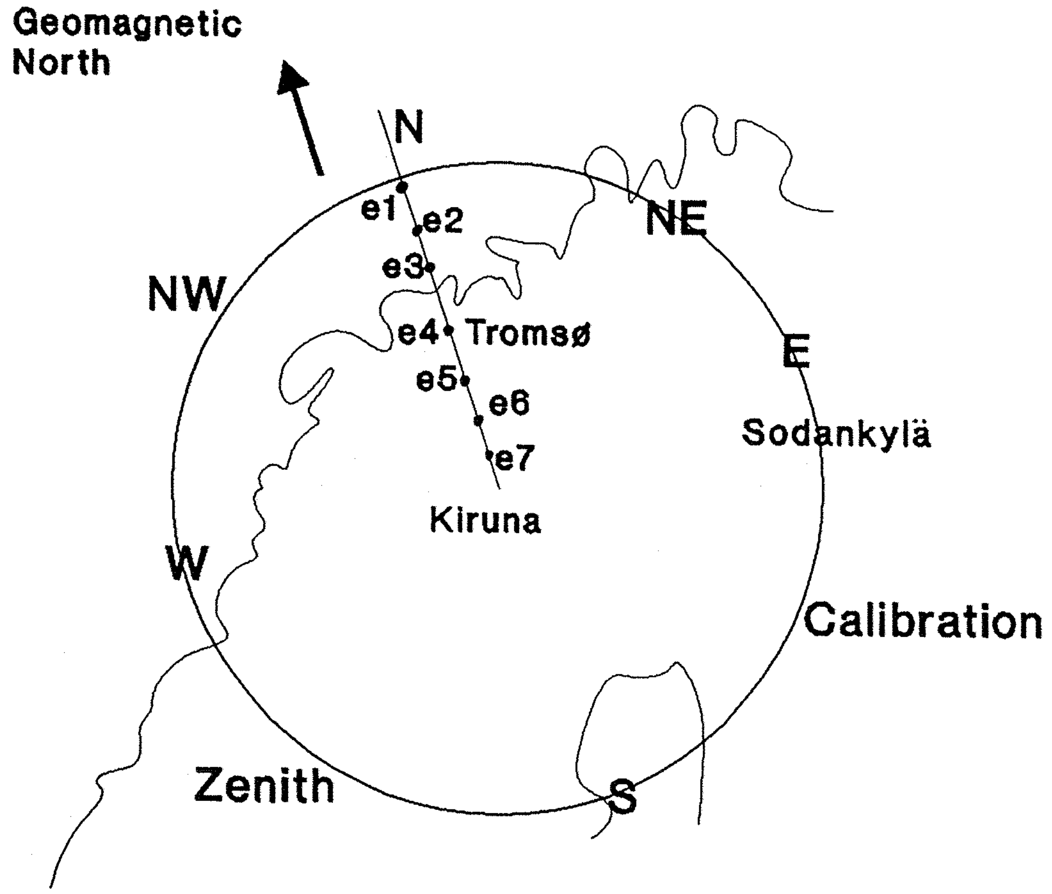

figure 2.3.1 A plan view of the EISCAT viewing volumes in relation to those of the FPI in the INDI experiment.

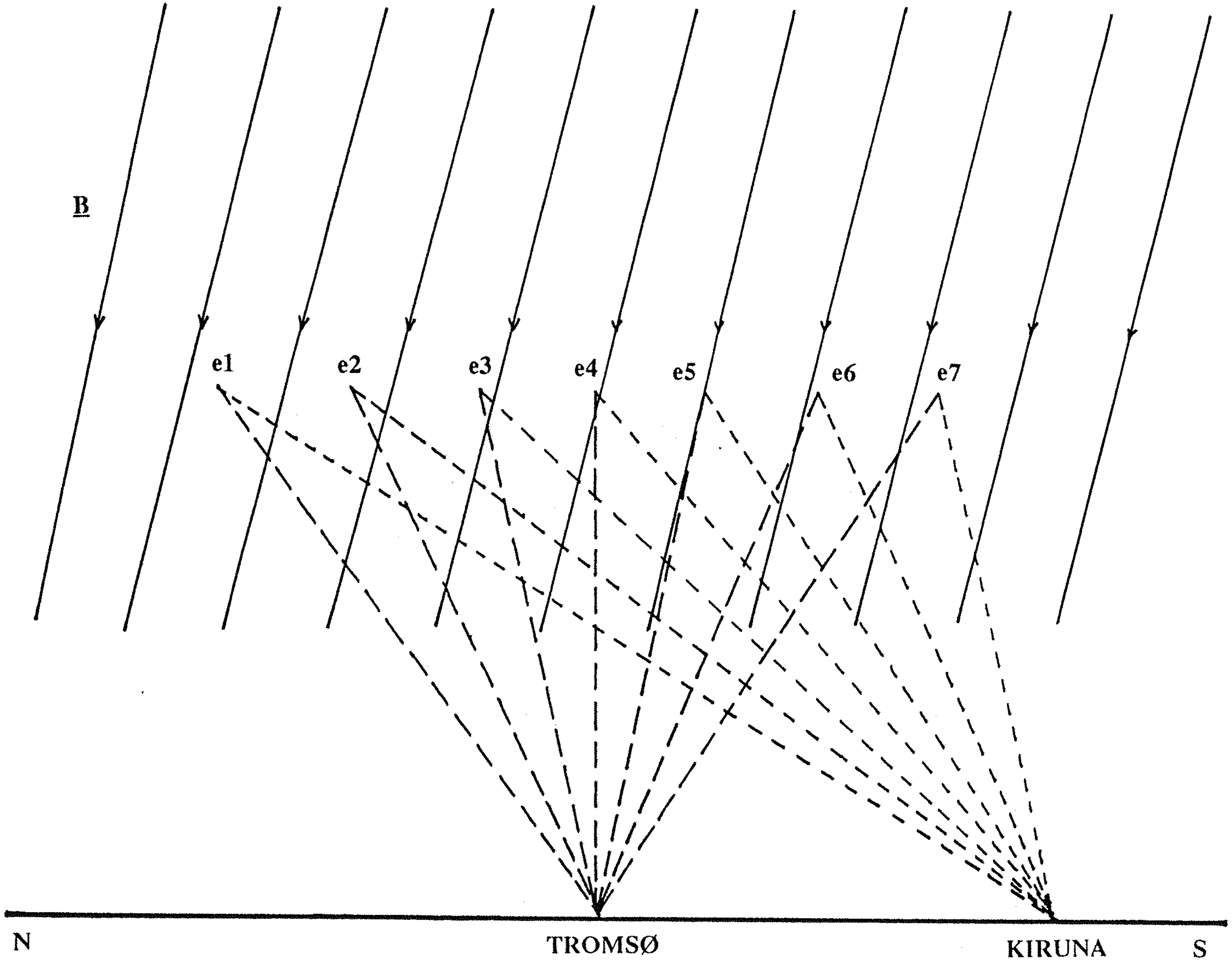

figure 2.3.2 A cross section of the INDI experiment from north to south through Tromsø and Kiruna showing the orientation of the EISCAT receivers with respect to the geomagnetic field at 240 km.

mean time is within two minutes of an EISCAT measurement. The zenith measurement is not used as part of the horizontal scan however, and these data have to be linearly interpolated before comparison. An advantage of this scanning procedure is that the FPI can be compared with common program data taken simultaneously but not originally designed for such a comparison. In Common Program 1 (CP1) the radar looks along the geomagnetic field line, corresponding to position e5 of the INDI scan. Common Program 2 (CP2) has four positions of which the present work uses three. CP2A is field aligned, CP2B is approximately vertical above Tromsø whilst CP2C is close to position e7 over Kiruna. These radar positions are plotted in figure 2.3.3.

With the FPI set at a zenith angle of 60°, the radius of the scan is approximately 400 km. By reducing the zenith angle to 45° for the winter of 1991 onwards, the area covered by the FPI scan was reduced to 250 km (represented by the inner circle in figure 2.3.3). This improves the approximation of a linear wind field within the scan radius.

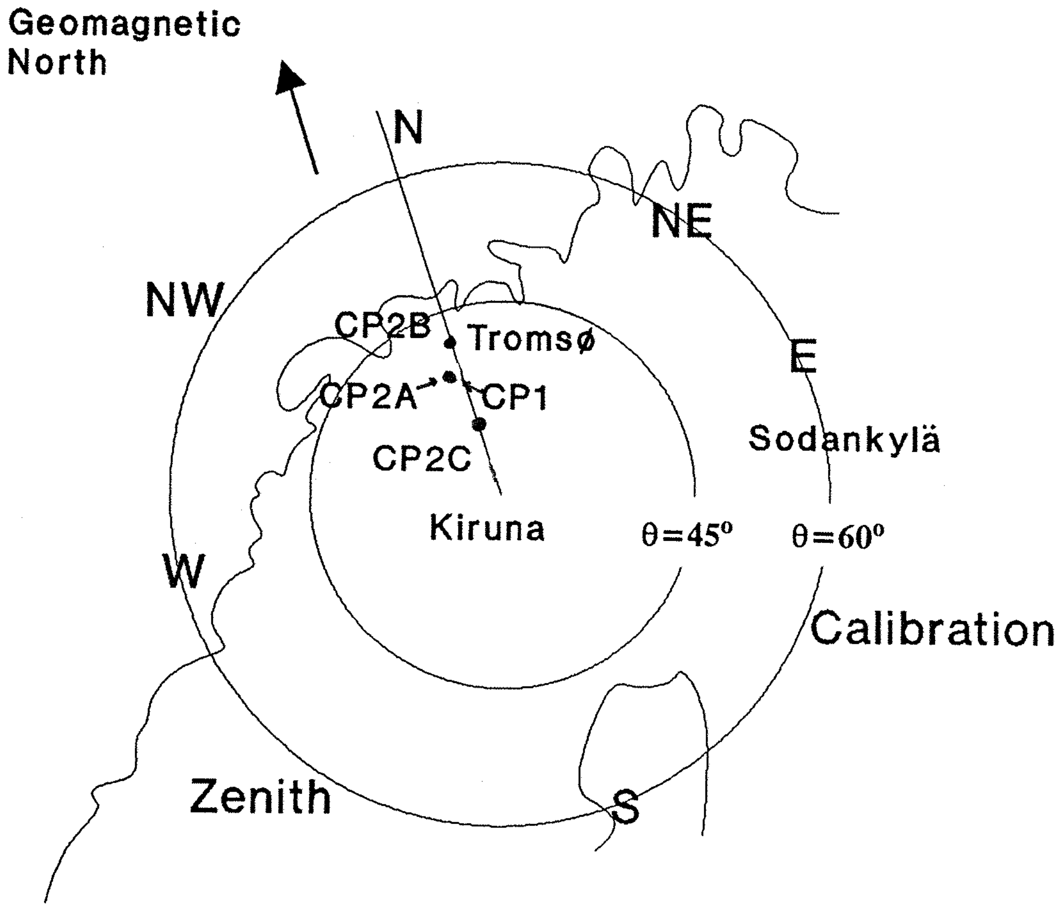

figure 2.3.3 A plan view of the EISCAT viewing volumes in relation to those of the FPI for Common Programmes 1 and 2. The inner circle represents the scan radius of an FPI set at a zenith angle of 45°.

Chapter 3

The derivation of meridional winds from radar data and its application.

In the F-region, the movement of the plasma parallel to the magnetic field is controlled by collision with neutral particles, ambipolar diffusion and gravity. If a neutral wind blows across the magnetic field, the component of the wind parallel to the field will induce a parallel ion velocity, as momentum is transferred by collisions (equation 1.3.5). Since the density of the neutral atmosphere is $\sim 10^4$ times greater than the plasma density, the acceleration of the plasma by the neutral air can be considered to be instantaneous. At Tromsø, the declination of the Earth's field is very small ($\sim 3^\circ$), and so the field is approximately meridional. It is therefore the meridional component of the neutral wind which induces a parallel plasma velocity. In addition to the forcing by the neutral atmosphere, gradients in temperature and density cause the plasma to diffuse. The parallel ion velocity measured by the radar is the difference between the parallel neutral velocity and the component of the plasma diffusion velocity parallel to the field. If these forces are balanced, the system is said to be in diffusive equilibrium. The plasma diffusion velocity is dependent on the temperature gradients that exist in the ionosphere. If these are measured by the radar, along with the parallel ion velocity, the parallel neutral velocity can be inferred, and from this the meridional component of the wind is determined. When simultaneous optical measurements of the neutral wind are available, such as INDI data, obtaining meridional winds from both instruments provides a useful comparison. Since the ion diffusion velocity is dependent on the ion-neutral collision frequency, it also provides a means of studying the value of this important parameter. The plasma diffusion velocity, W_d, can be determined from the parallel component of the ion and electron momentum equations.

3.1 Meridional winds from radar data

It has been shown in section 1.3 that the momentum equations parallel to the magnetic field for the ions and electrons are;

$$\frac{dV_{i\parallel}}{dt} = \frac{N_i e E_\parallel}{\rho_i} + \nu_{in}(U_\parallel - V_{i\parallel}) - \sin I\left(\frac{1}{\rho_i}\frac{\partial P_i}{\partial h} + g\right) \qquad \textbf{(3.1.1)}$$

$$\frac{dV_{e\parallel}}{dt} = -\frac{N_e e E_\parallel}{\rho_e} + \nu_{en}(U_\parallel - V_{e\parallel}) - \sin I\left(\frac{1}{\rho_e}\frac{\partial P_e}{\partial h} + g\right) \qquad \textbf{(3.1.2)}$$

respectively. By assuming that the plasma is in diffusive equilibrium, dV_i/dt and dV_e/dt can be set to zero and the two equations can be solved for the polarisation field. After dropping all terms of the order of m_e/m_i and using the relations $P=NkT$ and $\rho=mn$ the solution can be written;

$$V_\parallel = U_\parallel - \frac{kT_i \sin I}{m_i \nu_{in}}\left[\frac{1}{T_i}\frac{\partial(T_i+T_e)}{\partial h} + \frac{1}{N_i}\frac{\partial N_i}{\partial h} + \frac{T_e}{T_i}\frac{1}{N_e}\frac{\partial N_e}{\partial h} + \frac{m_i g}{kT_i}\right]$$

(3.1.3)

If there is one dominant ion species, $N_e \approx N_i$ and the equation simplifies to

$$V_\parallel = U_\parallel - \frac{\sin I}{\nu_{in}}\left[\frac{k}{m_i}\frac{\partial(T_e+T_i)}{\partial h} + \frac{k(T_e+T_i)}{m_i N_e}\frac{\partial N_e}{\partial h} + g\right]$$

(3.1.4)

Which is equivalent to the equation used by Farmer et al (1990);

$$V_\parallel = U_\parallel + W_d \sin(I)$$

(3.1.5)

$$W_d = -\frac{1}{\nu_{in}}\left[g + \frac{k}{m_i N_e}\frac{\partial(N_e(T_e+T_i))}{\partial h}\right]$$

(3.1.6)

W_d represents the vertical diffusion velocity of the plasma.

At equilibrium, the velocity of the ions parallel to the magnetic field is the sum of the parallel neutral velocity and the diffusion of the ions due to temperature and density gradients and gravity.

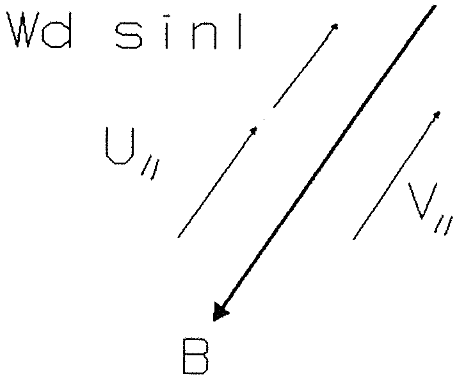

Figure 3.1.1 The Conditions For Diffusive Equilibrium.

For a plasma containing two ion species, the simple assumption that $N_i \approx N_e$ does not hold. Wickwar et al (1984) derived an expression for the diffusion of two ion species, O^+ and NO^+. By defining the terms

$$q=\frac{[O^+]}{N_e} \qquad p=\frac{[NO^+]}{N_e} \qquad p+q=1 \tag{3.1.7}$$

the expression for O^+ becomes

$$V_{\|}=U_{\|}-\frac{\sin I}{\nu_{in}^{O^+}}\left[\frac{k}{m_i^{O^+}N_e}\,\frac{\partial(N_e(T_e+T_i))}{\partial h}+g+\frac{kT_i}{m_i^{O^+}}\,\frac{1}{q}\,\frac{\partial q}{\partial h}\right] \tag{3.1.8}$$

and the expression for NO^+ becomes

$$V_{\|}=U_{\|}-\frac{\sin I}{\nu_{in}^{NO^+}}\left[\frac{k}{m_i^{NO^+}N_e}\,\frac{\partial(N_e(T_e+T_i))}{\partial h}+g+\frac{kT_i}{m_i^{NO^+}}\,\frac{1}{p}\,\frac{\partial p}{\partial h}\right] \tag{3.1.9}$$

The total collision frequency of O^+ is approximately double that of NO^+, whilst NO^+ is approximately twice the mass of O^+.

These two factors offset each other, and O^+ and NO^+ diffuse at approximately the same velocity. An average diffusion velocity can therefore be defined;

$$\overline{W_d}=qW_d^{O^+}+pW_d^{NO^+}$$

(3.1.10)

Above 250 km O^+ ions become dominant, but for heights between 150 and 250 km, the proportion of NO^+ is significant and must be considered.

The parallel neutral velocity can be considered in terms of vertical and horizontal components as shown in figure 3.1.2. Here I is the inclination angle of the magnetic field, U_N is the northward and U_Z the vertical component.

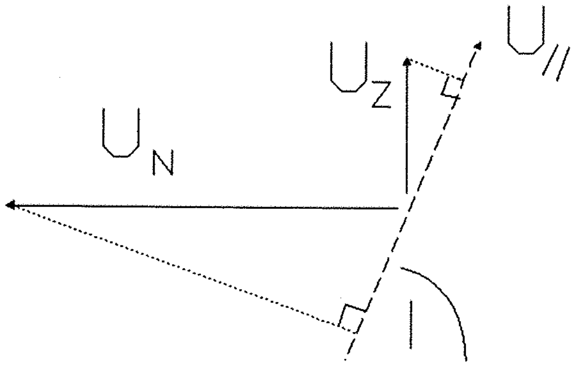

Figure 3.1.2 The vertical and horizontal components of $U_\parallel$

Since northward and upward are here defined as positive, $U_\parallel$ is written;

$$U_\parallel=-U_N\cos I+U_Z\sin I$$

(3.1.11)

By substituting for $U_\parallel$ in equation 3.1.5, the meridional wind, U_N, can be expressed in terms of the parallel ion velocity, the ion diffusion velocity and the vertical neutral wind.

$$U_N=\frac{-V_\parallel}{\cos I}+\overline{W_d}\tan I+U_Z\tan I$$

(3.1.12)

The use of this equation to derive meridional winds from incoherent scatter data was discussed by Vasseur (1969). Since then, the technique has been used by many authors (D. Rees et al (1984), Wickwar et al (1984), Burnside et al (1987), Winser et al (1988), Farmer et al (1990), Titheridge (1991), Sipler et al (1991)).

Apart from the vertical wind, all the terms on the right of equation 3.1.12 can be obtained from incoherent scatter data. If the vertical wind can be ignored, meridional winds are derived from radar data alone. It is important therefore, to know under what conditions this simplification can be made.

3.2 The importance of the vertical wind

Vertical winds are caused by the thermal expansion and contraction of the neutral atmosphere. As the temperature rises, the atmosphere expands and the scale height, kT_n/m_ng, increases. Conversely, a reduction in temperature leads to a contraction of the atmosphere and a smaller scale height. During the day, the expansion is dominated by solar heating. At dusk, the atmosphere is no longer heated by the sun and without any other energy input, it slowly cools over the course of the night. This is the case at low latitudes, where the night-time vertical winds rarely exceed 5 ms^{-1} (Burnside et al 1983). As long as the parallel ion and diffusion velocities are larger than this, it is justifiable to ignore the vertical winds when deriving meridional winds from radar data.

At high latitudes, plasma flows of several kilometres per second, caused by enhanced electric fields, are common. Frictional, or Joule heating occurs as the ions and neutrals collide with large relative velocities. In addition to this, precipitation of auroral electrons can contribute to the energy of the atmosphere. In combination, or individually, precipitation and Joule heating can cause vertical winds of many tens of ms^{-1} at night. Winds of this magnitude are comparable with the parallel ion velocity, $V_{//}$, and ambipolar diffusion velocity, W_d. Under such circumstances the vertical winds cannot be ignored. Auroral heating can be highly localised and if vertical winds are significant, it is important that the radar observes an area very close to the FPI zenith measurement. This will ensure that the two instruments measure the same feature.

3.3 Calculating the O^+-O collision parameter.

Burnside et al (1987) used the Arecibo ISR to derive meridional neutral winds for nine nights when they had simultaneous FPI measurements. For each night of data, a meridional wind was derived from the radar measurements and compared with the meridional wind measured by the FPI. Their diffusion velocity also included the effects of thermal diffusion, the force due to the temperature difference between ions and neutrals. Work by others (Titheridge et al 1991, J. Lilensten et al 1992) has indicated that thermal diffusion is much less important than was first thought.

As the vertical wind at Arecibo rarely exceeds $5ms^{-1}$, it was assumed that it could be ignored in the analysis. Because the airglow profile at this latitude is not complicated by auroral excitation, they were able to model the profile and estimate the height of the peak emission. This proved to be sufficiently high that only O^+ ions need be considered and $W_d \equiv W_d^{O+-O}$.

The O^+-O collision parameter, K_{in}^{O+-O}, was treated as the variable. In order to determine the best fit between measured and derived winds, the residual, R^2, between measured and derived winds was calculated for a range of values of a scaling factor, F, times Banks' O^+-O collision parameter.

$$R^2(F) = \frac{1}{n}\sum_{i=1}^{n}\left[U(F)_{RAD_i} - U_{FPI_i}\right]^2 \tag{3.3.1}$$

where n is the number of data points. The 'correct' value of F was taken to be where R^2 was the smallest, in other words where the derived and measured winds best agreed. The diffusion velocity, W_d is proportional to $1/\nu_{in}$, as shown in equation 3.1.6. For large values of F, equation 1.4.6 is dominated by ν_{in}^{O+-O} and as $F \to \infty$, $W_d \to$ Constant. At large values of

F therefore, the residual, R^2, becomes constant. At small values of F, the diffusion velocity is very sensitive to changes in F. This leads to an asymmetric curve when R^2 is plotted against F. Plots of R^2 against F from the data of Burnside et al (1987) are shown in figure 3.3.1. Because R^2 is less sensitive to F when F is large, F_{min} tends to have asymmetric error bars. Burnside et al defined the errors in F_{min} as the points above and below F_{min} where $R^2=2R^2_{min}$. For some of the data presented, the curve of R^2 against F does not reach $2R^2_{min}$ above F_{min} and it is not clear how the final upper error bar of 0.7 is obtained. If there is poor agreement in the comparison of the two data sets, R^2_{min} will be large. The better the agreement, the smaller R^2_{min}. From a plot of R^2 against F therefore, the accuracy of F_{min} is given by the width of the minimum, and the significance of F_{min} is determined by the value of R^2_{min}. From these nine nights of data it was found that the best agreement between the derived and measured winds occurred when the value of the O^+-O collision cross section was increased to $1.7^{+0.7}_{-0.3}$ times Banks' theoretical value. This value was just the average of all the minima. As has already been stated, the significance of each F_{min} is determined by the value of R^2_{min}. This fact seems not to have been taken into account in the final analysis.

Sipler et al (1991) used a very similar technique at Millstone Hill, to that of Burnside et al. They used 22 days of data to obtain a value of 1.9±0.15 times Banks' value.

Winser et al (1988) and Farmer et al (1990), using INDI data, inverted equation 3.1.5 to form an expression for the collision frequency. For one night of data, Winser et al (1988) obtained a value for ν_{in}^{O+-O} of 0.3 times Banks' value. Farmer et al (1990) considered the data of Winser et al and one other night of INDI data. From this, they derived a similar value to that of Winser et al. It is not clear whether either took into account the effect of O^+ ions colliding with N_2 and O_2, or the contribution of NO^+ collisions, despite (in the case of Winser et al) assuming a mean ion mass of 21 amu. This may have contributed to such an anomalous result. The contribution of the vertical winds over

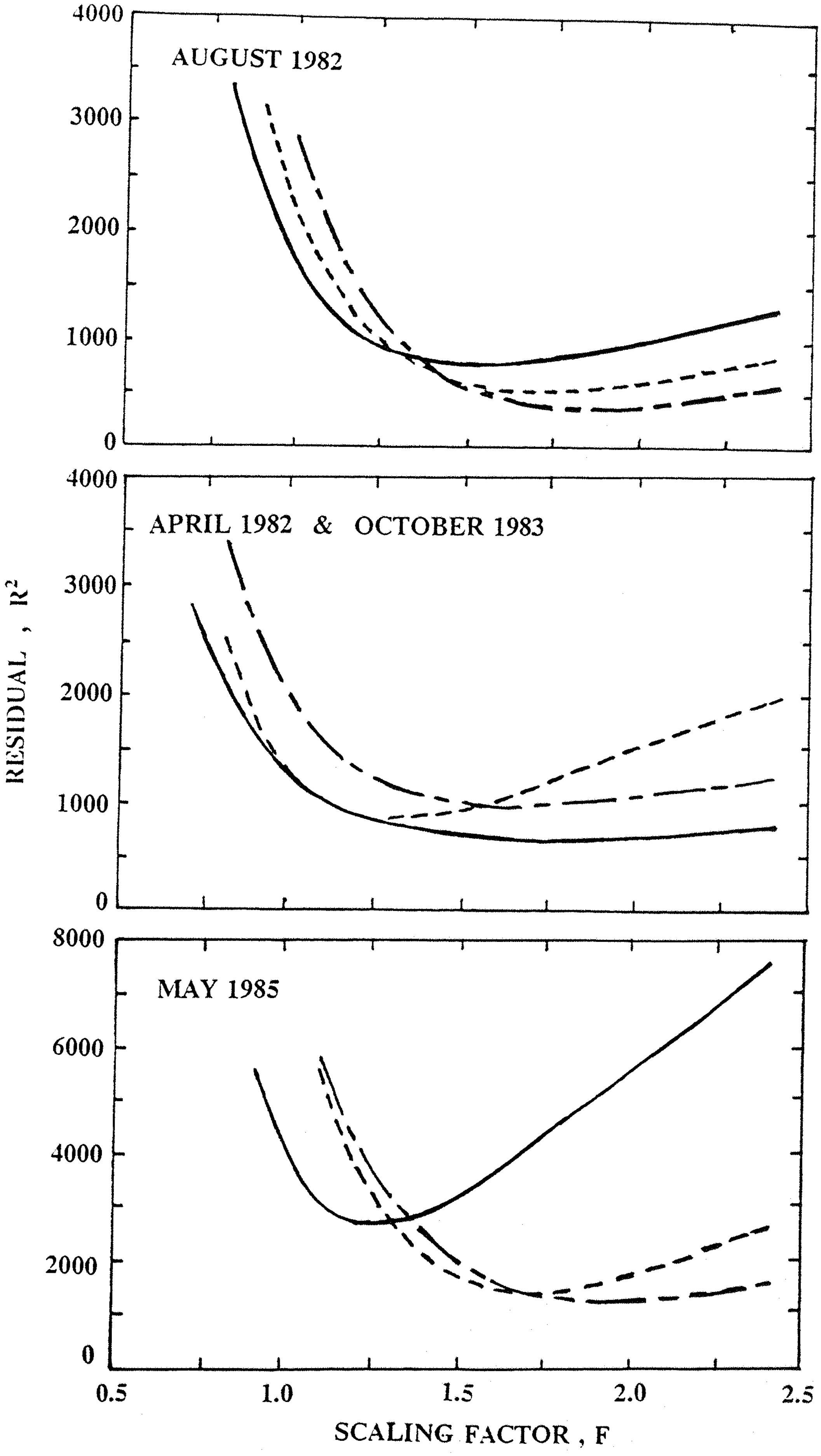

figure 3.3.1 Plots of residual against scaling factor for the data used in Burnside et al (1987). For nine nights of data.

Kiruna was discussed in both papers, with different conclusions. Winser et al found that including the vertical winds improved the agreement between the derived and measured meridional winds, whilst Farmer et al concluded the opposite. These different conclusions were based on analyses of the same data set, acquired on 9 January 1986. From a re-assessment of both data sets, and applying a consistent sign convention (positive to the north, east and up), the results of Farmer et al appear to be correct. Winser et al used the assumption that the vertical winds are constant over the scan radius of the FPI. The validity of this assumption is questionable.

Chapter 4.

An Optimised method for estimating the O^+-O collision parameter using INDI and CP data.

The purpose of this chapter is to improve upon the analysis of Winser et al (1988) and Farmer et al (1990) leading to the calculation of the O^+-O collision parameter. The FPI data were analyzed in more detail, and careful consideration was given to the collisional processes involved. Before meridional winds were derived, each data set was screened for times at which the approximations made did not apply.

Radar measurements are made at 240 km in the INDI experiment and at 278 km in the CP programs. The altitude of the peak airglow emission is difficult to model at high latitudes because of the effects of auroral precipitation (as detailed in chapter 2). The FPI measures the Doppler shift of the airglow to infer the wind speed. Vertical wind shear is limited by viscosity and as a result, the horizontal wind does not vary much over a scale height. The assumption that the neutral velocity is being measured at 240 km (Winser et al, 1988) is therefore not a critical one.

4.1 Estimating the plasma diffusion velocity, W_d.

The expression for the diffusion velocity, W_d, is given in equation 3.1.6. The pressure gradient was estimated by fitting a polynomial to the $N(T_e+T_i)$ profile at each scan position and the gradient was estimated at 240 km. The profile is only truly vertical for position e5 of INDI, and position A of the CP2 scan. For the other profiles, it is assumed that there is no horizontal variation. As the tristatic velocities in the CP scans are taken at 278 km, it is assumed that these velocities do not change with height and these values are used at 240 km. If the F2 peak is high, as in this data, this approximation is not a critical one, as the $Ne(T_e+T_i)$ gradient does not change rapidly with height between 240 and 278 km. A better approximation however would be to calculate the $Ne(T_e+T_i)$ gradient at 278 km and assume that the neutral velocity does not change rapidly with height so that its value at 240 km can be used in the comparison.

At 240 km, O^+ is the dominant ion under quiet conditions, with the proportion of NO^+ increasing with the level of auroral activity. The composition assumed at 240 km in the EISCAT analysis is 85 per cent O^+ and 15 per cent NO^+. This proportion of NO^+ was considered significantly large to be taken into account in calculating W_d. The expression for diffusion of two ion species was adopted using equation 3.1.10. By studying the assumed composition profile, p, q and dq/dh were estimated. At 240 km, p=0.15, q=0.85 and $dq/dh=5x10^{-6}\ m^{-1}$.

The neutral atmosphere model, MSIS86, was run for the appropriate time and latitude and auroral conditions. The amount of auroral activity for the model was estimated using measurements of the 10.7cm solar flux and Ap index. The output from the MSIS model was used to estimate the neutral composition. The accuracy of the model during auroral activity is not well known, and so this may well introduce a systematic error in the final analysis. With no measured neutral temperatures, it was impossible to calibrate the MSIS model. For the purposes of this study, the neutral atmosphere was considered to consist entirely of N_2, O and O_2. These concentrations were used to calculate ν_{in} for each ion species. Where neutral temperatures were required, the MSIS value was used.

Using the above method, W_d was calculated for both O^+ and NO^+ ions (equations 3.1.8 and 3.1.9). These were then combined to give an average diffusion velocity using equation 3.1.10.

4.2 Treatment of the FPI data.

The previous INDI work by Winser et al (1988) and Farmer et al (1990) assumed a constant horizontal wind velocity throughout the FPI scan, despite evidence for horizontal gradients. For this work, a more comprehensive FPI analysis was adopted (as detailed in Appendix C), following the method of Burnside et al (1981). A linear velocity gradient is assumed to exist across the area of the FPI scan, and by considering this to be caused by the divergence, shear and vorticity of the wind (Hess, 1959), the horizontal velocity gradients can be estimated. From these gradients, the wind can be modelled at any point within the FPI scan radius. In this way, it was possible to estimate the wind velocity at each position of the radar. The errors in the wind gradients mean that the most accurately modelled positions are in the centre of the scan, over Kiruna. Since the wind can be estimated at the positions viewed by the radar, it was possible to use EISCAT common program data for which there was simultaneous FPI data. Common Program 1 (CP1) and Common Program 2 (CP2) have viewing positions close to the centre of the FPI scan. The scan time of CP2, about six minutes, is within the scan time of the FPI, while in CP1, the radar remains field aligned. Common Program 3 (CP3) data was not included, as the cycle time of half an hour was considered too long.

The precision of the FPI measurements is determined by the intensity of the airglow. Typically the errors are ~30ms^{-1} and this is sufficient to observe any variation in the horizontal winds, since they can be much larger than the error. However, the vertical winds are comparatively small, even during times of auroral activity and the errors could therefore be ~100 per cent. In addition, only one vertical measurement is made per scan (every 19 minutes) and these data have to be linearly interpolated to coincide with any radar measurement. As U_z is poorly defined, this is adds to the uncertainty. As a result, U_z is the major source of error in the analysis. In order that the vertical winds may be ignored, data from times of auroral heating should be rejected.

4.3 Rejection of data with an anomalous ion composition.

One of the parameters fitted to the incoherent scatter spectrum is T_i/m_i (Appendix A). By assuming an ion composition model, m_i is estimated and hence T_i is obtained. At 240 km, the composition is assumed to be 15 per cent NO^+ and 85 per cent O^+. This gives a mean ion mass of 18.1 amu. At times of extreme auroral activity, Joule heating enhances the ion temperature. This alters the reaction rates so that chemical equilibrium favours a larger fraction of molecular ions and the mean ion mass increases. As m_i is fixed in the analysis, T_i is underestimated at these times. After such an event, the enhanced ion temperature quickly dissipates as the energy is transferred to the neutral atmosphere by collisions. As the ion temperature decreases, the plasma returns to its original composition. The neutral temperature only increases slightly because of the large thermal capacity of the neutral atmosphere.

Since the determination of the ion-neutral collision frequency critically depends on the temperature and composition of the ionosphere, it is important to reject data from times when the ion composition differs greatly from the model value. Since the composition changes rapidly in comparison with the time between measurements, the composition at the time of each measurement can be considered to be independent of each other.

By considering the simplified ion energy equation,

$$T_i = T_n + \left(\frac{m_n}{3k}\right) |V-U|^2 \qquad \textbf{(4.3.1)}$$

it is possible to estimate the approximate ion temperature enhancement due to Joule heating. If the estimate of T_i is very different from the measured T_i, it is likely that the actual ion composition differs from the assumed value. Comparing the expected and measured ion temperatures in this way enables a criterion for rejecting data to be established. If the estimate of T_i differs from the measured T_i by more than 20 per cent, the data are discarded. This method has the added advantage of rejecting data from times when the vertical winds are expected to be large.

By restricting the derivation of neutral winds to times of little or no ion heating, the problems of ion composition and large vertical winds are reduced. At these times, the simple composition model can be applied to the incoherent scatter data and the vertical winds are likely to be small. The latter may not be true for a single night, but the combination of several nights of data should remove any systematic errors in this assumption. Because the vertical wind is so poorly defined, it is desirable to use data from times when it can be ignored.

4.4 Calculating the O^+-O collision parameter.

It was decided to analyze all the INDI data using a method similar to that of Burnside et al, but instead of considering R^2 for each value of F it would be ideal to calculate χ^2, a measure of the quality of the fit between the derived and measured winds. χ^2 is written

$$\chi^2(F) = \sum_{i=1}^{n} \frac{[U(F)_{RAD_i} - U_{FPI_i}]^2}{\sigma_i^2} \qquad \textbf{(4.4.1)}$$

where σ_i is the expected error for each pair of points, n is the number of points, F is the scaling factor for the O^+-O collision parameter, U_{RAD} is the radar derived wind and U_{FPI} is the FPI measured wind. Using this method, each data set is weighted by its standard deviation and the values of χ^2 can be summed over all the data. This incorporates any variation in the quality of the data. From the resultant sum, the most probable value of F can be found using the relationship;

$$P(F) \propto \exp\left(-\frac{1}{2}\chi^2(F)\right) \qquad \textbf{(4.4.2)}$$

(e.g. Smart, 1958), where P(F) is the probability distribution of F. The most probable value of F corresponds to the maximum value of this function.

In order to adjust the value of K_{in}^{O+-O}, the expression for the O^+ collision frequency was rewritten as;

$$\nu_{in}^{O^+} = 6.82x10^{-16}[N_2] + 6.64x10^{-16}[O_2] + K_{in}^{(O^+-O)}[O].F \qquad \textbf{(4.4.3)}$$

where F is a multiplication factor.

W_d was calculated over the course of each night and the meridional winds were derived using equation 3.1.12. By comparing the derived wind with the FPI measurements, a residual R^2 was calculated, where;

$$R^2(F) = \frac{1}{n}\sum_{i=1}^{n}\,[U_{RAD_i} - U_{FPI_i}]^2 \qquad \textbf{(4.4.4)}$$

This process was repeated, and R^2 was calculated for values of F from 0.1 to 5.0. R^2 was then plotted as a function of F. The minimum of such a curve corresponds to the value of F which produced the closest agreement between measured and derived winds. For this minimum value of R^2, a histogram of N(r) per r was plotted, where r is the size of an individual residual. A check that the distribution of residuals was approximately Gaussian ensured that no one data point dominates the minimisation process.

Owing to the spatial variability of the ionosphere, the precision of the radar data is not representative of the true uncertainty. As a result, σ_i, the expected error between two data points cannot be calculated reliably so that the full χ^2 test cannot be used for each individual case to show the extent to which the residual deviations, r, can be explained by the expected errors, σ_i. However, the χ^2 test can be used to identify cases where the mean value of r is significantly different from zero i.e. where there is a systematic offset between U_{RAD} and U_{FPI} which cannot be explained by the uncertainty in F. To carry out this test σ^2 is determined from the root mean square (r.m.s.) deviation of N(r) about zero, and the expression for χ^2 can be written as;

$$\chi^2 \approx \frac{1}{\sigma^2}\sum\,[U_{RAD_i} - U_{FPI_i}]^2 \qquad \textbf{(4.4.5)}$$

For purely random errors in U_{RAD} or U_{FPI} this will, of course, give a value of n but if there is a significant offset of U_{RAD} from U_{FPI} then the minimum value of χ^2 will be greater than $n \pm \sqrt{2n}$. For example, in the initial analysis, where the vertical wind U_z was ignored, the results from CP2C on 12 January 1991 could be eliminated on this criterion (see table 4.5.1). In this case there was a large vertical wind which, if ignored, introduced a significant systematic error. This was confirmed when the analysis was repeated with a correction for the vertical wind: the results from CP2C on 12

January 1991 are now acceptable (see table 4.5.2) but four other sets of data presented in this table (the results from INDI on 17 February 1988 and from CP1 on 13 February 1991) must now be eliminated, presumably because the correction for U_Z is itself incorrect.

In addition to the vertical wind data, a low signal to noise ratio (SNR) in the radar data can also lead to poor agreement between derived and measured winds. This can be seen by comparing the quality of the data from the seven positions of the INDI scan (see Appendix D). The northern most positions are furthest from the receiving sites and this poor geometry results in a lower SNR. The quality of the radar data also improved after the summer of 1987, when the SNR was increased by the addition of cooled pre-amplifiers at Kiruna and Sodankylä which reduced the system noise.

Even if χ^2 is less than $n \pm \sqrt{2n}$, however, it still does not follow that the value of F which gives a minimum value of χ^2 using the above procedure is always valid. It is possible that a systematic offset between U_{RAD} and U_{FPI} is too large to be explained by the uncertainty in F but too small compared with the random errors in measurement to give a value of χ^2 greater than $n \pm \sqrt{2n}$. This occurs, for example, when the first three positions of INDI are used and deviations as large as 2000 ms^{-1} are observed. It is, of course, an advantage of using χ^2 rather than R^2 that after aggregation of several sets of data, those with large values of σ^2 will be given very low weight. Nevertheless, the principle of χ^2 aggregation assumes that the errors are random and Gaussian and where very large deviations are observed, any systematic errors will escape the "$n \pm \sqrt{2n}$" test. In other words, data with large errors can - at best - make very little contribution to the determination of F and - at worst - can introduce a small systematic error. It was therefore decided to eliminate data sets where deviations greater that 300 ms^{-1} were recorded.

Finally, there are some cases which pass the "$n \pm \sqrt{2n}$" criterion and where the calculated deviations are always less than 300 ms^{-1}, but the plot of χ^2 versus F shows a monotonic decrease as F increases from 0.1 to 5.0 (e.g. 12 January 1991 in figure 4.4.3). In such cases, W_d is so small for F=5.0 that any further increase in F (by increasing K_{in}^{O+-O}) has virtually no effect on the residual ($U_{RAD} - U_{FPI}$). In such cases, where changes in the collision frequency cannot remove a systematic offset, the deviations must be determined by some other error and hence cannot provide any information on the true value of F. Although the results may appear to reject low values of K_{in}^{O+-O}, even this is invalid. The only certain interpretation is that when W_d is small, some systematic error overwhelms the variation of F and only by chance appears to reject low values of K_{in}^{O+-O}. Such cases must therefore be rejected.

A similar argument applies when χ^2 appears to increase monotonically as F increases from 0.1 to 5.0 (e.g. positions e1 and e2 of INDI on 21 January 1990). Such data sets usually occur for small values of W_d with the consequent insensitivity to K_{in}^{O+-O} and although further reduction of F must eventually lead to a minimum value of χ^2, these data sets are also invalid. Only when $\chi^2(F)$ shows a clear minimum in the range $n \pm \sqrt{2n}$ for a value of F between 0.1 and 5.0 (e.g. 21 January 1990 in figure 4.4.3) can the data be used to determine the optimum value of F. However, even for these cases, the possibility of a biased value resulting from an unknown systematic error must be considered.

These criteria can be illustrated if the analysis of two data sets is examined in detail. The two examples were chosen to demonstrate the effect of the quality of fit in the determination of the O^+-O collision parameter. In the first example, position e7 of the INDI scan from 21 January 1990, ambipolar diffusion makes a small but significant contribution to the determination of the meridional wind, while on the 12 January 1991, the vertical wind dominates the derived meridional wind. Figure 4.4.1 shows the relative magnitude of each component for both examples. After removing data which does not conform to the assumptions made about the ion composition, the total residual, R^2, between measured and derived winds is calculated for the given range of values of F. The lowest value of R^2 corresponds to the value of F which produces the best agreement between measured and derived winds. At R^2_{min} the standard deviation, σ, is determined from

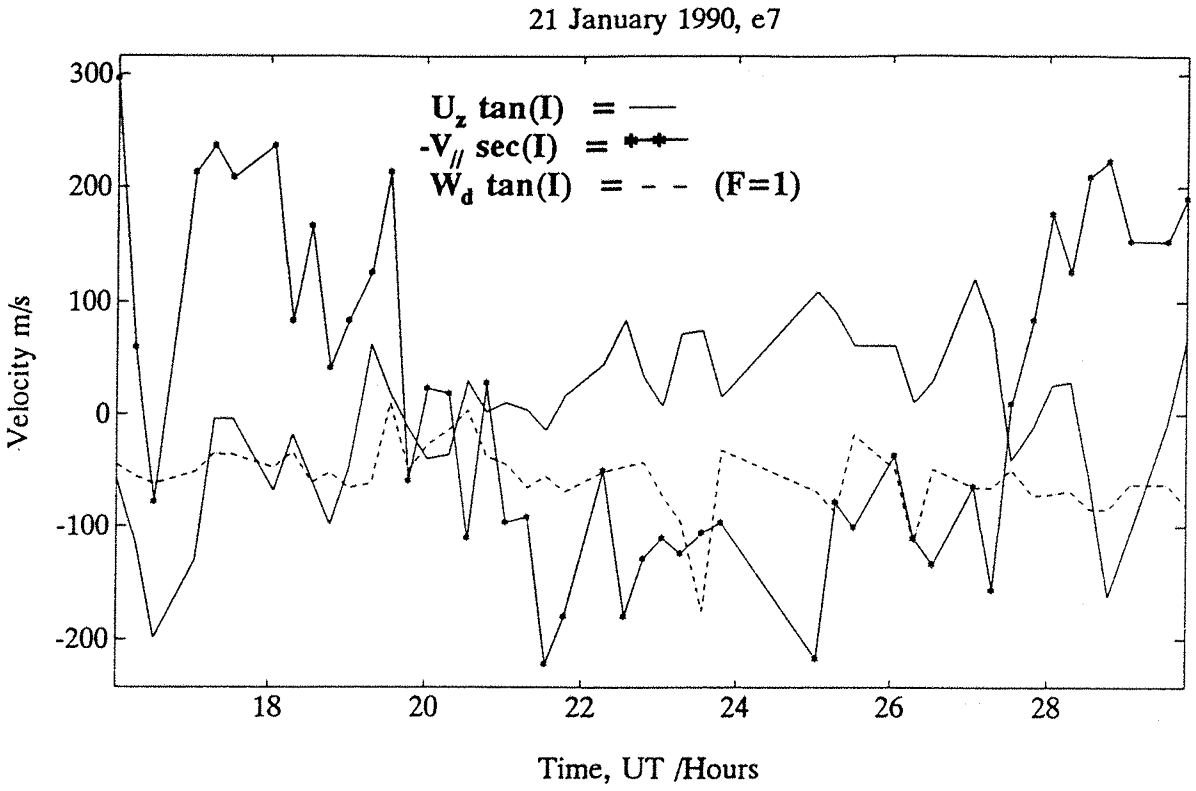

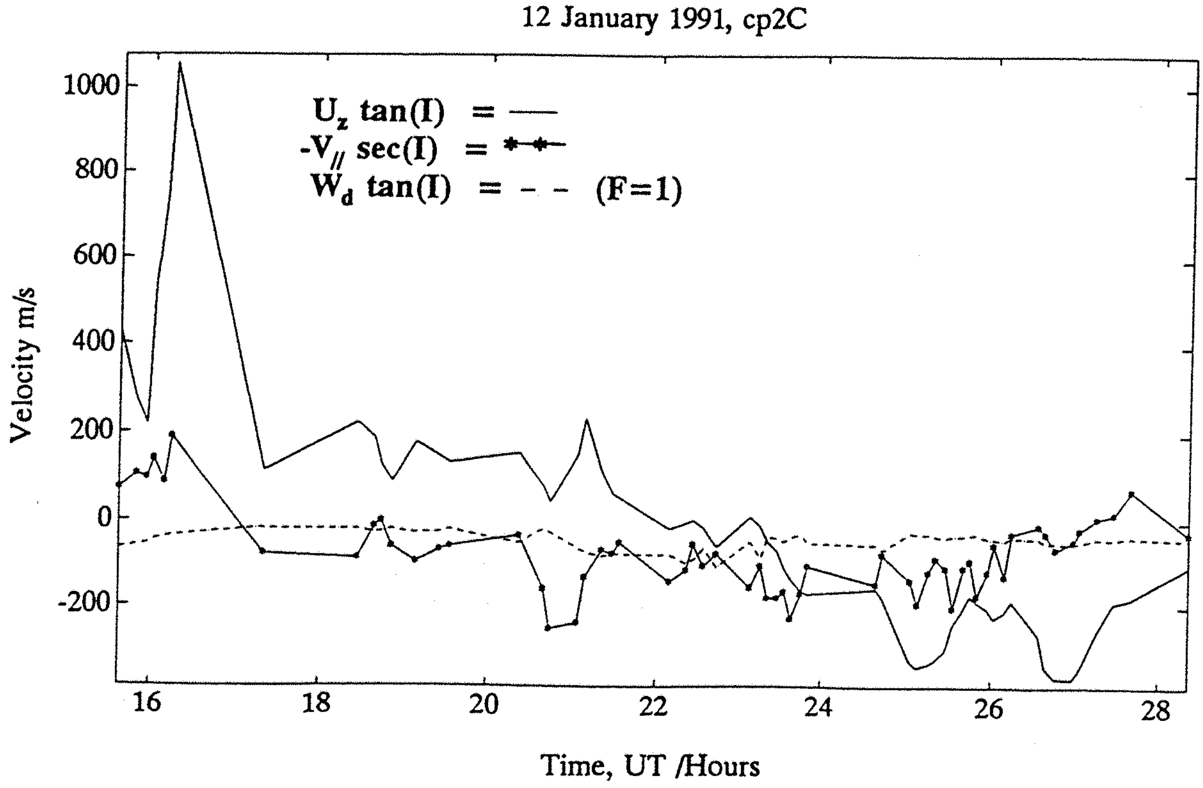

figure 4.4.1 **Two plots showing the contribution to the derived meridional wind of the vertical wind U_z, parallel ion velocity $V_{//}$, and ambipolar diffusion velocity W_d. All three components contribute to the derived wind on 21 January 1990, but the vertical wind dominates the fitting process for the 12 January 1991 data.**

the distribution of the individual residuals, r_i. Figure 4.4.2 shows the distribution of residuals on each night. The agreement is much better for the 21 January 1990 than for 12 January 1991. As a result the distribution is much narrower and the standard deviation is smaller. χ^2 is calculated by weighting R^2 for each data set by its standard deviation. The plots of χ^2 against F for the two examples are given in figure 4.4.3. Both sets of data meet the first criterion, with the value of χ^2_{min} lying within the range $n \pm \sqrt{2n}$. For 21 January 1990 $\chi^2_{min}=46$ and n=46 which gives a range of 46 ± 10. For 12 January 1991 $\chi^2=53$ and n=50 which gives a range of 50 ± 10.

Both examples also meet the second criterion, with the residual values being smaller than 300 ms^{-1}. However, only one of the days meets the final criterion.

The ambipolar diffusion term contains the collision frequency and so the sensitivity of χ^2 to the value of F is determined by the contribution of W_d to the derived wind. Since the derived winds are not dominated by any one component on 21 January 1990, the contribution of W_d is significant and the plot of χ^2 against F has a pronounced minimum. The sharper the minima, the more sensitive χ^2 is to the value of F. In contrast, the poorly defined vertical wind dominates the derived meridional wind on 12 January 1991. This results in a poor agreement between the derived and measured meridional winds. Since U_z dominates the derived wind, χ^2 is not sensitive to the value of F and so no minimum occurs. It is clear that no value of F can give a clear minimum value for χ^2. In other words, the deviation of U_{RAD} from U_{FPI} is not a result of an incorrect collision frequency which can be adjusted by varying F but is dominated by some other error. In this case, the error is almost certainly an error in the assumed value for the vertical wind.

The precision of a result is more easily visualised by plotting the probability distribution, P(F) as given in equation 4.4.2. Figure 4.4.4 shows the probability distributions for the chosen range of values of F. These distributions have been normalised since it is the shape which is of interest. For the 21 January 1990, the most probable value of F is 1.0 with a range of possible values

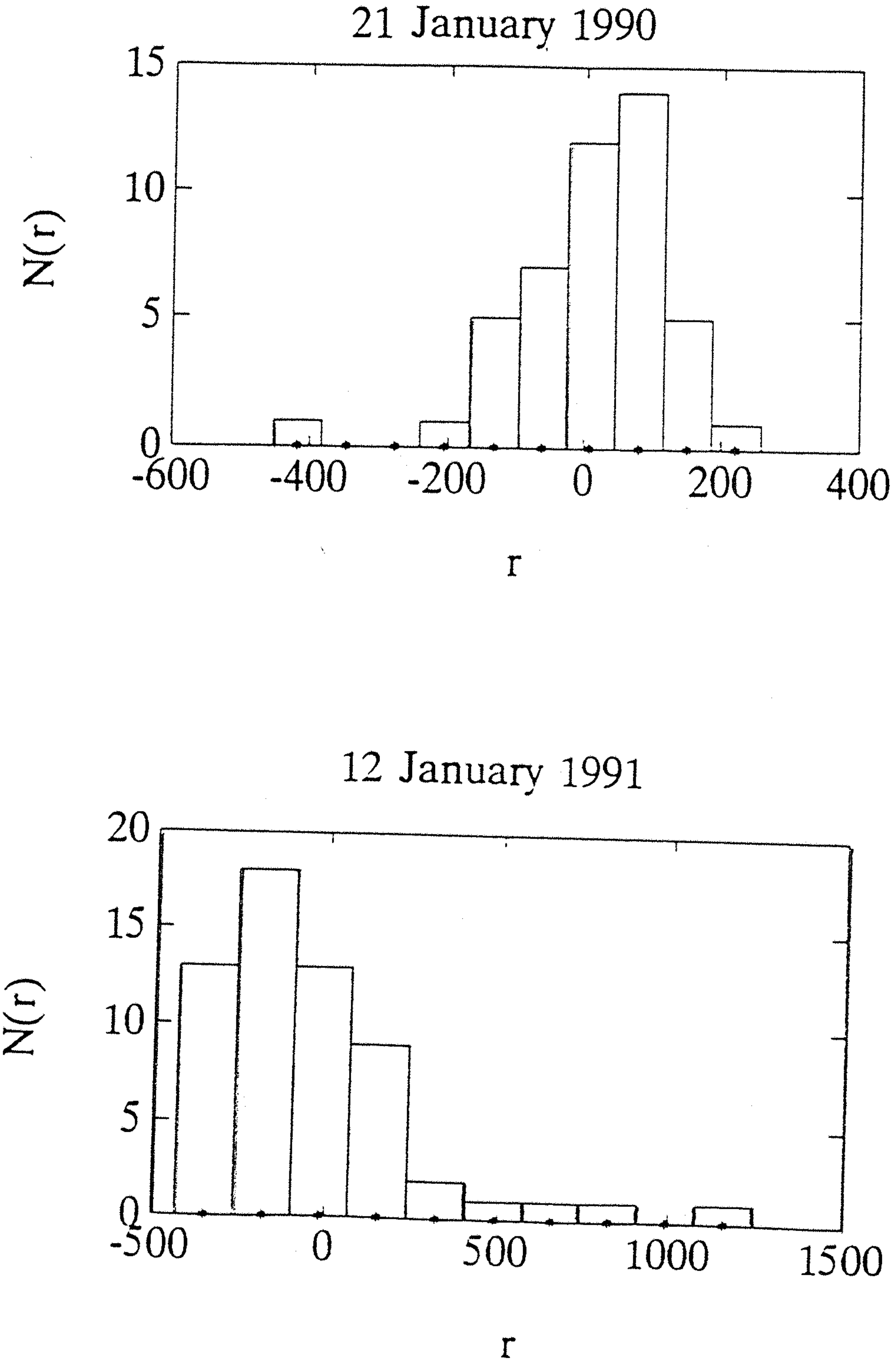

figure 4.4.2 The distribution of residuals between measured and derived winds for 21 January 1990 and 12 January 1991. It can be seen that the standard deviation is much larger for 12 January 1991, implying a poorer fit of the data on this night.

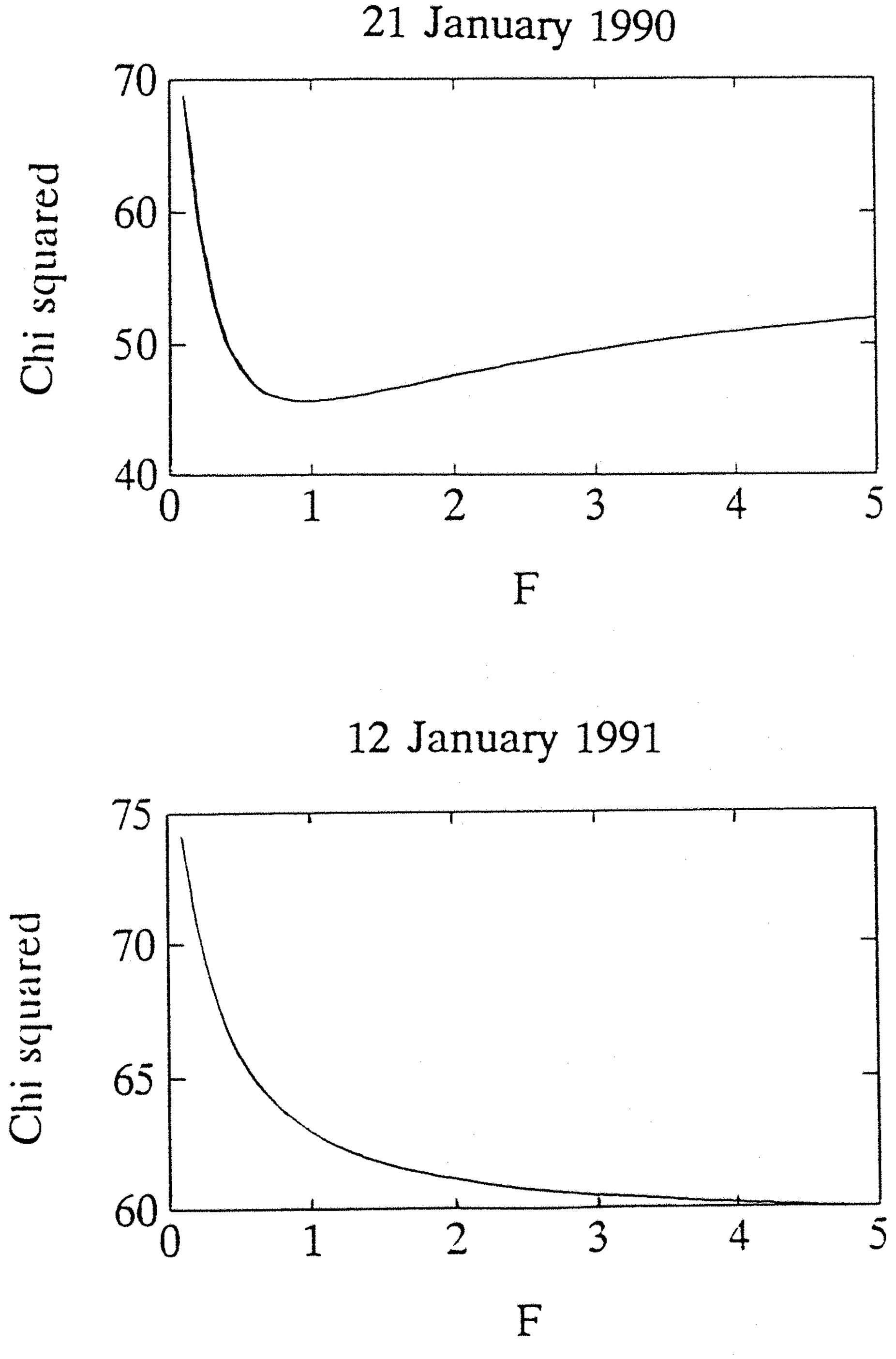

figure 4.4.3 χ^2 **against F for 21 January 1990 and 12 January 1991. Because the derived wind was dominated by the vertical wind in the 12 January 1991 data,** χ^2 **is less sensitive to changes in F and there is no minimum.**

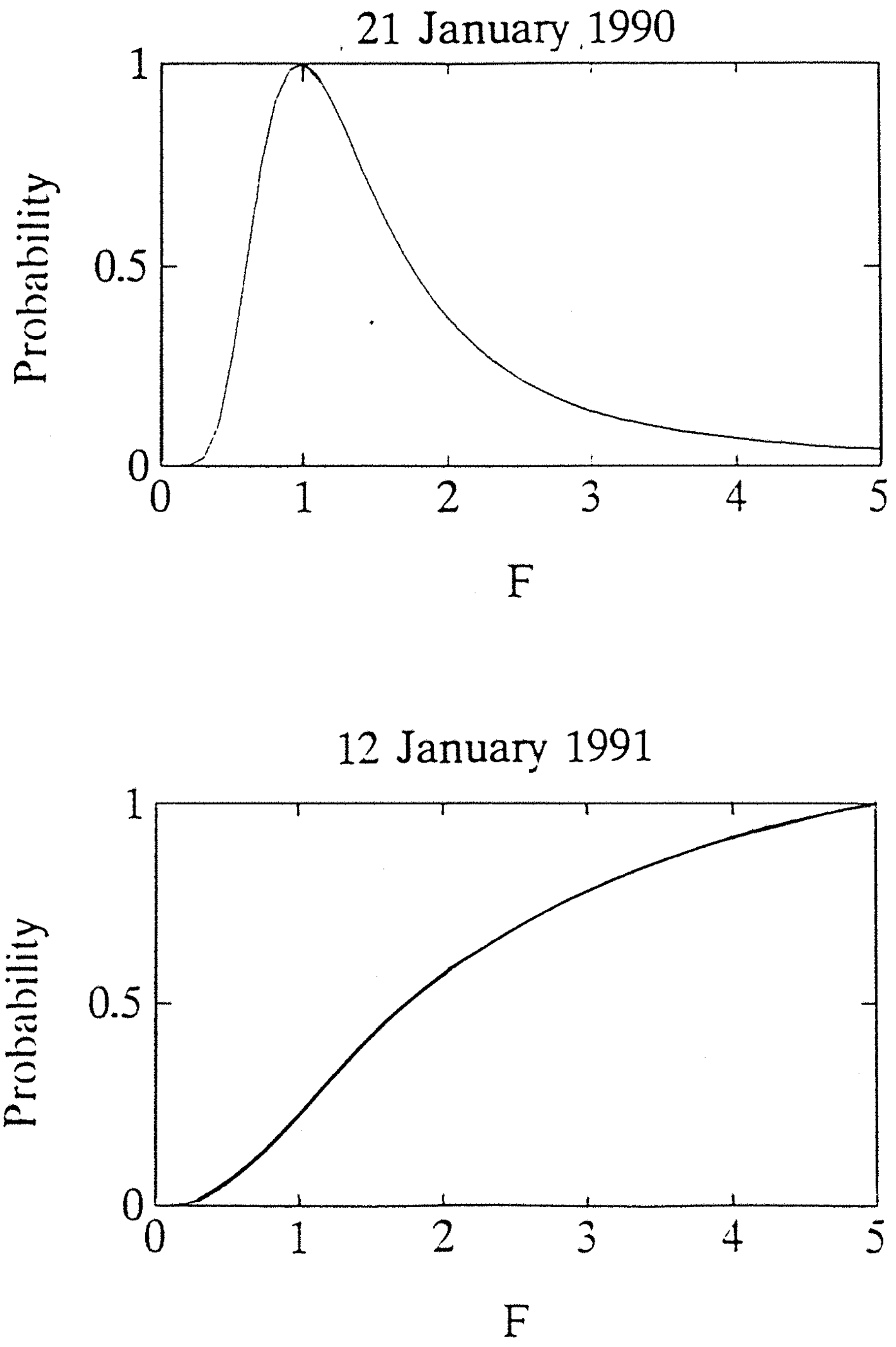

figure 4.4.4 Normalised probability distributions for 21 January 1990 and 12 January 1991. Since agreement between measured and derived winds was much better for 21 January 1990 than for 12 January 1991, the most probable value of F is better defined on this night.

from 0.3 to above 5.0. The value of F indicated by the 12 January 1991 data appears to be greater than 0.6 but even this cannot be assumed to be valid.

4.5 The data and results.

Not all the original INDI data were suitable for the analysis. Before each data set was analyzed, the FPI data were compared with measurements from an all sky camera to ensure that cloud was not affecting a true reading from the airglow. From seven nights of INDI data, only four had clear skies. In addition to these, four nights of CP data from the winter of 1991 were used for which simultaneous FPI data were available.

For all the nights used, the effect of Joule heating was estimated, and data which did not conform to the assumptions made in section 4.3 were rejected. The remaining data were analyzed both with and without the vertical winds. If the vertical winds are ignored, all positions of the radar can be used. However, since the vertical wind velocity may be different at different positions and no information about this variation is available, only the radar positions nearest Kiruna can be considered if the vertical winds are included.

4.5a Analysis without vertical wind data.

For all positions on the seven nights of data, vertical winds were ignored and meridional winds were derived from the radar data for a range of values of the O^+-O collision parameter. These were compared with the concomitant FPI data and χ^2 was calculated as a function of F for each position of the radar.

For each position of the radar, plots are presented of the zonal and meridional ion velocities, V_{pe} and V_{pn}, ion temperature, T_i and vertical winds, U_z. These give an indication as to the activity throughout each night. Times of excessive Joule heating are removed before the radar data are compared with the FPI data in the last four plots. The first of these compares the derived and measured meridional winds at $F=F_{min}$. The second is the distribution of residuals. The third plot demonstrates how χ^2 varies with F, and the last is the resultant (normalised) probability distribution.

The data used are listed in table 4.5.1, along with the number of points, χ^2_{min} and F_{min} for each radar position. Plots for each position are presented in Appendix D.

DATE	TYPE	POS.	n_{USED}	$n_{REJECTED}$	χ^2_{min}	F_{min}
9:01:86	INDI	e1	16	2	19.1	0.1
9:01:86	INDI	e2	14	3	13.0	> 5.0
9:01:86	INDI	e3	18	1	21.7	> 5.0
9:01:86	INDI	e4	16	0	15.2	3.2
9:01:86	INDI	e5	17	1	16.9	> 5.0
9:01:86	INDI	e6	15	3	14.4	4.3
9:01:86	INDI	e7	17	2	19.6	> 5.0
17:02:88	INDI	e1	25	12	24.0	> 5.0
17:02:88	INDI	e2	26	11	27.1	> 5.0
17:02:88	INDI	e3	22	14	24.7	> 5.0
17:02:88	INDI	e4	27	10	31.4	> 5.0
17:02:88	INDI	e5	25	13	25.2	> 5.0
17:02:88	INDI	e6	30	10	30.7	> 5.0
17:02:88	INDI	e7	23	12	22.0	1.1
11:01:89	INDI	e1	54	2	55.9	> 5.0
11:01:89	INDI	e2	37	3	36.0	2.4
11:01:89	INDI	e3	49	7	50.7	3.5
11:01:89	INDI	e4	52	4	52.6	> 5.0
11:01:89	INDI	e5	52	4	58.9	> 5.0
11:01:89	INDI	e6	45	9	44.2	1.4
11:01:89	INDI	e7	48	6	47.2	1.2
21:01:90	INDI	e1	40	15	39.1	0.1

21:01:90	INDI	e2	41	11	40.3	0.1
21:01:90	INDI	e3	42	11	41.0	1.5
21:01:90	INDI	e4	37	11	38.5	1.0
21:01:90	INDI	e5	43	12	42.9	0.5
21:01:90	INDI	e6	43	9	44.0	0.3
21:01:90	INDI	e7	46	6	46.7	1.0
11:01:91	CP2	CP2A	79	68	78.0	1.1
11:01:91	CP2	CP2B	83	57	82.7	3.8
11:01:91	CP2	CP2C	101	39	101.0	1.3
12:01:91	CP2	CP2A	50	36	59.9	> 5.0
12:01:91	CP2	CP2B	57	40	56.1	> 5.0
12:01:91	CP2	CP2C	59	34	75.3	> 5.0
12:02:91	CP1	F. Aln	115	20	114.0	0.8
13:02:91	CP1	F. Aln	109	5	108.5	0.5

Table 4.5.1

The three criteria are then applied in turn. For each of the radar positions taken individually, χ^2_{min} lies within the range $n \pm \sqrt{2n}$, with the exception of CP2C from 12 January 1991. On the other hand, all examples from position e1 to e4 of the INDI experiment (with the exception of position e4 on 21 January 1990) included values of r greater than 300 ms^{-1}, partly due to random noise errors in the tristatic radar measurements made with an unsuitable geometry. Most of these data sets would also have been eliminated on the third criterion as χ^2_{min} suggested values of F greater than 5 or less than 0.1. In addition, positions e5, e6 and e7 on 9 January 1986 are eliminated on this criterion. Similarly, data from CP2A and CP2B on 12 January 1991 should be eliminated.

Summarising this section, it appears that the only observations that always provided valid data with $\chi^2_{min} < n \pm \sqrt{2n}$, the largest deviations between U_{RAD} and U_{FPI} < 300 ms^{-1} and a clear minimum are positions e6 and e7 of the

INDI experiment and position C of CP2. These were, of course, the very positions where it was possible to include vertical winds in the analysis and this was the next step in the study.

4.5b Analysis with vertical winds.

If the vertical winds are included in the analysis, the positions used must be restricted to those nearest Kiruna, where the vertical measurement is made. Plots for each position used in this analysis are presented in Appendix E. The data used are summarised in table 4.5.2.

DATE	TYPE	POS.	n_{USED}	$n_{REJECTED}$	χ^2_{min}	F_{min}
9:01:86	INDI	e5	17	1	17.7	> 5.0
9:01:86	INDI	e6	15	3	14.0	> 5.0
9:01:86	INDI	e7	17	2	20.4	> 5.0
17:02:88	INDI	e5	25	13	52.0	> 5.0
17:02:88	INDI	e6	30	10	63.0	> 5.0
17:02:88	INDI	e7	23	12	30.8	> 5.0
11:01:89	INDI	e5	52	4	53.2	4.4
11:01:89	INDI	e6	45	9	44.0	1.6
11:01:89	INDI	e7	48	6	47.0	1.0
21:01:90	INDI	e5	43	12	42.3	0.6
21:01:90	INDI	e6	43	9	42.3	0.3
21:01:90	INDI	e7	46	6	45.6	1.0
11:01:91	CP2	A	79	68	78.1	0.8
11:01:91	CP2	C	102	39	102.2	1.4
12:01:91	CP2	A	50	36	54.1	> 5.0
12:01:91	CP2	C	59	34	60.6	> 5.0
12:02:91	CP1	F. Aln	115	20	114.8	> 5.0
13:02:91	CP1	F. Aln	109	5	127.6	> 5.0

Table 4.5.2

The horizontal extent of the vertical winds is unknown. It is likely that the winds are very localised, since it would require an enormous amount of energy to heat the atmosphere over a horizontal range of hundreds of kilometres. The vertical winds should strictly only be used with radar measurements from above Kiruna. This would mean only a small fraction of the data could be used. The initial set included all positions from those on the Tromsø field line to those above Kiruna (i.e. positions e5, e6 and e7 of the INDI experiment, positions A and C of CP2 and CP1) The statistical methods described in section 4.4 were applied. A smaller set of data was also considered which was restricted to the positions closest to Kiruna (i.e. e6 and e7 of the INDI experiment and CP2C) and these data were combined without regard to the selection criteria in order that a comparison of results could be made.

If we apply the first criteria, ($\chi^2_{min} < n \pm \sqrt{2n}$) all the data on 17 February 1988 is disregarded as well as the CP1 data from 13 February 1991. When the second and third criteria are applied, the noisy data from 1986, together with data from CP2A and CP1 must also be eliminated. This results in a data set consisting of positions e5 to e7 from the INDI experiment on 11 January 1989 and 21 January 1990.

It is encouraging that the data selection criteria derived in section 4.4 are almost exactly the same data as those restricted to the positions chosen to provide the most reliable direct measurement of the vertical wind.

For the data sets it is valid to aggregate the different data sets to give a combined determination of $\chi^2(F)$ as indicated in equation 4.4.1, and in this context it is also valid to take the individual values of σ^2 as σ_i^2 in the equation.

For the data selected by the three criteria, $\chi^2_{min}=295.1$ for 287 points, and so the minimum value lies well within the expected range. The most probable value of F suggested by this analysis is 1.2. These results are illustrated in figure 4.5.1.

When the analysis is restricted to positions e6, e7 and CP2C only, and the selection criteria are dropped, the total

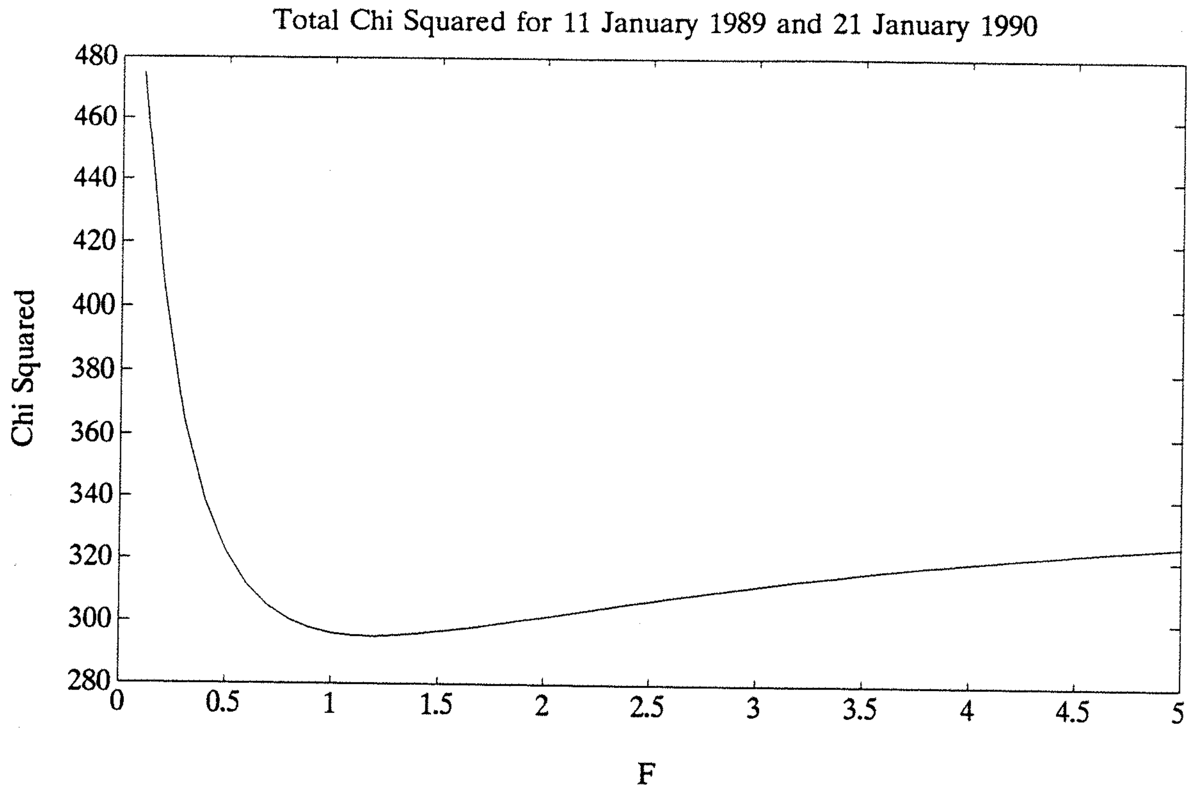

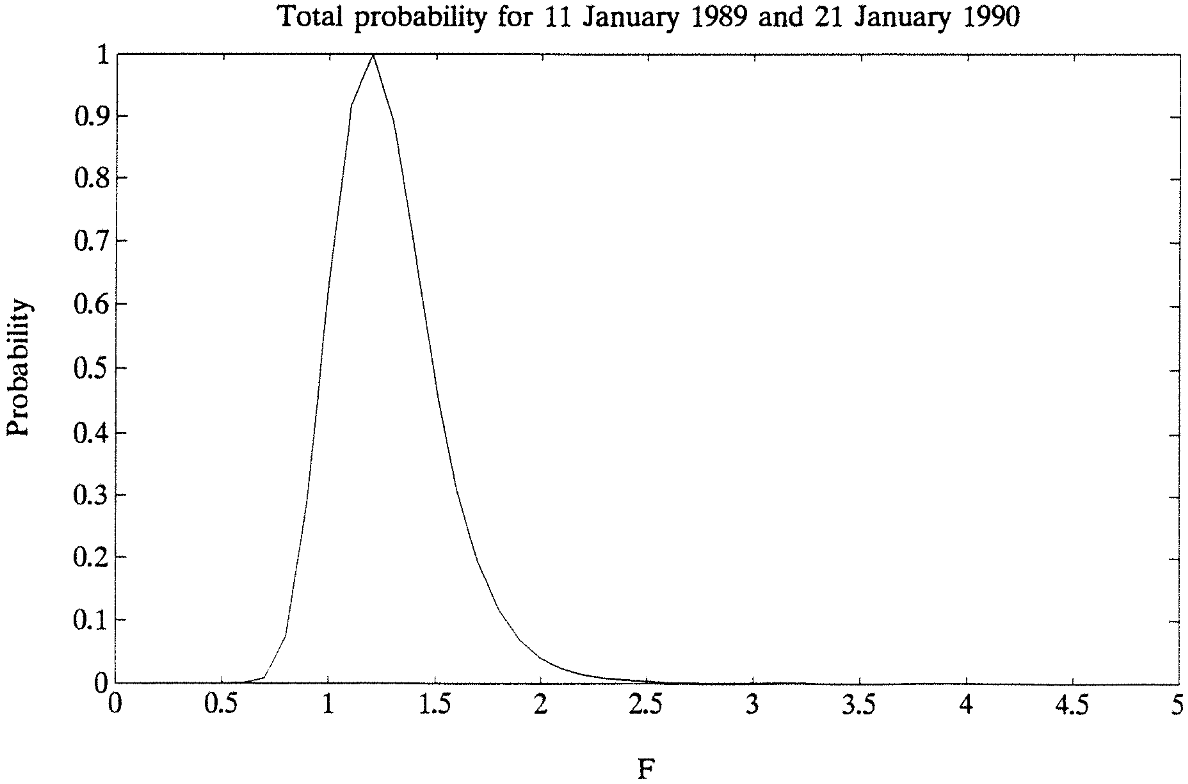

figure 4.5.1 Plot of χ^2 and probability against F for positions e5, e6 and e7 from the INDI data taken on 11 January 1989 and 21 January 1990. Vertical wind data has been included in the analysis.

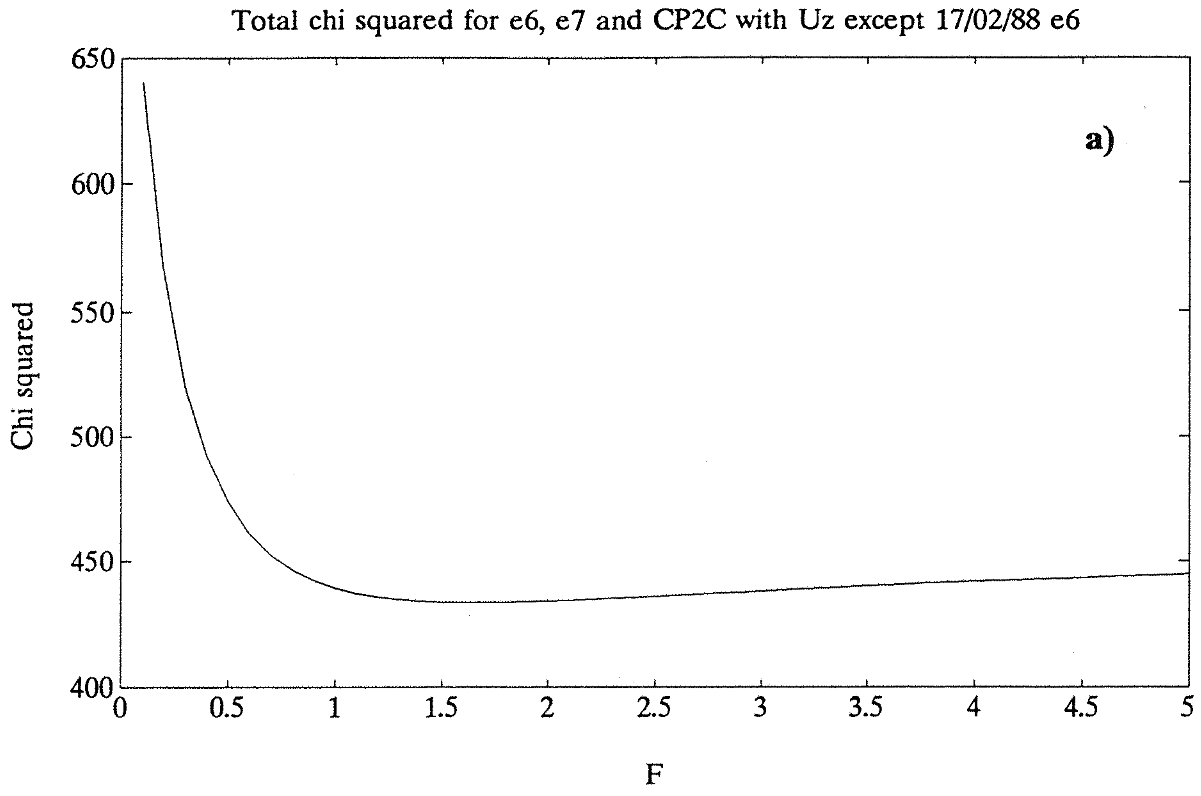

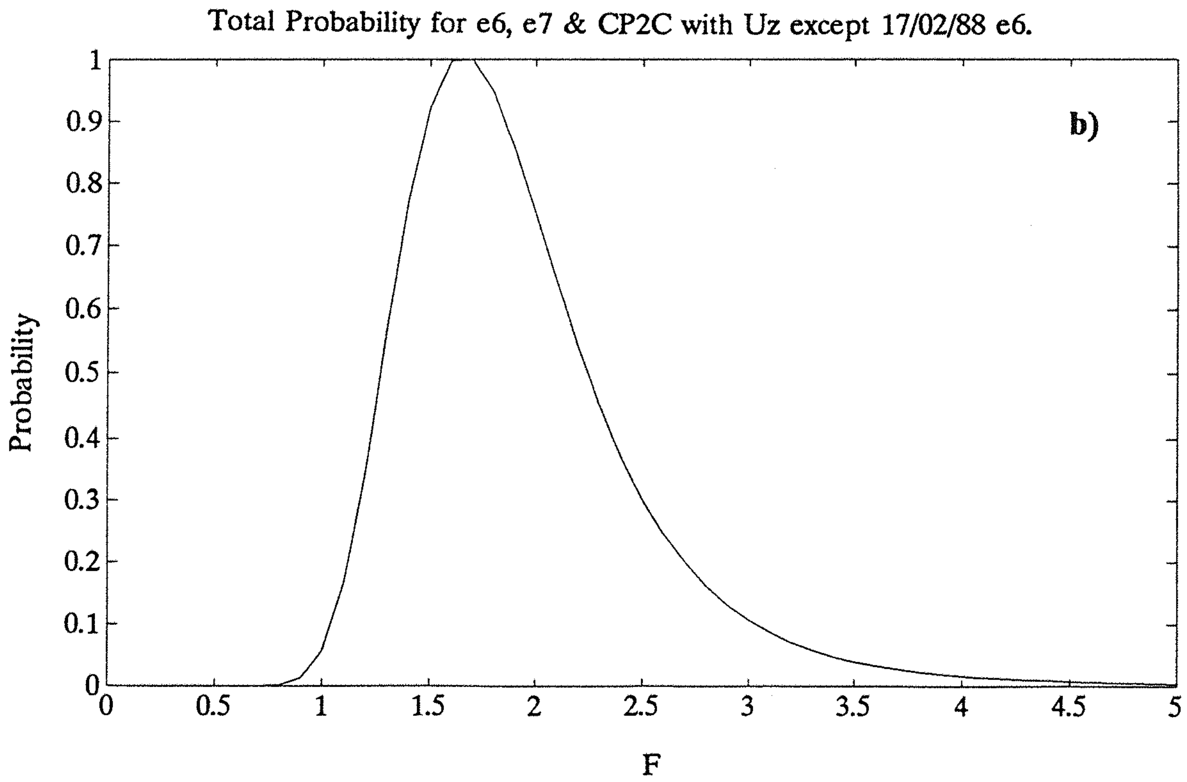

figure 4.5.2 Plot of χ^2 and probability against F if the data is restricted to positions e6 and e7 from INDI and CP2C. Vertical wind data has been included in the analysis.

χ^2_{min} is 433 for 397 points. The expected χ^2 for this is 397 ± 28. χ^2 against F for these data is plotted in figure 4.5.2(a). By considering the data in this way, the most probable value of F becomes 1.7.

4.6 Conclusions

In section 4.5a the analysis did not include the vertical wind and data from all the radar positions were used. By applying the selection criteria, the analysis suggested that the best data were taken at positions nearest to Kiruna, where the vertical wind measurement is made. Since at these positions, it is possible to include the vertical wind data in the analysis, this was done and the results were considered in section 4.5b.

The data taken at the centre of the FPI scan were analyzed in two ways. Firstly by applying selection criteria to the data in order to eliminate bad data. This resulted in a value of F=1.2.

In addition, data was considered which was chosen purely on the grounds of its proximity to Kiruna. The result of this analysis was a most probable value of F=1.7. The range of possible values extends from 1 to 4. More data needs to be added if the width of this distribution is to be reduced. The fact that the value of F is very dependent on the type of analysis used suggests that more work is needed if a reliable method of determining K_{in}^{O+-O} is to be found.

It is also important to determine the spatial extent of the vertical winds in order to determine which data should be used in the analysis. Ideally the analysis should be restricted to those positions for which there is a direct measurement of the vertical wind.

It is very important that the significance of data in similar studies be determined. If this is done, the results from all such studies can be combined in a weighted average value of F.

Chapter 5

The contribution of ion drag to the acceleration of the neutral wind.

In section 1.2 the forces controlling the horizontal movement of the neutral atmosphere were discussed. In this chapter, the importance of ion drag will be considered, using examples from three data sets containing different amounts of ion drag (using, in this case, the Banks value).

It was stated in section 1.1 that at EISCAT, most of the enhanced ion drifts occur zonally, as this latitude is at the outer boundary of the plasma convection cell. As a result, the effect of ion drag on the neutral wind is most apparent in the zonal direction, where the relative velocity between the ions and the neutrals is greatest. The dominance of ion drag is governed by the electron density and the magnitude of the ion drifts. In the absence of ion drag, the neutral wind is accelerated by advection, pressure gradients, the coriolis effect and viscosity.

For the first example, 11 January 1989, the direction of the ion drift throughout the night is indicated by figure 5.1. The frequency with which the ion drift occurred in a particular direction is indicated by the size of each bin. This plot does not contain information about the magnitude of the ion drift. The velocity of the ions rarely exceeded 500 ms^{-1} in either the zonal or the meridional directions (figures 5.2a and 5.2b) and so the ion drag term, although contributing to the neutral wind momentum equation, does not dominate. The zonal wind (figure 5.2c) was small, not exceeding 80 ms^{-1}, while meridionally, the wind was dominated by the diurnal variation of the pressure gradient (figure 5.2d). The advection and coriolis force, the two other terms which can be modelled from the data, did not dominate either. These terms are plotted in figure 5.3 along with the ion drag expected for an ionospheric composition of 85% O^+ ions and 15% NO^+ ions.

Larger ion velocities occurred on the 21 January 1990. Figure 5.4 shows that most ion drift occurred zonally. A major enhancement in the ion velocity occurred in the zonal

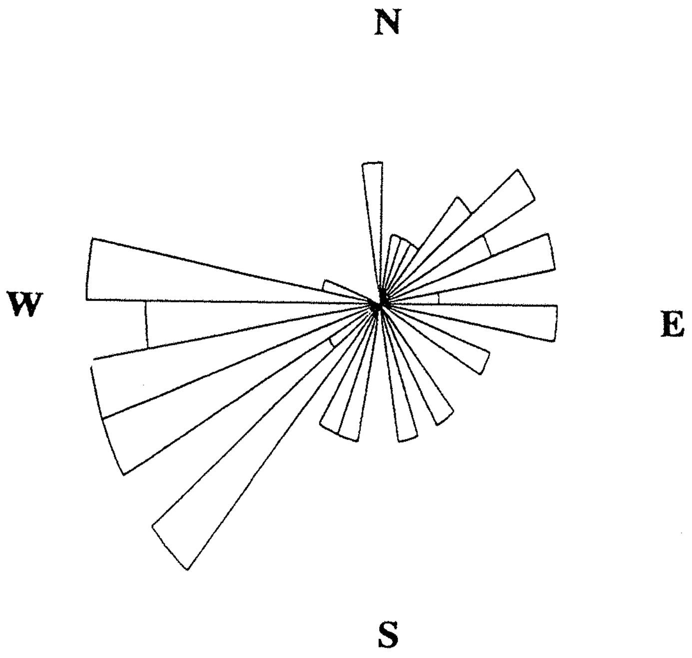

figure 5.1 The distribution of ion drift direction on 11 January 1989 between 15 and 6 UT.

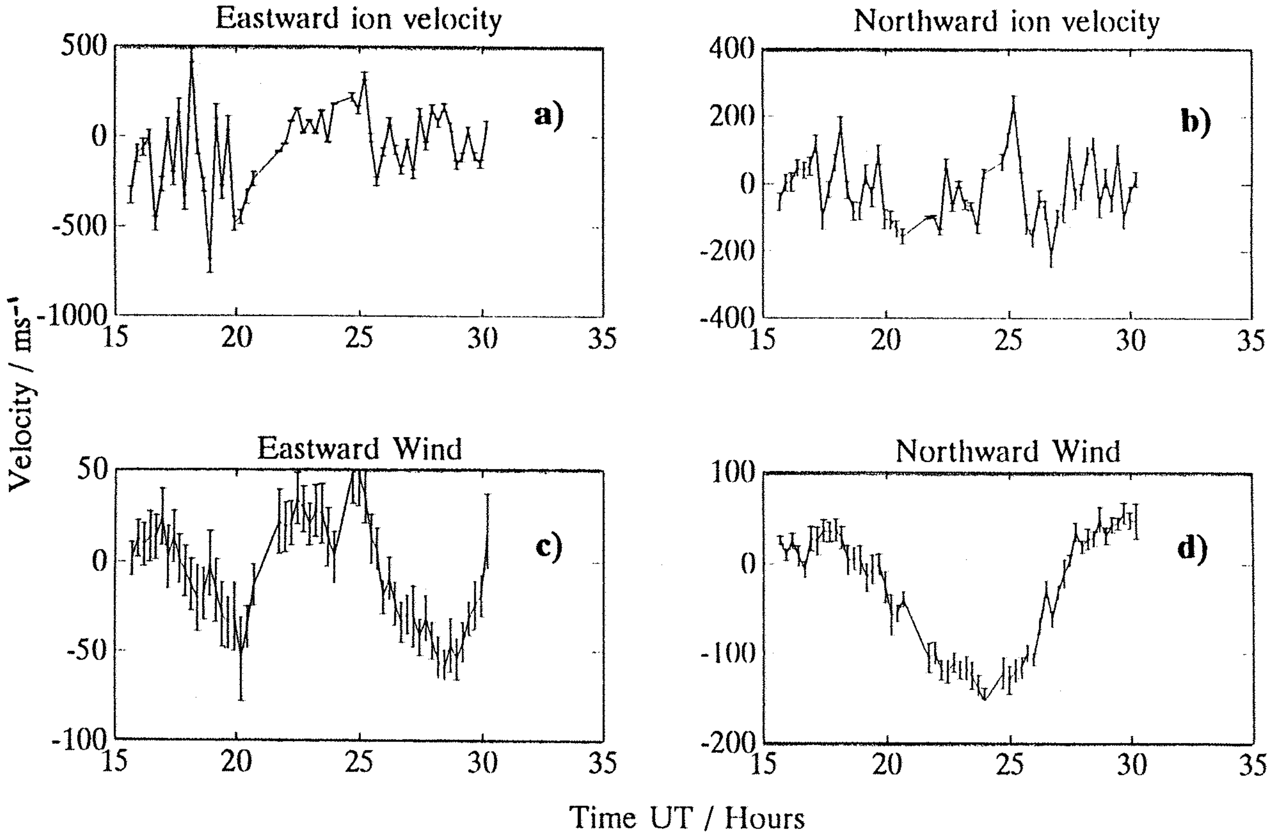

figure 5.2 Ion drifts and neutral winds from 11 January 1989.

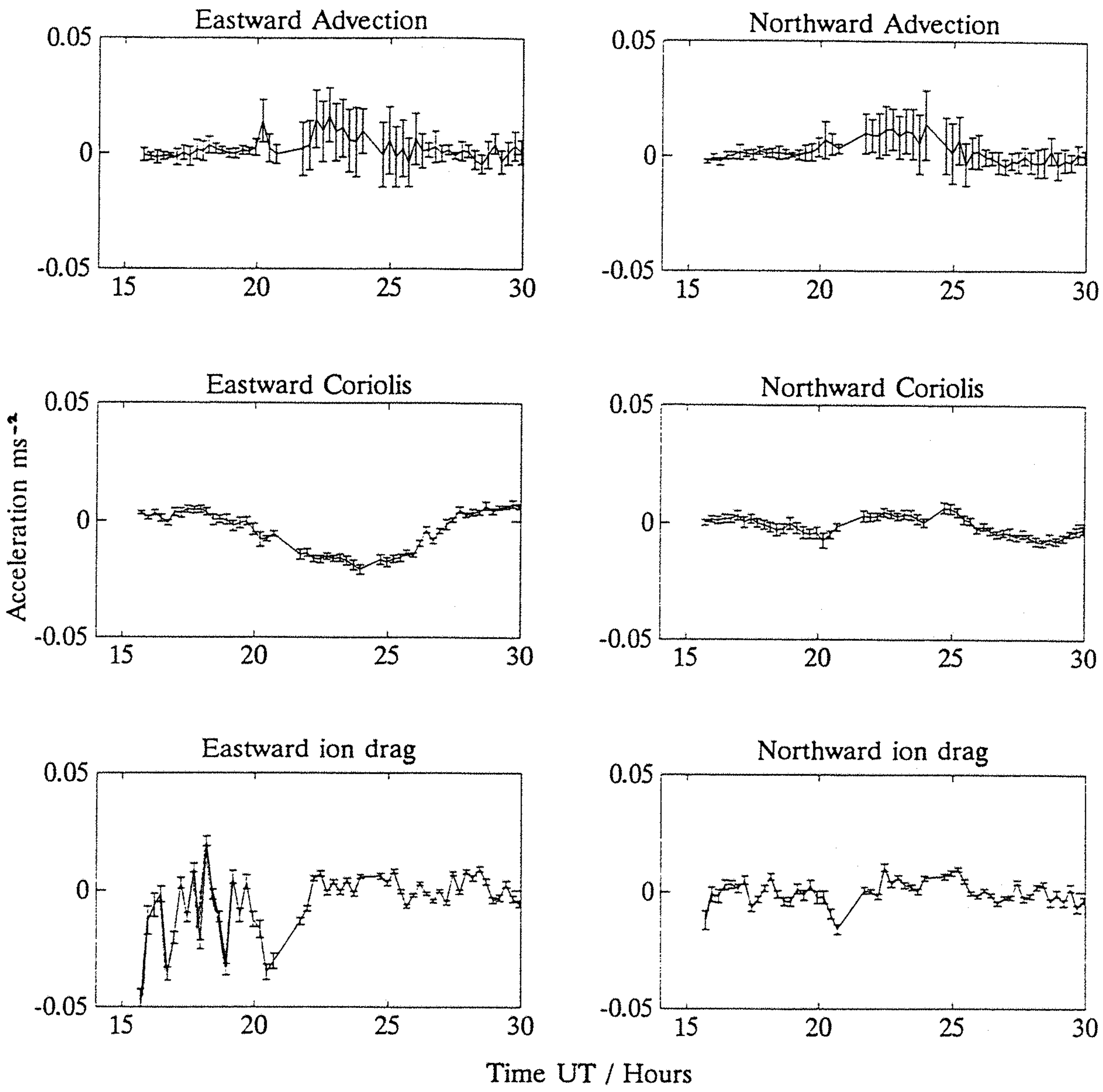

figure 5.3 Advection, coriolis and ion drag acceleration, 11 January 1989.

direction between 15 and 16 UT (figure 5.5a). The westward ion velocity peaked at 2200 ms^{-1}. As a result, the zonal wind, shown in figure 5.5c, was accelerated and peaked at a westward velocity of 175 ms^{-1}, 45 minutes after the largest ion velocity. Unfortunately, the FPI started to collect data just after the heating event, and so the only evidence of the ion drag forcing is the recovery phase in the zonal wind as ion drag ceased to dominate. Without knowing the starting velocity of the zonal wind before the heating event, it is impossible to estimate the acceleration due to ion drag. The meridional ion velocities (figure 5.5b) were small in comparison, rarely exceeding 300 ms^{-1} and the meridional wind followed the diurnal variation of the pressure gradient (figure 5.5d). Ion drag dominated during the heating event, and dominated advection and coriolis forces at periods throughout the night. This can be seen in figure 5.6.

Finally, for the 12 January 1991, most ion drifts were again zonal, as shown by figure 5.7. This night's data contain the largest ion velocities of the three examples. The zonal ion velocity, figure 5.8a, is enhanced between 16 and 18 UT, reaching a peak of 2500 ms^{-1} at 18 UT. This enhancement was mirrored in the zonal wind, figure 5.8c. The neutral air was accelerated to a maximum of 130 ms^{-1} with no time lag relative to the ion velocity. The ion velocity on this day demonstrates how rapidly the electric field and therefore the ion velocity can change. In this example, the radar scan time was 6 minutes and information about the exact time and value of the peaks in velocity is lost. This could account for the lack of an obvious time delay between the ions and the neutrals. To estimate accurately the total amount of ion drag it is necessary to make measurements of the ion drift as frequently as possible within the period of one FPI scan (19 minutes). The meridional winds were not dominated by ion drag (figure 5.8d), as the meridional ion velocities (figure 5.8b) did not exceed 500 ms^{-1}. Coriolis and advection forces, figure 5.9 were negligible in comparison with ion drag during the heating event.

These data sets show the effect of different levels of ion drag. Since the acceleration of the neutral air is so

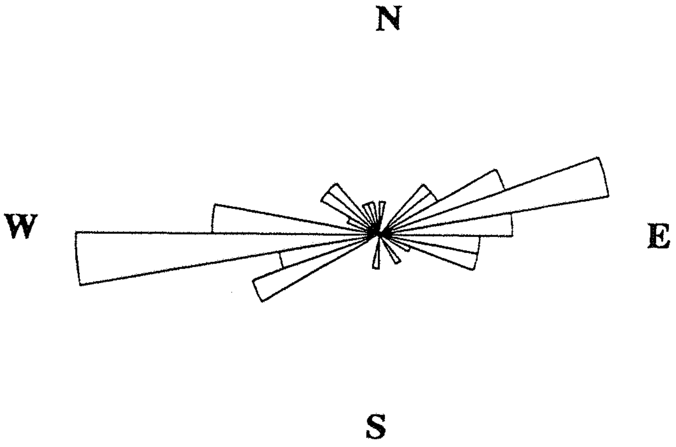

figure 5.4 The distribution of ion drift direction on 21 January 1990 between 15 and 6 UT.

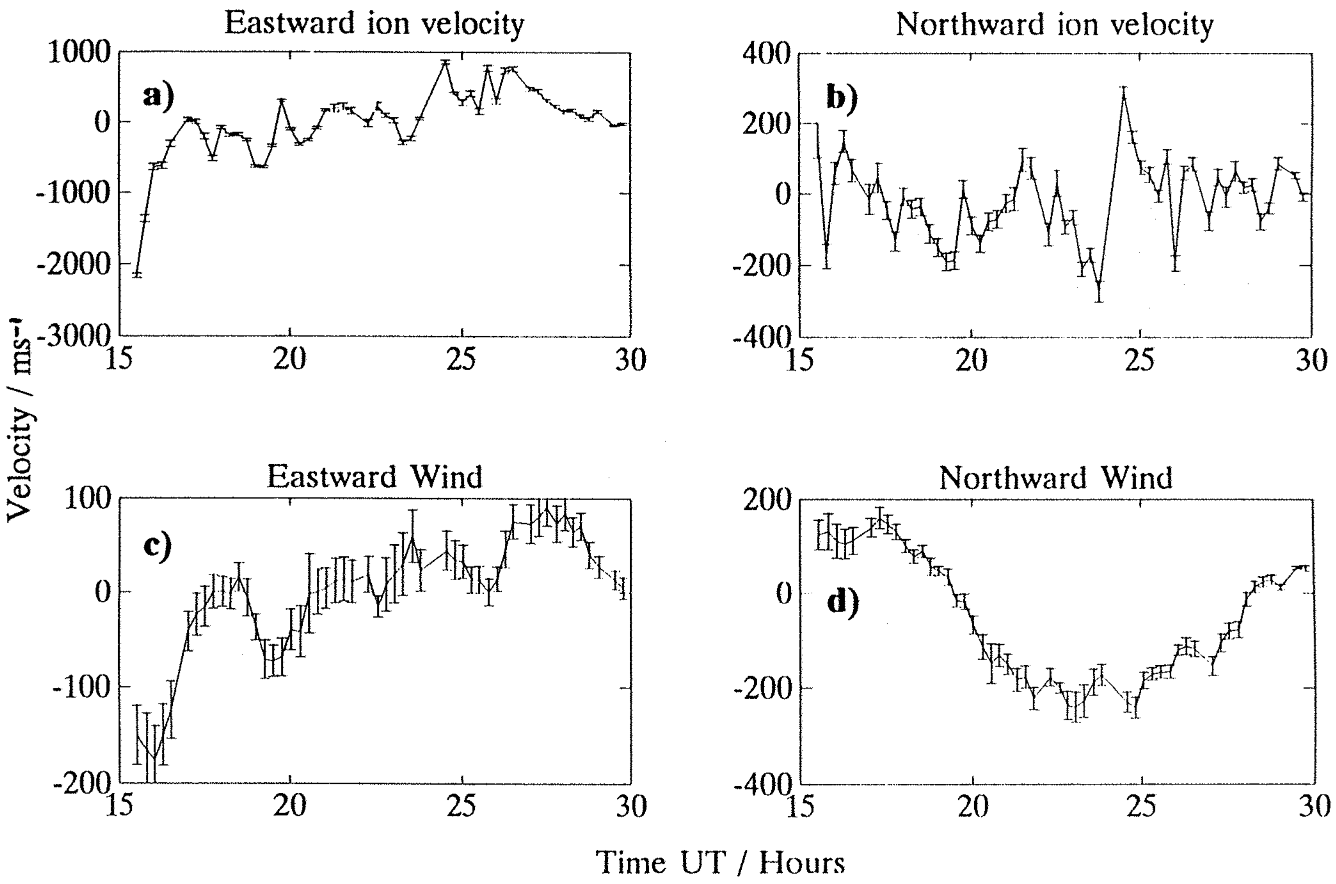

figure 5.5 Ion drifts and neutral winds from 21 January 1990.

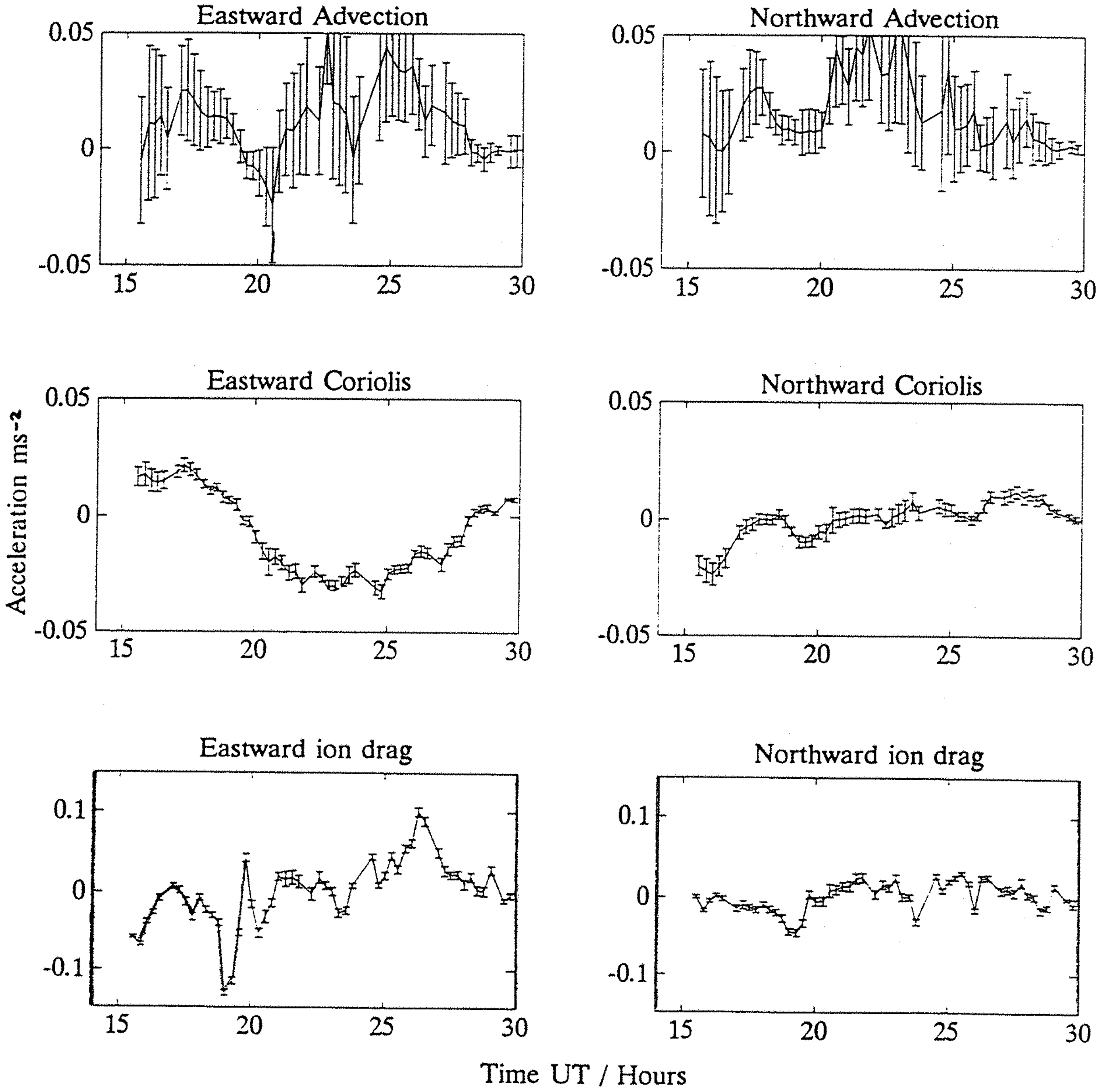

figure 5.6 Advection, coriolis and ion drag acceleration, 21 January 1990.

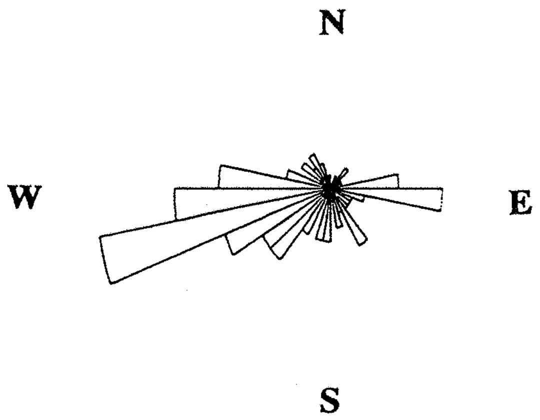

figure 5.7 The distribution of ion drift direction on 12 January 1991 between 16 and 4 UT.

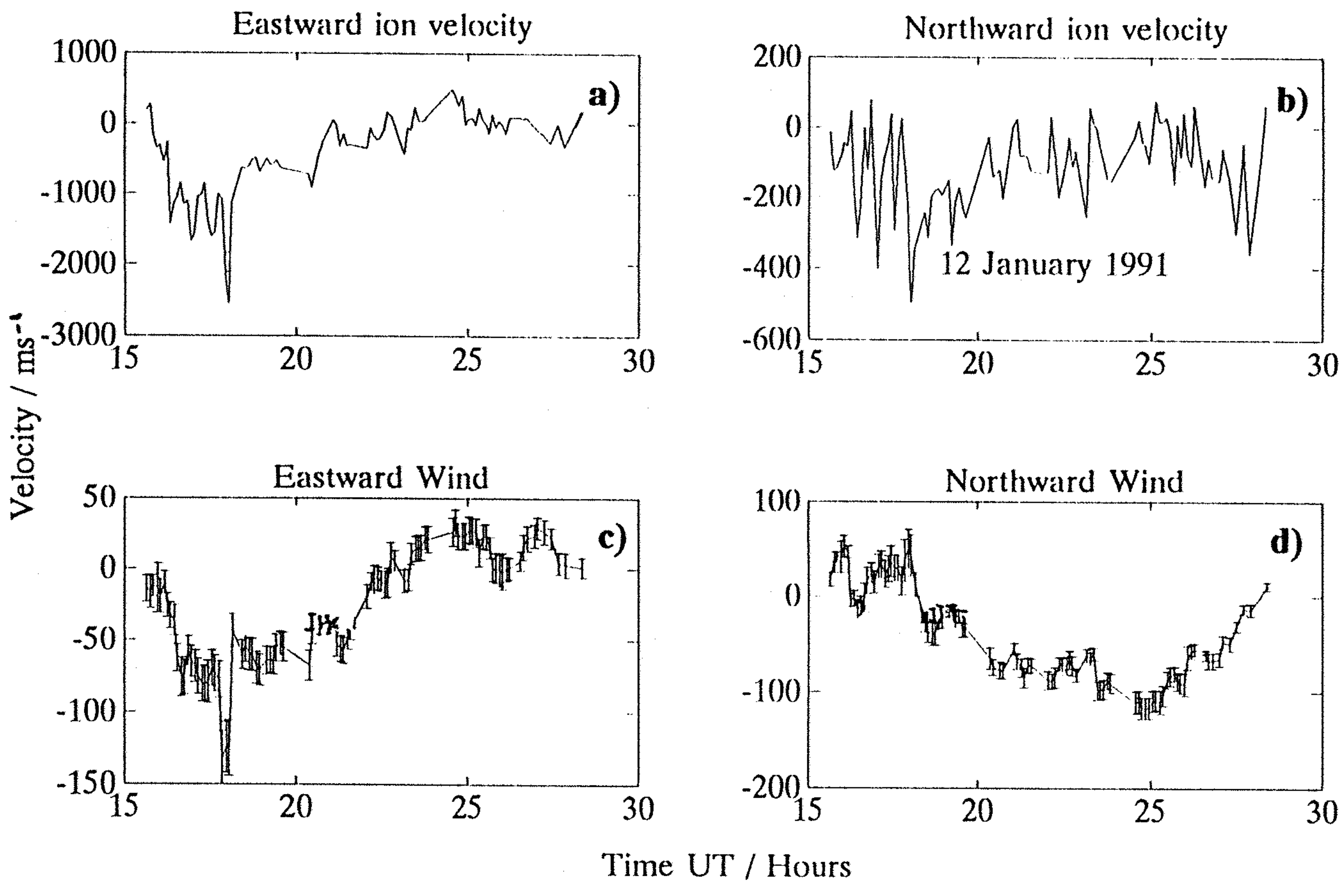

figure 5.8 Ion drifts and neutral winds from 12 January 1991.

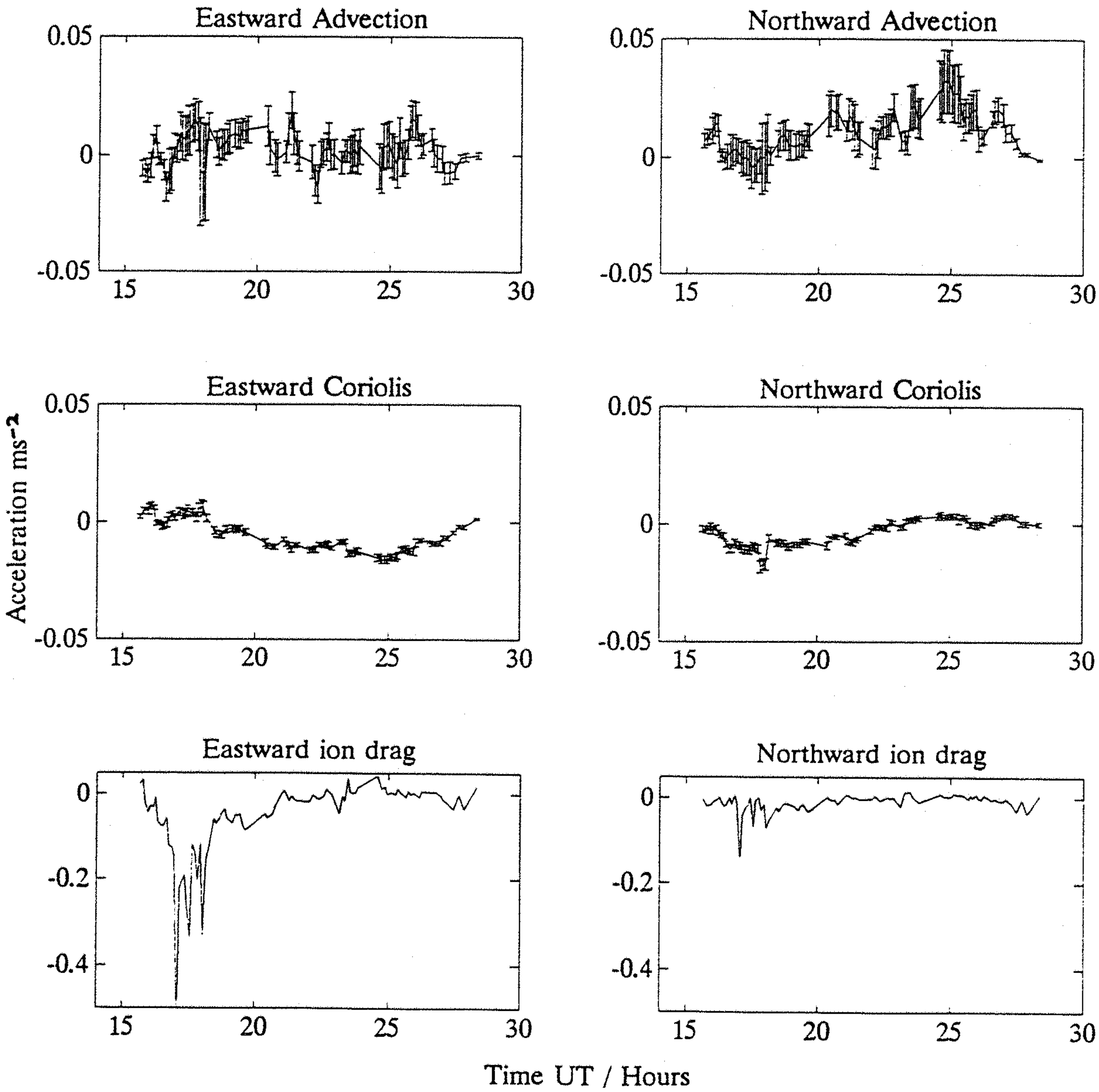

figure 5.9 Advection, coriolis and ion drag acceleration, 12 January 1991.

clear in the two most active examples, it was thought that a study of the zonal wind momentum equation could provide another method of determining the total neutral ion collision frequency, and from this the O^+-O rate coefficient could be determined. The neutral wind momentum equation was written in the simplified form

$$\frac{\partial \underline{U}}{\partial t} = \nu_{ni}(\underline{V}-\underline{U}) + \sum \underline{F} \qquad \textbf{(5.1)}$$

where ΣF represents the sum of all the other forces. This equation was then solved to give

$$(\underline{U}_n-\underline{U}_{n-1}) = (\overline{\underline{V}}-\underline{U}_{n-1})(1-e^{-\nu_{ni}(t_n-t_{n-1})}) + \frac{\overline{\sum \underline{F}}}{\nu_{ni}}(1-e^{-\nu_{ni}(t_n-t_{n-1})}) \qquad \textbf{(5.2)}$$

where

$$\overline{\sum \underline{F}} = \frac{\sum \underline{F}_{t_{n-1}} + \sum \underline{F}_{t_n}}{2} \qquad \overline{\underline{V}} = \frac{\underline{V}_{t_{n-1}} + \underline{V}_{t_n}}{2} \qquad \textbf{(5.3)}$$

It can be seen from equation 5.2 that if ion drag dominates and the electron density remains constant (ensuring ν_{ni} remains constant) then for a fixed time interval, ΣF can be considered a constant (as the forces making up F are all small or slowly varying). A graph of (U_n-U_{n-1}) versus $(V-U_{n-1})$ would then be linear, with a gradient of $1-\exp[-\nu_{ni}(t_n-t_{n-1})]$. From this, and the value of the electron density, the total collision parameter, K_{ni} could be obtained. If ion drag is to dominate, it must exceed the variation in ΣF. From the available data, it is estimated that within an hour the total acceleration due to these forces will not vary by more than ~0.05 ms^{-2}.

$$\nu_{ni}(\underline{V}-\underline{U}) \simeq \nu_{ni}\underline{V} > 0.05$$

$$e.g. \quad For \quad \Delta\overline{\sum \underline{F}} \sim 0.05, \quad N = 5x10^{10}, \quad \underline{V} > 1100 ms^{-1} \qquad \textbf{(5.4)}$$

Both 21 January 1990 and 12 January 1991 contain ion velocities which meet this criterion and it was thought that a collision frequency could be calculated for these times. Unfortunately, the electron density was extremely variable during the event of 12 January 1991 and so this technique could not be used as the collision frequency was too variable. On the 21 January 1990, the initial response of the zonal wind to ion drag forcing was not recorded. The electron densities are low but reasonably constant for the interval between 15 and 17 UT, when the response of the zonal wind was measured. During this time, the magnitude of the eastward ion velocity was decreasing to zero, reaching 500 ms^{-1} by 16 UT. As the radar was taking measurements every 15 minutes, the small time interval between the first FPI measurement (15.5 UT) and the time at which ion drag ceased to be dominant limits the number of usable data points to 2, which is insufficient to continue with the analysis.

The limitation of this method is that it requires such exacting conditions that the data are severely restricted.

It is expected that the total neutral ion collision frequency during such an event will be lower than at quiet times. This is the result of two effects.

1) The ion composition changes to favour molecular ions which have smaller collision parameters than O^+ ions.

2) The dissociative recombination of the molecular ions results in a depletion of the electron density.

As the ion velocity increases, the resulting ion drag causes frictional heating of the ions and the ion temperature increases. This increase can be estimated from the ion heating equation given in section 4.3. If the heating is sustained, it will eventually cause the neutral temperature, T_n, and the electron temperature, T_e, to rise. For a velocity difference of 2000 ms^{-1}, similar to the event observed on 21 January 1990, the ion temperature increases to approximately 4500 K. At such a temperature, the chemistry of the ionosphere favours the production of NO^+ ions in the reaction

$$O^{+}+N_2\rightarrow NO^{+}+N \qquad \textbf{(5.5)}$$

This increases the proportion of NO^+ ions, which are rapidly lost by dissociative recombination. This depletes the electron density.

Since the collision parameters for the reactions between NO^+ and the neutral constituents are much smaller than for similar collisions with O^+ ions, a change in composition would reduce the total neutral ion collision frequency considerably. This was discussed in section 1.4. The previous plots of ion drag did not account for this change in composition during the ion heating events. The change in the total neutral ion collision frequency for a range of compositions is shown in figure 1.4.1. For this figure, Banks' value was used to calculate the O^+-O collision parameter at a reduced temperature of 1000 K. Since the O^+-O collision parameter increases with temperature and the reduced temperature may increase to several thousand Kelvin during a heating event, figure 1.4.1 underestimates the possible effect on the total neutral ion collision frequency.

If the ion and electron temperatures are known, the rate coefficients for the relevant reactions can be calculated and the ion composition can be estimated. The ion temperature is obtained from the ratio T_i/m_i, which is a function of the width of the incoherent scatter spectrum. This value of T_i is used to calculate T_e from the ratio T_e/T_i (Appendix A). The mean ion mass, m_i is estimated from a model ion composition. If the composition changes, the proportion of NO^+ ions present in the ionosphere is larger than assumed in the model, m_i is underestimated and so T_i is underestimated. Thus T_e is underestimated. For the 21 January 1990, the ion heating equation predicts an ion temperature of 4500 K. The EISCAT data suggests a maximum temperature of 2500 K. If this discrepancy is due to a change in composition, it indicates a large increase in the proportion of molecular ions. It is not possible to use the discrepancy between the measured and modelled ion temperatures to estimate the change in ion composition because the basic analysis of incoherent scatter data also assumes that the temperature of the ions has a Maxwellian distribution. At large plasma velocities, this assumption breaks down and so a detailed study of the behaviour of the total neutral-ion collision frequency during an ion heating event is very complicated. An experiment has been devised to study non-Maxwellian plasma during an ion heating event (Winser et al, 1990, Lockwood et al, 1993) but there were no simultaneous optical data for the observed ion heating event and so the behaviour of the neutral air during the event is unknown.

If the neutral-ion collision frequency during such an event is to be studied, the ion composition, electron density, and the plasma velocity must be accurately determined from incoherent scatter data. Once this has been achieved, the radar data can be compared with the optical data, and the effects of ion drag modelled.

Chapter 6
Future work

It was shown in chapter 3 that in order to derive meridional neutral winds from radar data the effect of the vertical wind must be considered at high latitudes. Incoherent scatter data should be used with great care if meridional winds are to be obtained without any measure of the vertical wind, especially in the presence of auroral activity.

The determination of the O^+-O collision parameter obtained in chapter 4 (~1.7 times Banks' theoretical value) requires the addition of much more data to reduce the large uncertainty in the result. Since the quality of the data in all studies of the O^+-O collision parameter is variable, it is important that all the data from such studies be reanalysed to account for this variability and the results weighted accordingly. If this analysis is adopted as standard, all data can be combined to produce the definitive value of the O^+-O collision parameter.

The final result is dependent on the quality of the data used. The data in this thesis contain large uncertainties in the value of the vertical winds. This introduced a significant scatter into the derived meridional winds and the quality of the fit between measured and derived winds was reduced. In addition to this, no radar measurements were taken directly above Kiruna, where the vertical wind measurements were made. This necessitated assumptions about the horizontal extent of the vertical wind, which is an unknown quantity. The quality of the data should be improved considerably if the radar and the FPI observe the same vertical profile. In this way, the ambipolar diffusion velocity, derived by the radar coincides with the vertical wind measurement from the FPI.

An improved experiment would require two FPIs, one situated at Kiruna and the other at Tromsø, as shown in figure 6.1. The radar at Tromsø would measure a vertical profile, as in position e4 of the INDI scan. The FPI at Tromsø would be dedicated to measuring the vertical wind from the same profile as the radar. This would enable the FPI measurements to be integrated over a longer period of time and thus reduce the uncertainty in the vertical measurement. If the vertical winds vary rapidly, this would limit the maximum integration time. The meridional component of the neutral wind would be measured by the original FPI situated at Kiruna. This would remain fixed in the direction of Tromsø, with the mirror at a zenith angle of 45°. The centre of the airglow profile from this measurement would approximately coincide with the volume measured by the FPI at Tromsø. Since all three instruments look in a fixed direction during this experiment, the integration time can be varied to suit the conditions on each night. In addition, it would not be necessary to interpolate between measurements in order to compare data from the three instruments.

This experiment would therefore;

1) Improve the uncertainty in the vertical wind measurement.
2) Ensure that the vertical wind measurement coincided with the volume of the ambipolar diffusion velocity measurement.
3) Enable the meridional component of the neutral wind to be also measured over Tromsø.

Of course, this experiment requires clear skies over both Kiruna and Tromsø at the same time for the two FPI measurements. Tromsø, being near the coast, has cloud cover more often that Kiruna.

The study of the neutral wind momentum equation would be more complete if the FPI could measure the neutral temperature, T_n. The difference in temperature at viewing positions on opposite sides of the complete scan would help in the estimation of pressure gradients, although the neutral density would still have to be modelled (as $P=nkT_n$, where P is pressure, n is the neutral density and k is Boltzmann's constant). This would leave viscosity as the only unknown quantity in the neutral wind momentum equation and would give a better understanding of the interaction between the forces.

If the neutral-ion collision frequency is to be studied during an ion heating event, EISCAT should be used in an experiment similar to ISO-A (Winser et al, 1990), which accounts for the non-Maxwellian distribution of the ion

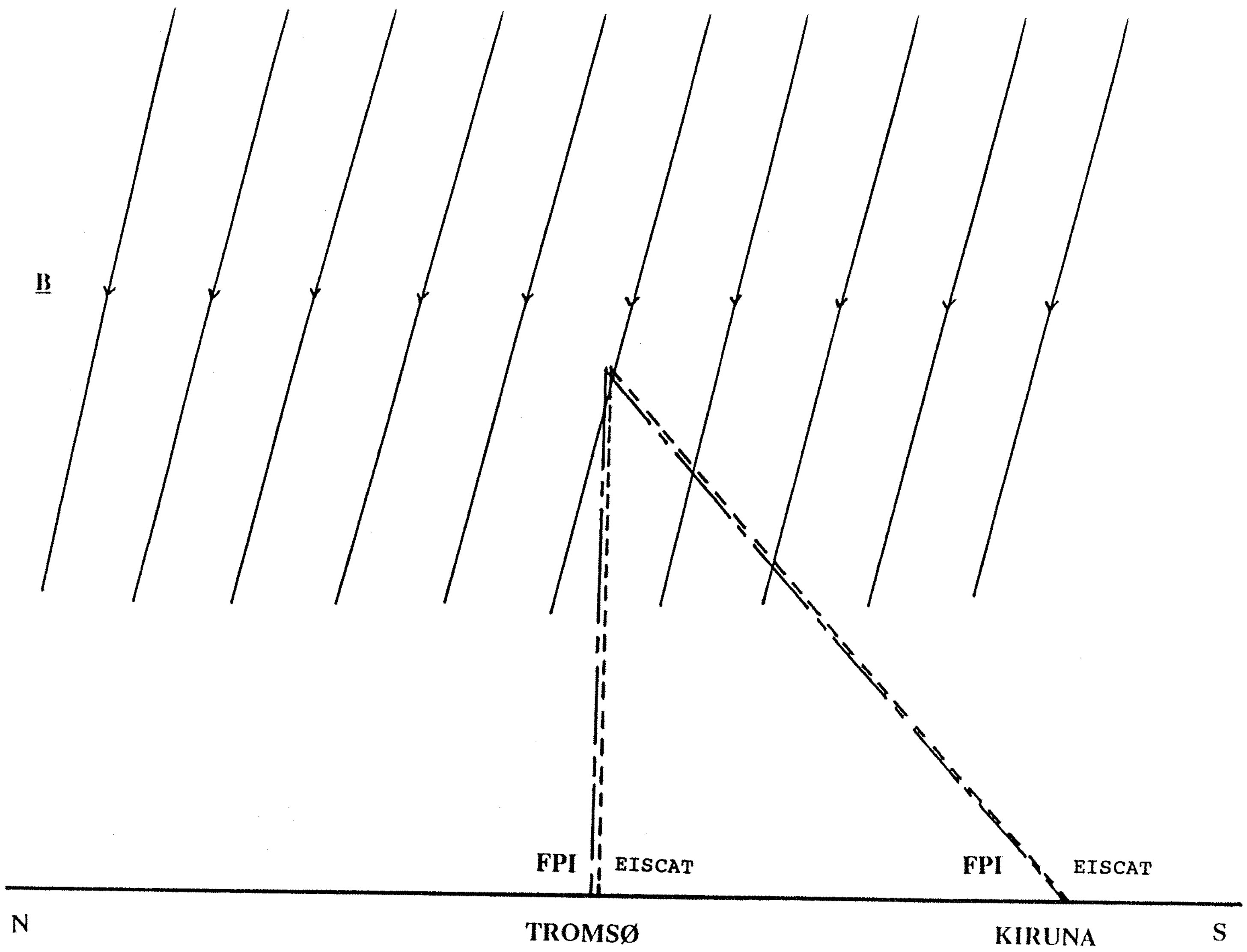

figure 6.1 A cross section from north to south through Tromsø and Kiruna showing the orientation of EISCAT and the two FPIs in the proposed version of the INDI experiment.

temperature. By viewing the plasma at an angle of 54.7 degrees to the magnetic field, the line of sight temperature is the average temperature of the non-Maxwellian distribution. The resulting radar position is close to e1 of the INDI scan. Because this position is so far north of the EISCAT receiving sites, data from this position can have a poor SNR in comparison with other positions further south. However, with simultaneous FPI measurements, the effect of the enhanced ion drifts on the neutral wind may be possible. The better the time resolution of the radar measurements, the more accurately the neutral-ion collision frequency can be estimated. If the radar data are analyzed for a series of values of the mean ion mass, $<m_i>$, and the difference between measured ion temperature and the ion temperature expected from the ion heating equation is minimised at each measurement, then $<m_i>$ can be estimated throughout the data set. If the ion composition can be estimated, the neutral ion collision frequency can be modelled. The resulting ion drag force and estimates of the other components from the neutral wind momentum equation, would enable the effects of ion drag on the zonal neutral wind to be modelled. The accuracy of such a model could be determined by comparison with the FPI measurements.

If possible, the neutral ion collision frequency could also be obtained by using the method described in chapter 5, and the two values could be compared.

Since the collision parameters for NO^+ ions are much smaller than those of O^+ ions, any change in composition will result in a marked change in the total neutral ion collision frequency (as shown in figure 1.4.1). If the composition is unknown, the acceleration of the neutral air by ion drag could be modelled for a range of neutral ion collision frequencies. By comparing the winds modelled in this way with winds measured by an FPI, it may be possible to estimate the ionospheric composition during an ion heating event.

Appendix A

The European Incoherent Scatter Radar, (EISCAT)

The EISCAT facility (Rishbeth & Williams, 1985) consists of one VHF parabolic trough antenna and a UHF system comprising of three 32 m steerable antennas. The transmitter site, at Tromsø in northern Norway, houses both the VHF and UHF transmitters (whose antennas also act as receivers for their respective systems), whilst the two other UHF receiving antennas are located in Kiruna, Sweden and Sodankylä, Finland. The UHF radar is the source of EISCAT data used in this study.

Incoherent Scatter.

EISCAT observes the ionosphere by Thomson or incoherent scattering of radio waves from free electrons. The interaction with ions in the plasma constrains the electrons, and the resulting scatter is not truly Thomson. As long as the wavelength used by the radar exceeds the Debye length of the plasma, information is gained about the plasma as a whole (Beynon & Williams, 1978). The Debye length is the distance at which the Coulomb interaction between plasma particles equals the thermal energy of the plasma. If the plasma is observed at a wavelength greater than this distance, the plasma is seen to act as a neutrally charged fluid. For wavelengths smaller than this scale distance, the plasma is seen to act as a collection of separate individual charges. This is true Thomson scatter.

The density of the plasma is not uniform, owing to the propagation of ion acoustic and electron acoustic waves. These waves have a broad continuous spectrum. If such a wave exists whose wavelength satisfies the Bragg condition, scattering occurs (Rishbeth and Williams, 1985). Such scattering arriving at the receiver is due to the component of the wave travelling along the bisecting angle between transmitter and receiver. The received signal consists of four components; the up and downward components of the ion and electron acoustic waves. If f is the transmitter frequency, then the return signal is centred around the frequencies

$$f \pm \Delta f^{+} \qquad f \pm \Delta f^{-} \tag{A.1}$$

$\Delta f = -2v.\cos(\frac{1}{2}\gamma)/\lambda$, where v is the velocity of the plasma, γ is the angle between transmitted and received beams and λ is the wavelength of the transmitted signal. It can be shown from the fundamental theory (Evans, 1969) that;

$$\Delta f^{+} = \frac{\left[\left(\frac{kT_i}{m_i}\right)\left(1+\frac{T_e}{T_i}\right)\right]^{\frac{1}{2}}}{\left(\frac{1}{2}\lambda\right)}\cos\left(\frac{1}{2}\gamma\right) \tag{A.2}$$

$$\Delta f^{-} = f_p\left(1+\frac{12\pi^2 l_D^2}{\left(\frac{1}{2}\lambda\right)^2}\right)^{\frac{1}{2}}\cos\left(\frac{1}{2}\gamma\right) \tag{A.3}$$

where '+' denotes ions and '-' denotes electrons, T_i is the ion temperature, m_i is the ion mass, f_p is the plasma frequency and l_D is the Debye length. The velocity of the ion acoustic wave, V^+, is well within the Maxwell distribution of thermal ions at T_i and the resulting attenuation broadens the two ion lines, which merge to become a double humped spectrum. The velocity of the plasma particles will either enhance or deplete the wave, depending on whether their velocity is greater or less then the wave respectively, this is Landau damping.

For a given T_i, if T_e is increased, the velocity of the wave increases. As a result, the Maxwellian spectrum of ion velocity around the ion acoustic frequency becomes less steep. The degree of Landau damping decreases and the peaks sharpen. In this way, the ratio T_i/T_e affects the sharpness of the peaks.

The electron acoustic waves travel much faster than the thermal velocities of most electrons and so there is little attenuation. A typical incoherent scatter spectrum therefore consists of a double humped ion spectrum flanked by two sharp plasma lines.

The transmitter frequency is chosen as a compromise between several criteria. Firstly, for incoherent scatter, the wavelength must exceed the Debye length of the plasma.

$$l_D = \frac{1}{2\pi f_N}\left(\frac{kT_e}{m_e}\right)^{\frac{1}{2}} \qquad \textbf{(A.4)}$$

where

$$f_N = \frac{1}{2\pi}\left(\frac{Ne^2}{m_e \epsilon_o}\right)^{\frac{1}{2}} \qquad \textbf{(A.5)}$$

Up to 300 km, l_D < 1 cm. Secondly, the resolution of the radar is determined by the wavelength used. The longer the wavelength, the poorer the resolution. Finally, practical considerations must be made such as avoiding commercially used frequencies and those bands where galactic radio noise is strongest. The EISCAT UHF radar operates at frequencies around 933 MHz with a peak transmitted power of 2MW.

There are several advantages to the incoherent scatter technique over previous sounding methods, such as ionosondes. The number of parameters that can be measured or inferred is much greater, and information can be obtained about the ionosphere above the F2 peak. By combining the line of sight information from each receiver, it is possible to calculate the full vector velocity of the plasma. This is a tristatic measurement.

Incoherent scatter data provides information about many ionospheric parameters. The only parameters considered in detail are those that have been used in, or are relevant to this investigation. They are;

1. Electron density.

This is a measurement of the return power received, corrected for the effects of T_e/T_i. By calibration with an ionosonde the instrument function of the radar can be determined. An alternative to this method is to measure the plasma line frequency, and hence determine N. A significant effort is being made to realise this potential.

2. The temperatures, T_e and T_i.

In general, the ions of a plasma have a Maxwellian velocity distribution, where;

$$N(V_i) \propto T_i^{-\frac{1}{2}} \exp\left[\frac{-m_i V^2}{2kT_i}\right] \qquad \textbf{(A.6)}$$

The velocity of the ion acoustic wave is given by equation A.2. Landau damping depends on the gradient of ion velocity distribution at the velocity of the ion acoustic wave and so the sharpness of the ion lines depends on T_e/T_i. The frequency of the returned signal can be normalised, by dividing by

$$\left(\frac{8kT_i}{m_i\lambda^2}\right)^{\frac{1}{2}} \cos\left(\frac{1}{2}\gamma\right) \qquad \textbf{(A.7)}$$

This is the Doppler shift of ions moving with a mean thermal velocity T_i. In this way, the spectrum can be standardised so that the only variables are N and T_e/T_i. Using equation A.2;

$$\frac{\Delta f}{\left(\frac{8kT_i}{m_i\lambda^2}\right)^{\frac{1}{2}} \cos\left(\frac{1}{2}\gamma\right)} = \frac{1}{\sqrt{8}}\left(1+\frac{T_e}{T_i}\right)^{\frac{1}{2}} \qquad \textbf{(A.8)}$$

Once T_e/T_i has been found, the ratio of T_i/m_i can be determined from the separation of the two ion lines;

$$2\Delta f^{+} = \frac{4}{\lambda}\left[\frac{kT_i}{m_i}\left(1+\frac{T_e}{T_i}\right)\right]^{\frac{1}{2}} \cos\left(\frac{1}{2}\gamma\right) \qquad \textbf{(A.9)}$$

If m_i can be established, an absolute value of T_i can be found and thus T_e can be calculated. The composition of the ionosphere is well understood under quiet conditions. In the E region, NO^+ and O_2^+ ions dominate, both of which have very similar masses. The proportion of O^+ ions increases with altitude until in the F-region, O^+ ions are dominant. With an auroral energy input, the enhanced ion temperature affects the reaction rates and the proportion of molecular ions increases in the F-region, increasing the uncertainty in deriving T_i and T_e.

3. Plasma velocity.

Bulk movement of the plasma causes the whole spectrum to be Doppler shifted. For a bistatic system, the Doppler shift measured is along the bisector of the two lines of sight. The mean shift $\Delta f=-(2v/\lambda).\cos(\frac{1}{2}\gamma)$. This is small compared with the width of the ion spectrum. With a tristatic radar, such as EISCAT, three components of plasma velocity are measured. These three components are combined to produce a full vector velocity. The accuracy to which the plasma velocity can be determined is dependent on the position of the scattering volume. With EISCAT, positions to the east of Sodankylä or the west of Kiruna are unfavourable, as the two receivers have very similar lines of sight.

4. Ion-neutral collision frequency.

Where the frequency of the ion acoustic wave is greater than the collision frequency, most attenuation is by Landau damping. This is the case above 150 km. Below this height, the ion temperature decreases while the ion mass and neutral density increase This causes the ion acoustic frequency to drop to a much smaller value than the collision frequency. As a result, ion acoustic waves can no longer propagate and the spectrum loses its double hump. At an observing wavelength, λ, the shape of the spectrum is determined by

$$\psi_i=\frac{\lambda}{4\pi l_i} \qquad \textbf{(A.10)}$$

l_i is the mean free path of the ions, given by

$$l_i=\frac{1}{\nu_{in}}\left(\frac{2kT}{m_i}\right)^{\frac{1}{2}} \qquad \textbf{(A.11)}$$

At heights below approximately 120 km (depending on the time of day and the level of auroral activity), $T_i=T_e=T_n$. The spectrum width is determined by $T_i^{\frac{1}{2}}$ and so (from A.11), the shape of the spectrum will depend on $\nu_{in}T_i^{-\frac{1}{2}}$. Thus measurements of both width and shape will determine both T_i and ν_{in}. This method is only one of several ways of determining the collision frequency and it only applies to the narrow height range of 100 to 120 km. Other, more elaborate methods are required to determine ν_{in} in the F region and these are the subject of this thesis.

5. Electric field, E

In the F region, the gyro frequencies of both ions and electrons greatly exceed their corresponding collision frequencies. As a result of this, both species spiral along the magnetic field lines. When an electric field is present, the resulting force causes the plasma to drift across the magnetic field at a velocity given by;

$$V_{\perp}=\frac{E \wedge B}{B^2} \qquad \textbf{(A.12)}$$

where B is the magnetic field strength. B can be modelled with some accuracy and so any component of velocity measured perpendicular to B can be used to determine $E_{\perp}$. Plasma is highly conductive parallel to the magnetic field and as a result the field lines act as an equipotential for electrons moving parallel to them. No steady $B_{\parallel}$ component of the electric field can exist (except the small polarisation field due to gravitational separation of ions and electrons) and so it is assumed that $E=E_{\perp}$. Electric fields are generated from below by neutral winds at E region heights. Ions and electrons are separated because of the difference between the neutral-ion collision frequency and the neutral-electron collision frequency. This is known as the dynamo effect. These fields are mapped upwards along the highly conductive magnetic field lines. Also, the connection of the geomagnetic field with the interplanetary magnetic field (IMF) causes the geomagnetic field lines to be swept back over the poles. This generates an electric field in the magnetosphere which is mapped down onto the F region at high latitudes. Such an electric field is particularly large during times of auroral activity.

6. Neutral wind velocity.

In the E region, the plasma is collision dominated. The neutral air movement dominates plasma motion and a measurement of the plasma velocity is a direct measurement of the neutral wind.

At F region altitudes, plasma movement is constrained by the magnetic field. Any northward movement of the neutral air forces the plasma to move parallel to the magnetic field. By equating the parallel components of the neutral air and the plasma and taking into account the diffusion of the plasma, it is possible to estimate the meridional neutral wind purely from radar measurements. Under active conditions, vertical winds become significant and this technique should be used with care.

The EISCAT UHF System.

Each antenna is a circular paraboloid 32 m in diameter. They are driven in azimuth and elevation at a scan rate of 80° per minute. The antennae can scan 270° in azimuth, either side of geographic north and from 2° to 100° in elevation. The accuracy of the pointing direction, combined with a time precision of $1\mu s$ enables tristatic measurements to be made.

The UHF transmitter obtains its power from one klystron. The maximum fraction of transmitter time (the duty cycle) allowed is 12.5 per cent. Because it is possible to change the transmitter frequency within $1\mu s$, several different pulse schemes can be transmitted in one pulse repetition period (prp). With sixteen different transmitter frequencies, (929.5 to 937.0 every 0.5 MHz) many different pulse schemes may be transmitted or, alternatively, many similar pulse schemes to maximise the efficient use of transmitter time.

The receivers used have been designed to limit the noise of the system. Background noise from extragalactic sources and the sun as well as ground noise is unavoidable, but it is desirable for the hardware not to add significantly to this. At Tromsø, additional system noise is introduced by the polariser. With the uncooled GaAsFET pre-amplifier, the system noise is around 100 K, whilst at the remote stations, with cooled pre-amplifiers, the system noise is ~30 K.

After scattering, the received signal is preamplified and mixed with a 1053.5 MHz local oscillator signal, to produce a signal of 120 ± 4 MHz, depending on the actual rf. Each signal is sent to the control room on two channels, corresponding to the in-phase and quadrature components of the polariser. In the control room, the signals can be attenuated to the required level and then they are mixed with a second local oscillator frequency tuned to give an output at 30 MHz. Each signal is then put through a bandpass filter (of variable bandwidth) and sent to a detector. The detector receives the signal, along with a reference 30 MHz signal and uses this to produce two outputs in quadrature. These outputs are then filtered again and amplified to produce in-phase and quadrature inputs to the analogue/digital converter (ADC). Channels 3 to 8 have ADCs sampling at 500 kHz whilst channels 1 and 2 have ADCs sampling at 10 MHz.

From the ADCs, the output is sent to a correlator. At any time, half of the buffer memory is read by the correlator whilst the other half is reading from the ADC. These swap every pulse repetition period, (PRP). The correlator computes power profiles, autocorrelation functions and cross correlations. The output from the correlator is integrated up to a pre-selected time and then transferred to disk.

Although it is easier to think of the physics in terms of an IS spectrum (returned power per frequency), sampling this at regular frequency intervals is severely limited by hardware considerations in the filter design. Instead, the spectrum is represented by its fourier transform, the autocorrelation function. This can be thought of as returned power distribution per time, where time is represented in lags. The sampling of such a spectrum requires taking samples at discrete time intervals, and this can be achieved much more easily.

The spatial resolution is $c\tau/2$, for a pulse of length τ, where c is the speed of light. In general, it is only necessary to obtain a resolution of the order of the scale height at a given altitude (approximately 50 km in the F region) unless small scale features are the subject of investigation. Spatially, the resolution is determined by the beamwidth.

Common Programmes.

Programmes have been devised to run several times a year in order to generate a large data base of information pertinent to the high latitude ionosphere. These are known as common programmes. A brief description of the most basic of these is given below.

CP0

The Tromsø beam points along the geomagnetic field line, while the remote receivers obtain tristatic information from 312 km.

CP1

The Tromsø beam is field aligned, as in CP0, while the remote sites obtain tristatic information from four or six heights in the E region and one in the F region in a ten minute cycle. Since 1985, complex pulse codes have been used to obtain better height resolution in the E region.

CP2

The Tromsø beam scans in four directions which have a horizontal spread of about 100 km in the F region. The remote sites make tristatic measurements at 312 km and the complete cycle takes 6 minutes. This experiment has a sufficiently fast cycle time to remove some of the spatial and temporal ambiguity.

CP3

A 16 position scan, along the magnetic meridian from 74.25°N to 64.25°N. The scan includes positions above Kiruna and Tromsø. The remote sites take readings from 315 km. The cycle time is 30 minutes. This provides a cross section of a large part of the auroral zone.

Appendix B

The Fabry Perot Interferometer (FPI)

The instrument used in this study belongs to the Atmospheric Physics Group at University College, London and is housed at the Geophysical Institute in Kiruna, Sweden.

Instrument details were obtained from Aruliah (1992). A scanning mirror directs light on to a Fabry Perot etalon which produces an interference pattern. This is transmitted via a series of mirrors and through a filter, on to a two dimensional Imaging Photon Detector (IPD). The image is averaged over the integration period (one to two minutes) and is then stored as an x,y coordinate array. All components are mounted on a rigid optical bench which maintains instrument alignment. Figure B.1 is a schematic diagram of the FPI, showing the path of light through the instrument.

The mirror rotates clockwise, stopping when sensors detect marks on the rim, through eight positions; north, north-east, east, calibration, south, zenith, west, and north-west. The integration time is determined by the intensity of the airglow, the sensitivity of the IPD and the data quality control. At Kiruna the integration time is 100 - 120 seconds. The FPI has a field of view of 1°. Measurements are calibrated by comparing the airglow with a standard source - a neon calibration lamp. This enables the data to be corrected for any variation in the instrument function, due to a change in temperature for example. The etalon used consists of two silica etalon plates set 10 mm apart and separated by plates of zerodur - a polycrystalline ceramic with a very low coefficient of thermal expansion. Each plate has a diameter of 15 cm, producing a large aperture. The plates are flat to an accuracy of $\lambda/200$ and are coated with a dielectric which has a high reflection coefficient (81% at 630 nm). The etalon is sealed in an evacuated chamber whose temperature is maintained at a constant level (varying by only 0.1°). This minimises pressure and temperature changes in the etalon.

The IPD consists of a photocathode (diameter 18 or 25 mm) and a lens which projects the photo-electrons onto three

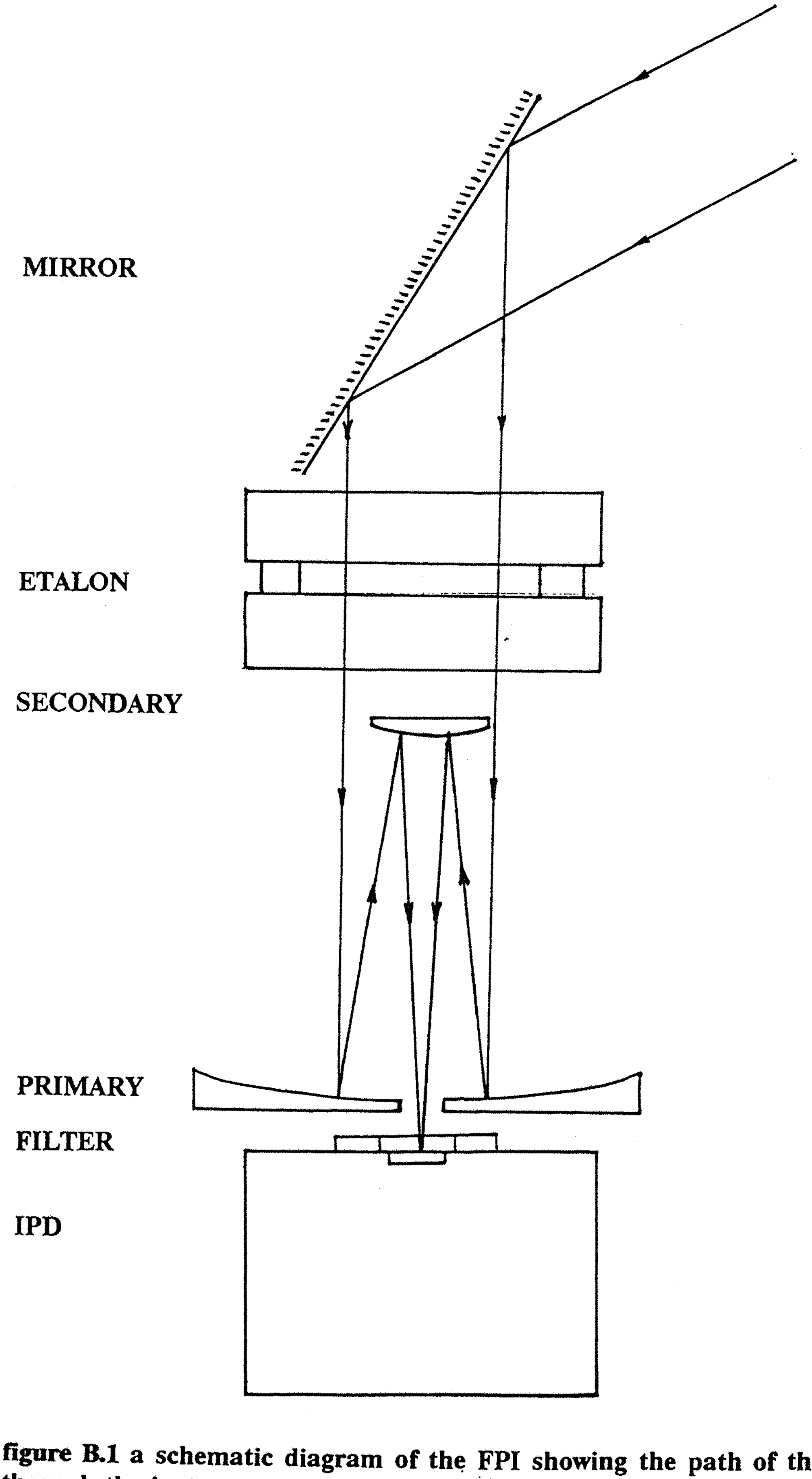

figure B.1 a schematic diagram of the FPI showing the path of the light through the instrument.

plates which intensify the image. Finally, the electrons are projected onto the anode, a metal sheet with four contacts around its edges. The x,y coordinates of the electrons are calculated by comparing the ratio of charge received at each contact. The output of the detector is converted to a digital two dimensional coordinate array of 256 x 256 positions.

Etalon Theory

The etalon consists of two prisms set up so that the two inner faces are exactly flat and parallel. The outer surfaces are not parallel with the inner surfaces, to reduce reflections from them. The inner surfaces are coated with a metal or dielectric film of high reflectance, R_f. The plates are separated by a distance, d. Light entering this gap is multiply reflected, losing a small fraction of its intensity with every reflection. The components emerging are different in amplitude and phase, determined by d and the angle of incidence, θ.

The path difference determines the extent of interference between the components. For light of wavelength λ, a path difference $n\lambda$ leads to constructive interference, whilst a path difference of $(n+\frac{1}{2})\lambda$ leads to destructive interference.

For constructive interference,

$$2d\cos(\theta_n) = n\lambda \qquad \textbf{(B.1)}$$

Interference produces a concentric ring pattern. The total intensity, I_{tot}, in terms of the peak intensity, I_o, depends on R_f and the phase difference δ - also known as the Airy function.

$$\frac{I_o}{I_{tot}} = \left[1 + \frac{4R_f \sin^2\frac{\delta}{2}}{(1-R_f)^2}\right] \qquad \textbf{(B.2)}$$

The sharpness of the peak is determined by R_f, where a high R_f produces greater contrast between maxima and minima. Even small changes in δ can have an appreciable effect on I_T. This is illustrated in figure B.2.

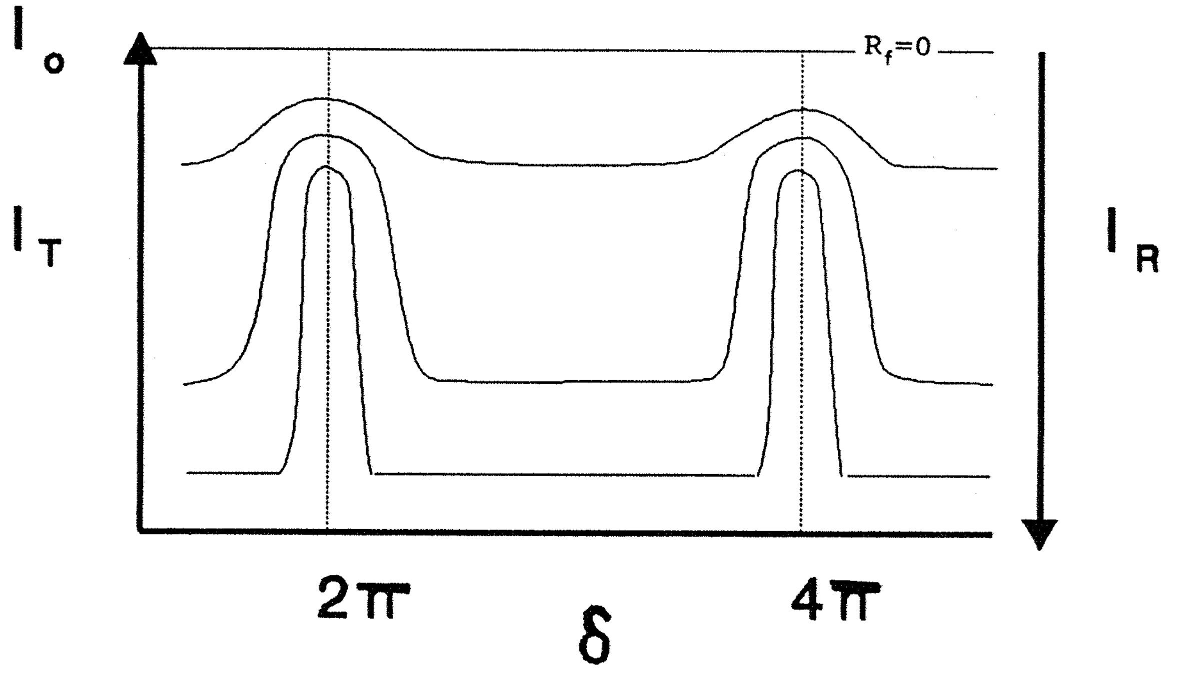

figure B.2 Change in intensity of the interference fringes with path difference δ.

Data reduction.

The light reaching the etalon is confined to a 1° spread. This allows the small angle approximation to be used in calculating the fringe position. It can be derived from the Airy formula that θ is proportional to D^2, where θ is the angle of the peak from the centre line of the apparatus and D is the distance from the centre of the fringe pattern. The two dimensional image is therefore collected and reduced to a one dimensional image in terms of D^2. The centre of the image is found by an annual calibration. FPIs are very stable and little drifting occurs.

Before reduction, the data must be corrected using a Flat Field Image (FFI) and Thermionic Emission Image (TEI). The FFI is an image collected from a diffuse white light source used to determine the response of each pixel. A comparison removes the instrument dependent factor. A TEI is generated when the instrument is used to measure 'dark counts'. These are due to the electronic noise of the image. The system noise can be reduced by cooling.

Fitting Peaks

On passing through the FPI, the emission line is convolved with the instrument function. This is made up of the Airy function of the ideal etalon, the departure from flatness of the plates, the microscopic flatness variations and the effect of any variation in pressure. These broaden the original profile. The final profile is a convolution of all these effects. Lloyd represented this convolution by a single function and used this to fit the peaks to an accuracy of 1 ms^{-1} (Aruliah, 1992). Although this method is efficient, it does not determine the full width half maxima which are needed to determine the neutral temperatures. A more comprehensive method would enable neutral temperatures to be measured, but the data processing takes much longer.

Wind speeds.

A Doppler shift away from the instrument (a red shift) will move the peaks closer to the centre of the image, while a blue shift will cause the peaks to move outwards. The wind speed, U, along any line of sight can be calculated by the relation;

$$U=\frac{c\Delta\lambda}{\lambda} \tag{B.10}$$

where λ is the wavelength, $\Delta\lambda$ the Doppler shift and c the speed of light. The determination of an absolute $\Delta\lambda$, or rather the equivalent shift in peak position, is difficult. The ideal situation would be to use a 630 nm calibration source, However because this emission line results from a forbidden transition, such a source is difficult to maintain under laboratory conditions. The calibration source used is a neon lamp which emits at 630.4 nm. This wavelength is sufficiently close to 630.0 nm to pass through the instrument filter. The peaks due to the calibration lamp provide information on the stability of the instrument. The peaks are narrower than those due to the airglow as the lamp is at a lower temperature. This means that they can be fitted more accurately. The central position of such a fringe system is determined at the beginning of an observing campaign. A drift in the temperature of the instrument appears as a shift in the position of the fringe peaks.

The zero Doppler shift baseline is determined from the peak positions of both the calibration lamp and the zenith measurements. It is assumed that the long term average vertical velocity is zero. This may not be the case for an instrument in the auroral region. Local heating can set up convection cells, with air rising through thermal expansion at one latitude and cooling and descending at another latitude. For the FPI, at a fixed latitude, the long term average vertical wind may not be zero. This may introduce a systematic error.

The winds are calculated by comparing all the peak positions with this baseline. The Doppler shifts are related to the change in peak position by the Free Spectral Range (FSR). The FSR Doppler shift is the change in wavelength needed to move a fringe pattern by one order (n to n+1) to produce a set of peaks which overlap the peaks due emission at the original wavelength. If (d'-d) is the small change in the radius of a fringe caused by the Doppler shift of the airglow, then the wind speed is determined by the ratio of change in d^2 to the equivalent FSR change in D^2.

$$V=\frac{(d'^2-d^2)}{(D_n^2-D_{n+1}^2)}\frac{c\lambda}{2d} \qquad \textbf{(B.11)}$$

Appendix C.
Analysis of the Fabry Perot Interferometer data.

In previous analyses of INDI data (Winser et al, 1988, Farmer et al, 1990) it was assumed that the neutral winds, as derived from the FPI were constant over the viewing area. This represents the simplest approximation but a more detailed analysis is possible. By comparing the velocities measured at opposite sides of a scan sequence (north and south for example) it is clear that horizontal velocity gradients exist within the viewing area (figure C.1). A better method would be to consider the winds as having linear velocity variations both meridionally and zonally. This was done by adopting the analysis techniques used by Burnside at Arecibo (Burnside et al, 1981). Care must be taken with this method at high latitudes to make sure that the assumptions made are valid for each particular data set.

The horizontal vector velocity $\underline{U}$ can be expanded in a Taylor series in both east and north directions (x is positive east, y is positive to the north).

$$U_x=u_o+\frac{\partial u}{\partial x}x+\frac{\partial u}{\partial y}y + \ldots . \qquad \textbf{(C.1)}$$

$$U_y=v_o+\frac{\partial v}{\partial x}x+\frac{\partial v}{\partial y}y + \ldots . \qquad \textbf{(C.2)}$$

An instrument, pointing at azimuth angle φ and zenith angle θ will measure a line of sight velocity, U_r, where

$$U_r=\sin\theta\,(U_x\sin\phi+U_y\cos\phi) \qquad \textbf{(C.3)}$$

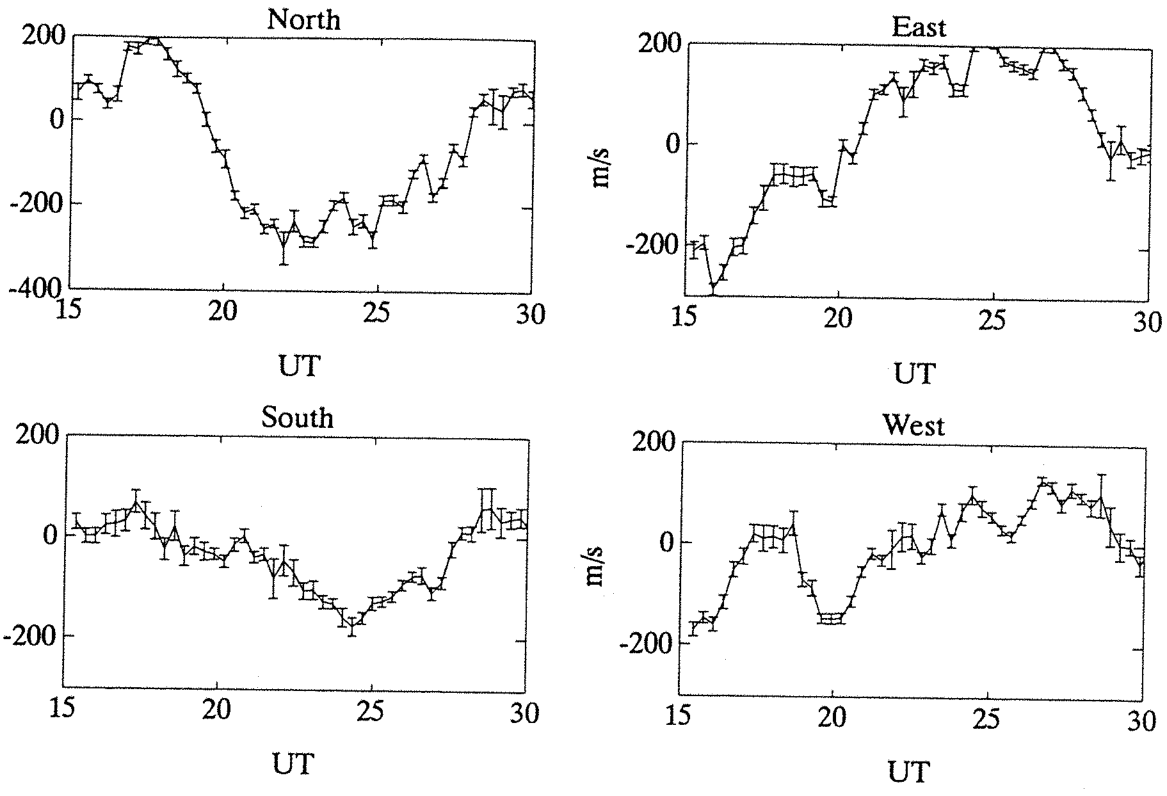

figure C.1 Line of sight velocities measured by the FPI on 21 January 1990 demonstrating the presence of velocity gradients across the scan area.

Rewriting equations C.1 & C.2,

$$U_x=u_o+\frac{1}{2}\left(\frac{\partial u}{\partial x}+\frac{\partial v}{\partial y}\right)x+\frac{1}{2}\left(\frac{\partial u}{\partial x}-\frac{\partial v}{\partial y}\right)x+\frac{1}{2}\left(\frac{\partial u}{\partial y}+\frac{\partial v}{\partial x}\right)y+\frac{1}{2}\left(\frac{\partial u}{\partial y}-\frac{\partial v}{\partial x}\right)y \tag{C.4}$$

$$U_y=v_o+\frac{1}{2}\left(\frac{\partial v}{\partial x}+\frac{\partial u}{\partial y}\right)x+\frac{1}{2}\left(\frac{\partial v}{\partial x}-\frac{\partial u}{\partial y}\right)x+\frac{1}{2}\left(\frac{\partial v}{\partial y}+\frac{\partial u}{\partial x}\right)y+\frac{1}{2}\left(\frac{\partial v}{\partial y}-\frac{\partial u}{\partial x}\right)y \tag{C.5}$$

where;

$$\frac{\partial u}{\partial x}+\frac{\partial v}{\partial y}\ (=K_1) \qquad \frac{\partial u}{\partial y}+\frac{\partial v}{\partial x}\ (=K_2) \tag{C.6}$$

$$\frac{\partial v}{\partial y}-\frac{\partial u}{\partial x}\ (=K_3) \qquad \frac{\partial v}{\partial x}-\frac{\partial u}{\partial y}\ (=\xi)$$

are the divergence, shear and stretching deformations and vorticity respectively (Hess, 1959). Substituting C.4, C.5, and C.6 into C.3 gives;

$$\begin{aligned}\frac{u_r}{\sin\theta} &= \left[U_o-\frac{1}{2}\xi y+\frac{1}{2}K_1x-\frac{1}{2}K_3x+\frac{1}{2}K_2y\right]\sin\phi \\ &+\left[v_o+\frac{1}{2}\xi x+\frac{1}{2}K_1y+\frac{1}{2}K_3y+\frac{1}{2}K_2x\right]\cos\phi\end{aligned} \tag{C.7}$$

By writing $R=h.\tan\theta$, where R is the horizontal radius of the scan, and h is the emission height (figure C.2), it follows that $y=R.\cos\phi$ and $x=R.\sin\phi$. Substituting for x and y and collecting terms,

$$U_r = u_o\sin\phi+v_o\cos\phi+\frac{R}{2}K_1+\frac{R}{2}\left[K_2\sin2\phi+K_3\cos2\phi\right] \tag{C.8}$$

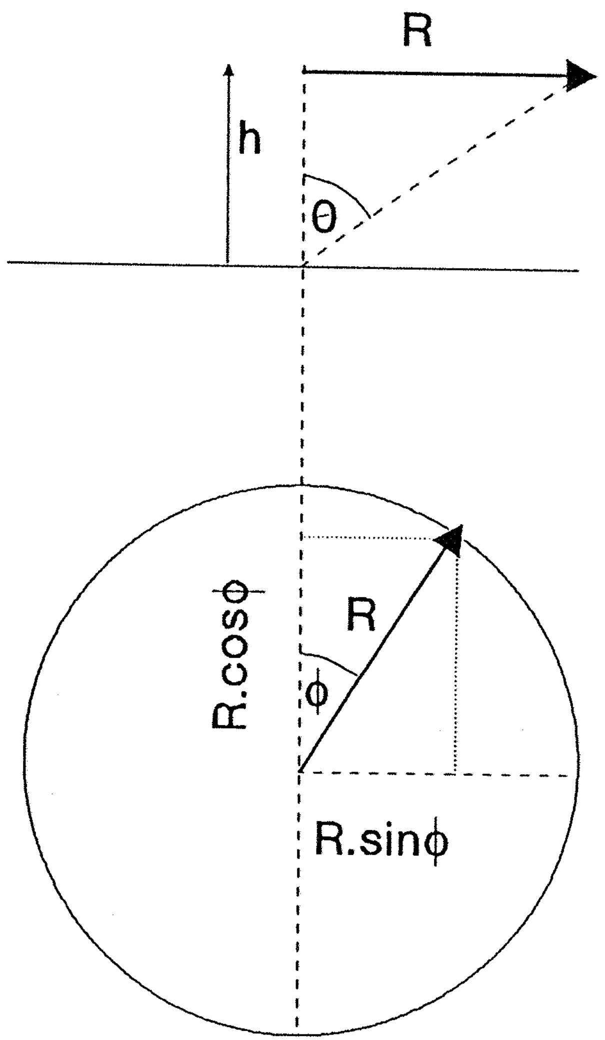

figure C.2 The relationship between scan radius, R, zenith angle, θ, azimuth angle, ϕ and the height of the airglow emission, h.

Thus U_r can be expressed as a truncated Fourier series in terms of the azimuth angle. The first three terms of this fourier series give values for u_o, v_o, K_1, K_2, and K_3. The individual gradients cannot yet be found, as without a value of ξ, there are only three equations and four unknowns. A true measurement of vorticity requires more than one instrument, but an estimate can be made by assuming that local time and longitude are interchangeable. The expression for ξ therefore becomes;

$$\xi = \frac{\partial v}{\partial x} - \frac{\partial u}{\partial y} = 2\left(\frac{1}{\epsilon}\frac{\partial v}{\partial t}\right) - K_2 \tag{C.9}$$

where

$$\epsilon = R_{\oplus}\Omega\cos\psi \tag{C.10}$$

is the tangential velocity of the station (latitude ψ) with respect to the sun. This assumption can only be made if the meridional wind has a well defined local time variation. A wind dominated by the day night pressure gradient has a strongly diurnal nature, as on 21 January 1990 (figure C.3). Ion drag can dominate the neutral forcing, but as long as the ion drifts occur zonally, which they generally do, the assumption holds. If a significant meridional ion drift occurs however, this assumption breaks down, and a different method of analysis must be used.

The wind field can now be reconstructed for a region inside the radius of the scan. If the wind field were constant over the whole region, with no horizontal gradients, it can be seen that $U_r = u_o \sin\phi + v_o \cos\phi$. A plot of line of sight velocity against azimuth angle would therefore be a simple sine function, whose phase indicates the direction of the wind. Generally, the gradients are non-zero and these distort the simple sinusoidal relationship. One of the advantages of this method for INDI data is that an estimate of the wind velocity can be made for any position, including those measured by EISCAT. Common programme data can also be compared with the FPI data, even though the radar positions

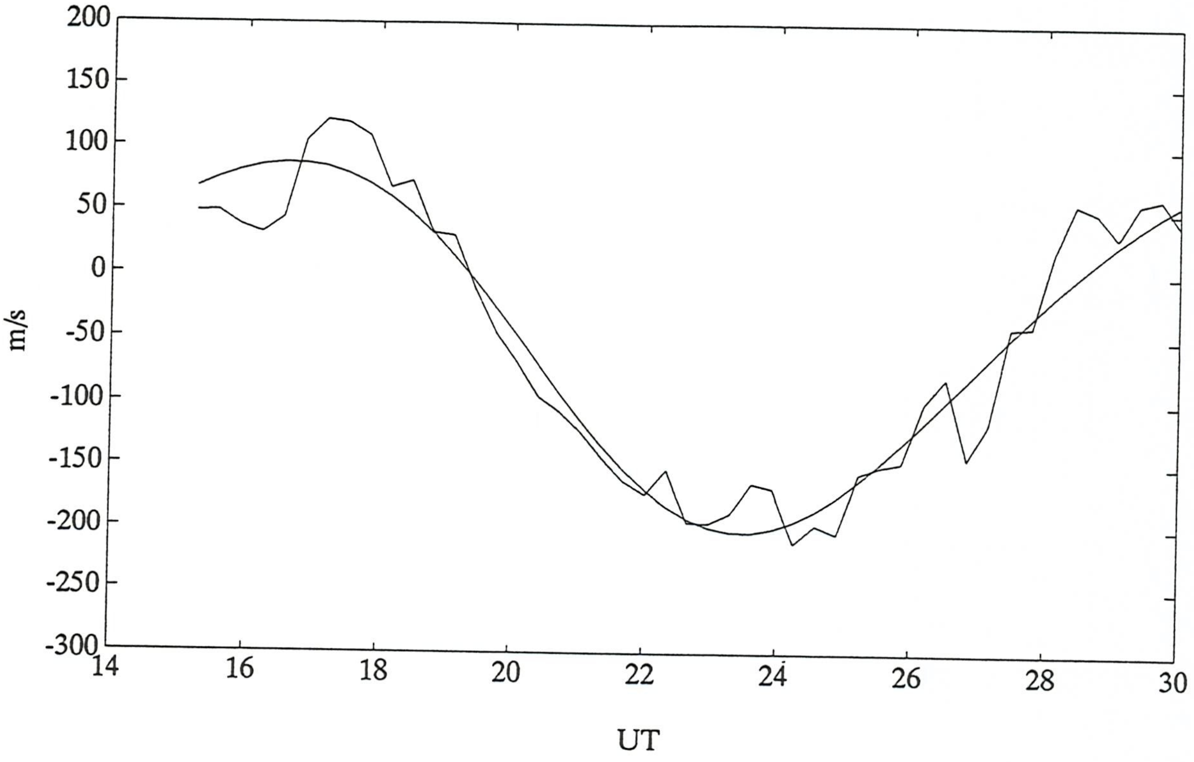

figure C.3 The variation in the meridional wind on 21 January 1990 and its fourier series, used to estimate the local time variation of the wind.

are not specifically designed for this type of investigation.

The first step required in the analysis of the FPI data is to estimate the line of sight velocities in the south east and south west scan positions. The lack of readings at these points produces an uneven sampling frequency. To simplify the analysis, these values were interpolated by fitting a low order polynomial to each cycle. Although this is far from ideal, tests were carried out to verify that the winds calculated using this method are not sensitive to the estimates used. Once this was done, the Fourier series of each scan was calculated. Figure C.4 shows a typical example of a scan compared with its Fourier series.

Fourier analysis of sampled data.

The Fourier routines used are based on the description given by Smart (1958) and are the basis of the FPI analysis program. The FPI data are not continuous as the wind field is sampled at discrete azimuth angles. The Fourier expansion is therefore expressed as a series of summations rather than as integrals. The line of sight velocity, U_r, is a function of azimuth angle, ϕ, and can be represented by the Fourier expansion

$$U_r \equiv f(\phi) = A_o + \sum_{k=1}^{\infty} (A_k \cos k\phi + B_k \sin k\phi) \qquad \textbf{(C.11)}$$

where k=1, 2, ... identify the order of the Fourier component. For data with a regular sampling frequency, the range is divided into n equal sections at ϕ_1, ϕ_2, $\ldots\phi_{n-1}$. If n measurements are made per scan,

$$\phi_r = \frac{2\pi r}{n} \qquad \textbf{(C.12)}$$

Considering the direction U_r, for any value of r between 1 and n;

$$U_r = A_o + \sum_k \left(A_k \cos\frac{2\pi kr}{n} + B_k \sin\frac{2\pi kr}{n}\right) \qquad \textbf{(C.13)}$$

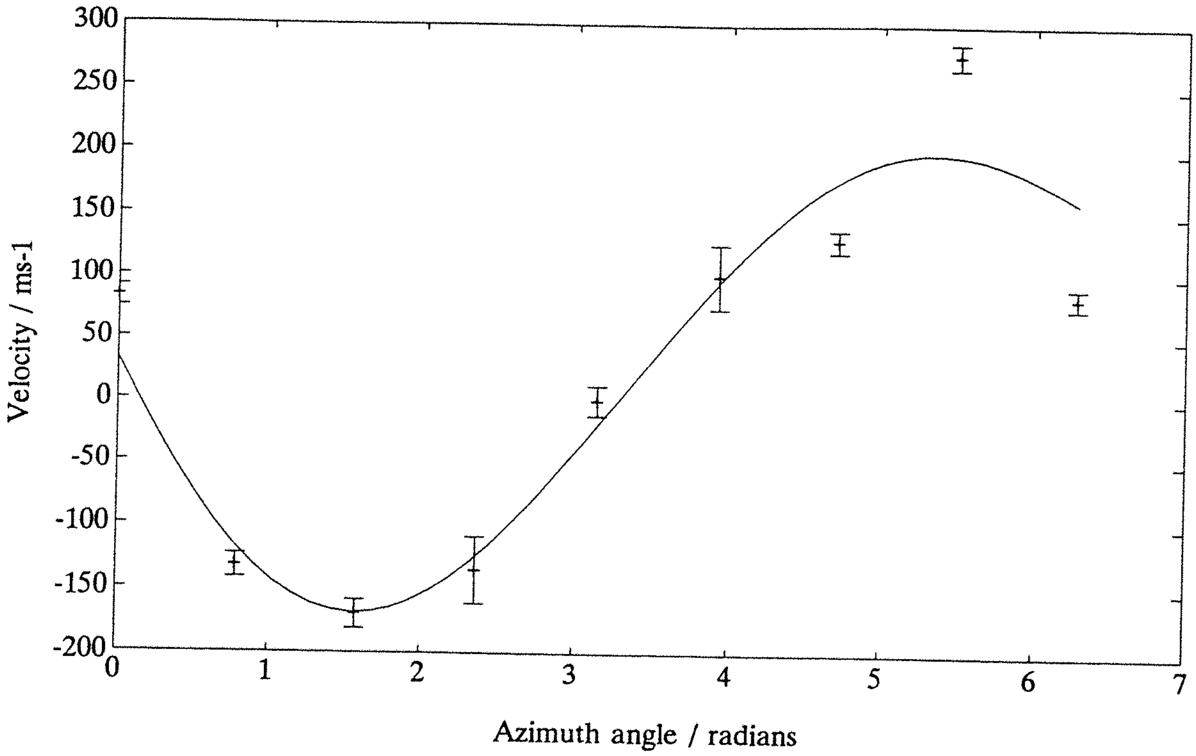

figure C.4 A typical example of wind velocity against azimuth angle compared with its fourier series.

This gives (2k+1) constants calculated in n positions of the FPI scan. For n=8, the data may be adequately represented by values of k=1, 2. These coefficients can now be calculated.

The sum of all n values of U_r can be written;

$$\sum_{r=1}^{n} U_r = nA_o+\sum_{k}\left[A_k\sum_{r=1}^{n}\cos\frac{2\pi kr}{n}+B_k\sum_{r=1}^{n}\sin\frac{2\pi kr}{n}\right] \qquad \textbf{(C.14)}$$

By using the identities;

$$\sum_{r=1}^{n}\cos r\alpha\equiv\frac{\sin\frac{1}{2}n\alpha}{\sin\frac{1}{2}\alpha}\cos\frac{1}{2}(n+1)\alpha \qquad \textbf{(C.15)}$$

$$\sum_{r=1}^{n}\sin r\alpha\equiv\frac{\sin\frac{1}{2}n\alpha}{\sin\frac{1}{2}\alpha}\sin\frac{1}{2}(n+1)\alpha \qquad \textbf{(C.16)}$$

it can be seen that if $\alpha=2\pi k/n$, then $\sin(\frac{1}{2}n\alpha) \equiv \sin(k\pi)=0$, leaving

$$A_o=\frac{1}{n}\sum_{r}U_r \qquad \textbf{(C.17)}$$

To obtain the individual values of A_k, equation C.13 is multiplied by $\cos 2\pi kr/n$ and summed over r. Then, for $j \neq k$,

$$\sum_{r}U_r\cos\frac{2\pi kr}{n}=A_o\sum_{r}\cos\frac{2\pi kr}{n}+A_k\sum_{r}\cos^2\frac{2\pi kr}{n}+\frac{1}{2}B_k\sum_{r}\sin\frac{4\pi kr}{n}$$

$$+\sum_{j}A_j\sum_{r}\cos\frac{2\pi kr}{n}\cos\frac{2\pi jr}{n}+\sum_{j}B_j\sum_{r}\cos\frac{2\pi kr}{n}\sin\frac{2\pi jr}{n} \qquad \textbf{(C.18)}$$

Using the identities C.15 and C.16, the coefficient A_o is zero and the coefficient A_k is;

$$\frac{1}{2}n+\frac{1}{2}\sum\cos\frac{4\pi kr}{n} \qquad \textbf{(C.19)}$$

while the coefficient A_j is;

$$\frac{1}{2}\sum_r\left[\cos\frac{2\pi(k+j)r}{n}+\cos\frac{2\pi(k-j)r}{n}\right] \tag{C.20}$$

By using these identities again, each summation vanishes along with the coefficients of B_k and B_j, leaving

$$A_k=\frac{2}{n}\sum_r U_r\cos\frac{2\pi kr}{n} \tag{C.21}$$

Similarly,

$$B_k=\frac{2}{n}\sum_r U_r\sin\frac{2\pi kr}{n} \tag{C.22}$$

To calculate these coefficients from the FPI data, each line of sight velocity, U_r, is multiplied by a cosine (or sine) determined by the order of the coefficient, k, and its azimuth angle, $\phi=2\pi r/n$. These are then summed for all points, r.

The errors in this analysis are the result of any residual between the data points and the sum of the first three Fourier components. In this way, if the Fourier series is not representative of the wind field observed, the large residuals will generate large errors (Smart, 1958).

The residual, v_r, is the difference between a measurement, U_r and its fourier series;

$$v_r=U_r-A_o-\sum_k\left[A_k\cos\frac{2\pi kr}{n}+B_k\sin\frac{2\pi kr}{n}\right] \tag{C.23}$$

The total residual is therefore;

$$\sum_r v_r=\sum_r U_r-nA_o-\sum_k\left[A_k\sum_r\cos\frac{2\pi kr}{n}+B_k\sum\sin\frac{2\pi kr}{n}\right] \tag{C.24}$$

By applying the previous identities and the expression for A_o

it can be shown that $\Sigma v_r=0$. The method used to calculate the coefficients of A and B is equivalent to a least squares fitting process, in which case, $V\equiv\Sigma v_r^2$ is a minimum with respect to the coefficients of A and B. For a particular A_k,

$$\frac{\partial V}{\partial A_k}\equiv 2\sum v_r\frac{\partial v_r}{\partial A_k}=0 \tag{C.25}$$

or from equation C.24,

$$\sum_r v_r\cos\frac{2\pi kr}{n}=0 \tag{C.26}$$

and similarly,

$$\sum_r v_r\sin\frac{2\pi kr}{n}=0 \tag{C.27}$$

and so V can be written,

$$V=\sum_r v_r\left[U_r-A_o-\sum_k\left(A_k\cos\frac{2\pi kr}{n}+B_k\sin\frac{2\pi kr}{n}\right)\right] \tag{C.28}$$

by equations c26 and c27 and knowing $\Sigma v_r=0$,

$$V=\sum v_r U_r \tag{C.29}$$

Hence,

$$[vv]=[UU]-A_o\sum U_r-\sum_k\left[A_k\sum_r U_r\cos\frac{2\pi kr}{n}+B_k\sum_r U_r\sin\frac{2\pi kr}{n}\right] \tag{C.30}$$

Where $[vv]=\Sigma v_r^2$ and $[UU]=\Sigma U_r^2$. Substituting for the values of the A and B coefficients calculated in the last section,

$$[vv]=[UU]-nA_o^2-\frac{n}{2}\sum\left(A_k^2+B_k^2\right) \tag{C.31}$$

[vv] is related to the standard deviation, σ, by;

$$\sigma^2=\frac{[vv]}{n-(2k+1)} \tag{C.32}$$

where (2k+1) is the number of unknowns. This leads to a standard error for each A_k and B_k of,

$$\sigma\sqrt{\frac{2}{n}} \tag{C.33}$$

whilst the standard error of A_o is given by;

$$\frac{\sigma}{\sqrt{n}} \tag{C.34}$$

The solutions and their precision can now be given.

$$A_o=\frac{1}{n}\sum U_r \quad \pm \quad \frac{\sigma}{\sqrt{n}} \tag{C.35}$$

$$A_k=\frac{2}{n}\sum U_r\cos\frac{2\pi kr}{n} \quad \pm \quad \sigma\sqrt{\frac{2}{n}} \tag{C.36}$$

$$B_k=\frac{2}{n}\sum U_r\sin\frac{2\pi kr}{n} \quad \pm \quad \sigma\sqrt{\frac{2}{n}} \tag{C.37}$$

By comparing the Fourier series with equation C.8, values of K_1, K_2, K_3 and ξ can be found, and from these, the individual gradients can be estimated.

For convenience, the rate of change of the meridional wind (required for the estimation of vorticity) is also calculated from its Fourier series. The average meridional wind (north+south)/2, is used for this purpose.

The wind field can now be reconstructed within the radius of the FPI scan, with Kiruna situated at the origin, x=y=0. The curvature of the Earth is not considered, as the scan area is small in comparison with the radius of the Earth. The origin is the most well defined position, having no uncertainties due to the gradients. The accuracy of the analysis can be seen by using the gradients to reconstruct the wind at the various observing positions. This was done for the 21 January 1990 data and the results are plotted in figures C.5 and C.6 (with and without error bars). In this example, all the line of sight readings are modelled well, except in the east. This indicates that the wind to the east does not conform to the approximation of a linear velocity variation. It should be noted that modelling the positions at the edge of the scan is a worst case situation.

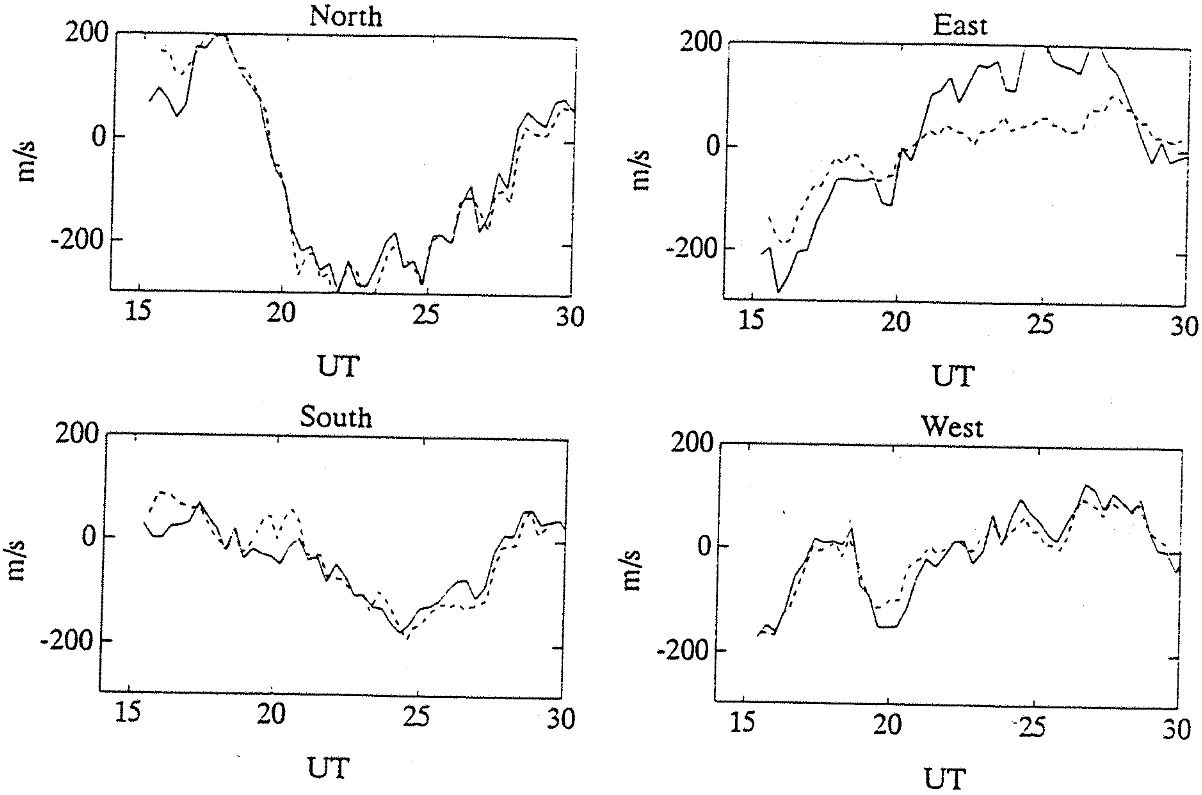

figure C.5 A comparison between the line of sight measurements of the FPI and the velocities predicted for those volumes by the FPI analysis (dotted lines).

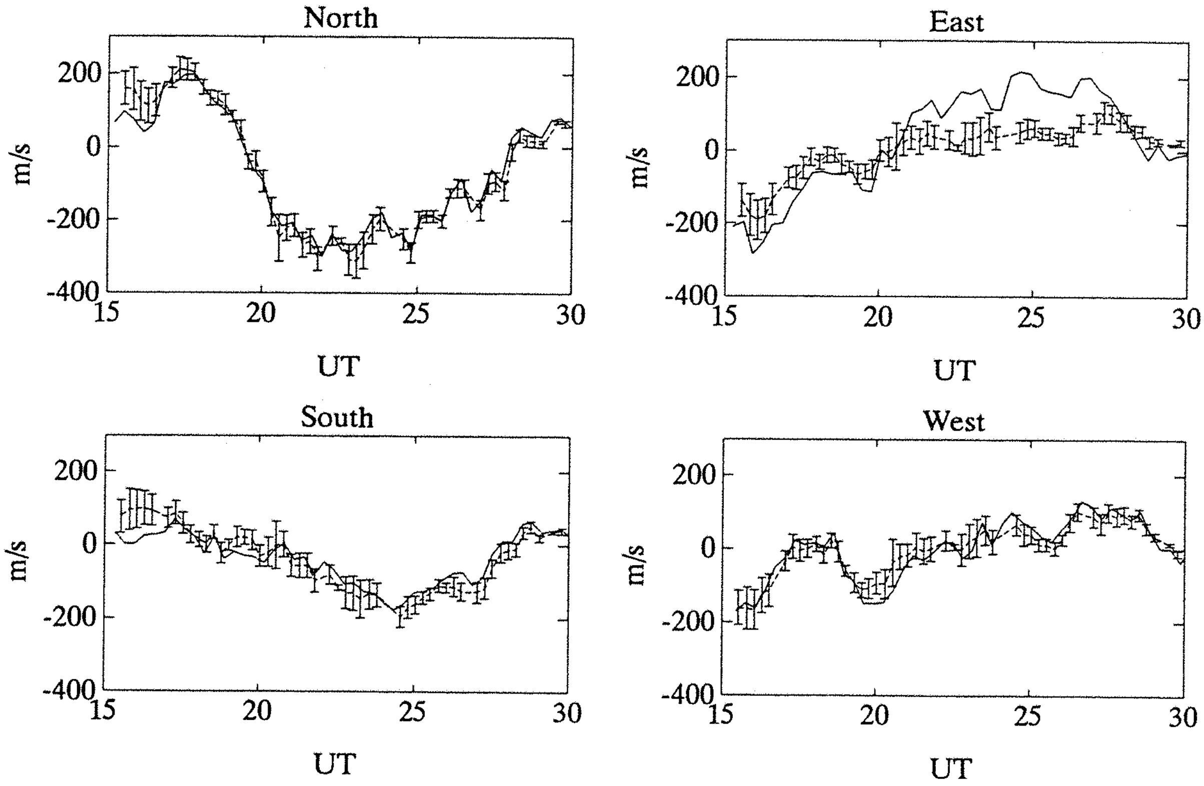

figure C.6 A comparison between the line of sight measurements of the FPI and the velocities predicted for those volumes by the FPI analysis (dotted lines), with errors.

Appendix D

Plots from analysis without vertical wind data

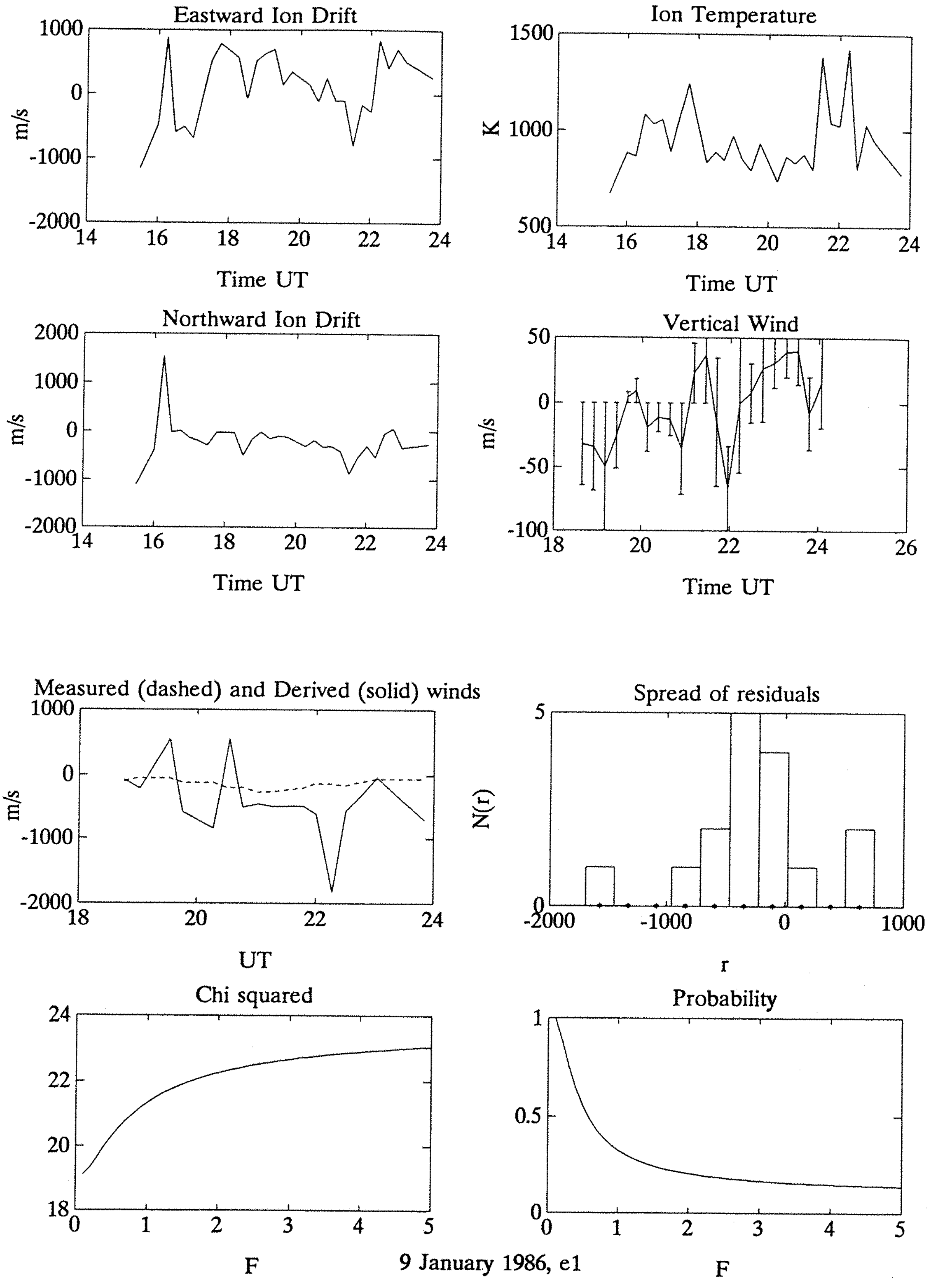

9 January 1986, e1

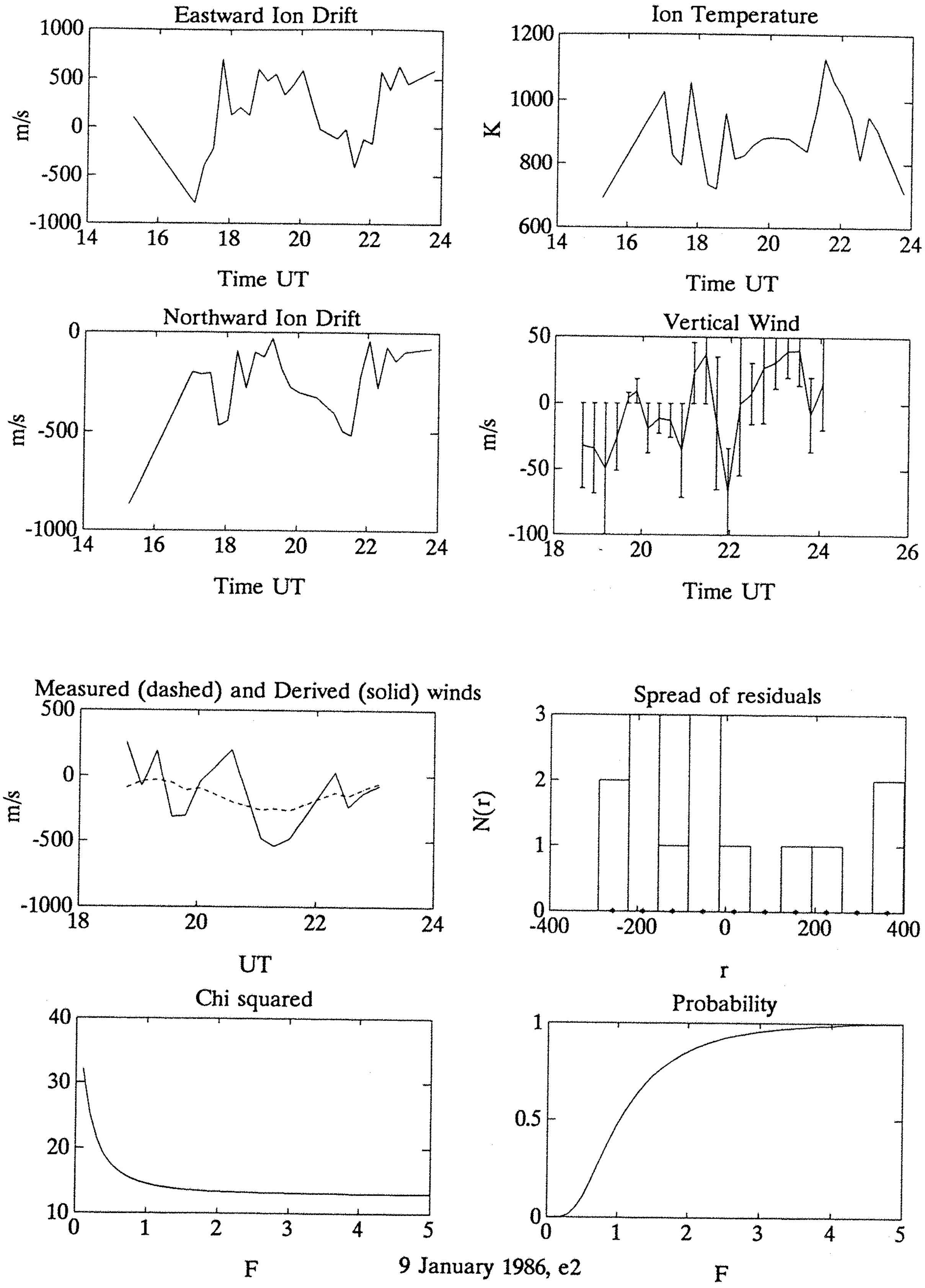

9 January 1986, e2

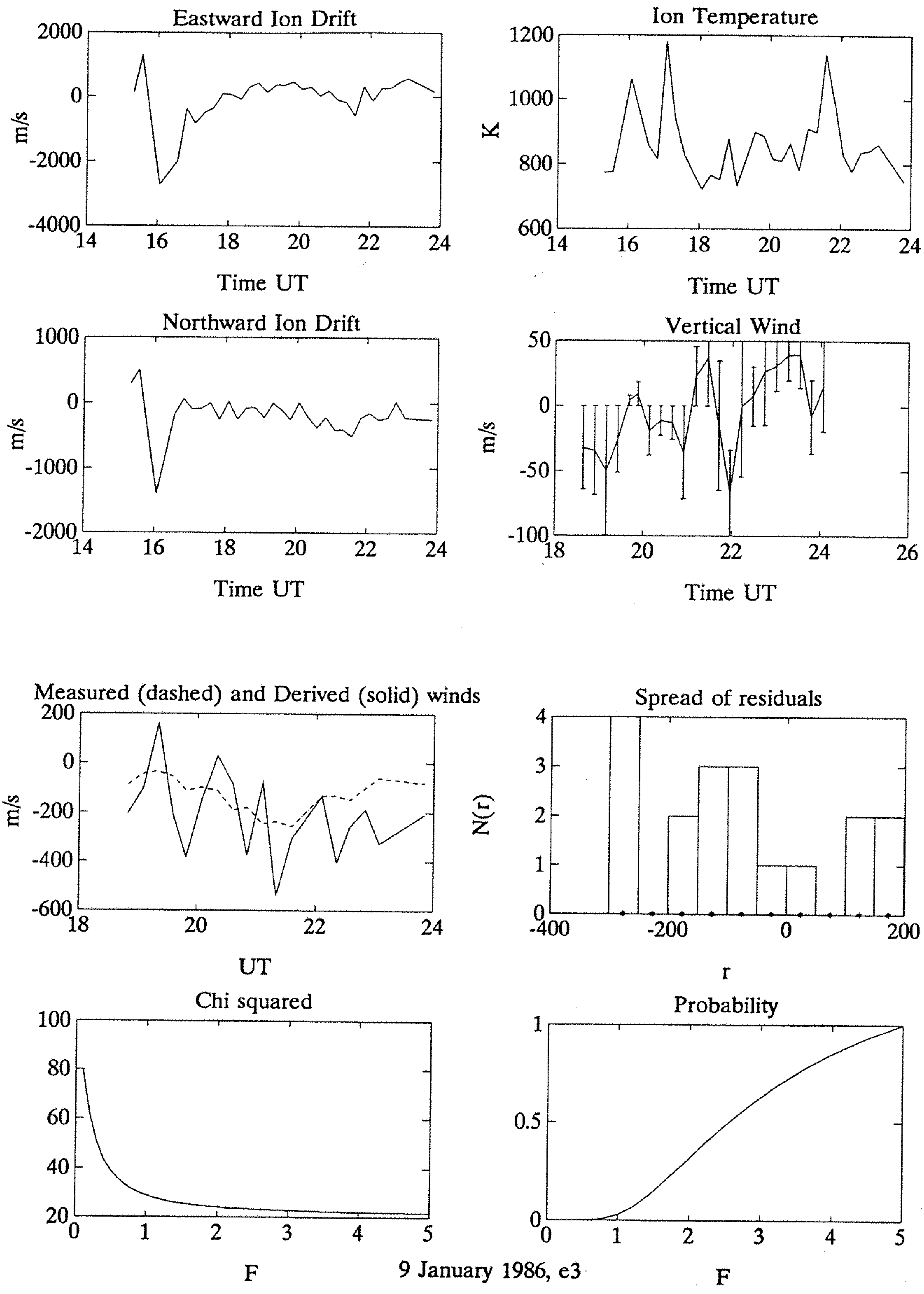

9 January 1986, e3

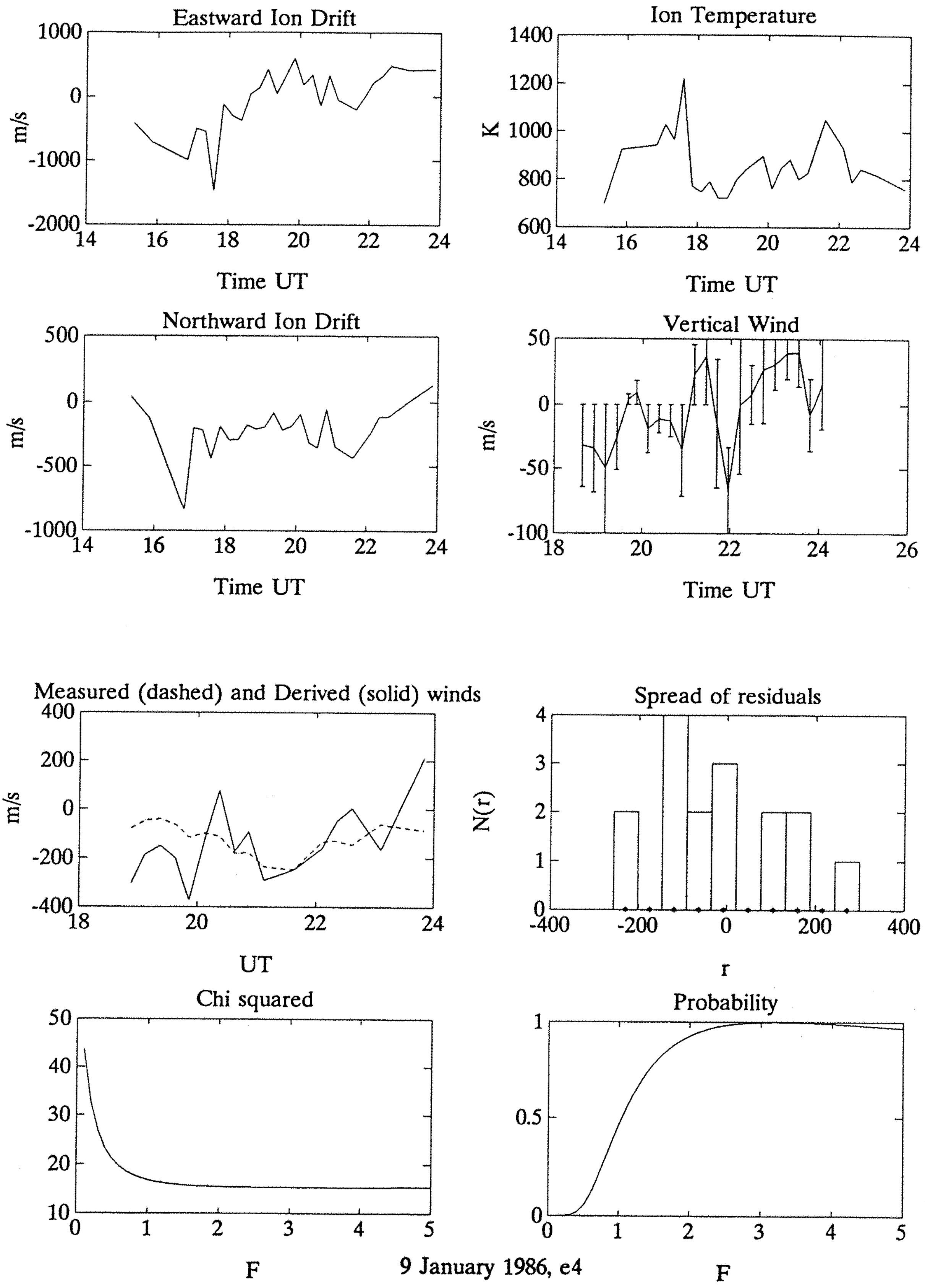

9 January 1986, e4

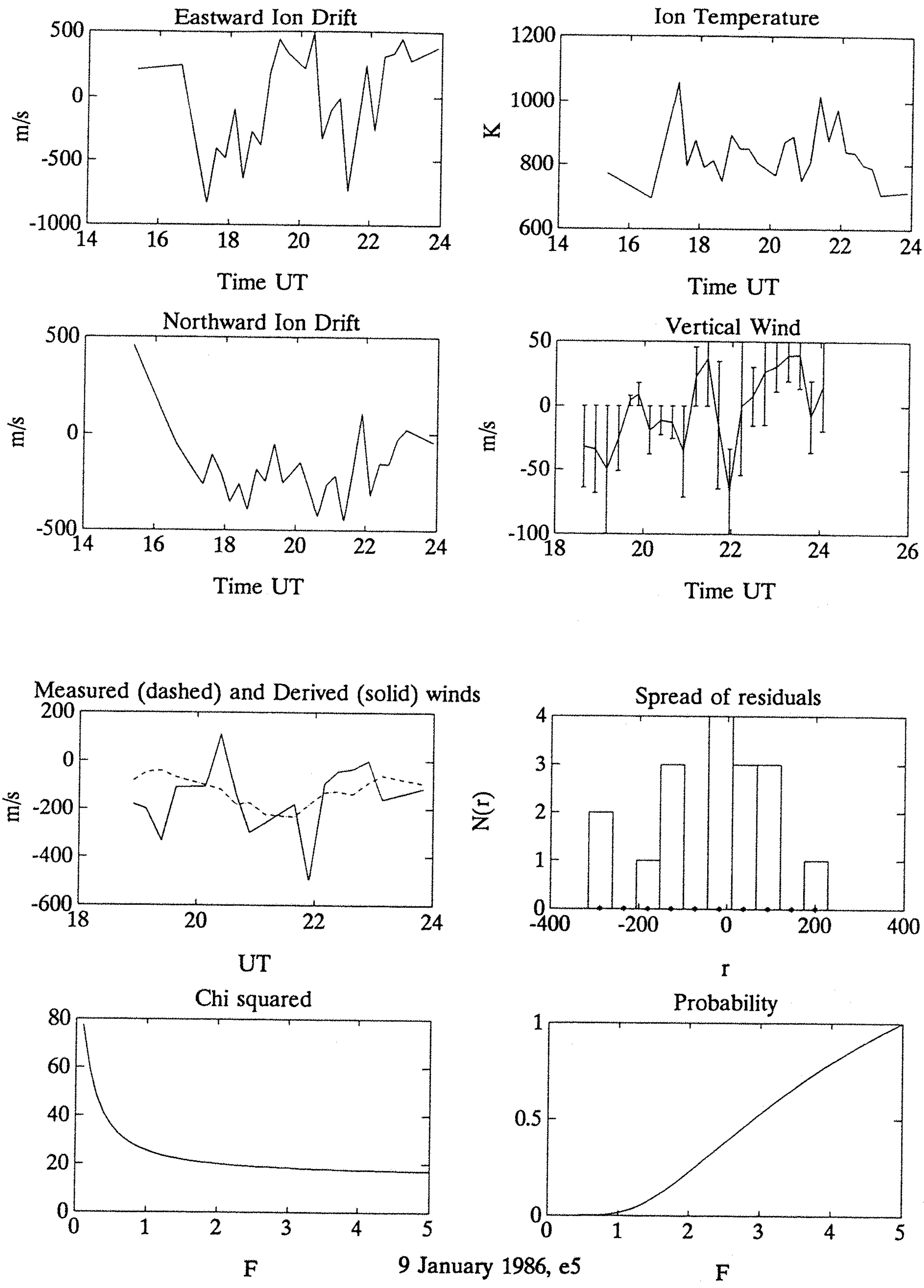

9 January 1986, e5

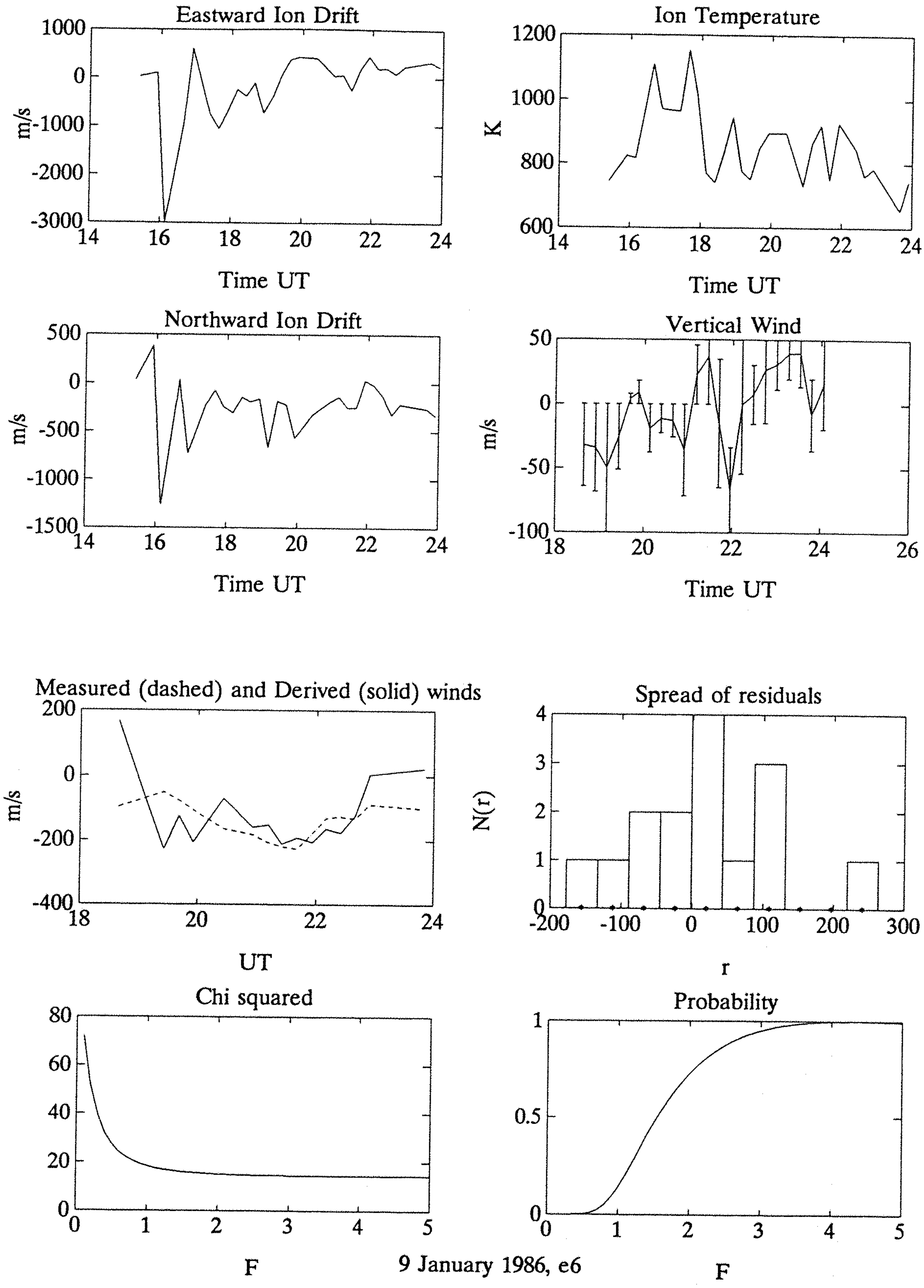

9 January 1986, e6

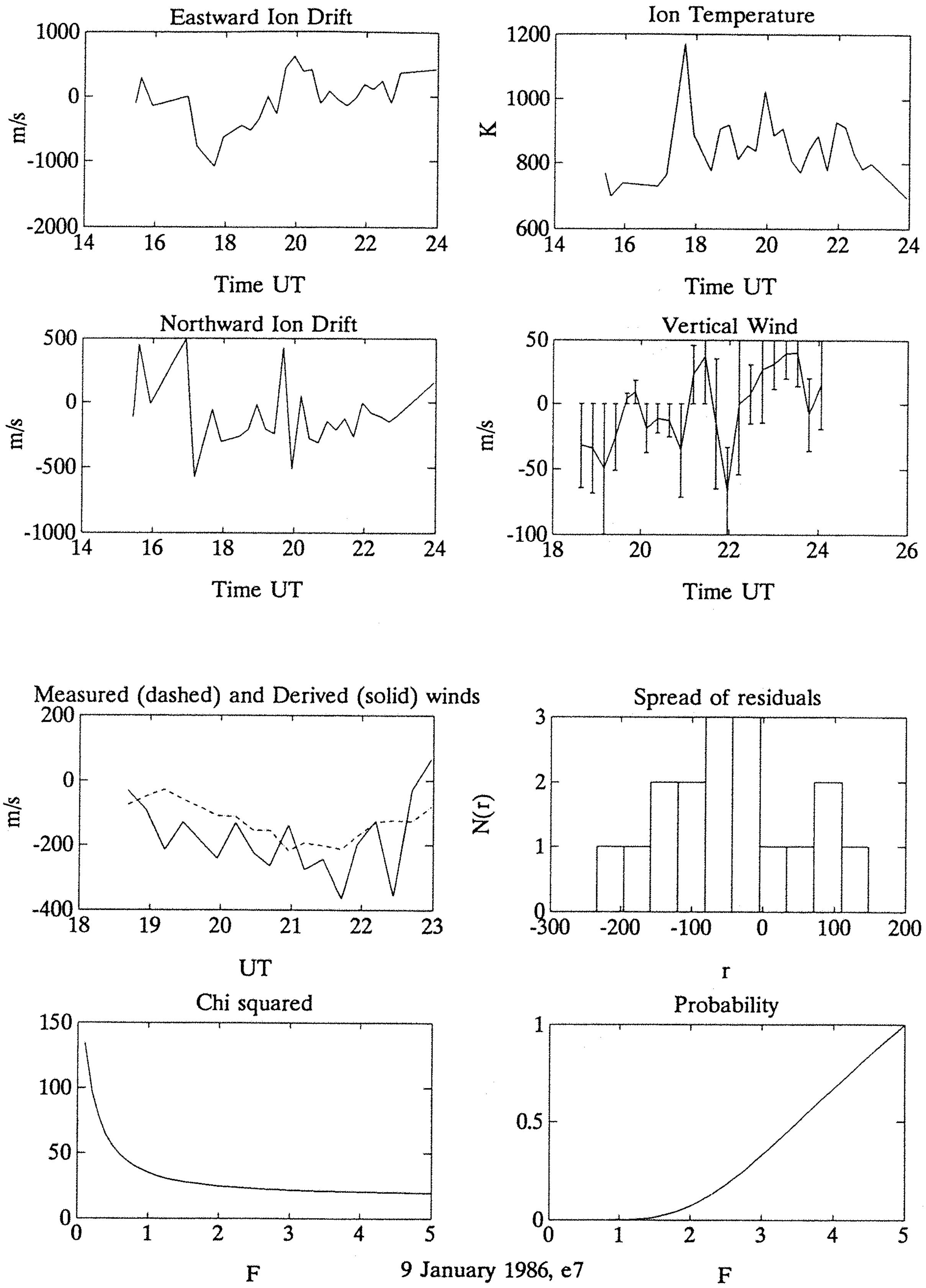

9 January 1986, e7

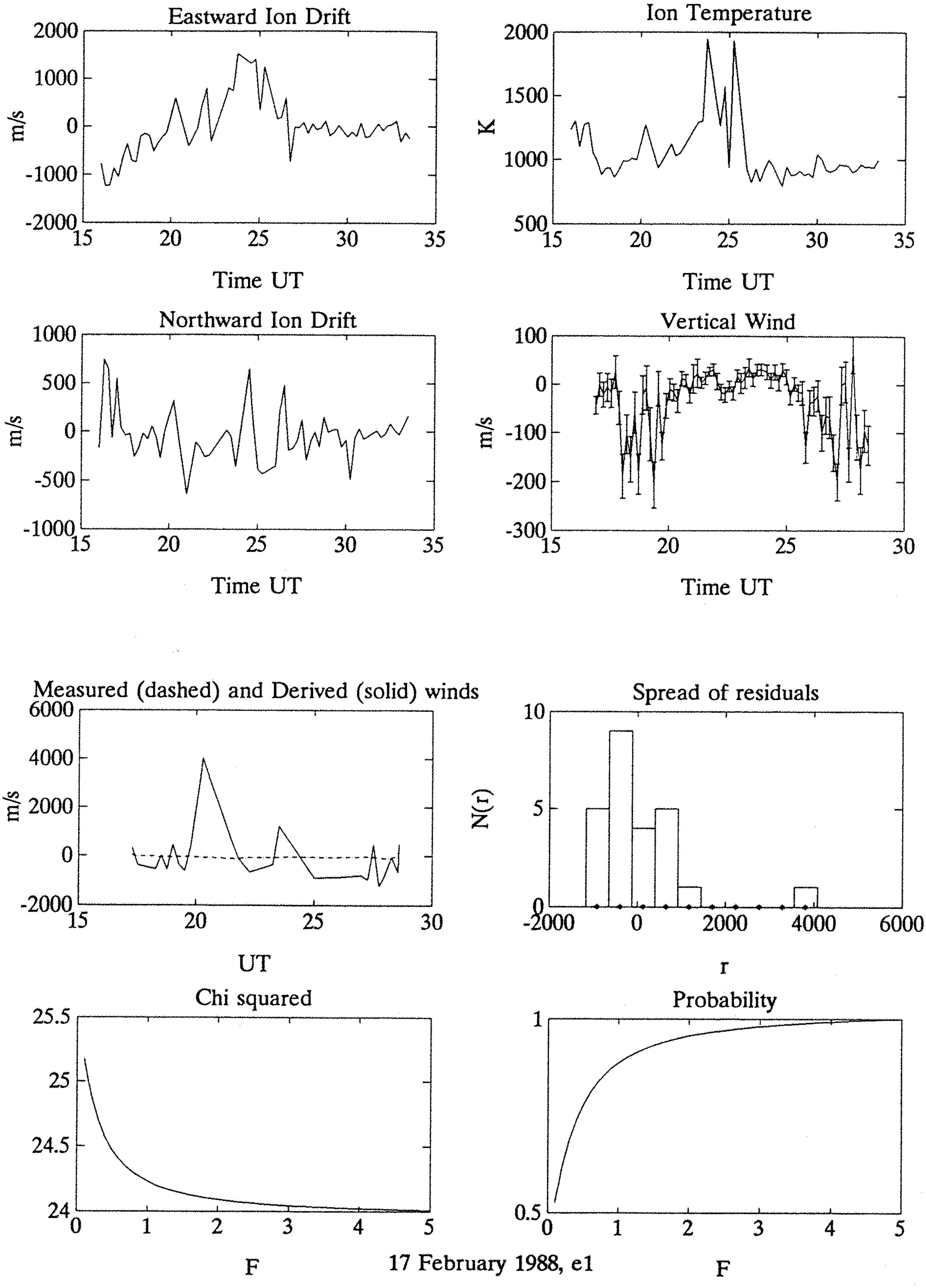

17 February 1988, e1

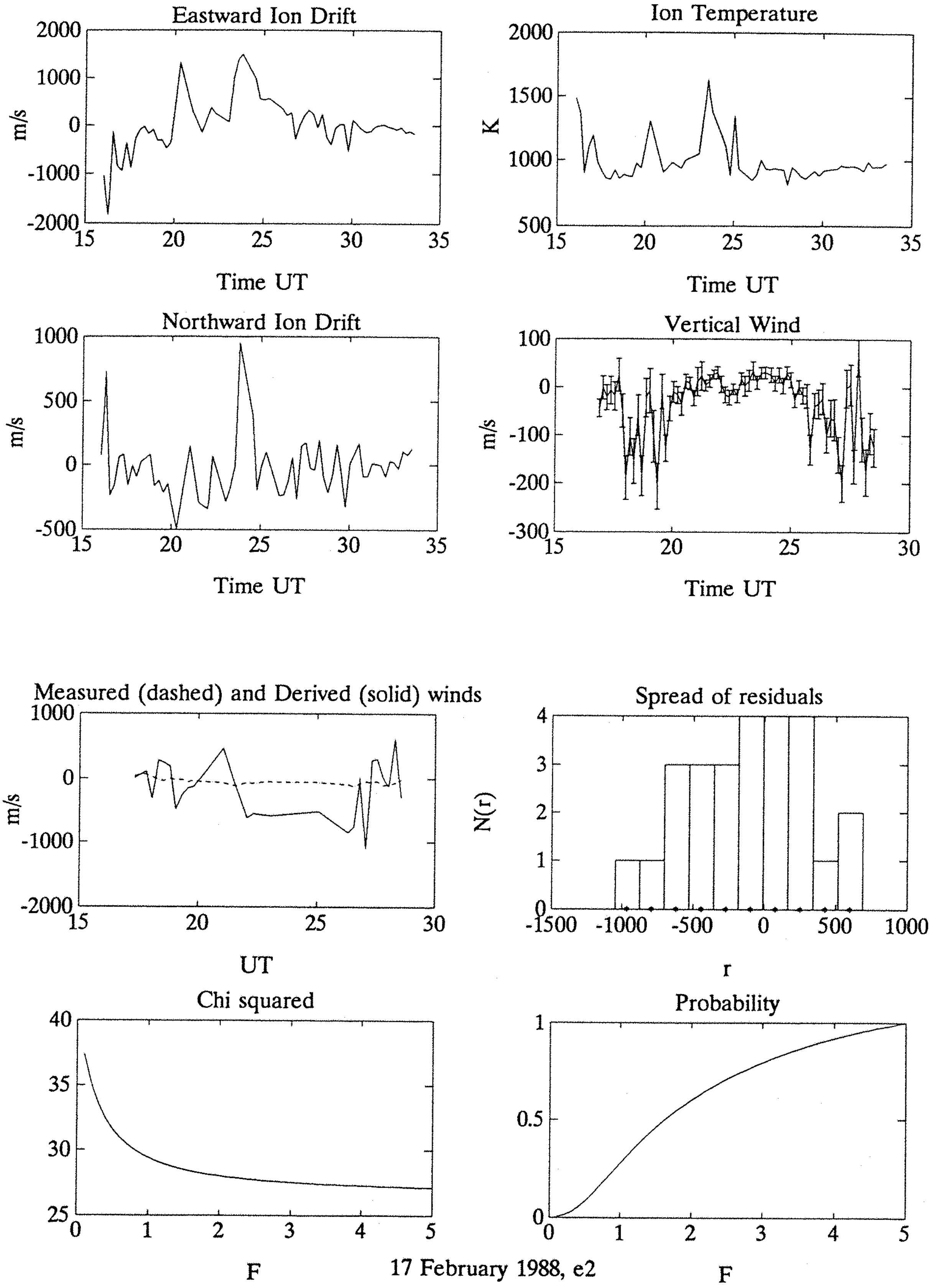

17 February 1988, e2

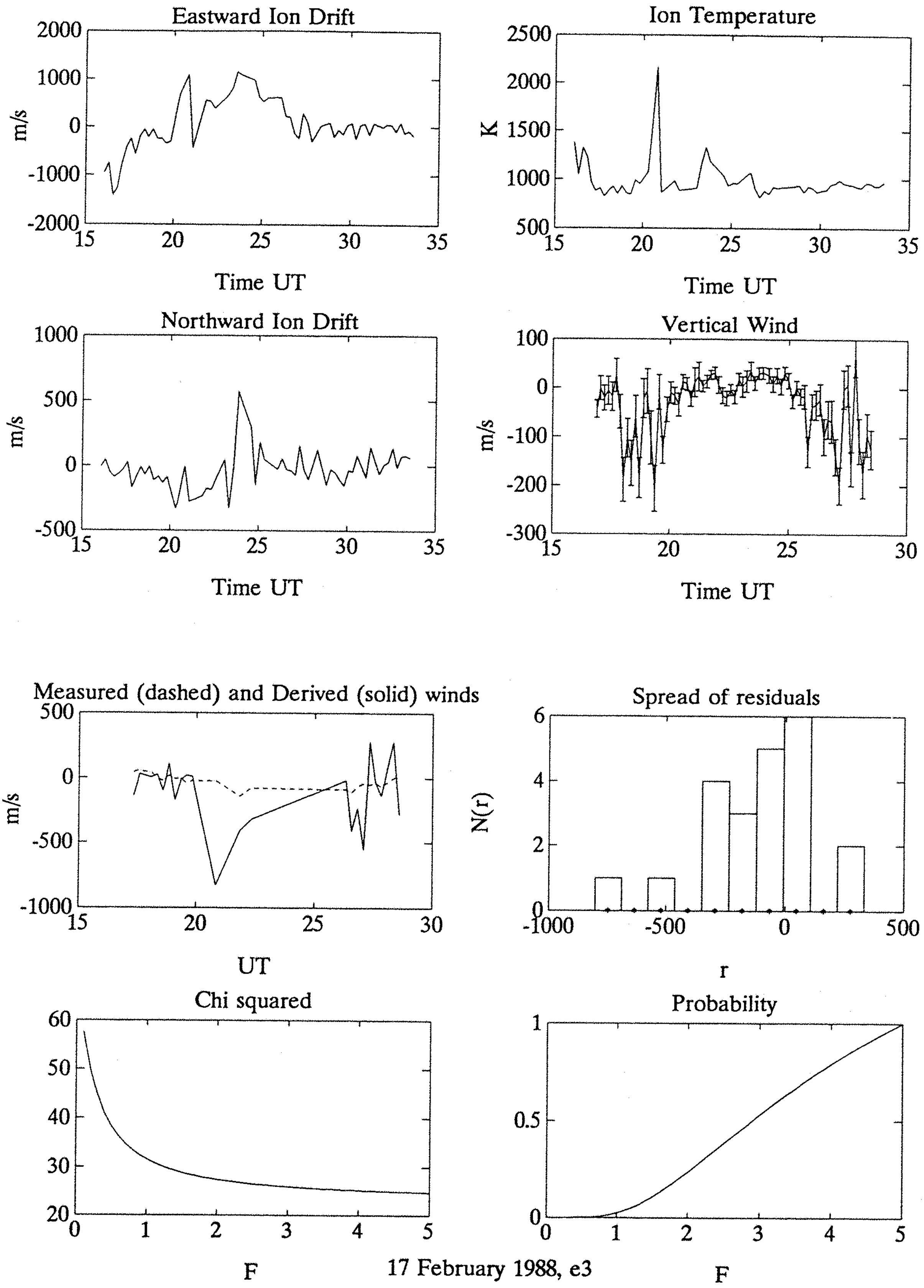

17 February 1988, e3

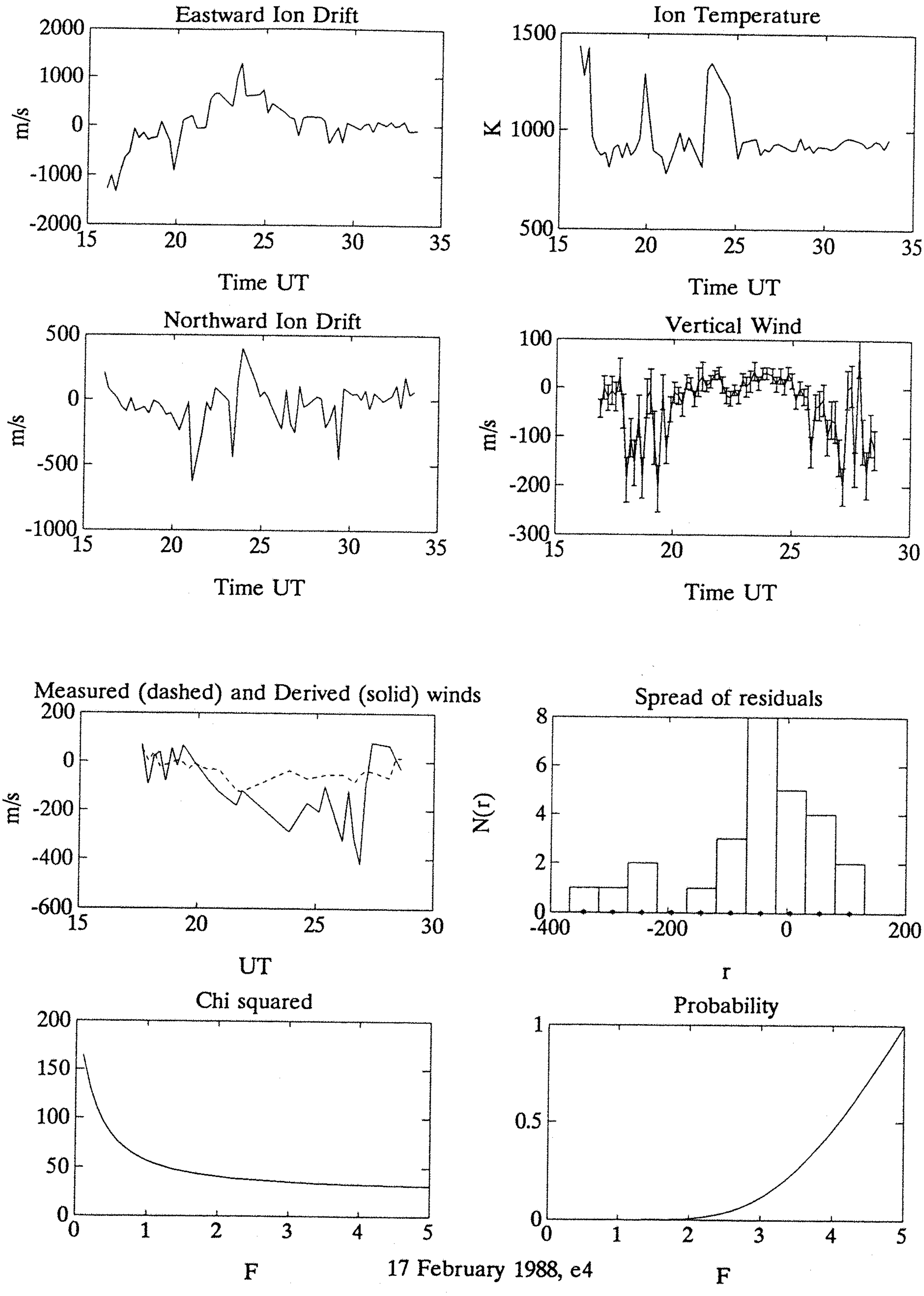

17 February 1988, e4

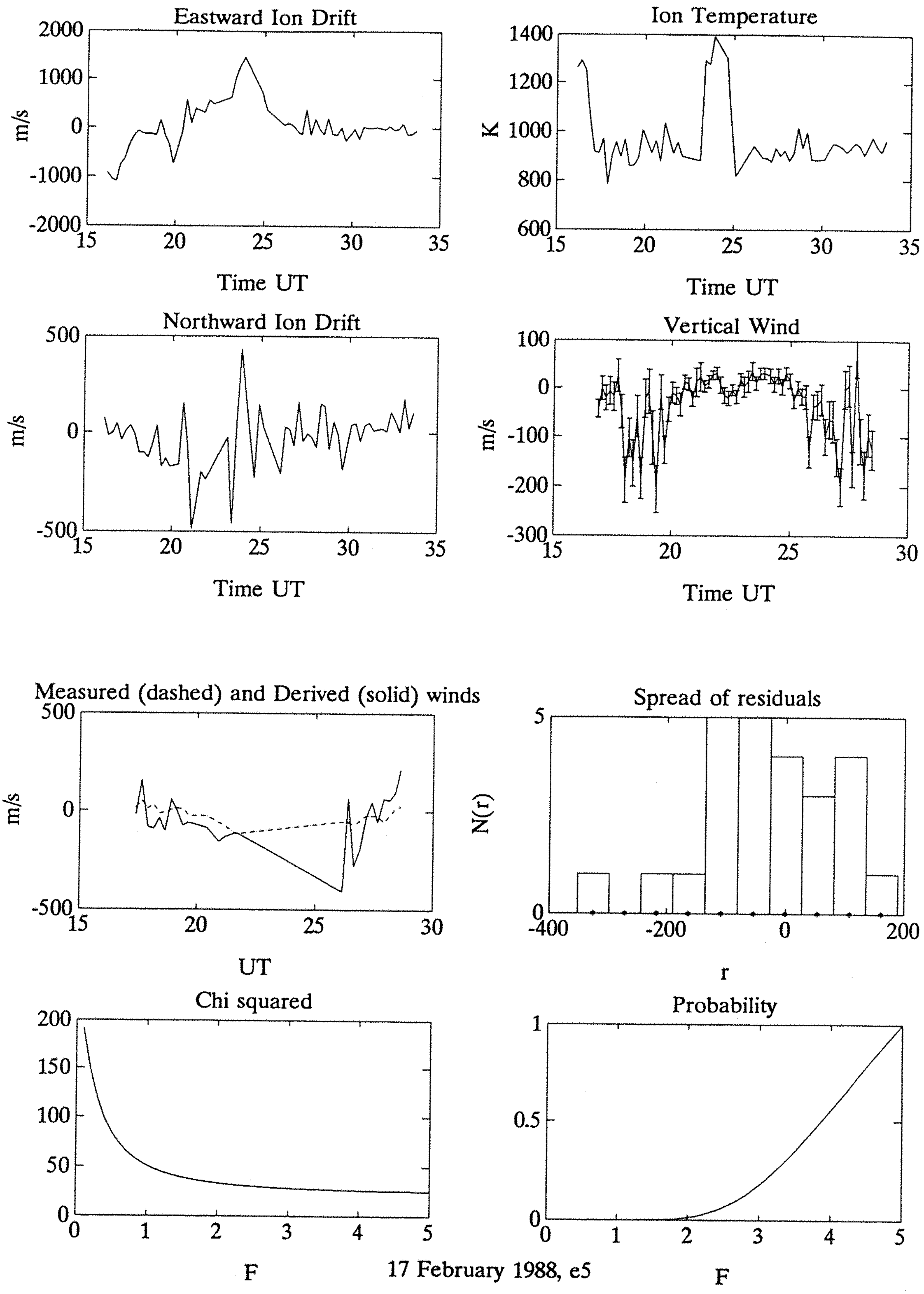

17 February 1988, e5

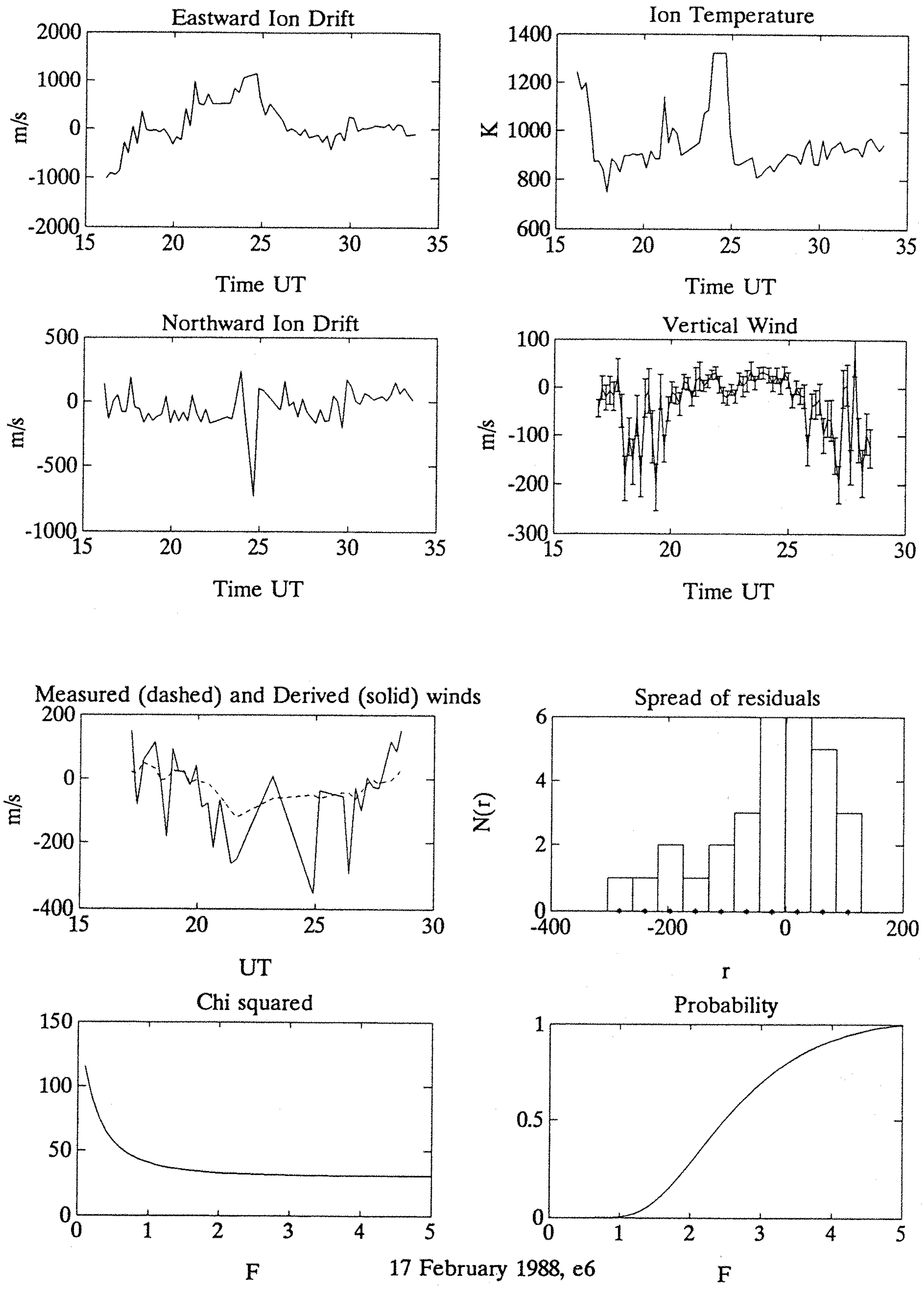

17 February 1988, e6

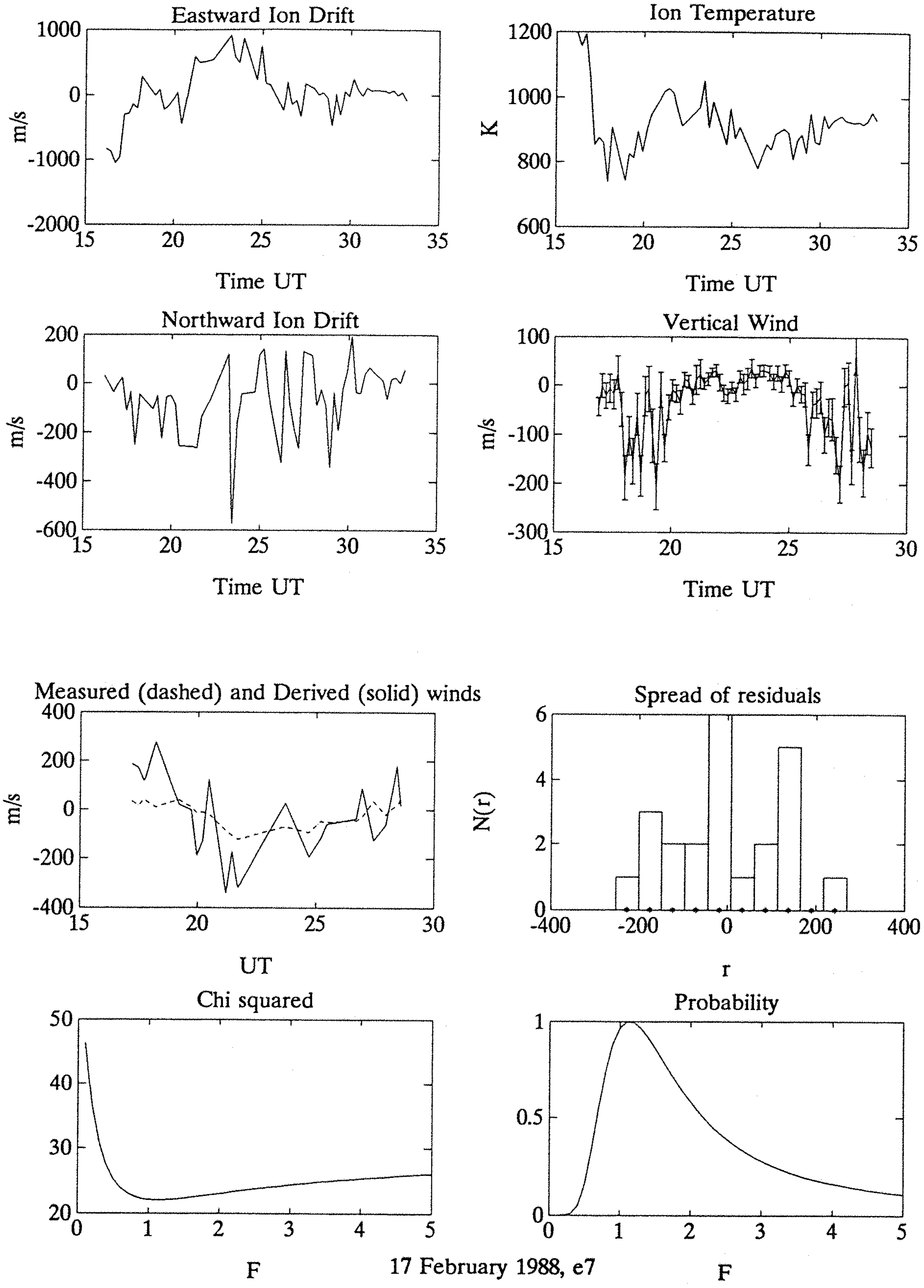

17 February 1988, e7

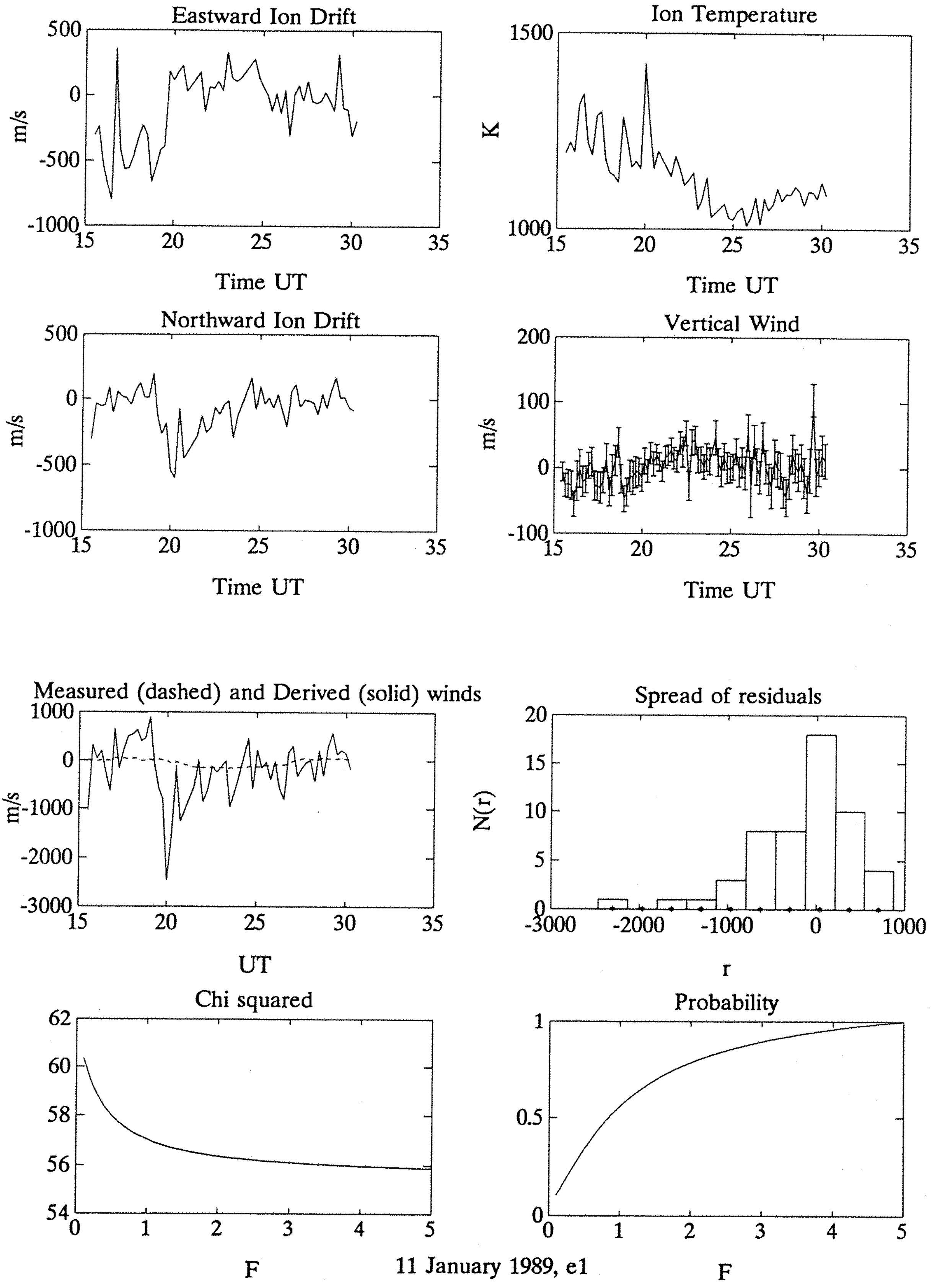

11 January 1989, e1

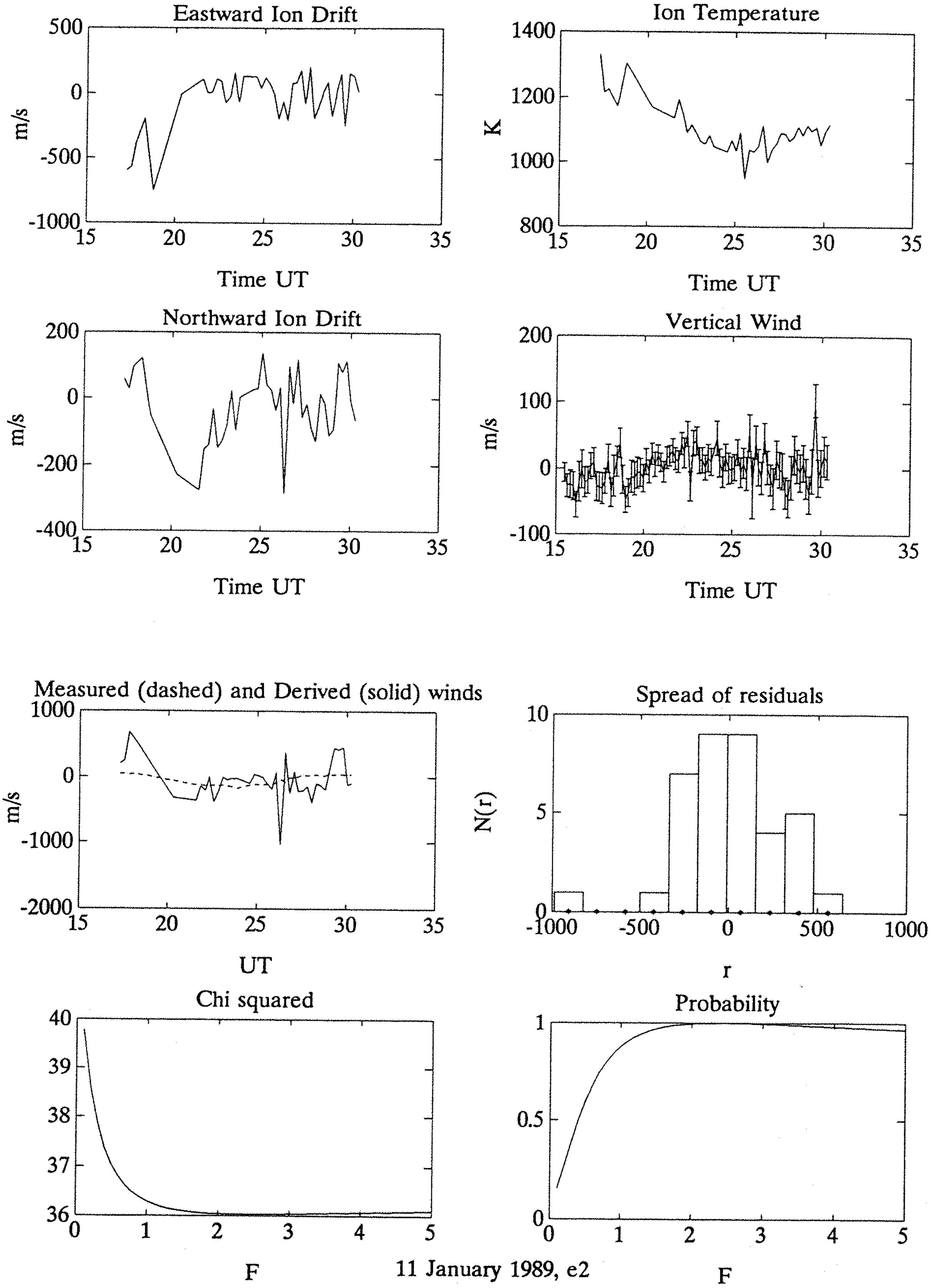

11 January 1989, e2

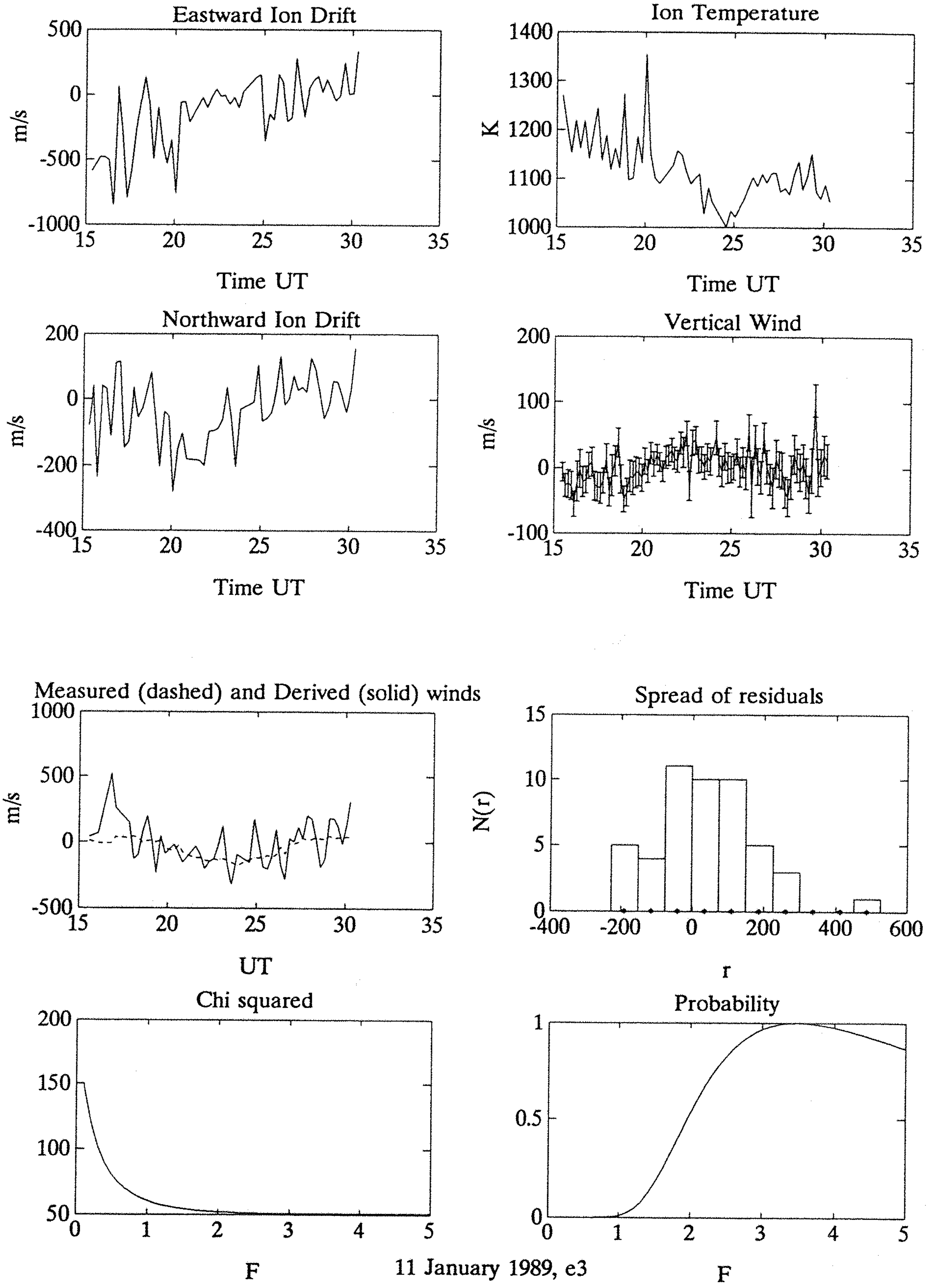

11 January 1989, e3

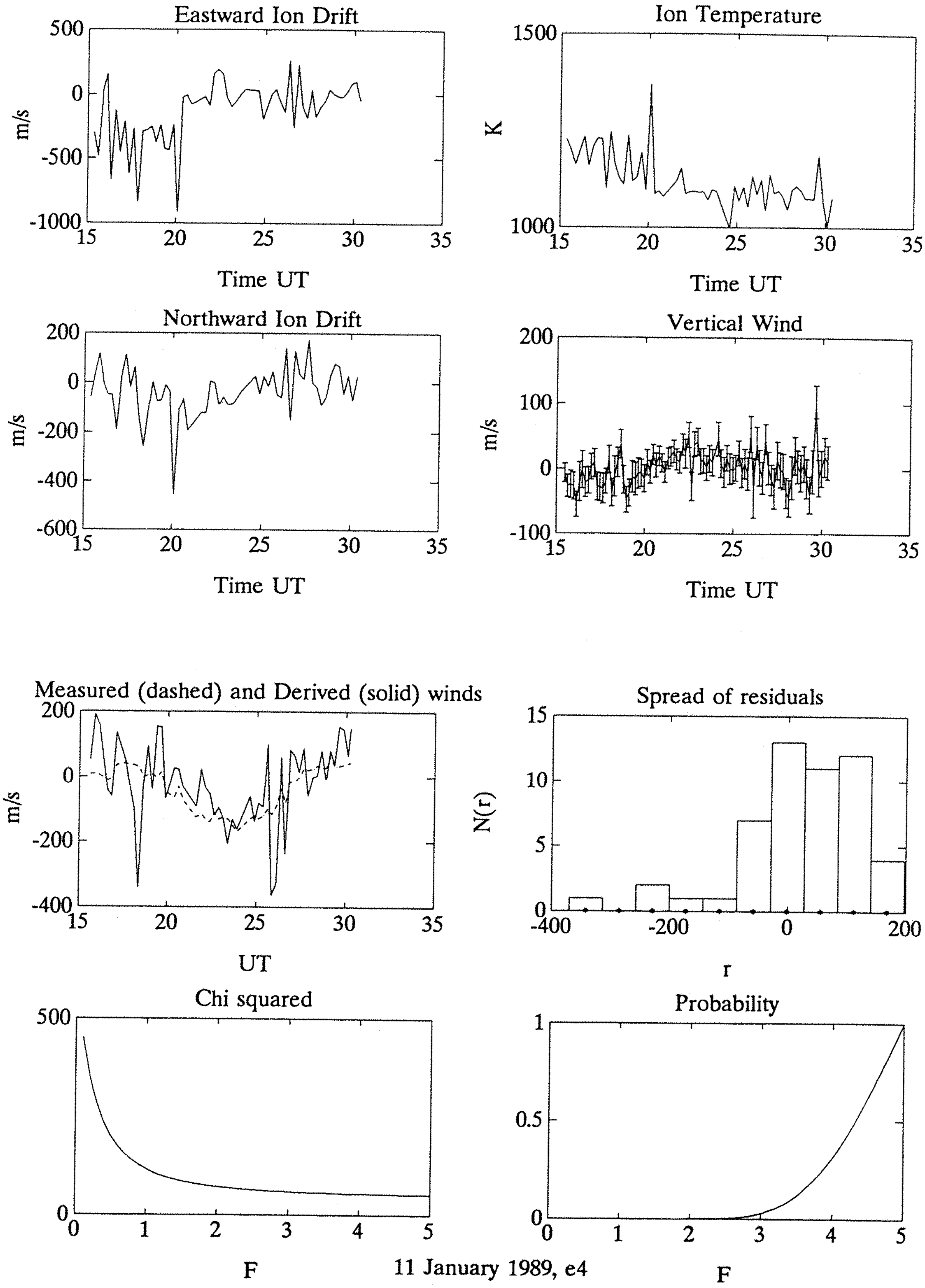

11 January 1989, e4

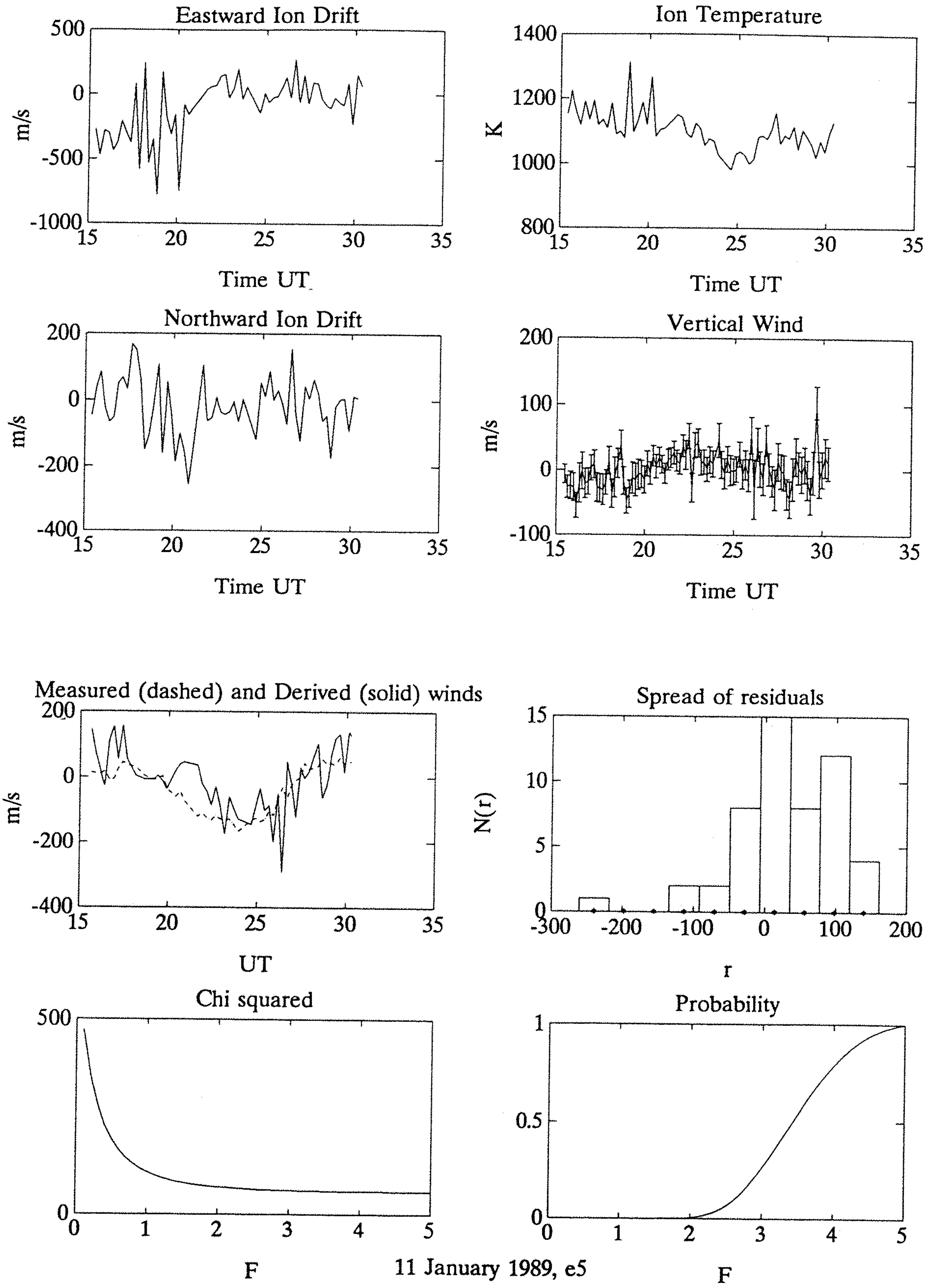

Eastward Ion Drift

Ion Temperature

Northward Ion Drift

Vertical Wind

Measured (dashed) and Derived (solid) winds

Spread of residuals

Chi squared

Probability

11 January 1989, e5

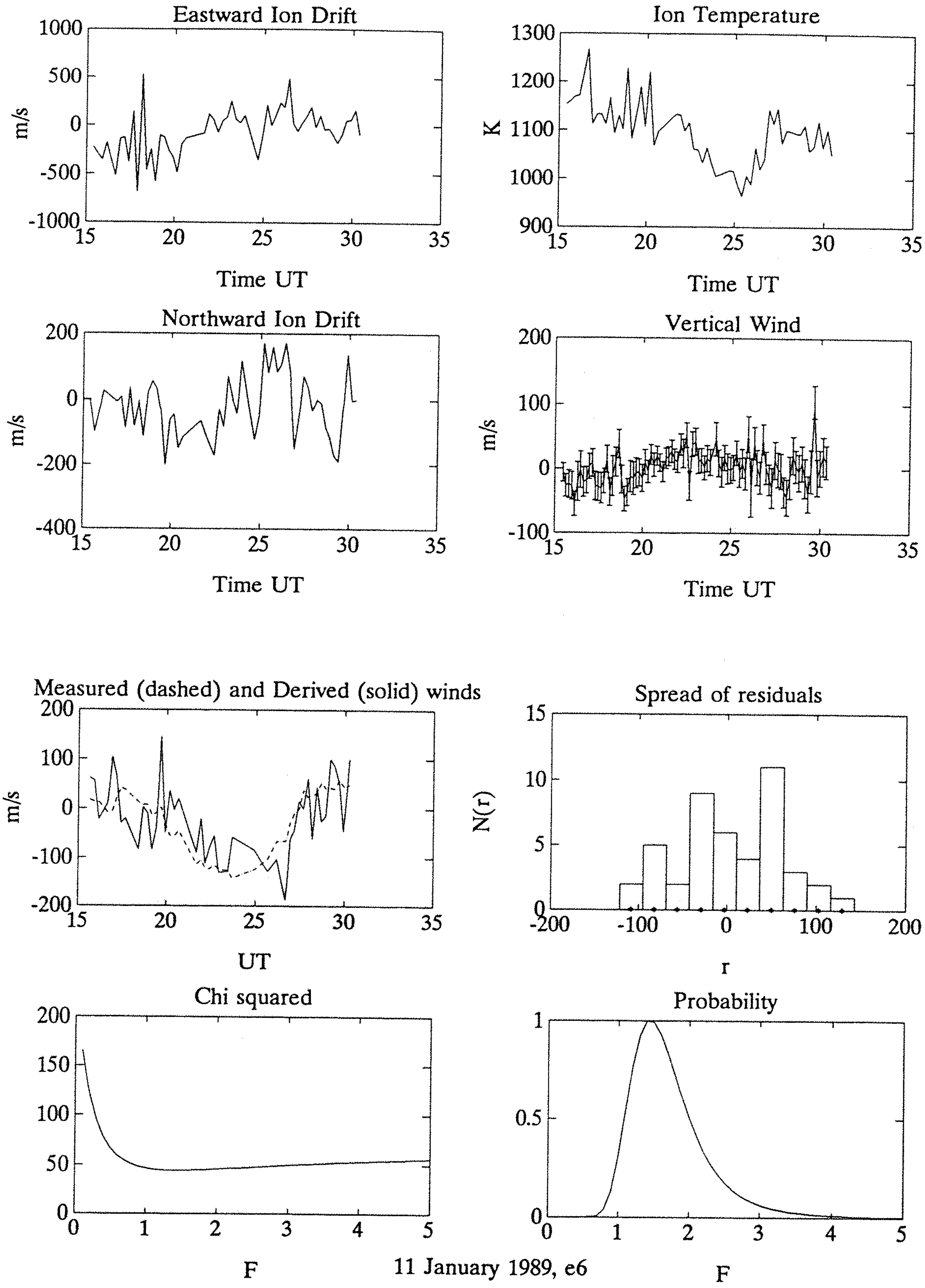

11 January 1989, e6

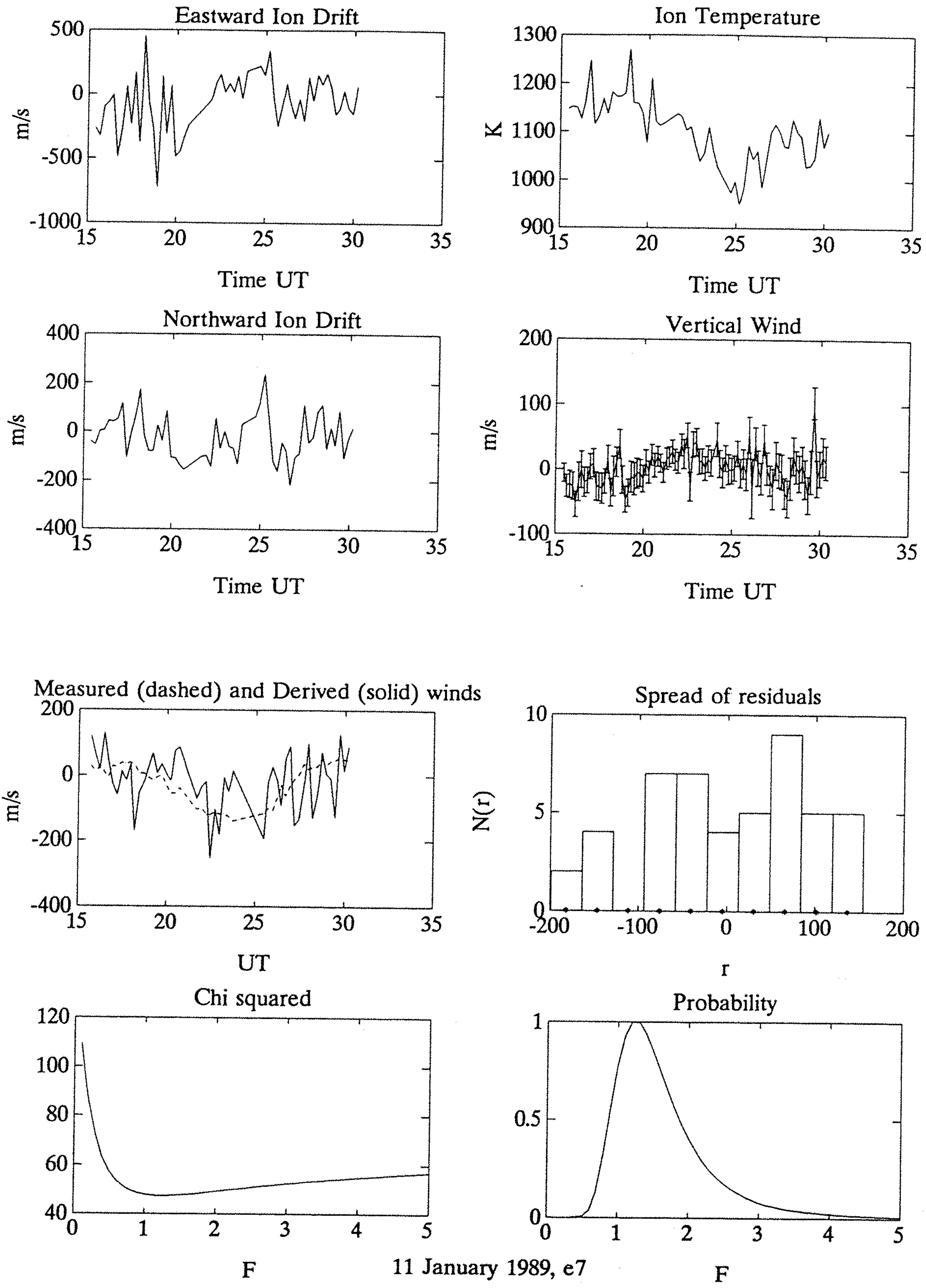

11 January 1989, e7

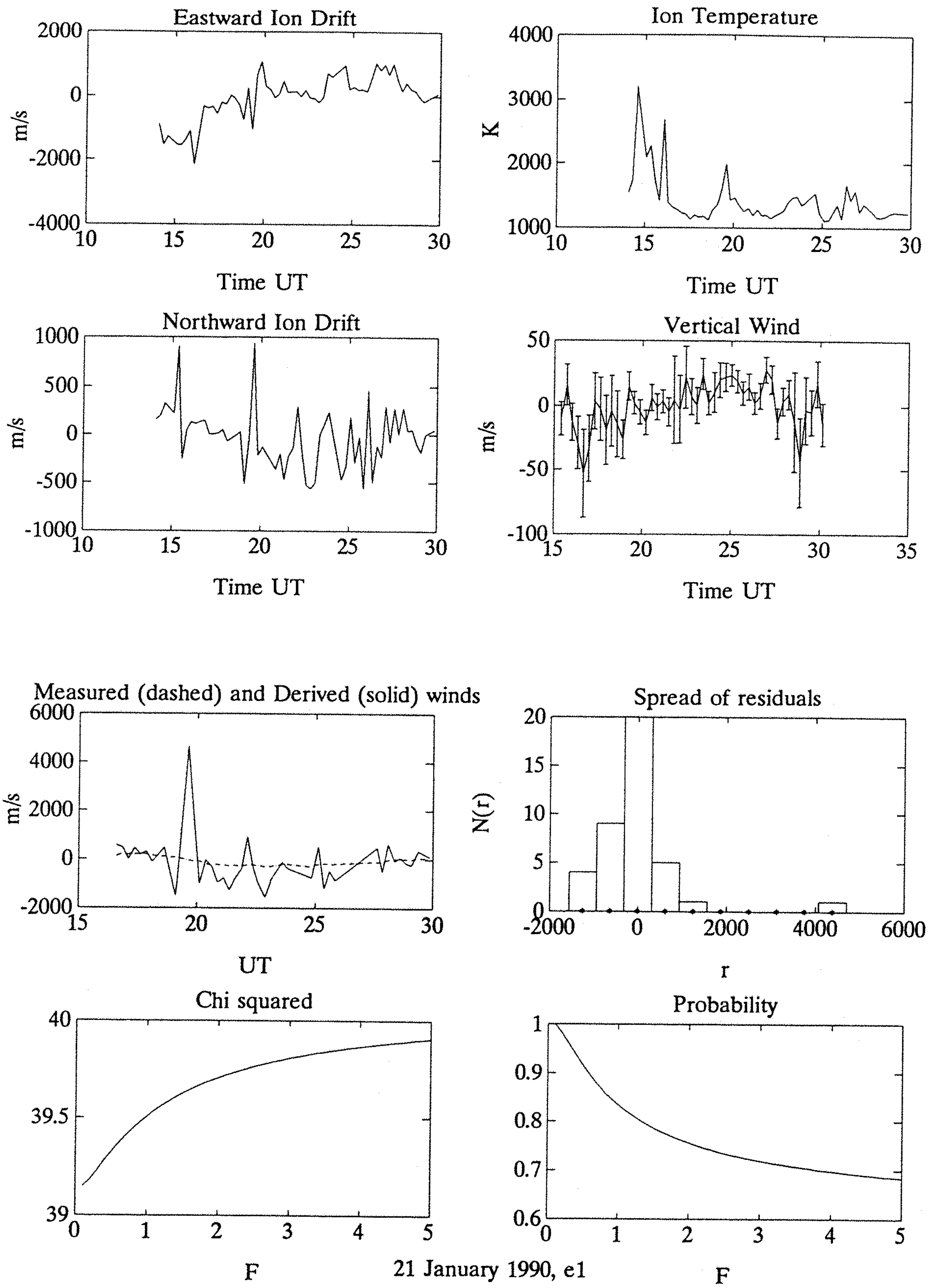

21 January 1990, e1

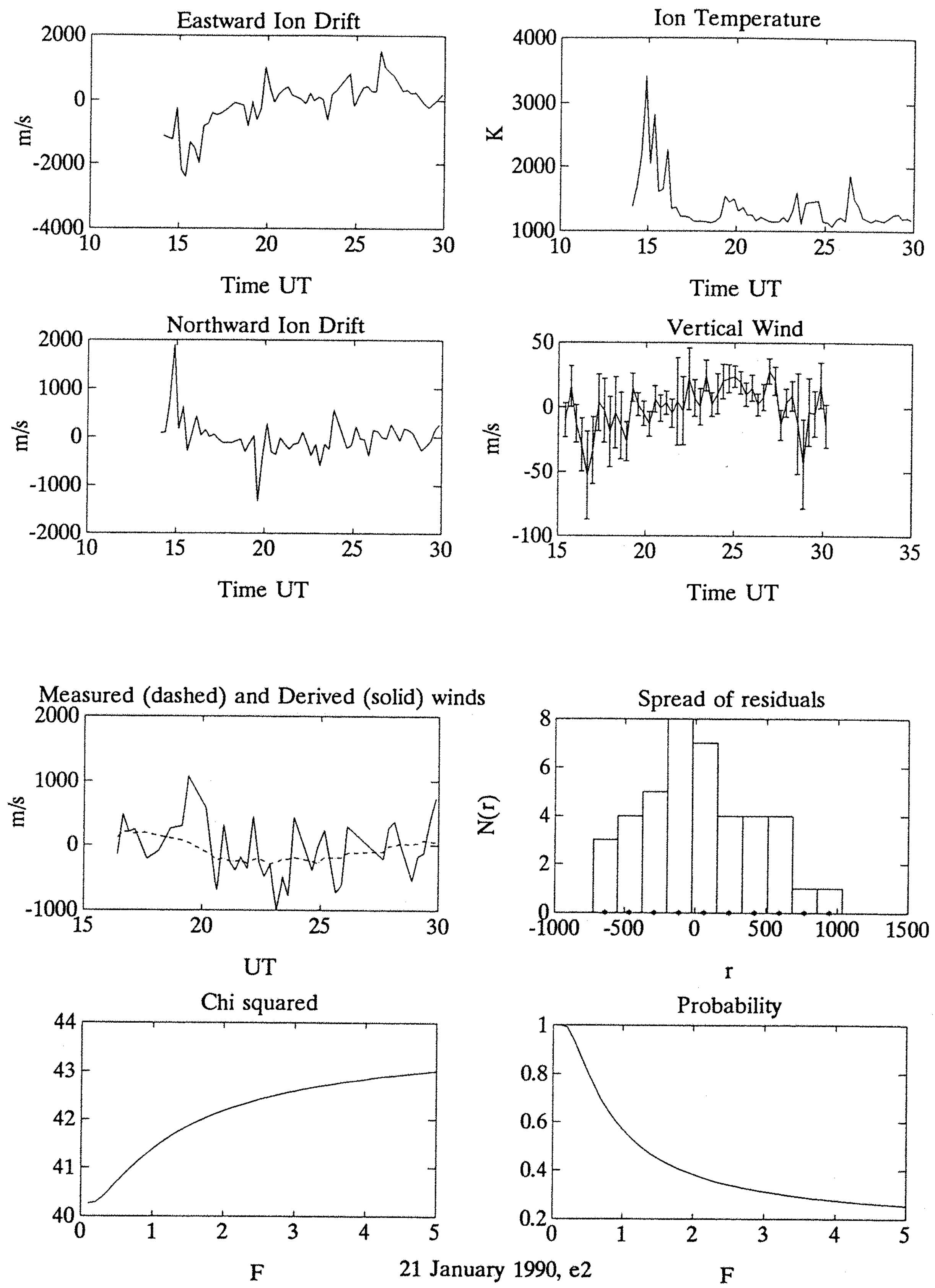

21 January 1990, e2

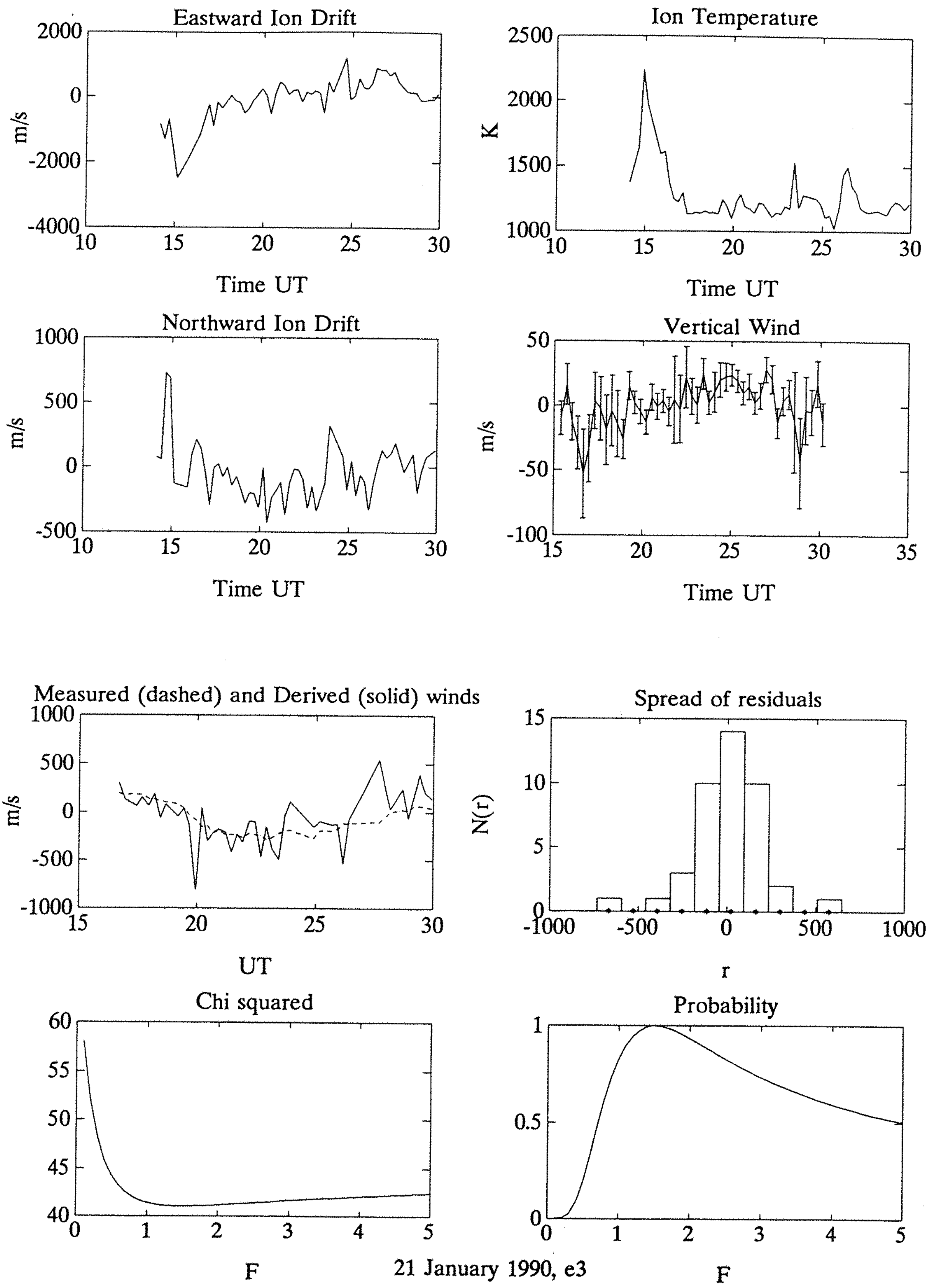
Eastward Ion Drift

Ion Temperature

Northward Ion Drift

Vertical Wind

Measured (dashed) and Derived (solid) winds

Spread of residuals

Chi squared

Probability

21 January 1990, e3

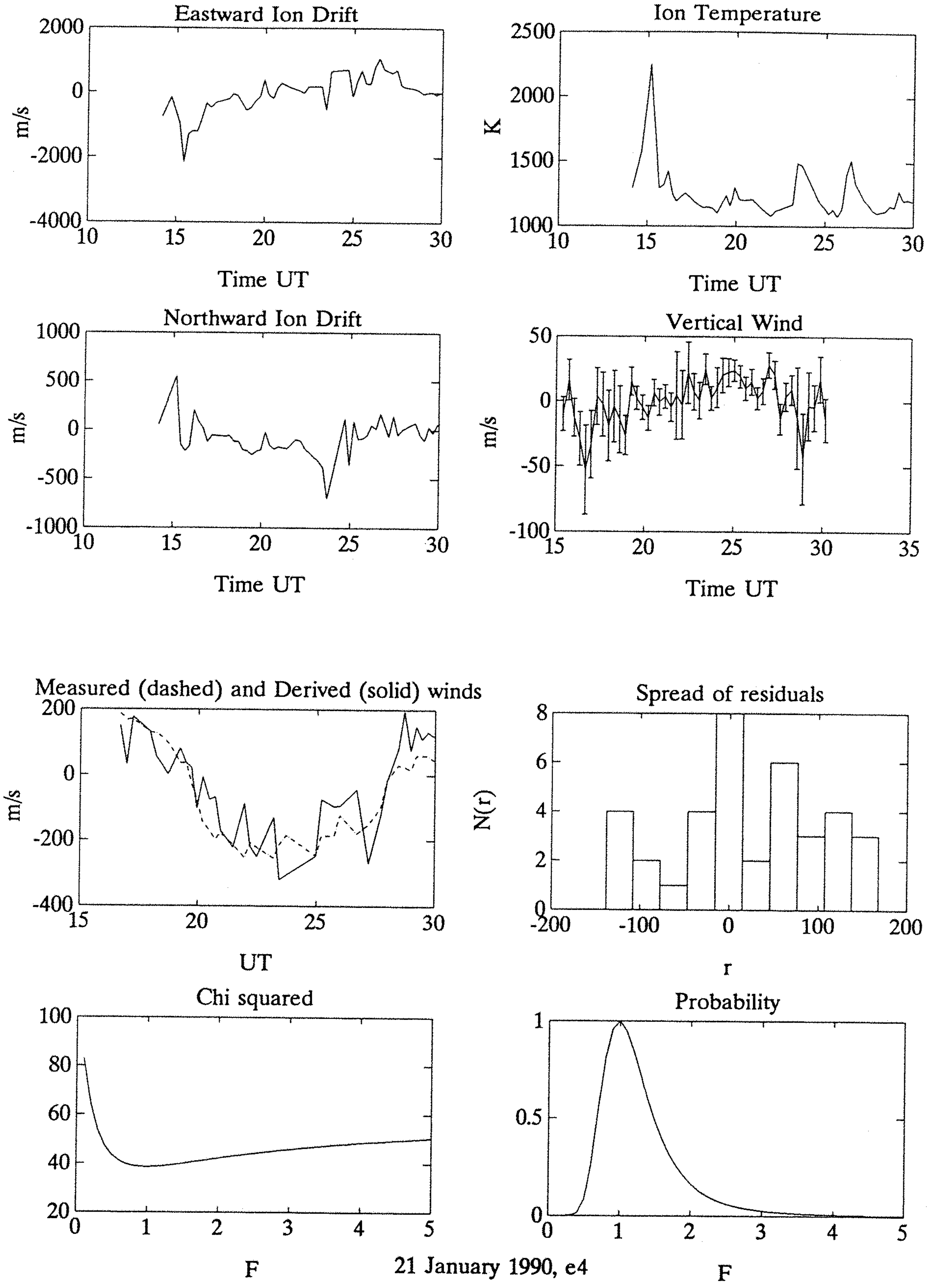

21 January 1990, e4

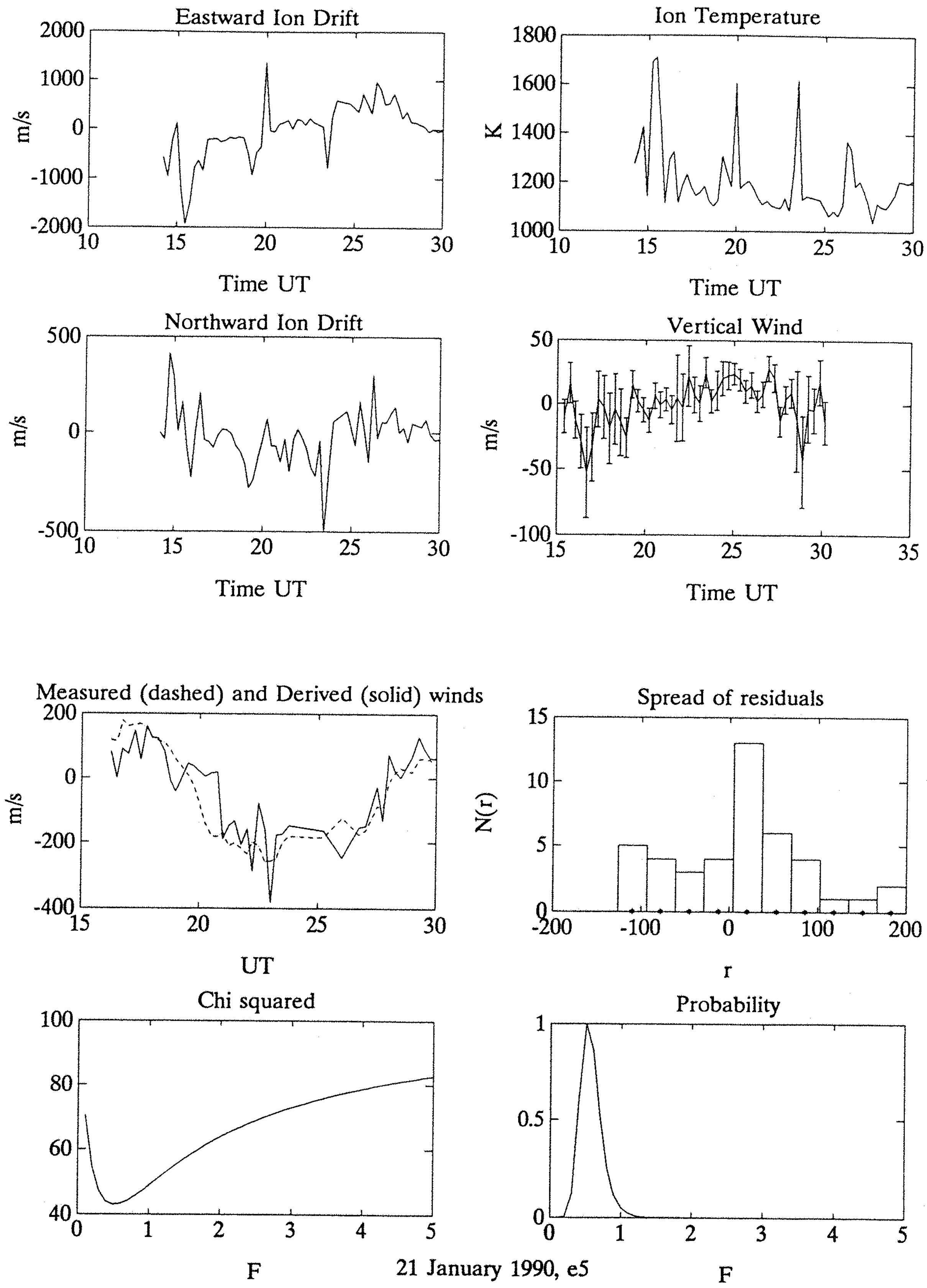

21 January 1990, e5

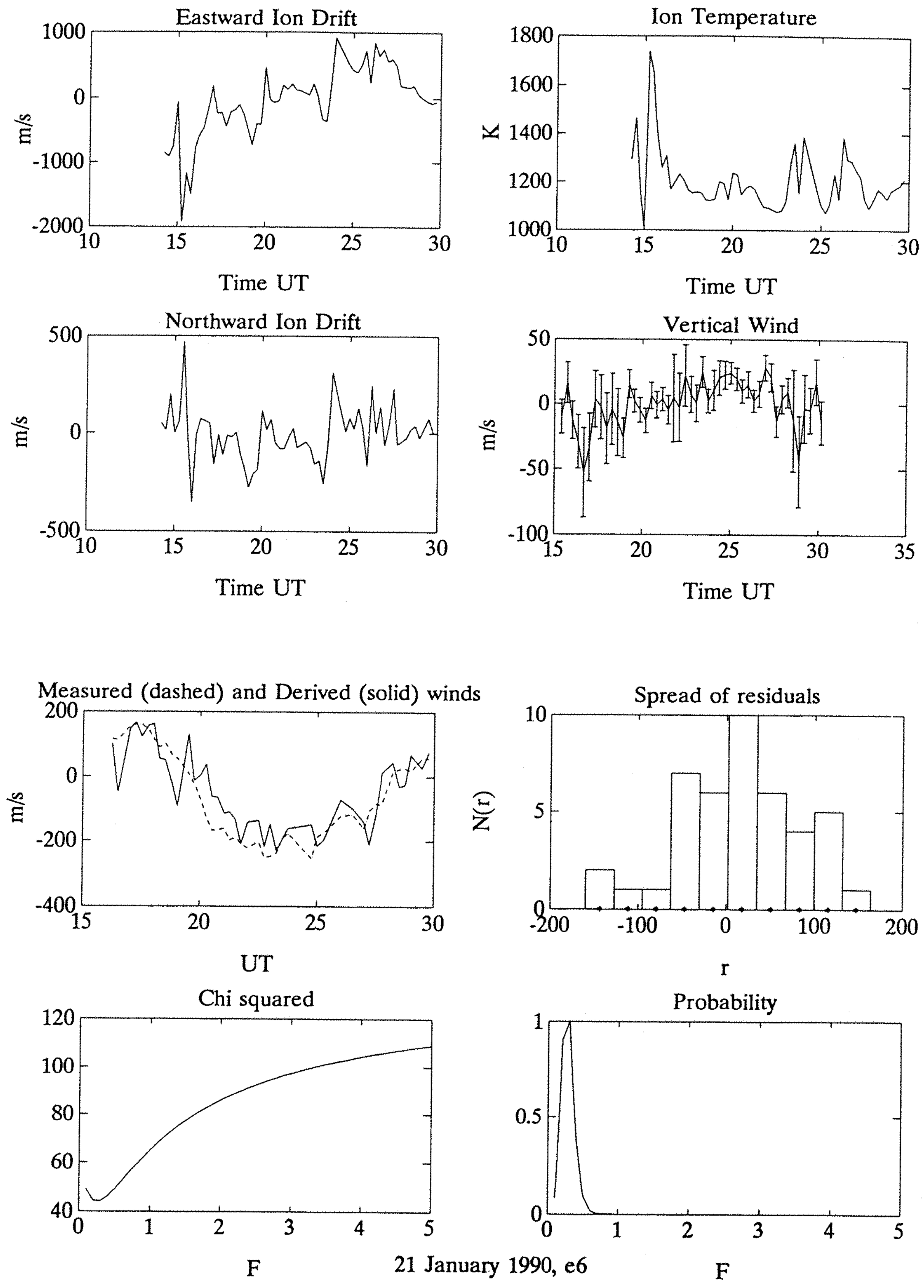

21 January 1990, e6

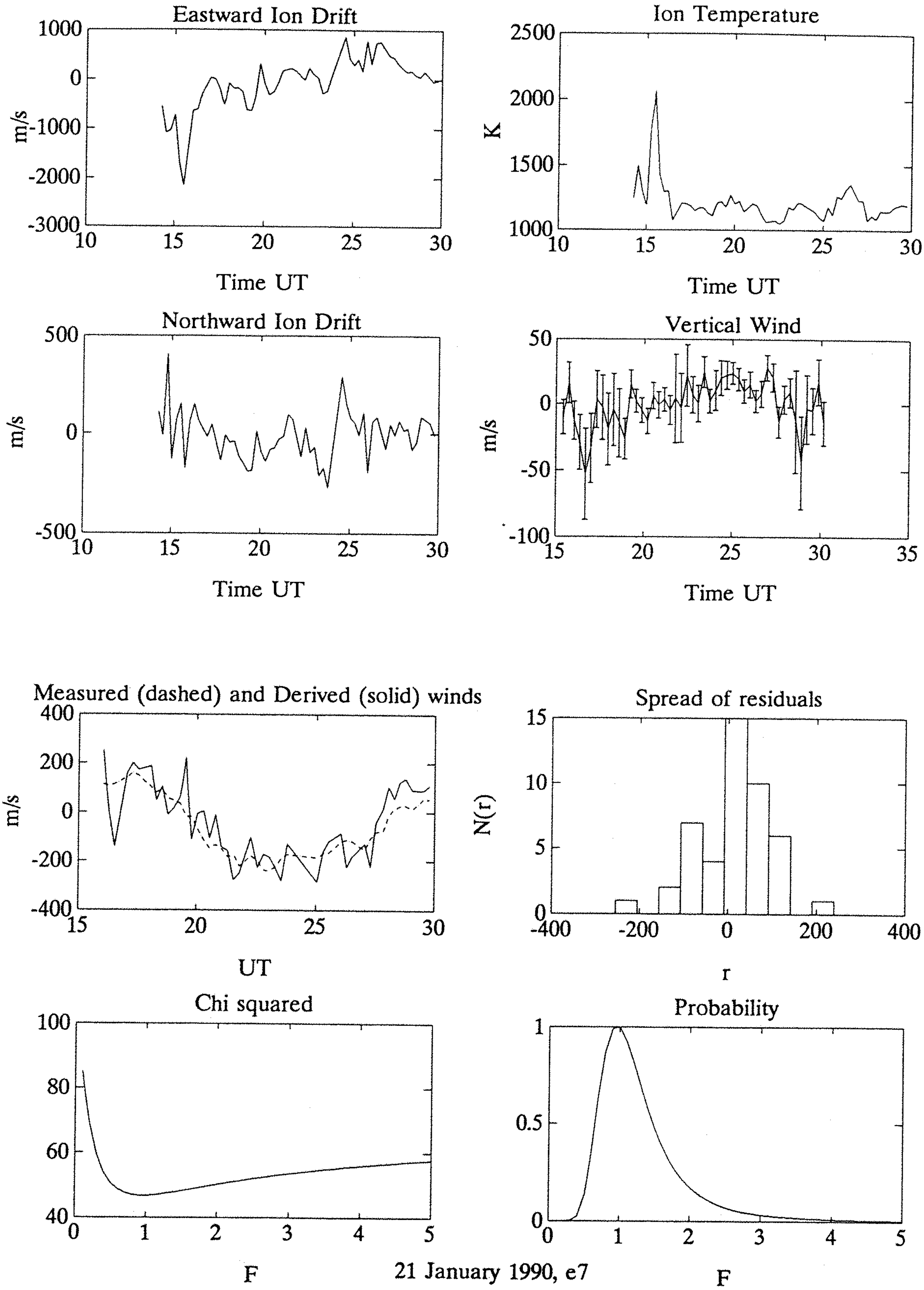

21 January 1990, e7

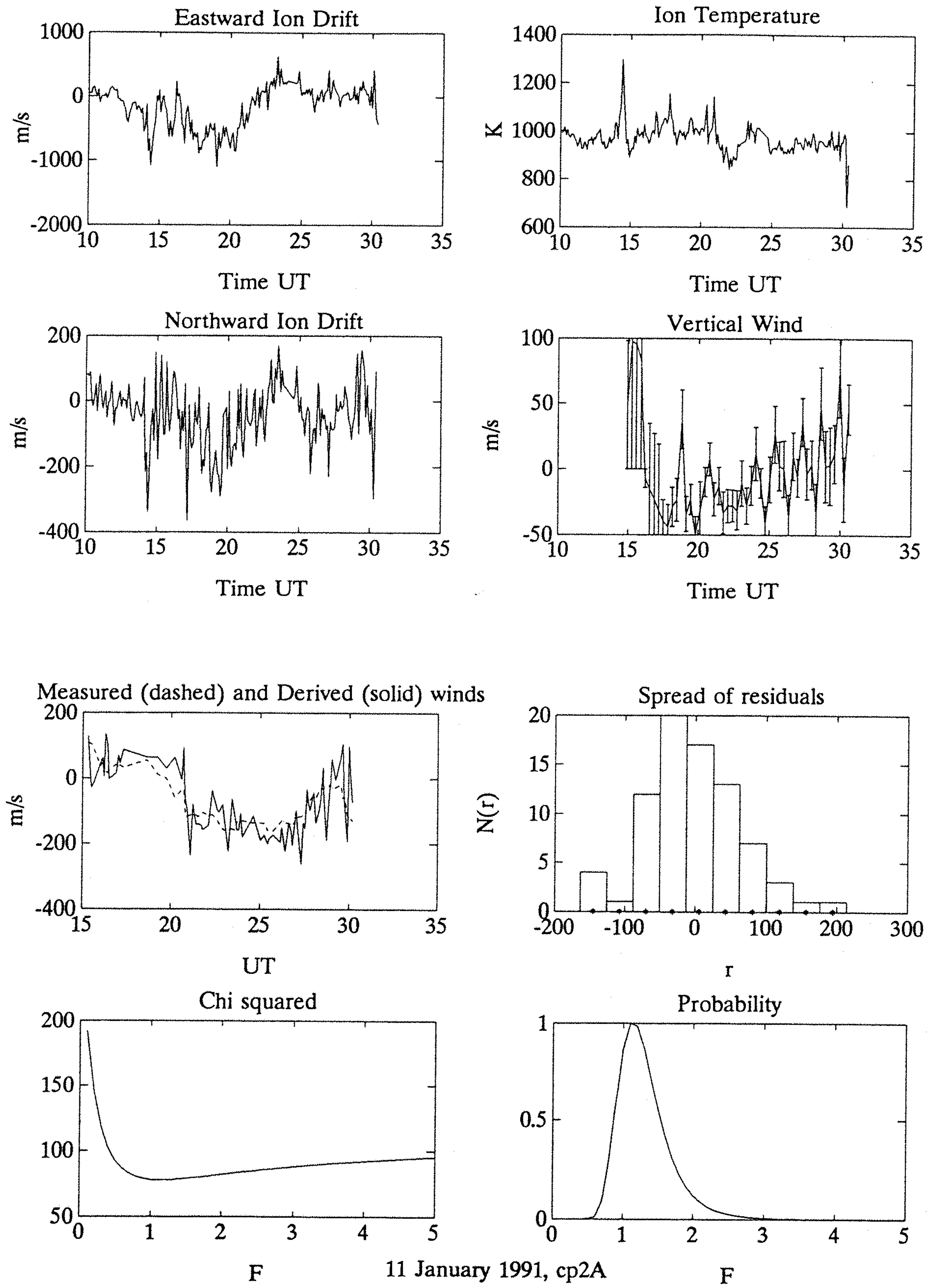

11 January 1991, cp2A

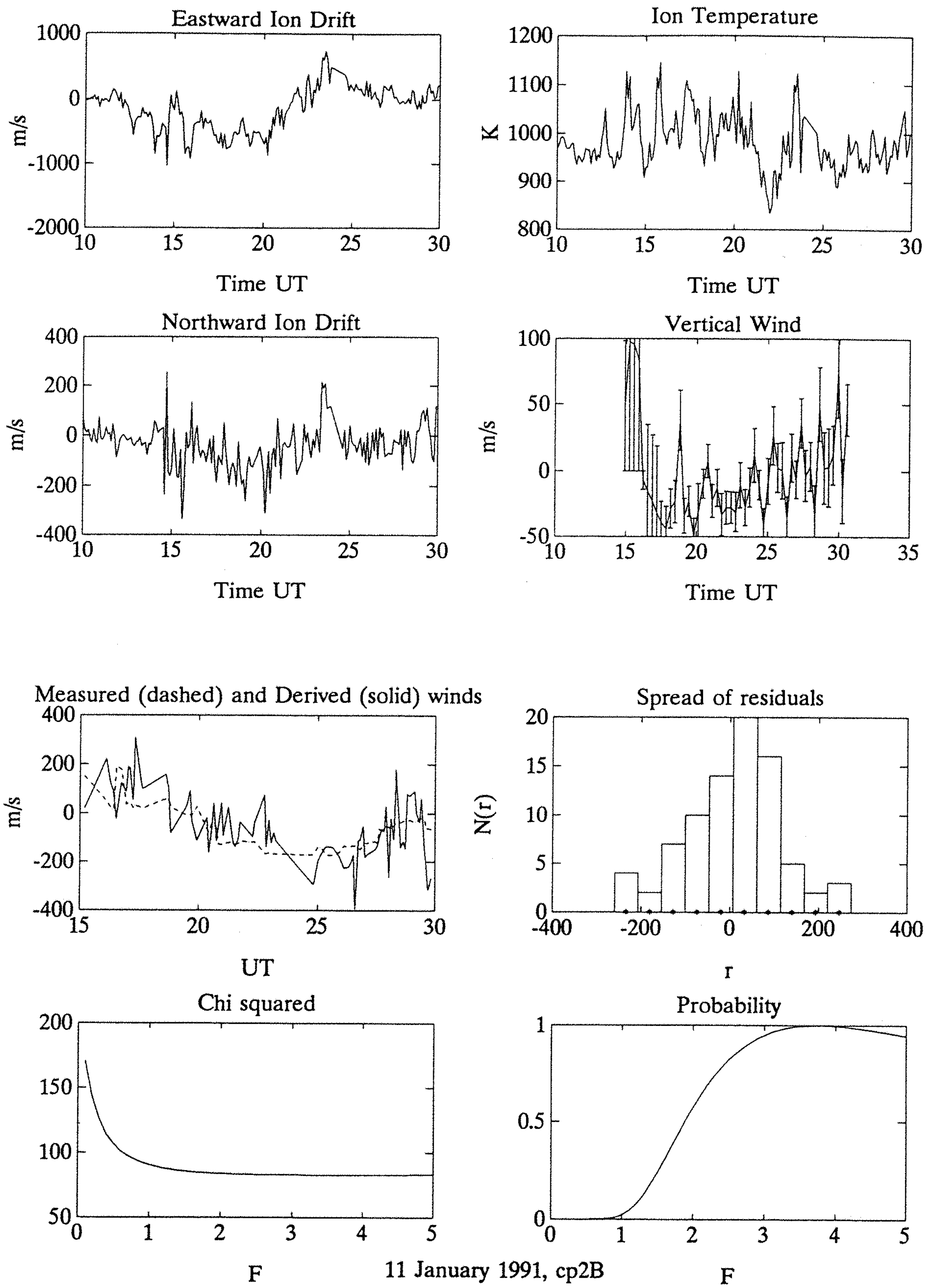

11 January 1991, cp2B

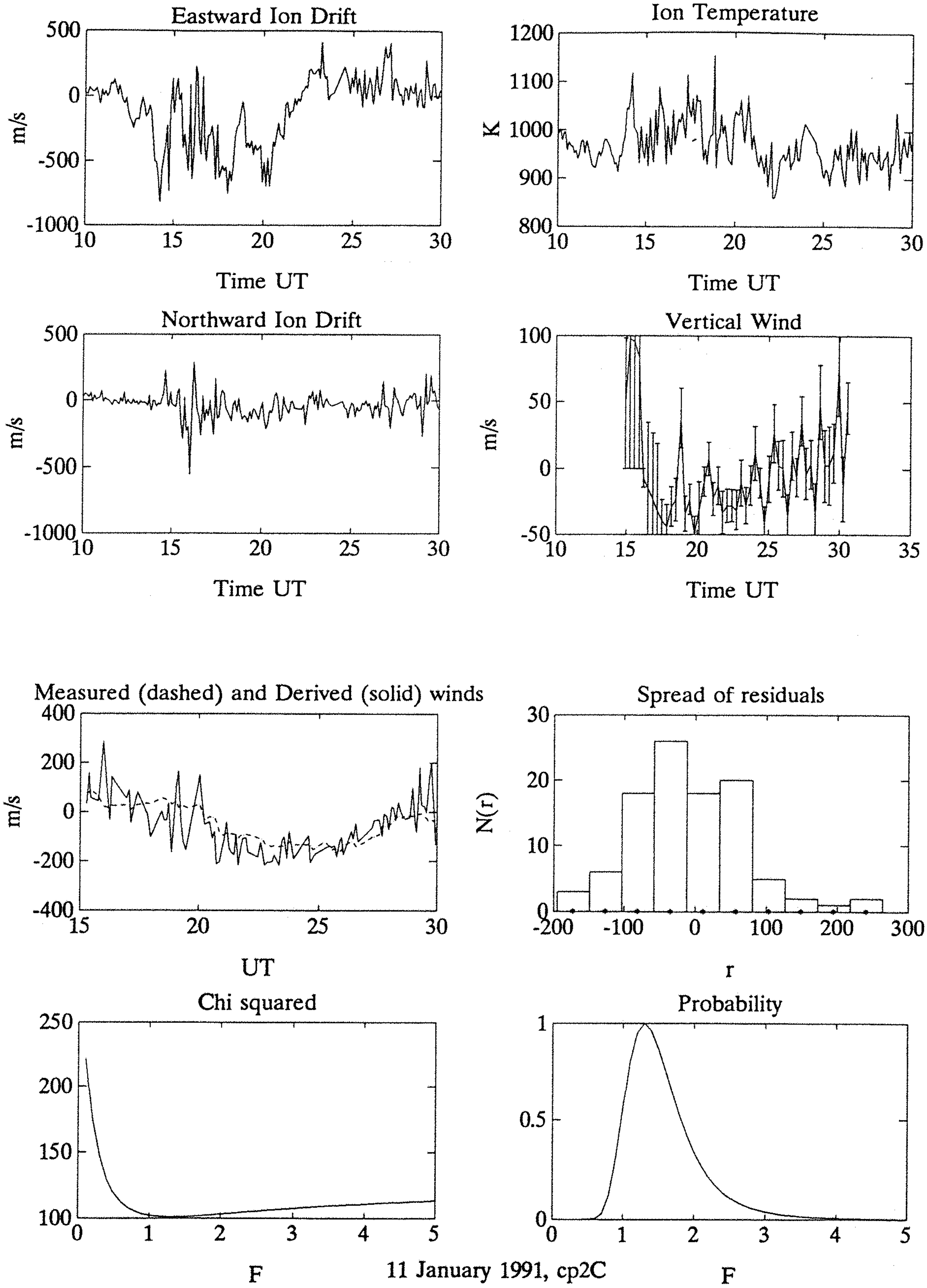

11 January 1991, cp2C

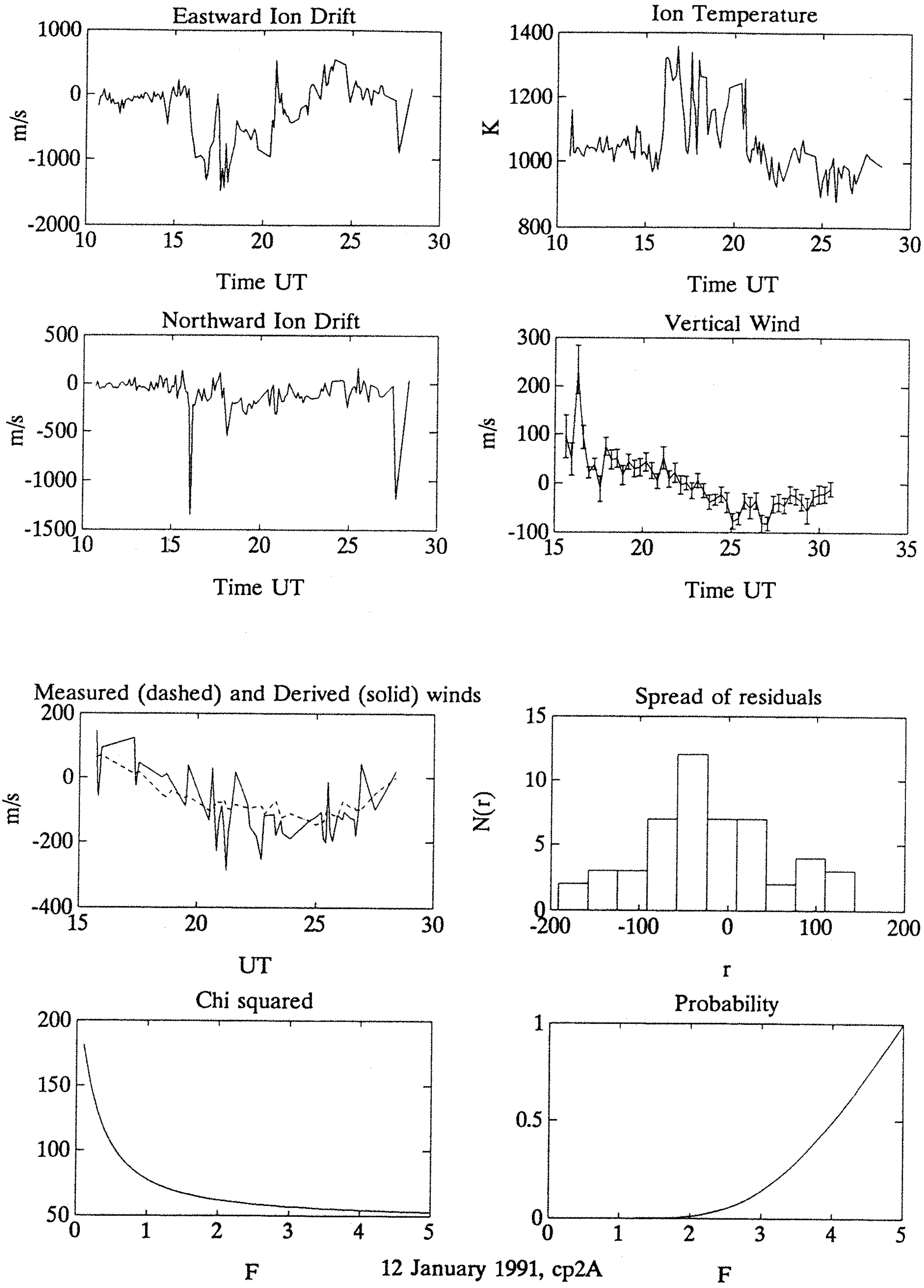

12 January 1991, cp2A

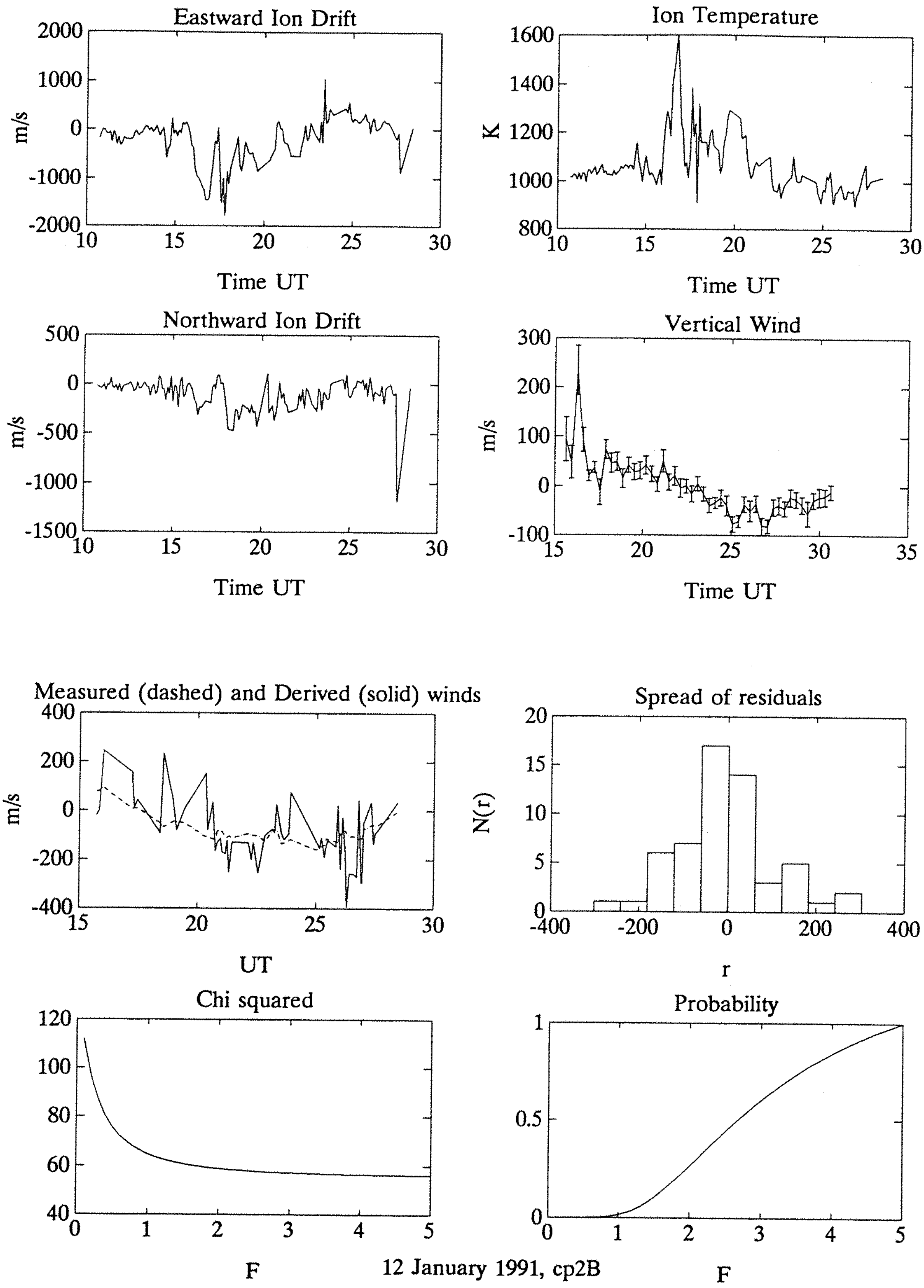

12 January 1991, cp2B

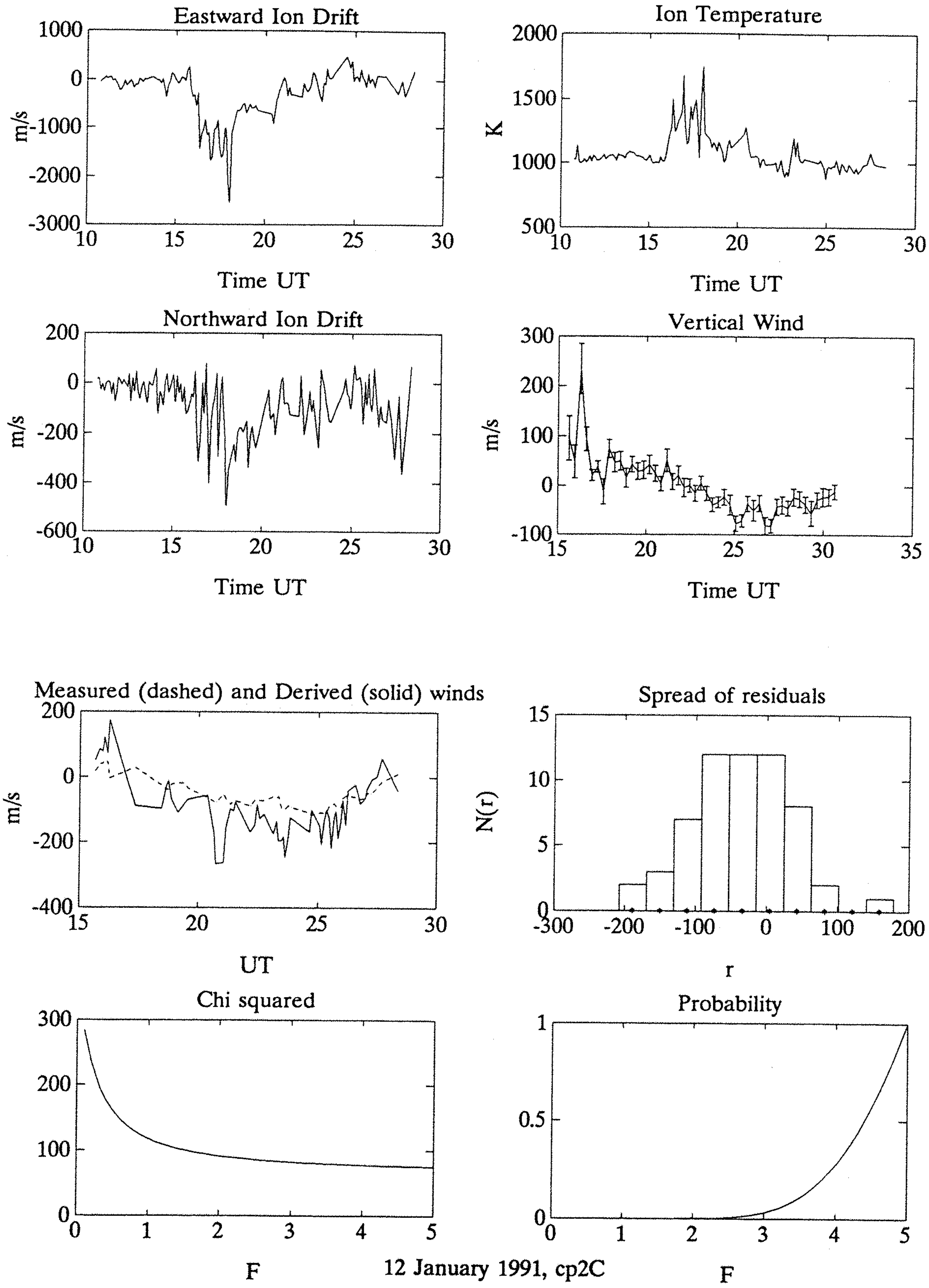

12 January 1991, cp2C

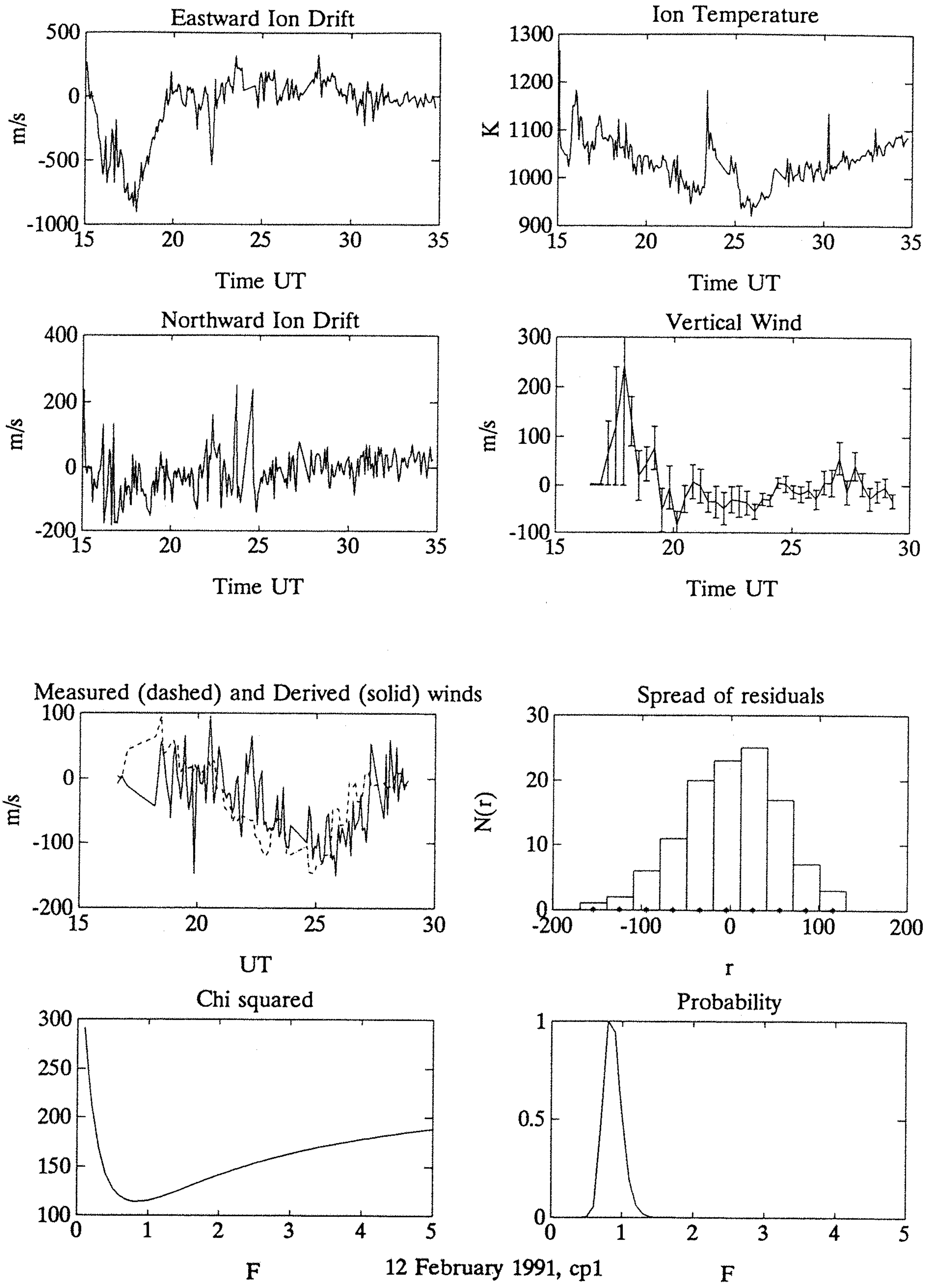

12 February 1991, cp1

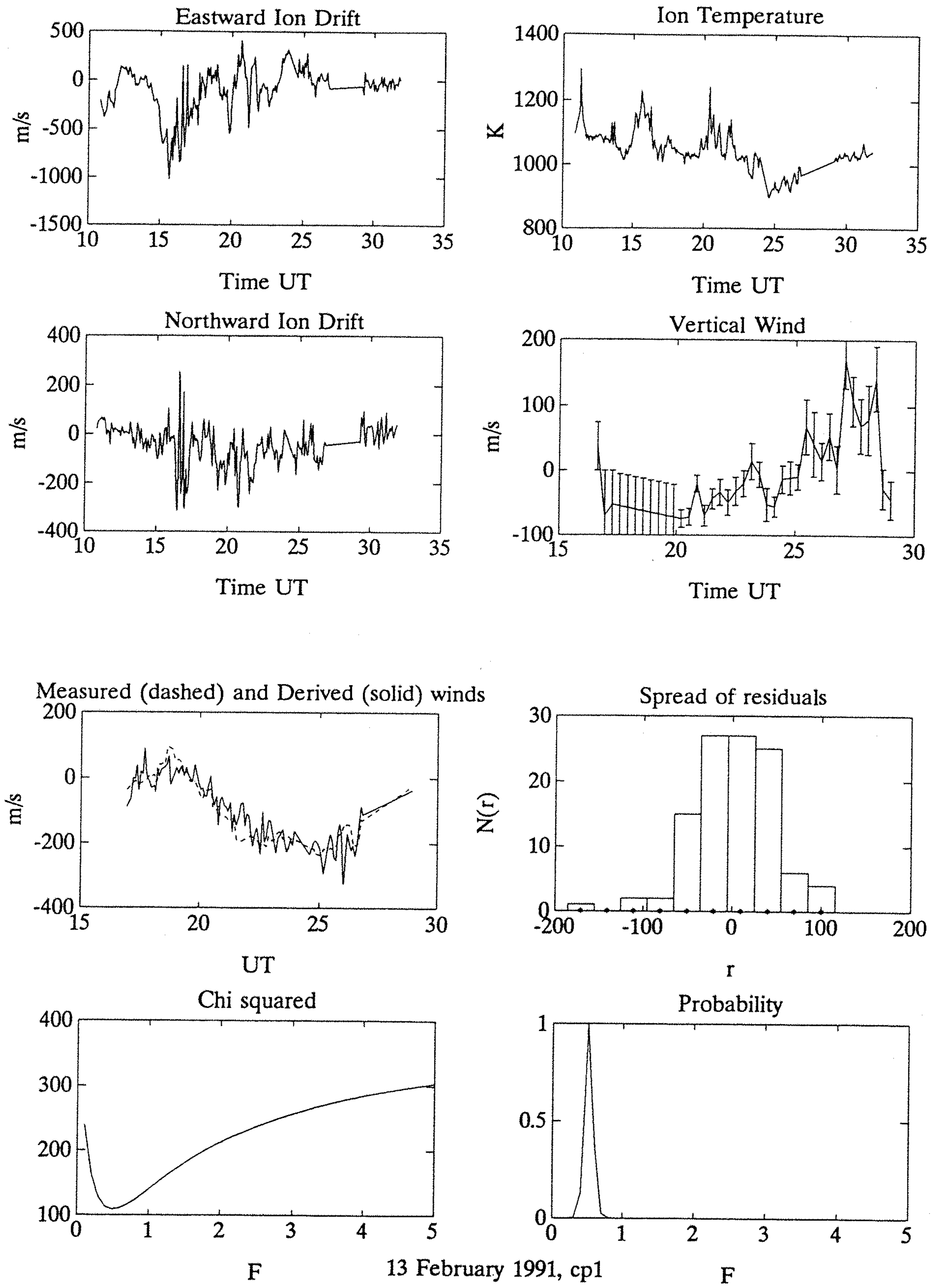

13 February 1991, cp1

Appendix E

Plots from analysis with vertical wind data

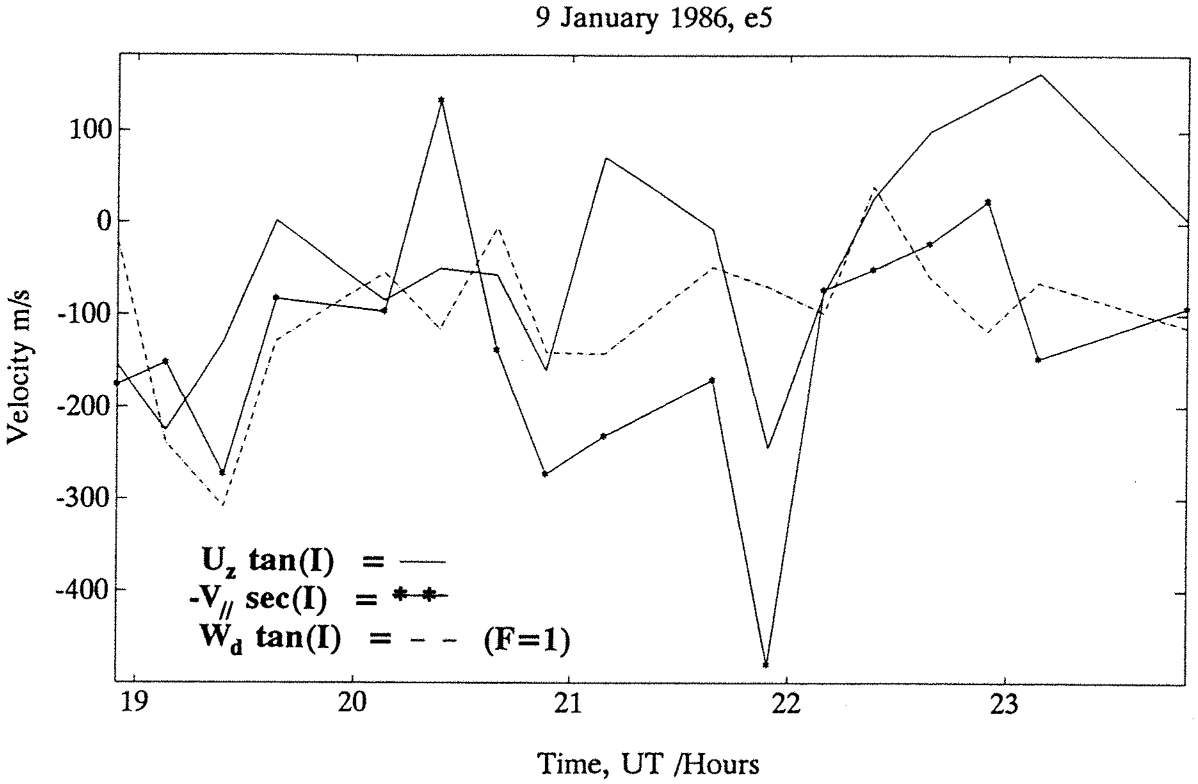
9 January 1986, e5
Velocity m/s
100
0
-100
-200
-300
-400
U_z tan(I) = —
$-V_{//}$ sec(I) = *-*
W_d tan(I) = - - - (F=1)
19
20
21
22
23
Time, UT /Hours

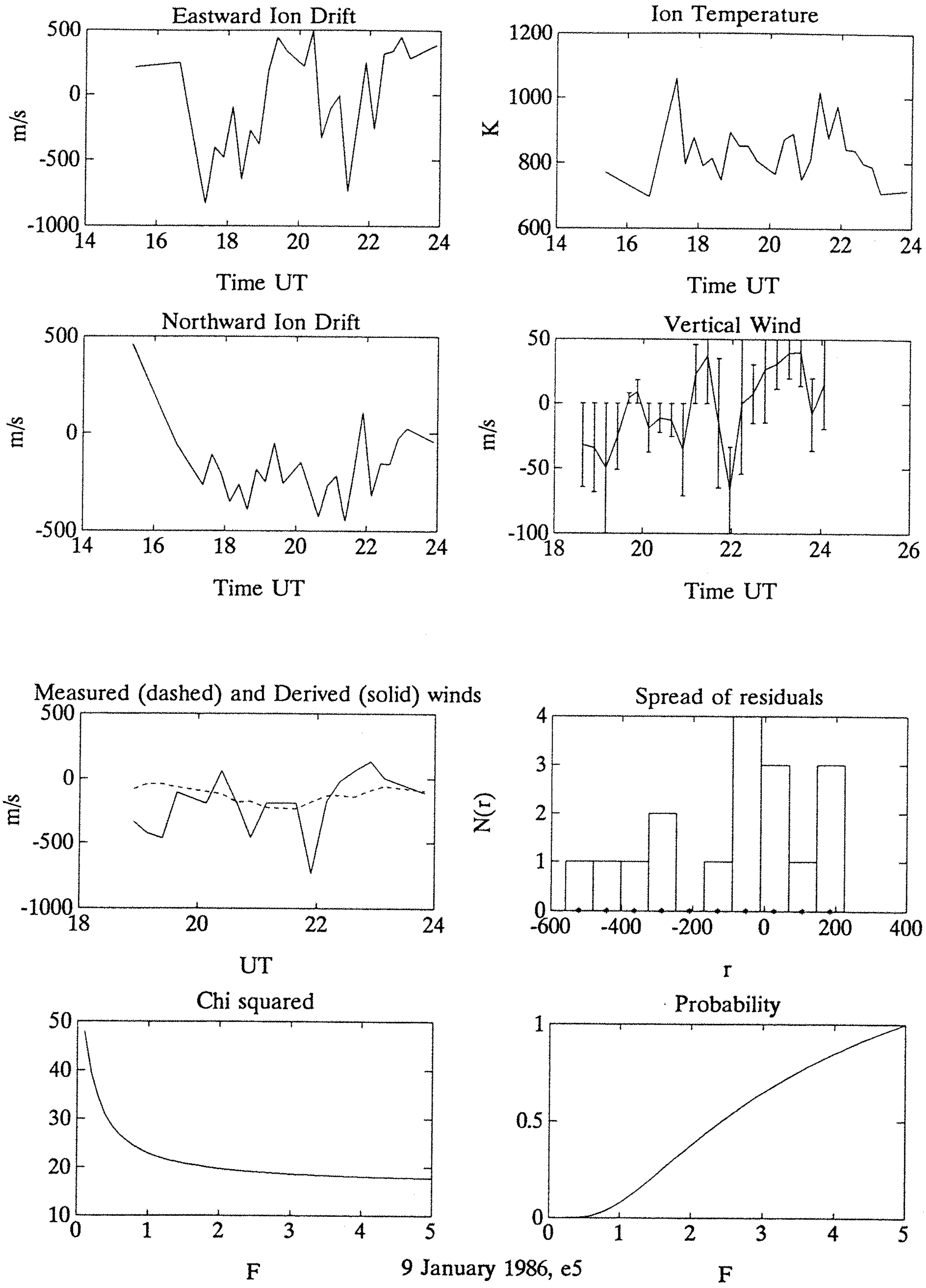

9 January 1986, e5

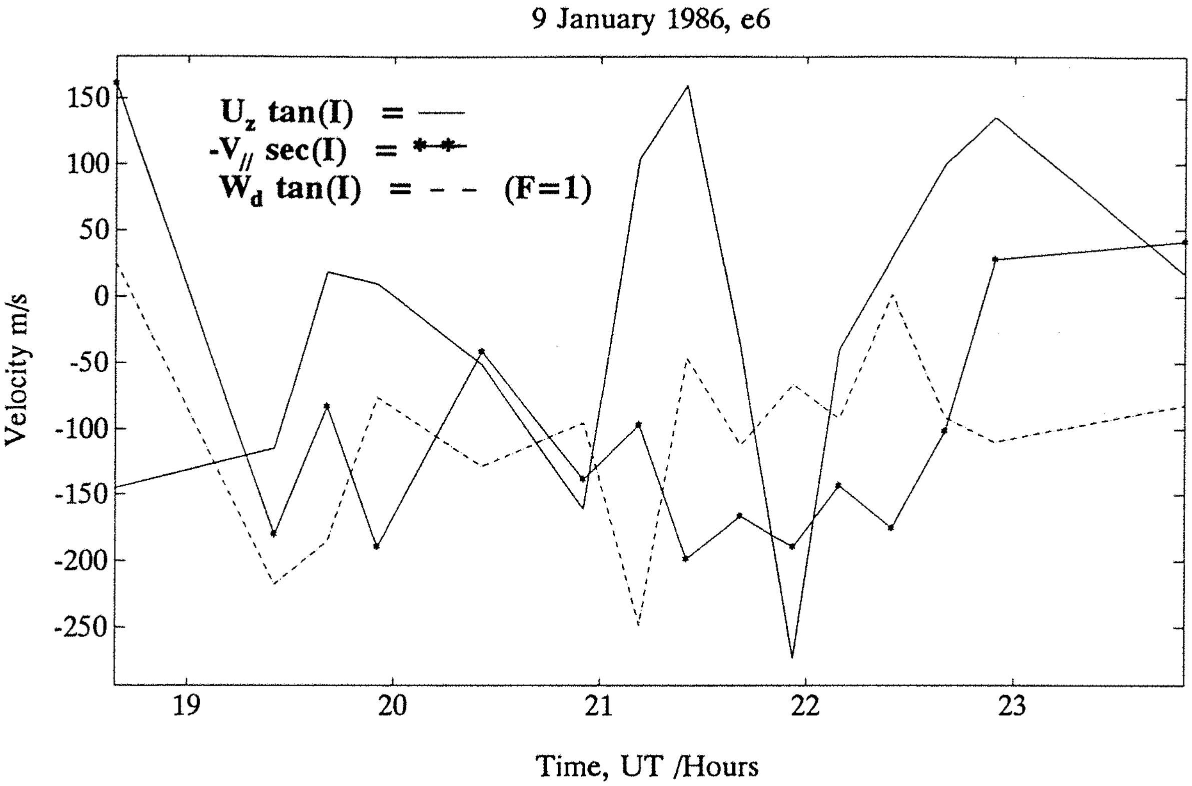
9 January 1986, e6
$U_z \tan(I)$ = ——
$-V_{//} \sec(I)$ = *-*-
$W_d \tan(I)$ = - - - (F=1)
Velocity m/s
150
100
50
0
-50
-100
-150
-200
-250
19
20
21
22
23
Time, UT /Hours

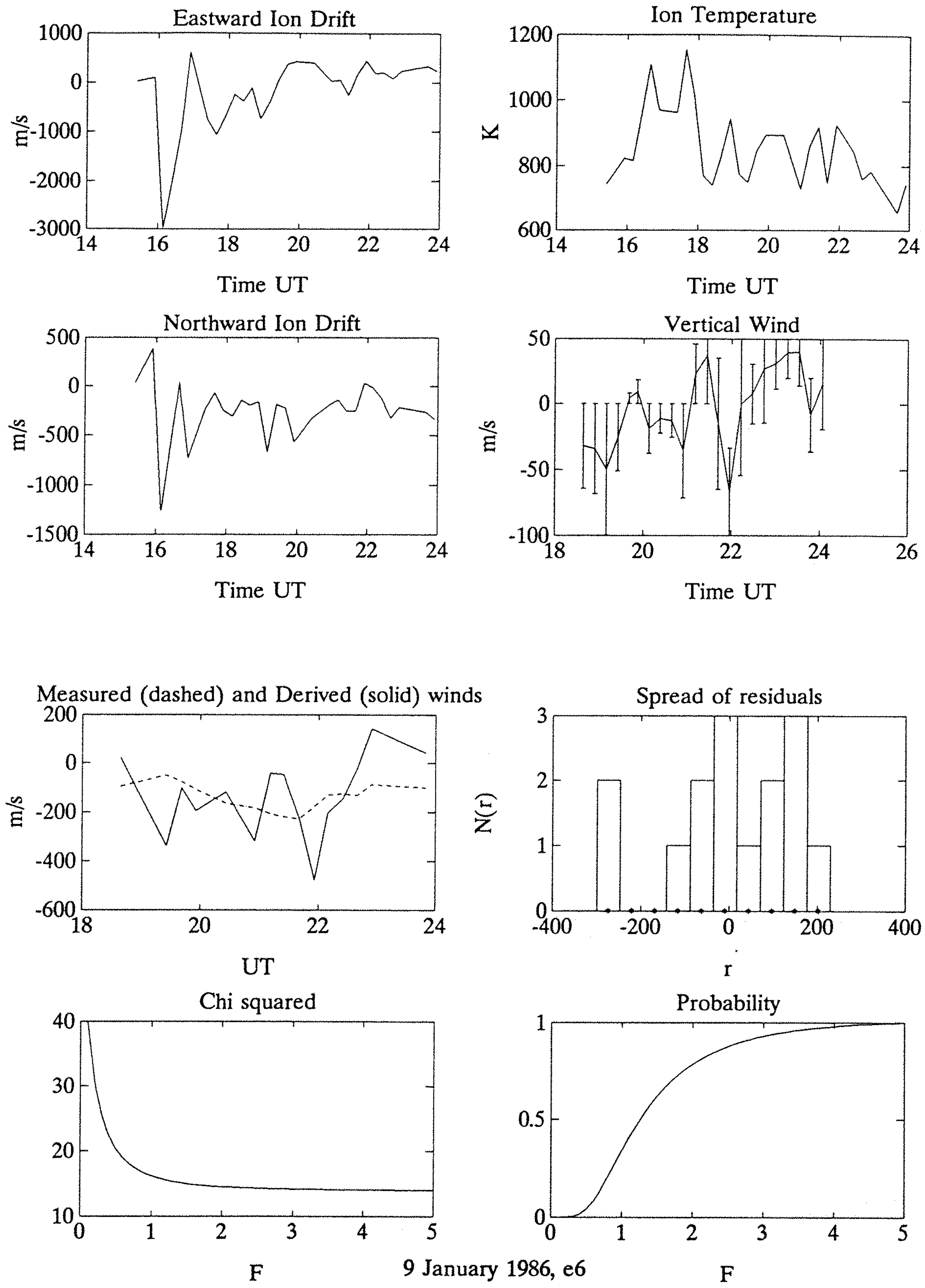

9 January 1986, e6

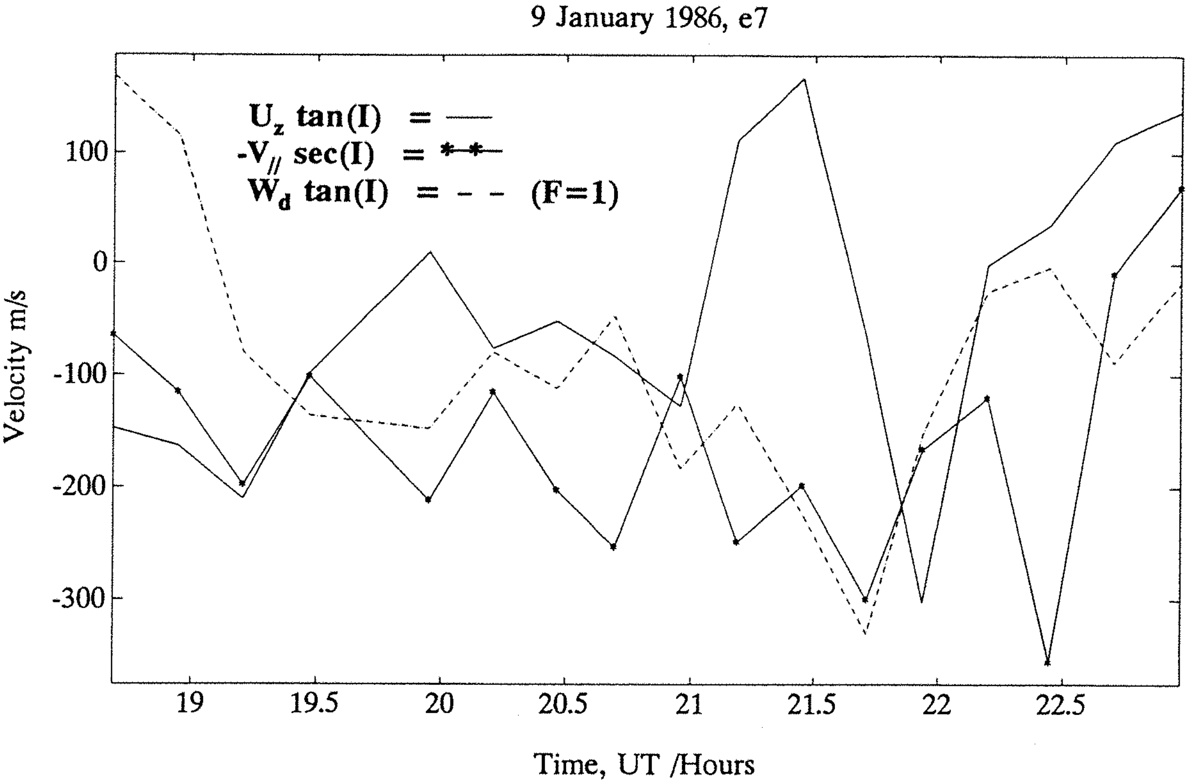
9 January 1986, e7
U_z tan(I) = —
$-V_{//}$ sec(I) = *-*-
W_d tan(I) = - - - (F=1)
Velocity m/s
100
0
-100
-200
-300
19
19.5
20
20.5
21
21.5
22
22.5
Time, UT /Hours

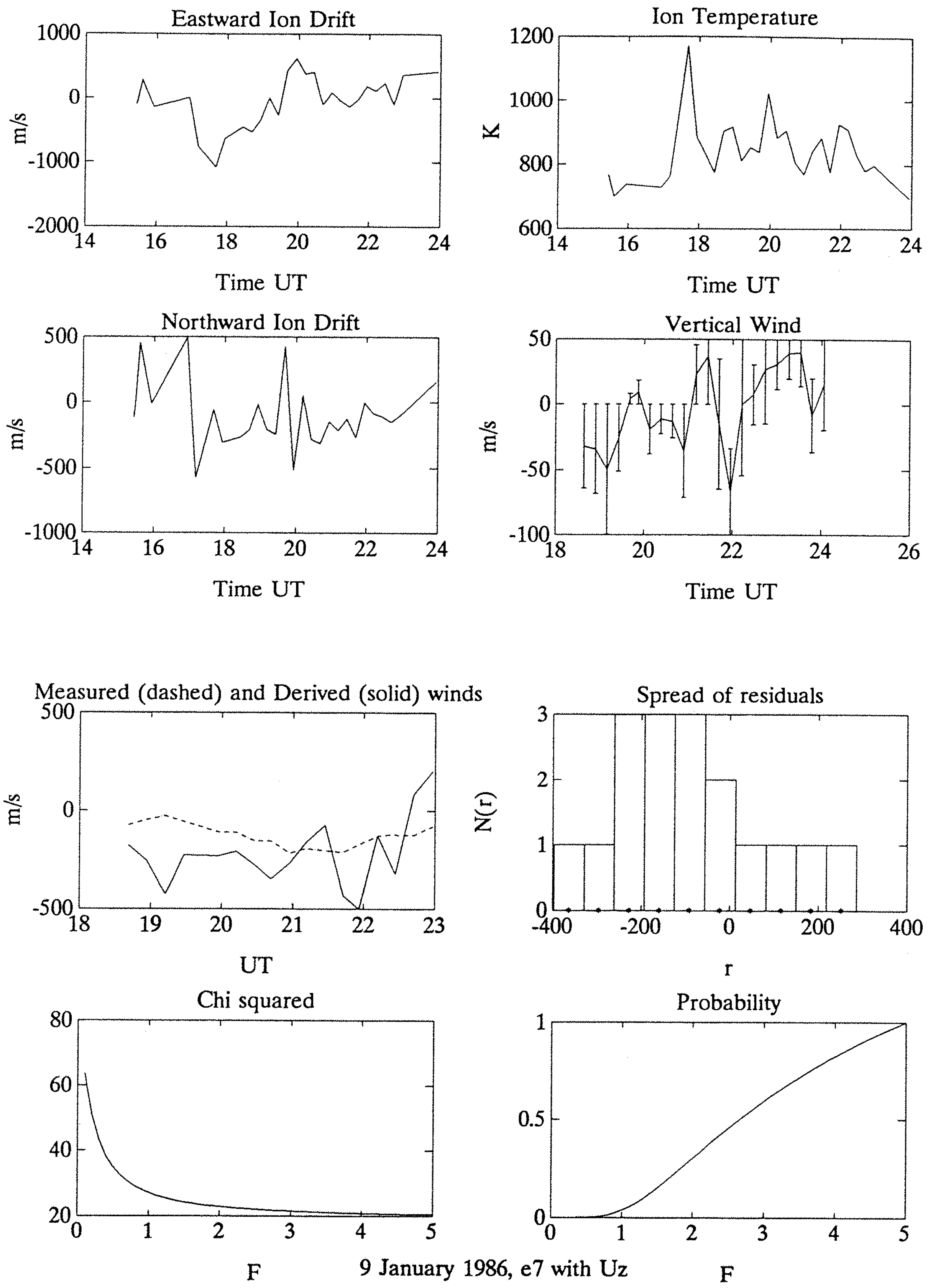

9 January 1986, e7 with Uz

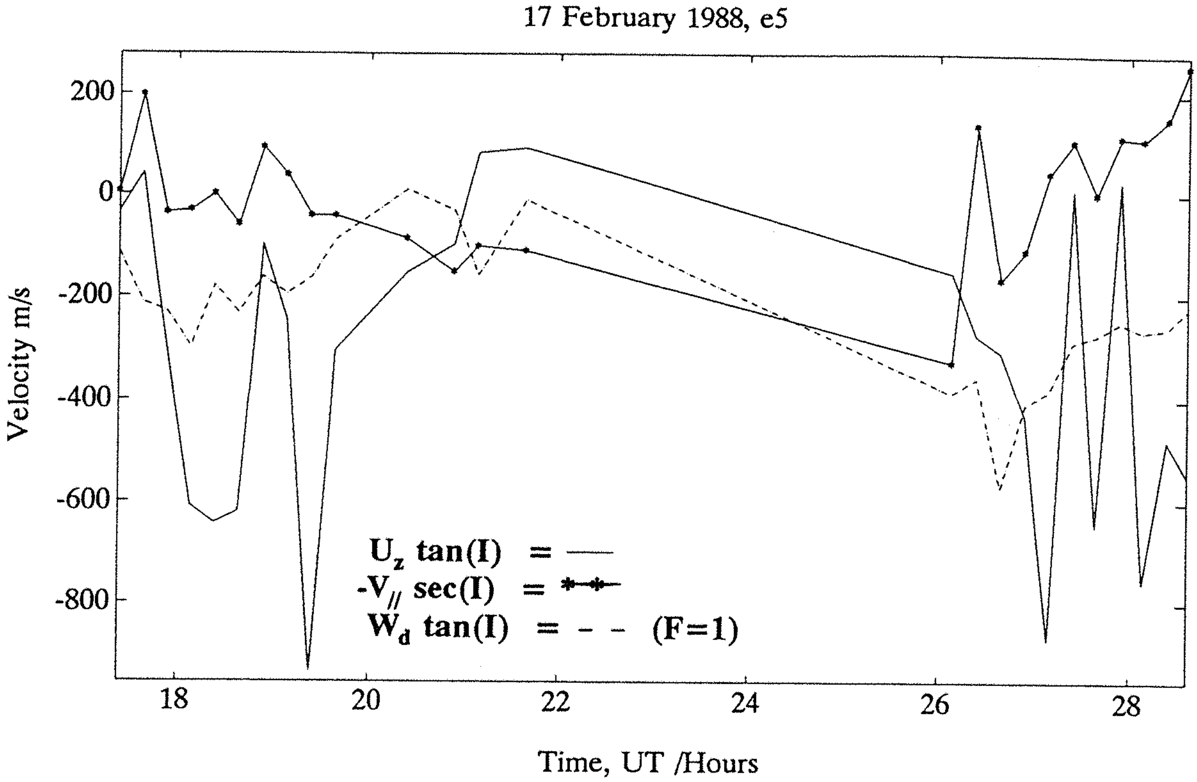
17 February 1988, e5
Velocity m/s
200
0
-200
-400
-600
-800
18
20
22
24
26
28
Time, UT /Hours
U_z tan(I) = —
$-V_{//}$ sec(I) = *—*
W_d tan(I) = - - - (F=1)

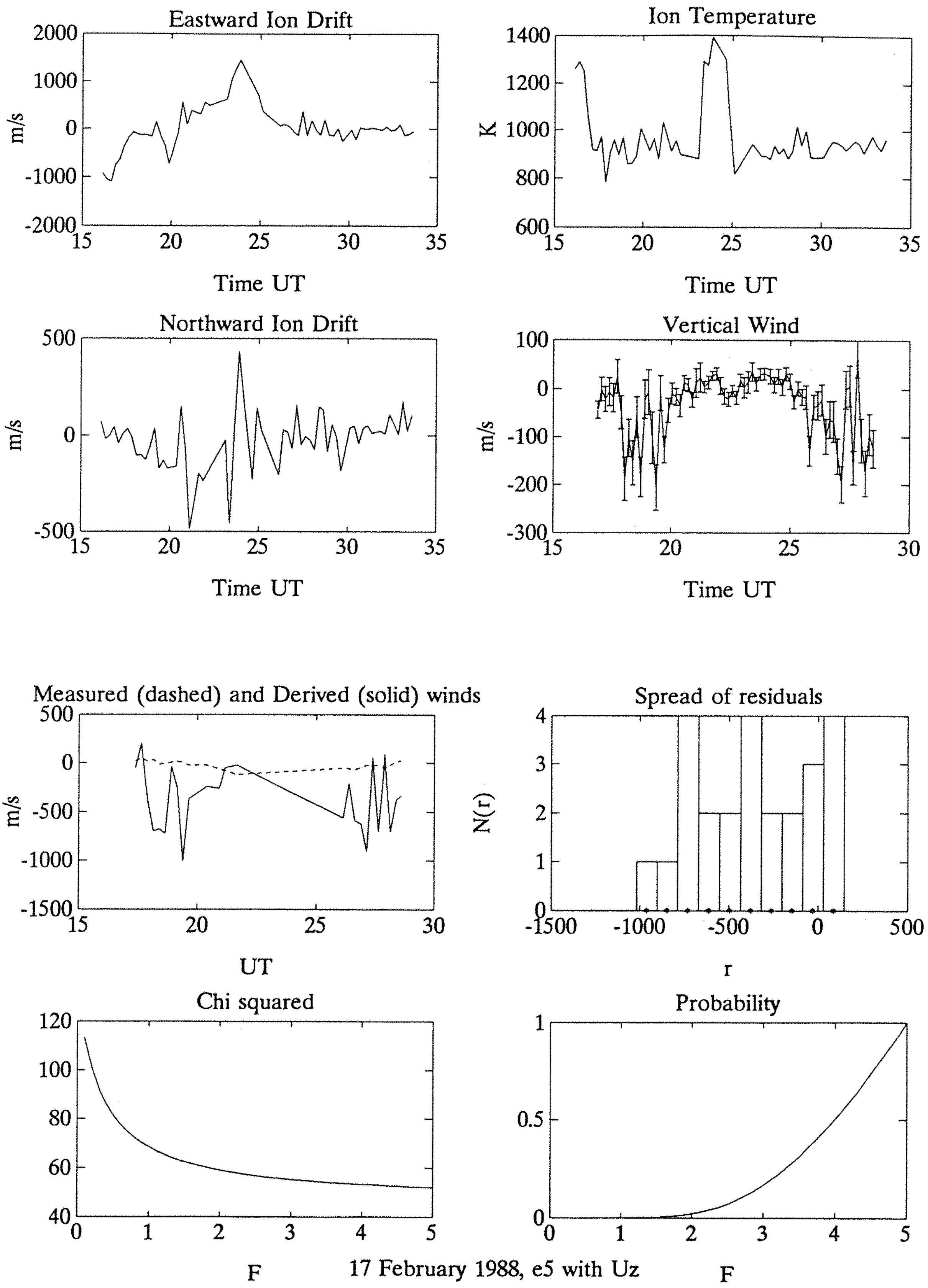

17 February 1988, e5 with Uz

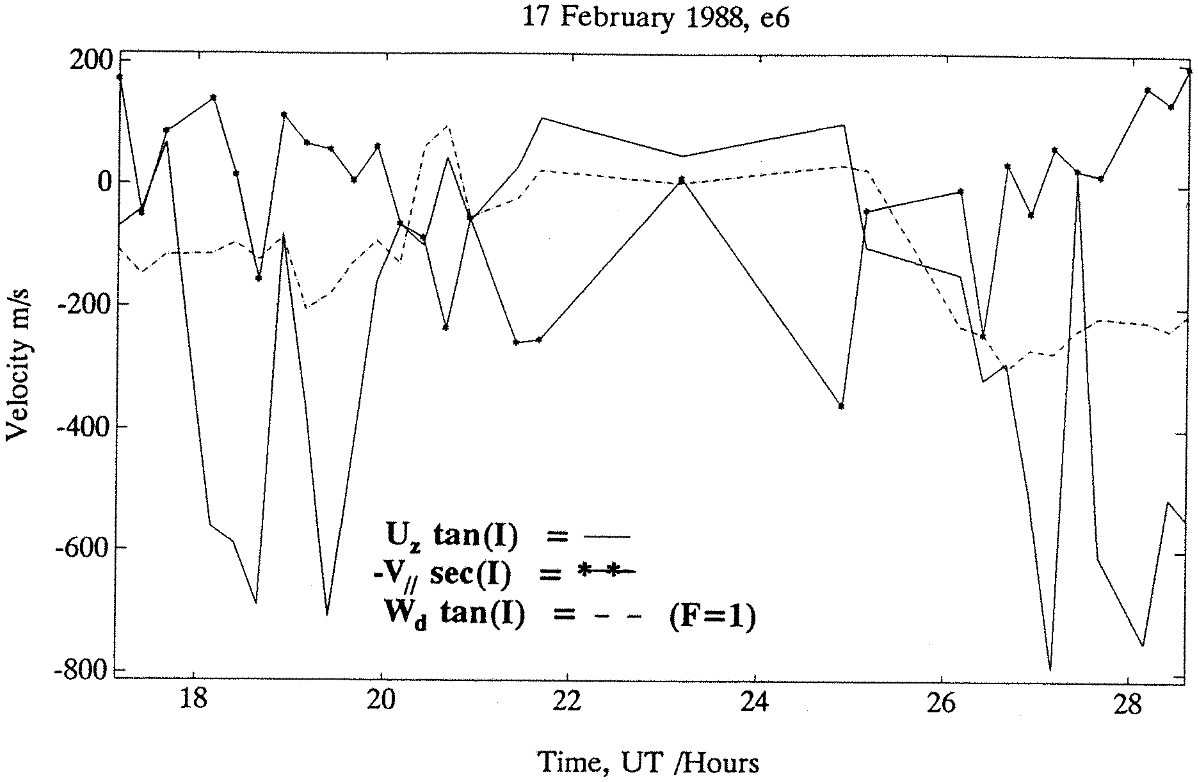
17 February 1988, e6
Velocity m/s
200
0
-200
-400
-600
-800
18
20
22
24
26
28
Time, UT /Hours
U_z tan(I) = —
$-V_{//}$ sec(I) = *-*-
W_d tan(I) = - - (F=1)

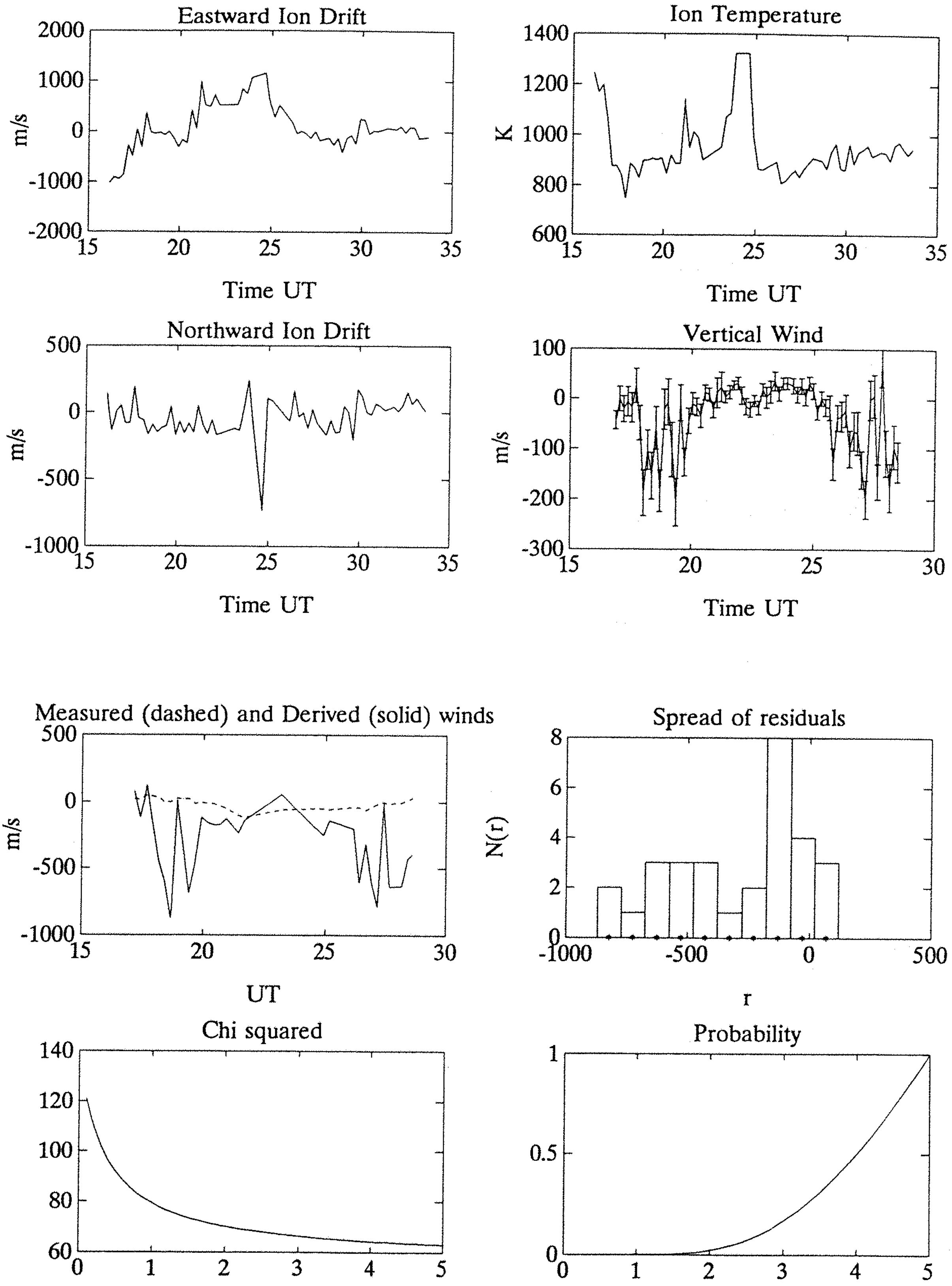

17 February 1988, e6 with Uz

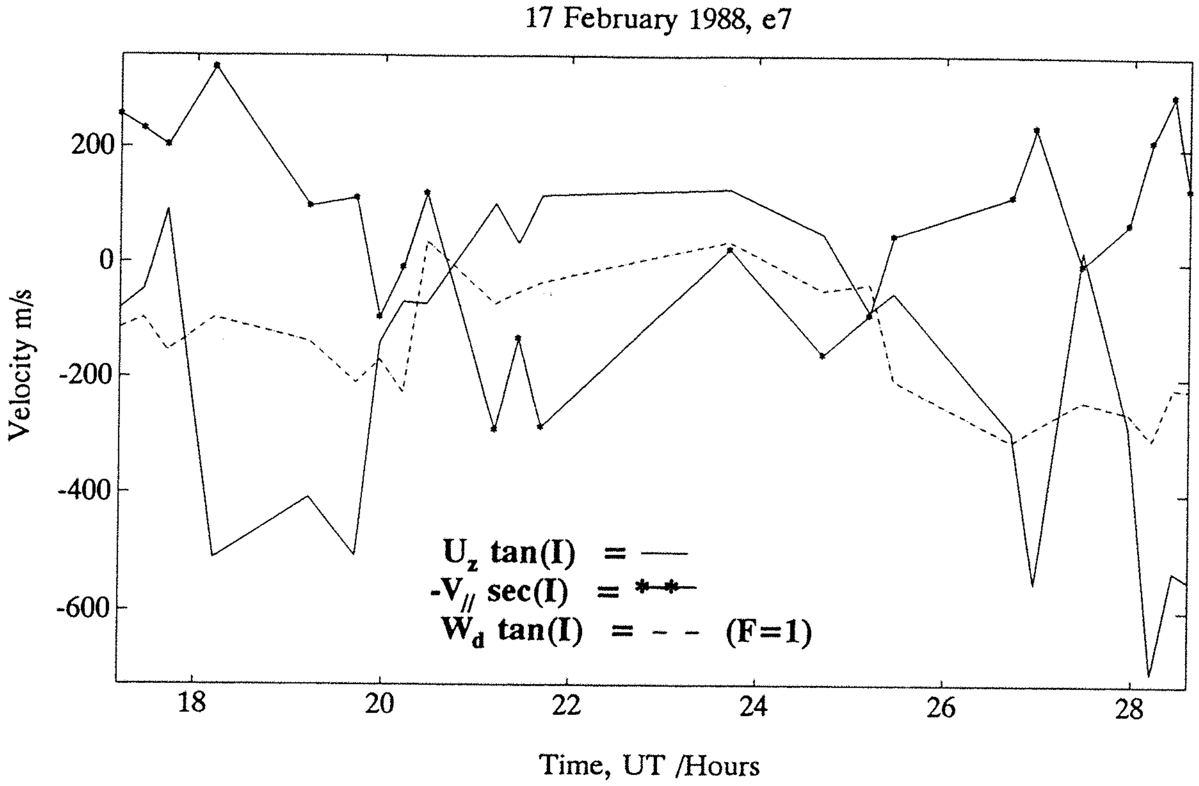

17 February 1988, e7

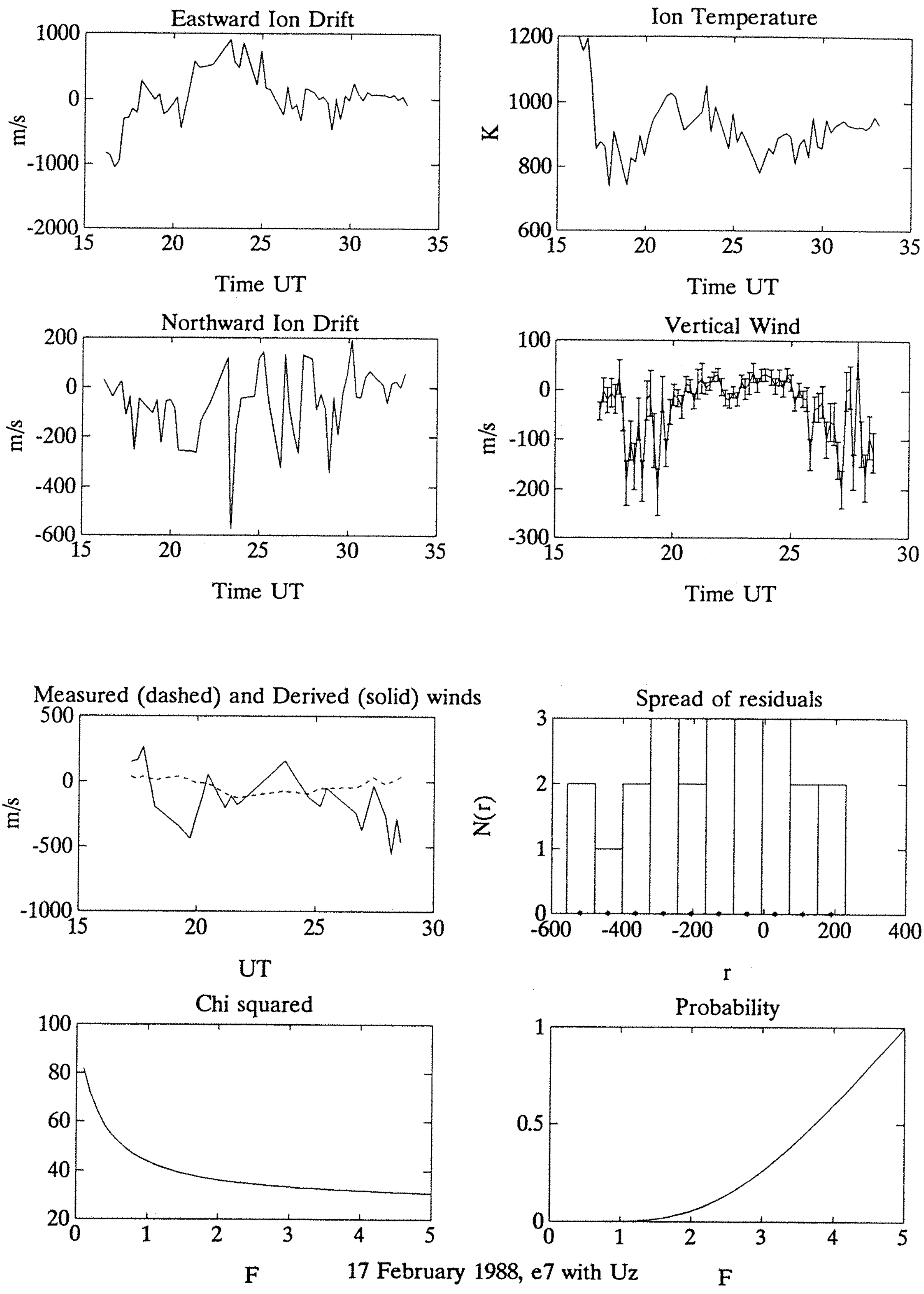

17 February 1988, e7 with Uz

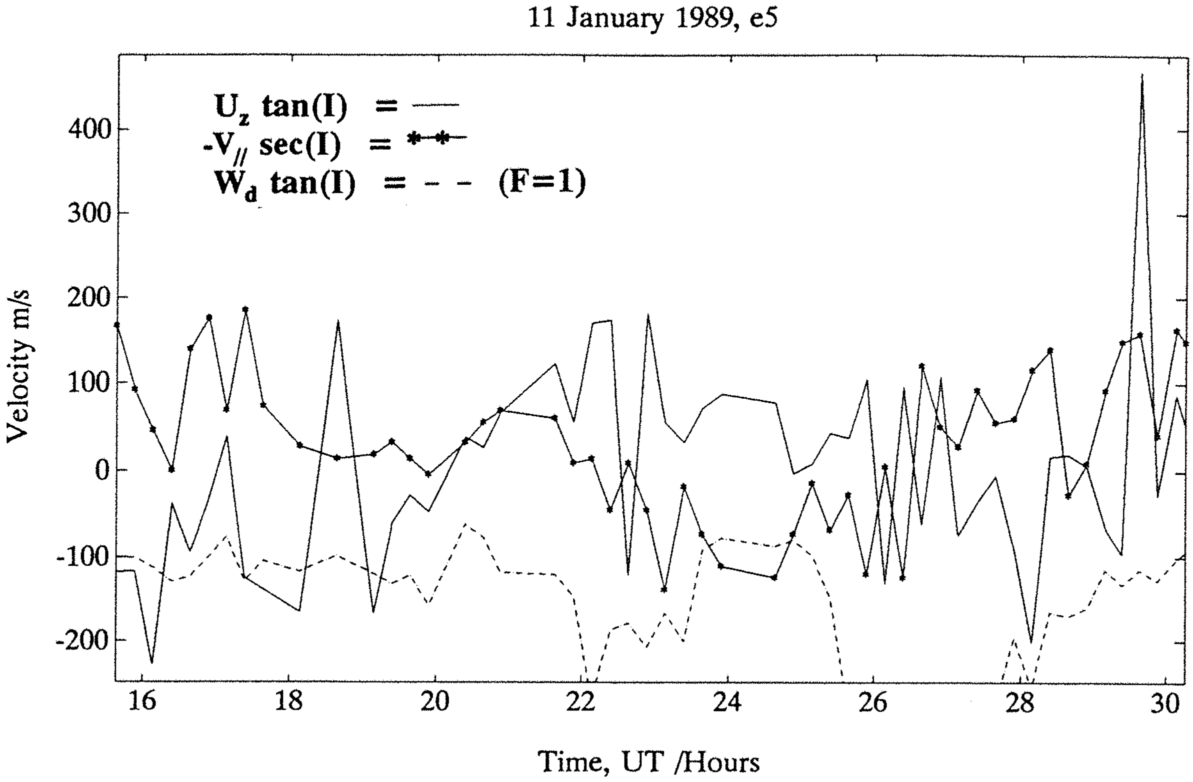
11 January 1989, e5
U_z tan(I) = ——
-$V_{//}$ sec(I) = *-*-
W_d tan(I) = - - (F=1)
Velocity m/s
400
300
200
100
0
-100
-200
16
18
20
22
24
26
28
30
Time, UT /Hours

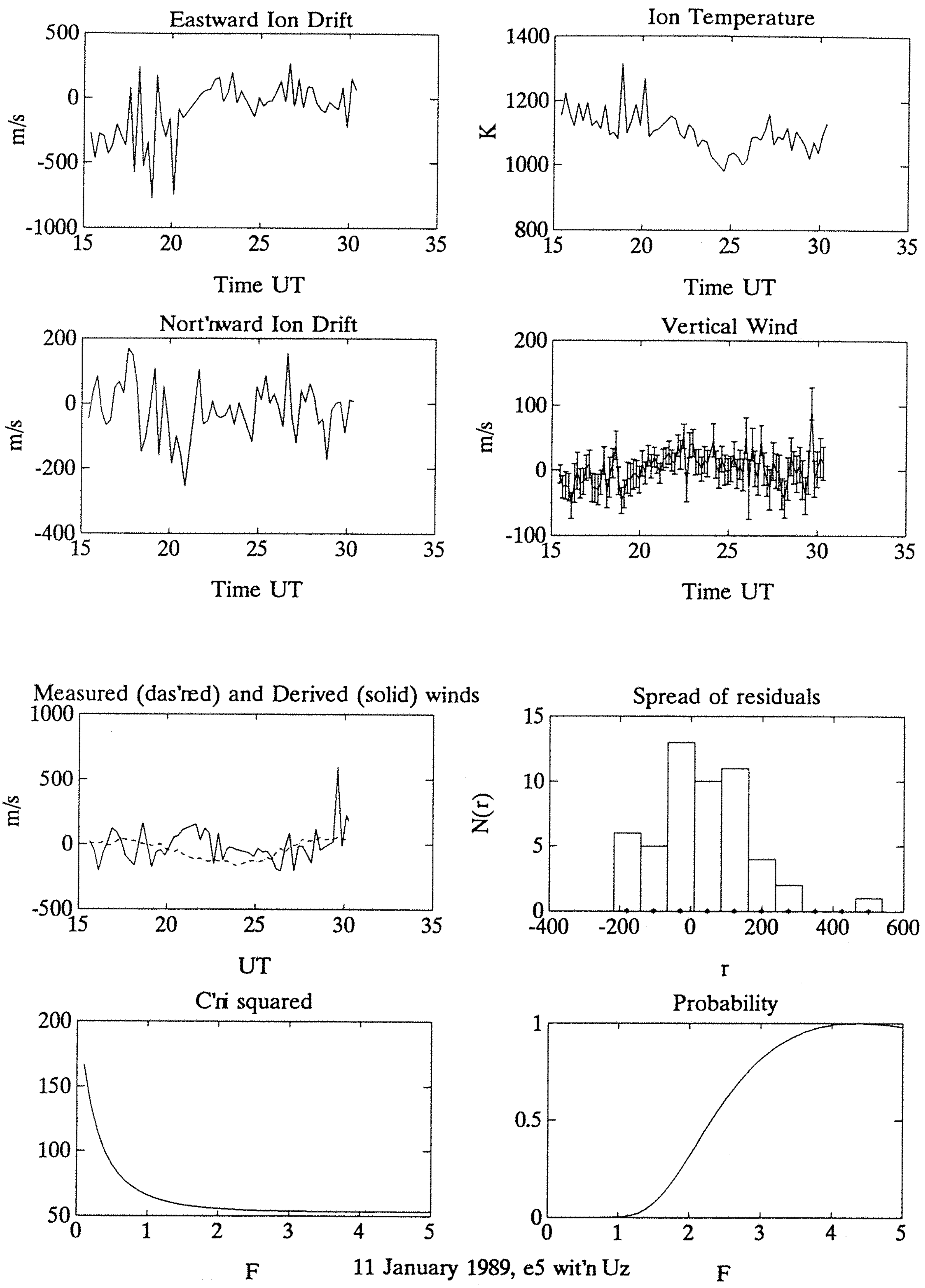

11 January 1989, e5 with Uz

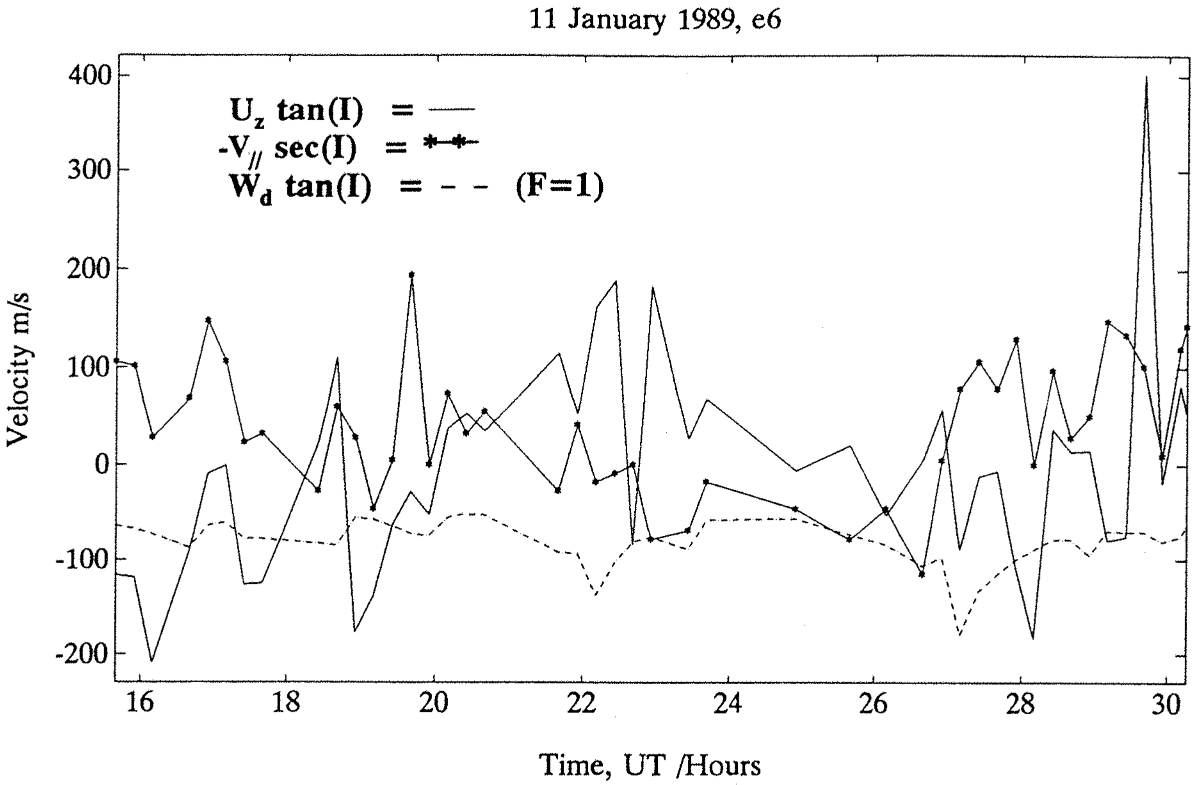
11 January 1989, e6
U_z tan(I) = —
$-V_{//}$ sec(I) = *–*–
W_d tan(I) = - - - (F=1)
Velocity m/s
400
300
200
100
0
-100
-200
16
18
20
22
24
26
28
30
Time, UT /Hours

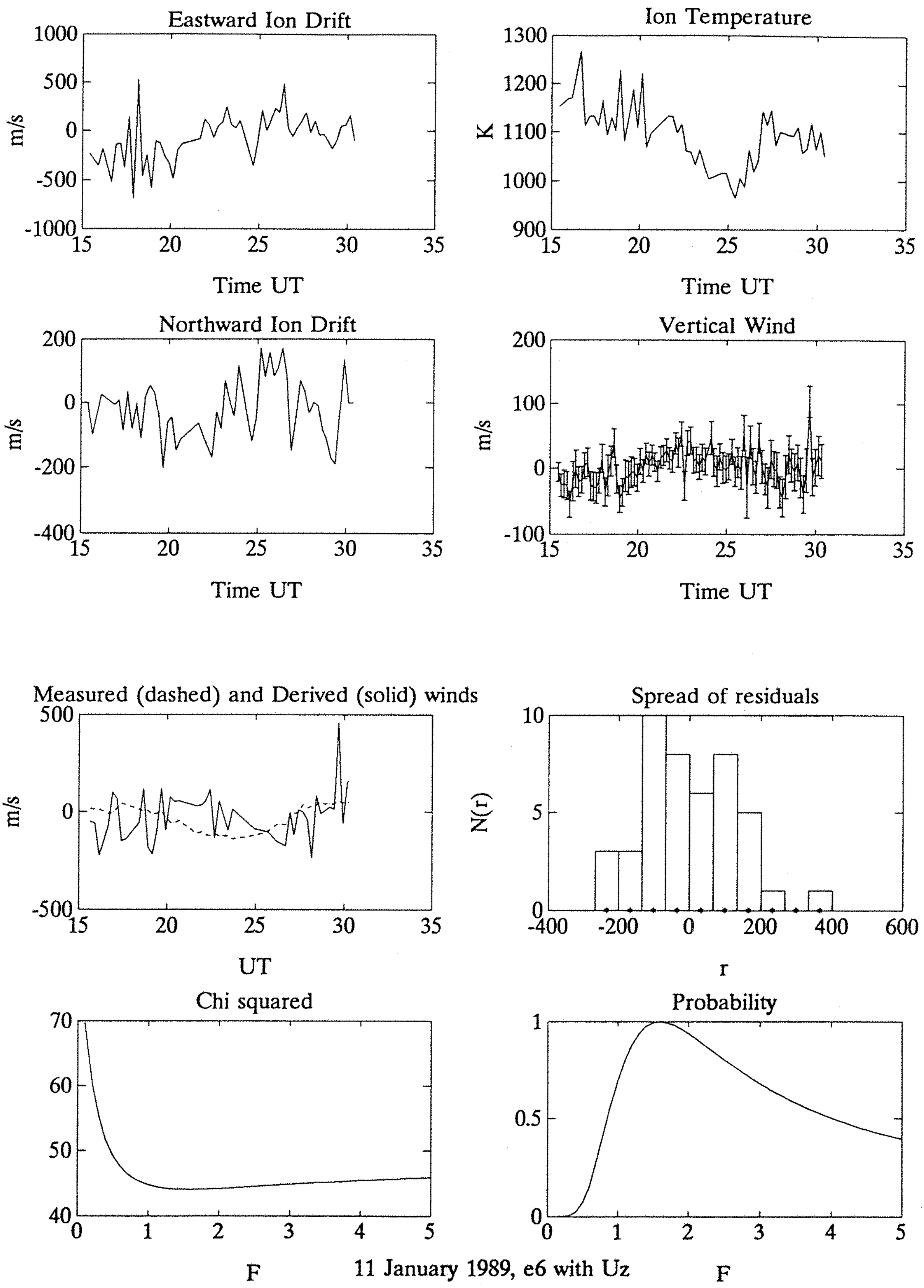

Eastward Ion Drift

Ion Temperature

Northward Ion Drift

Vertical Wind

Measured (dashed) and Derived (solid) winds

Spread of residuals

Chi squared

Probability

11 January 1989, e6 with Uz

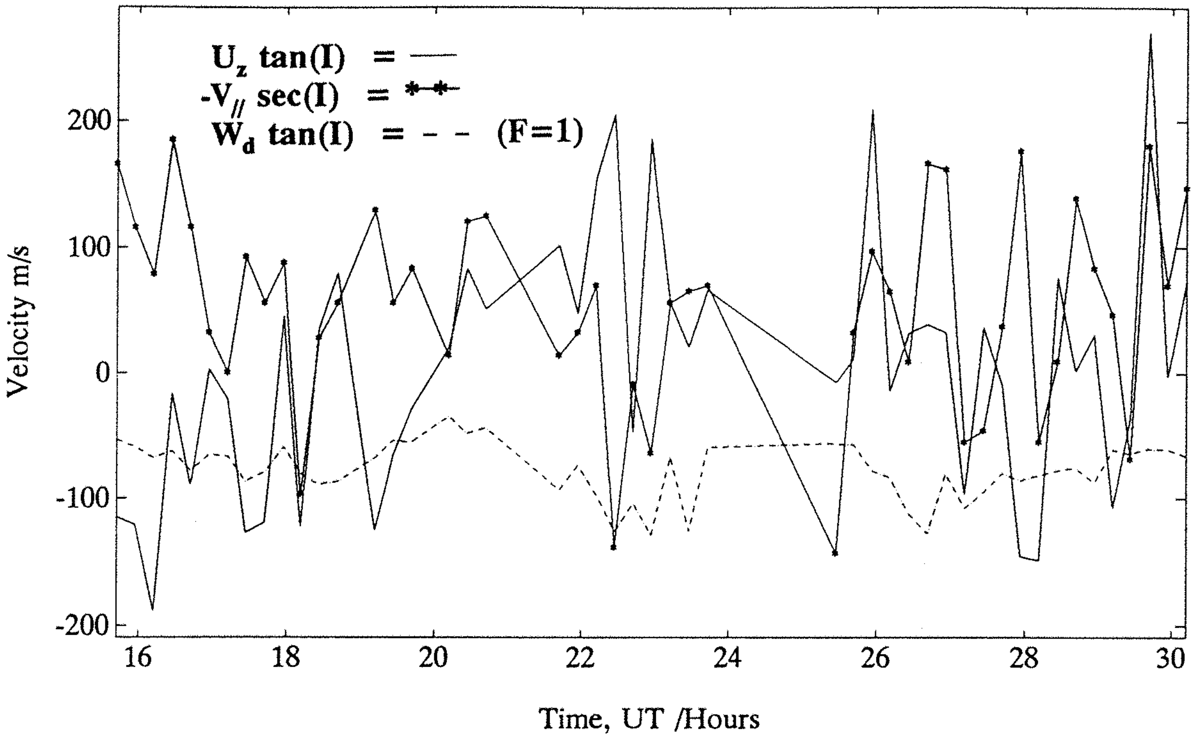

11 January 1989, e7

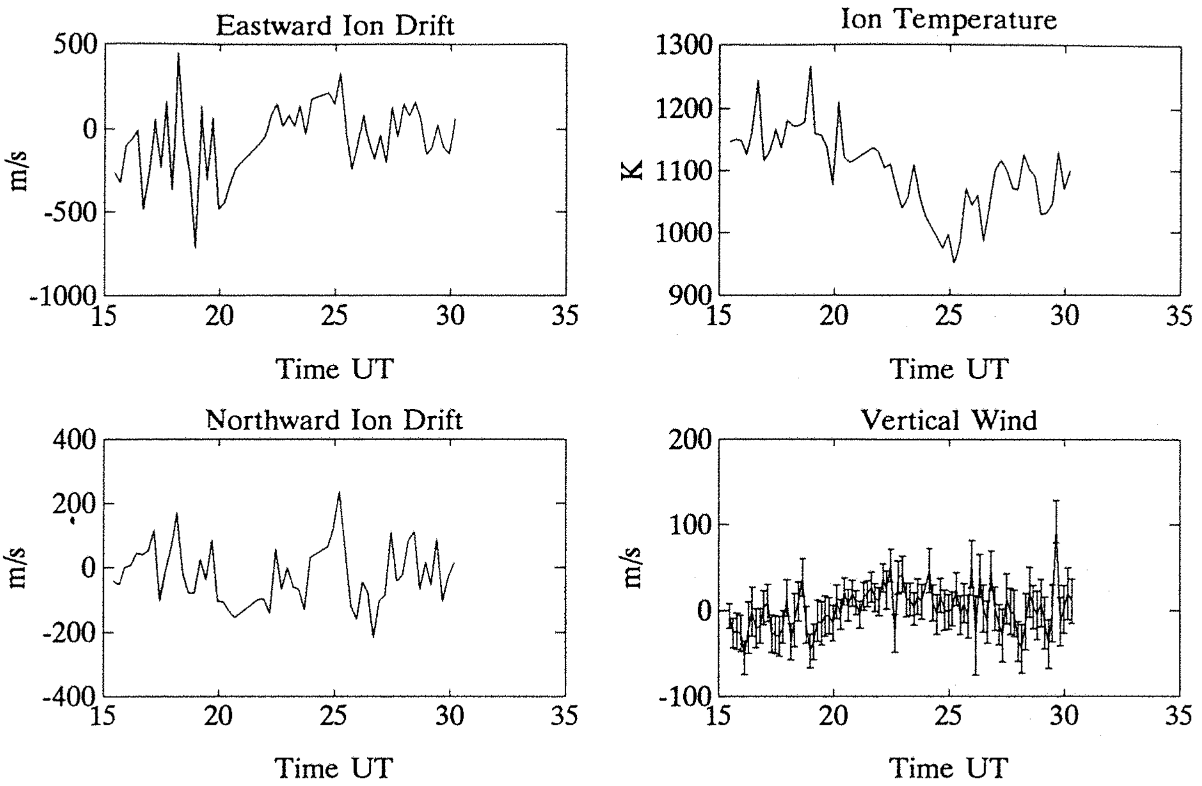

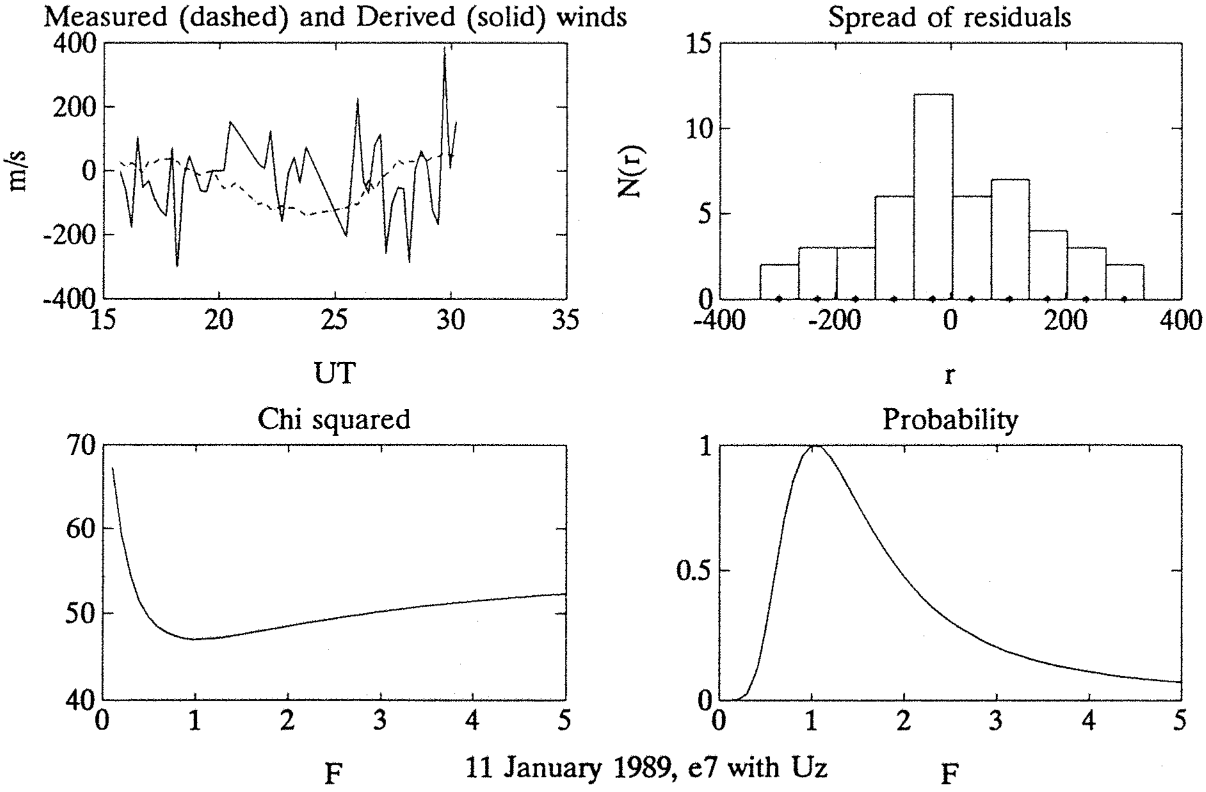

11 January 1989, e7 with Uz

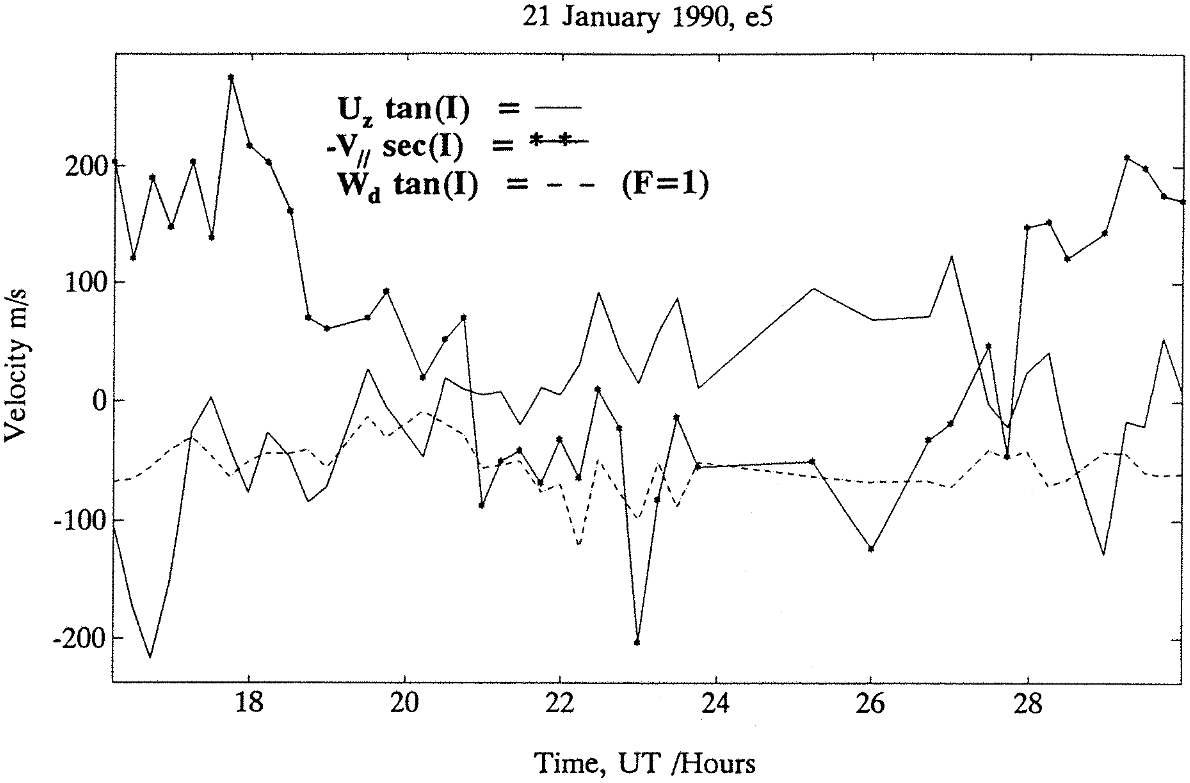
21 January 1990, e5
U_z tan(I) = ——
$-V_{//}$ sec(I) = *-*-
W_d tan(I) = - - - (F=1)
Velocity m/s
200
100
0
-100
-200
18
20
22
24
26
28
Time, UT /Hours

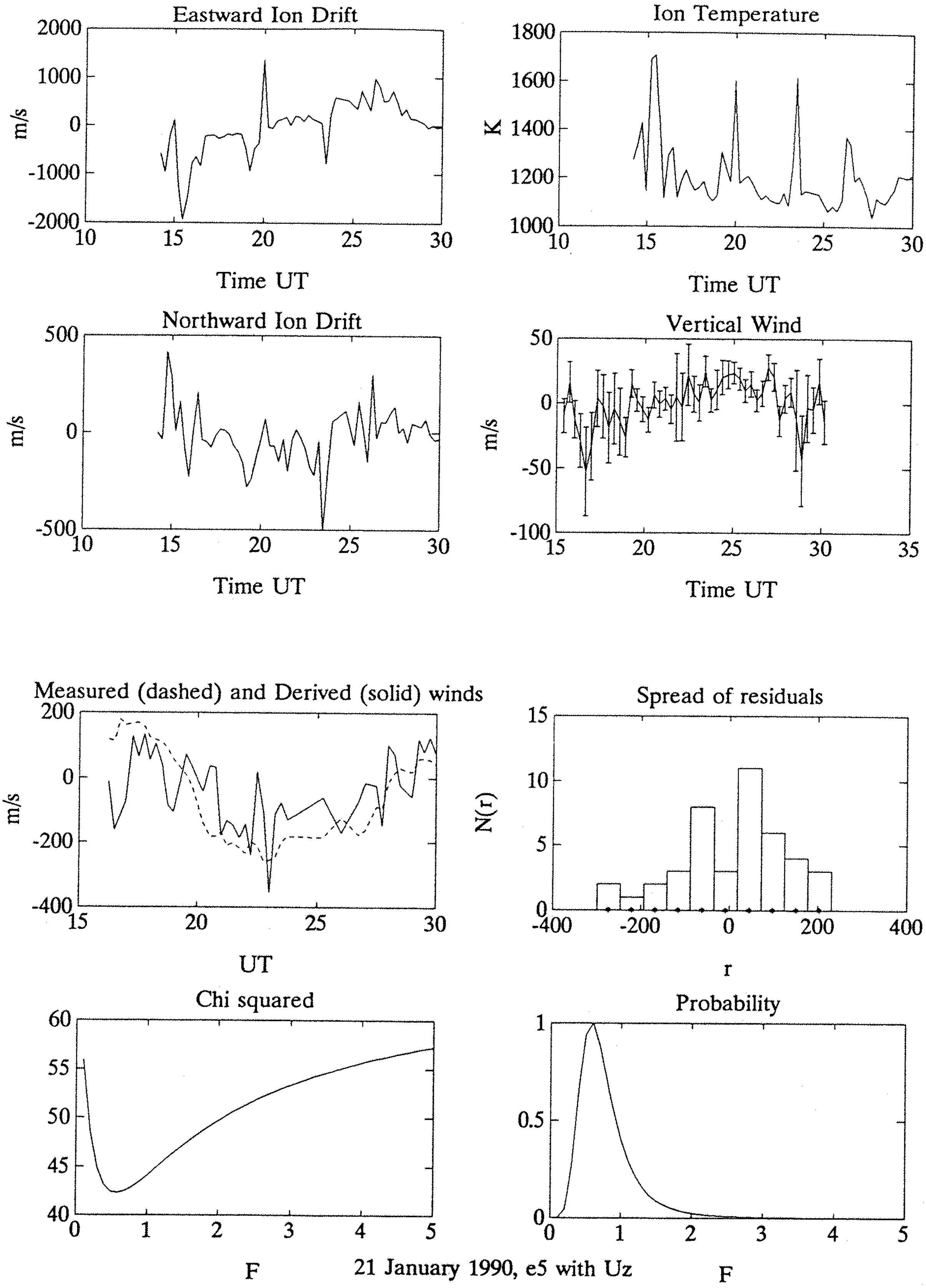

21 January 1990, e5 with Uz

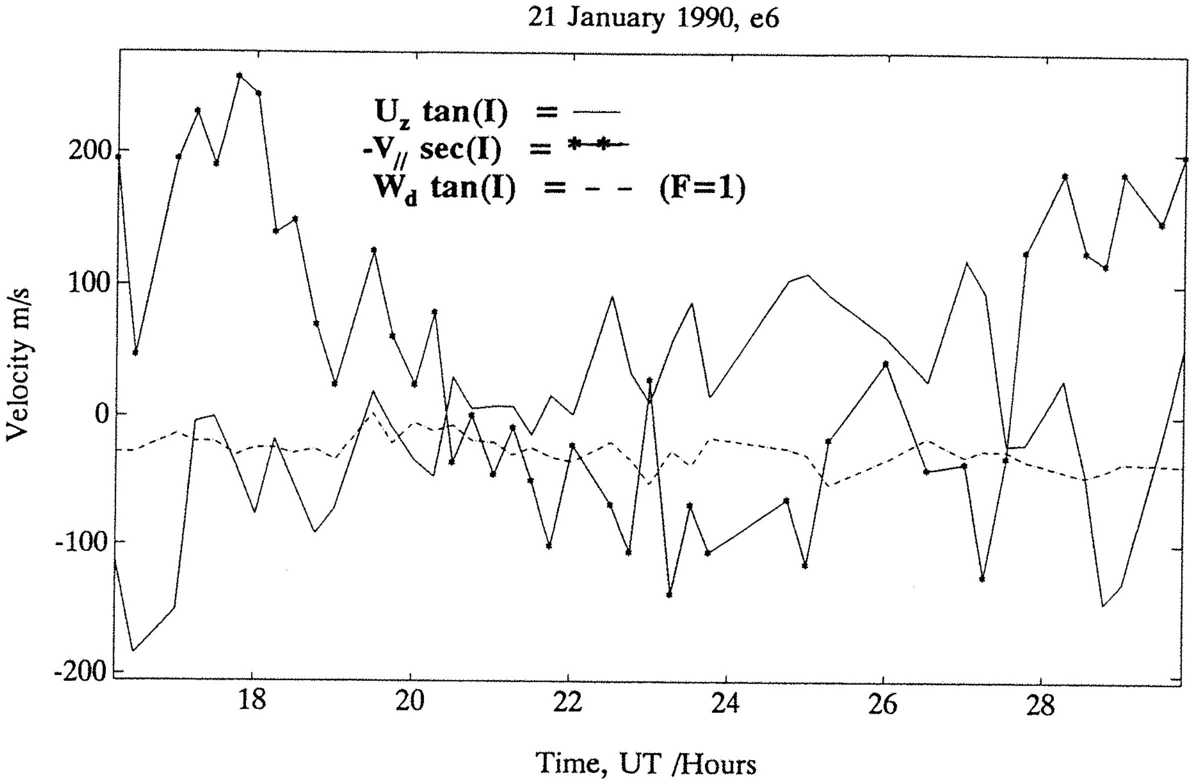
21 January 1990, e6
U_z tan(I) = —
$-V_{//}$ sec(I) = *-*-
W_d tan(I) = - - - (F=1)
Velocity m/s
200
100
0
-100
-200
18
20
22
24
26
28
Time, UT /Hours

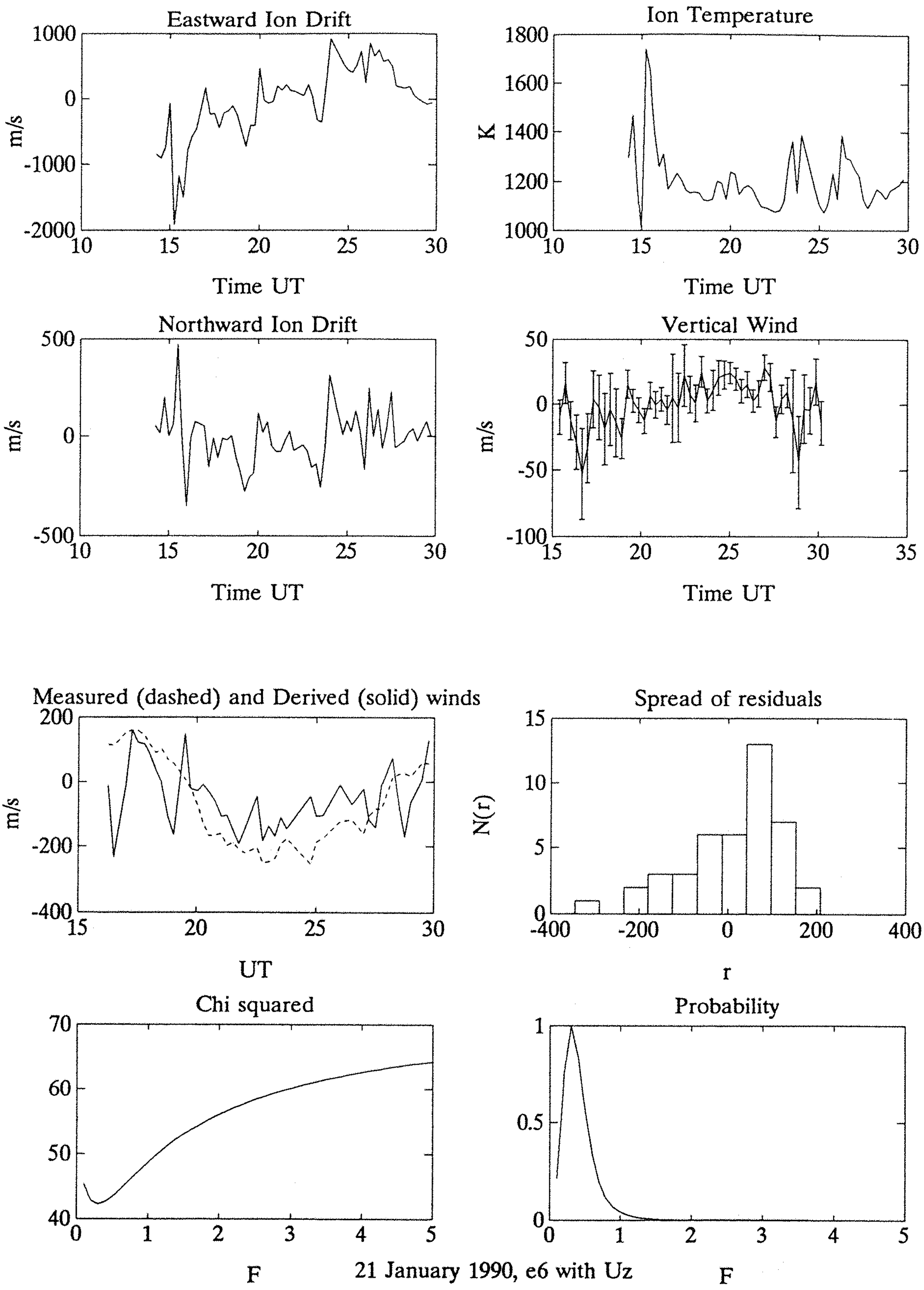

21 January 1990, e6 with Uz

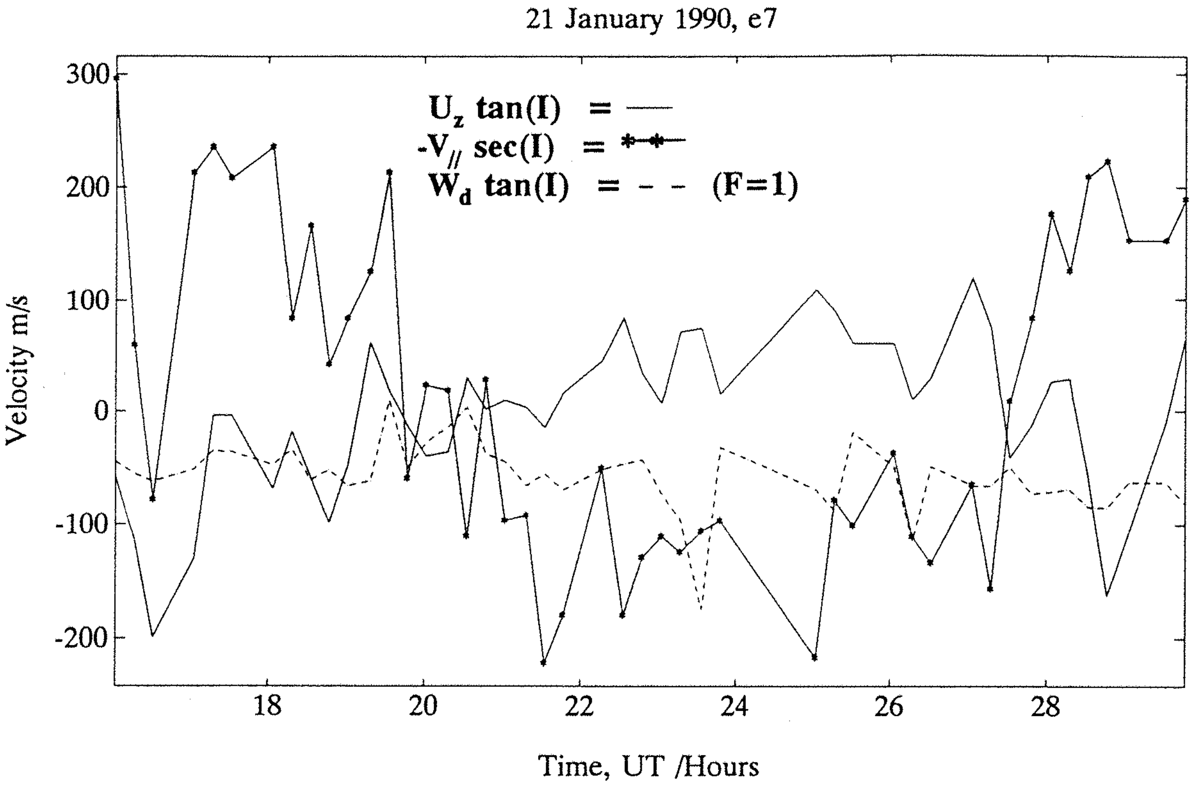
21 January 1990, e7
U_z tan(I) = —
$-V_{//}$ sec(I) = *—*
W_d tan(I) = - - - (F=1)
Velocity m/s
300
200
100
0
-100
-200
18
20
22
24
26
28
Time, UT /Hours

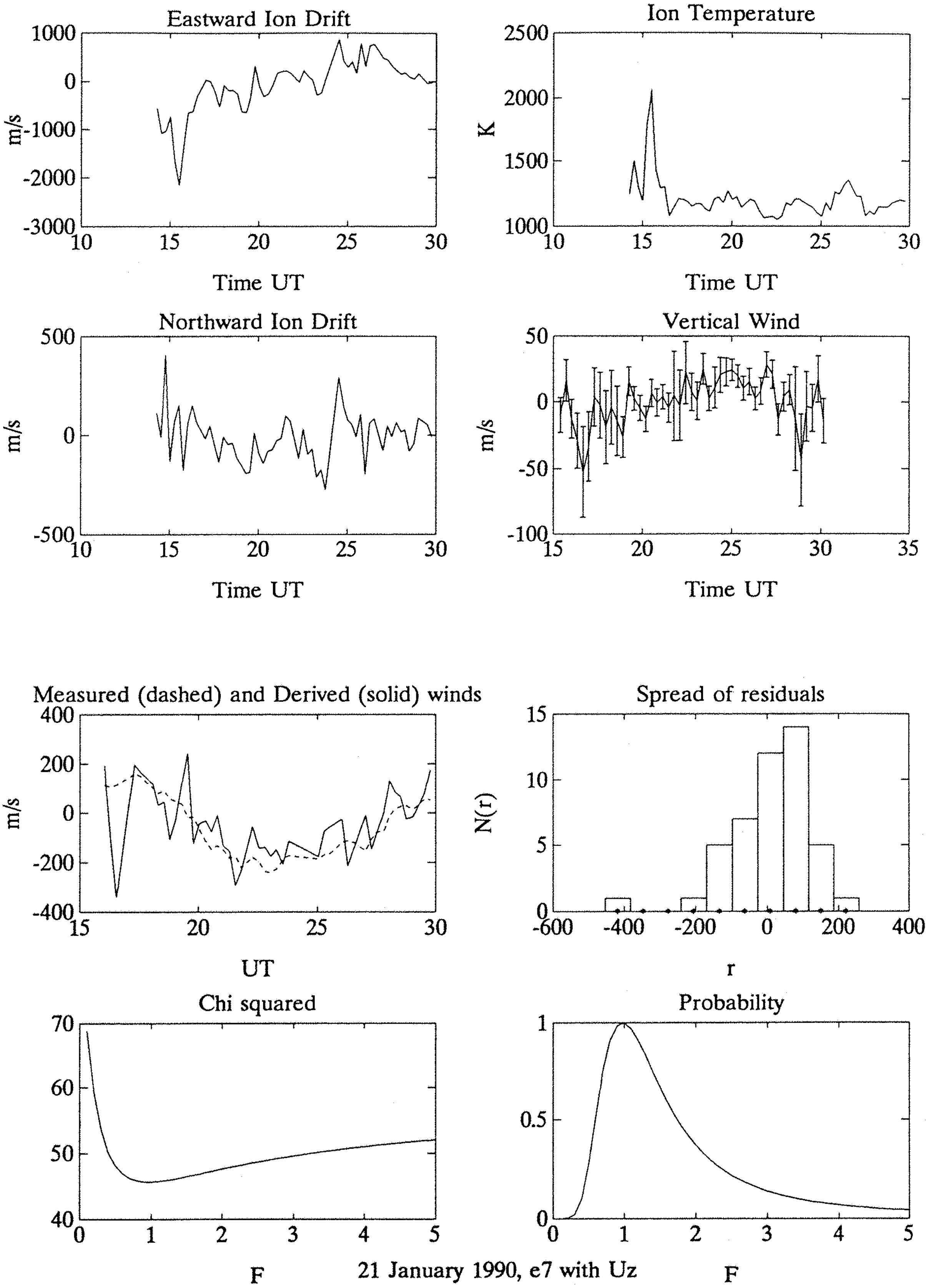

21 January 1990, e7 with Uz

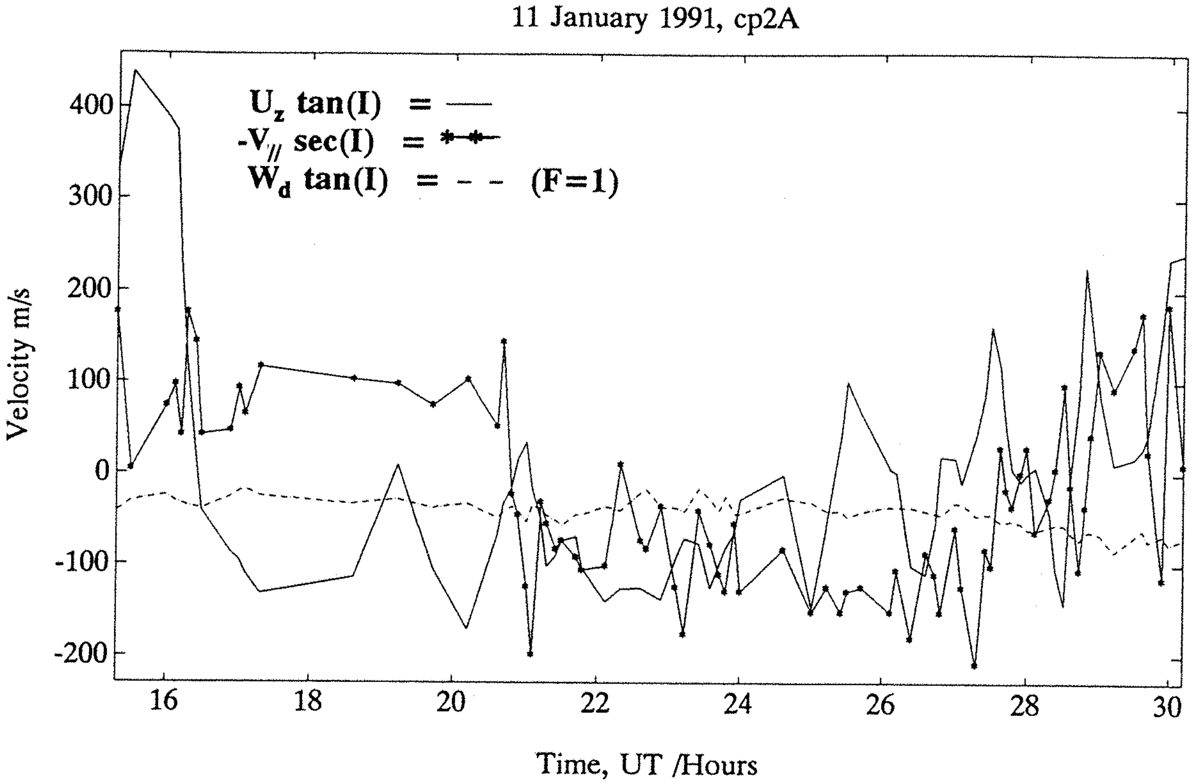
11 January 1991, cp2A
U_z tan(I) = ——
$-V_{//}$ sec(I) = *—*—
W_d tan(I) = - - - (F=1)
Velocity m/s
400
300
200
100
0
-100
-200
16
18
20
22
24
26
28
30
Time, UT /Hours

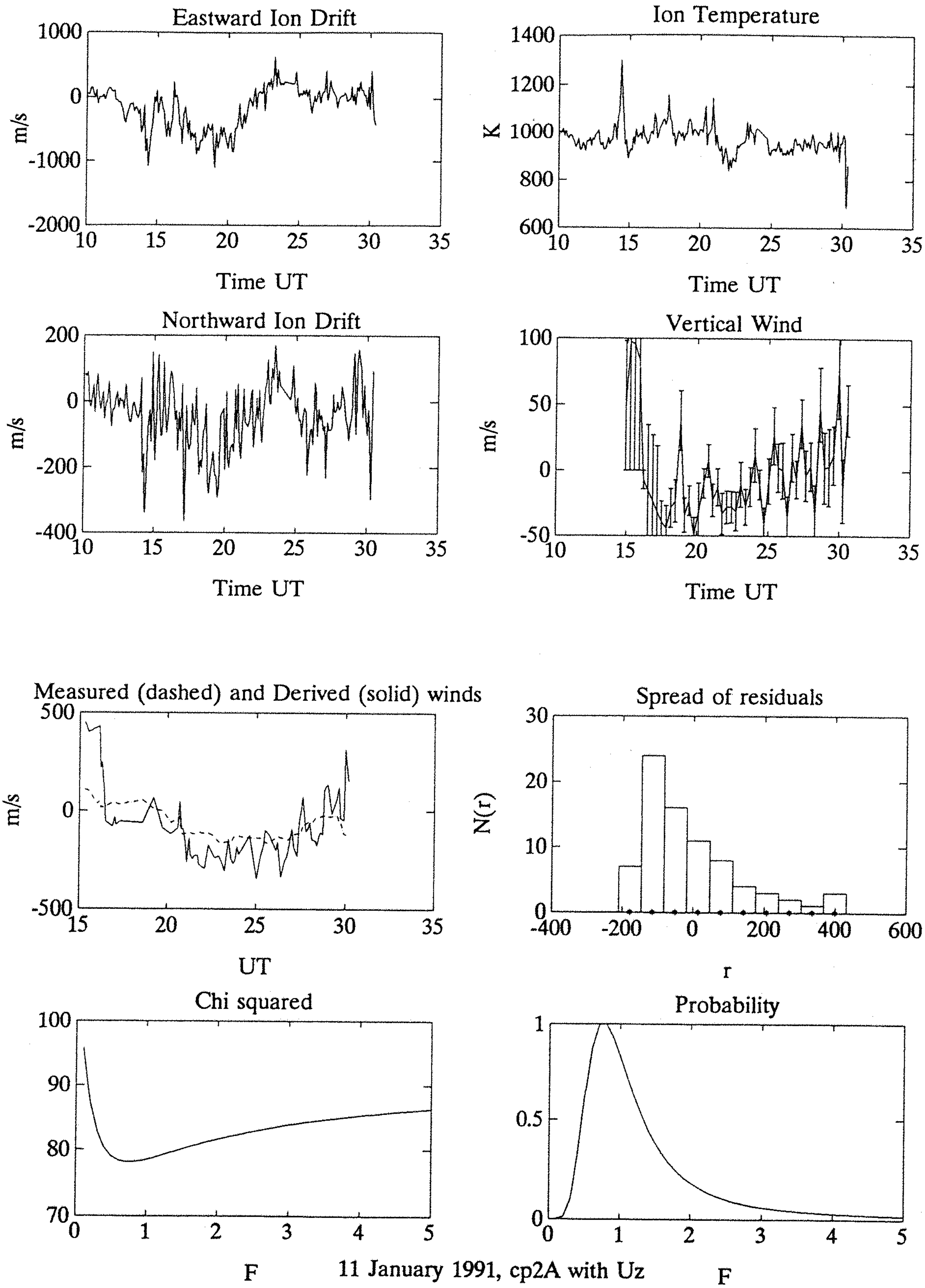

11 January 1991, cp2A with Uz

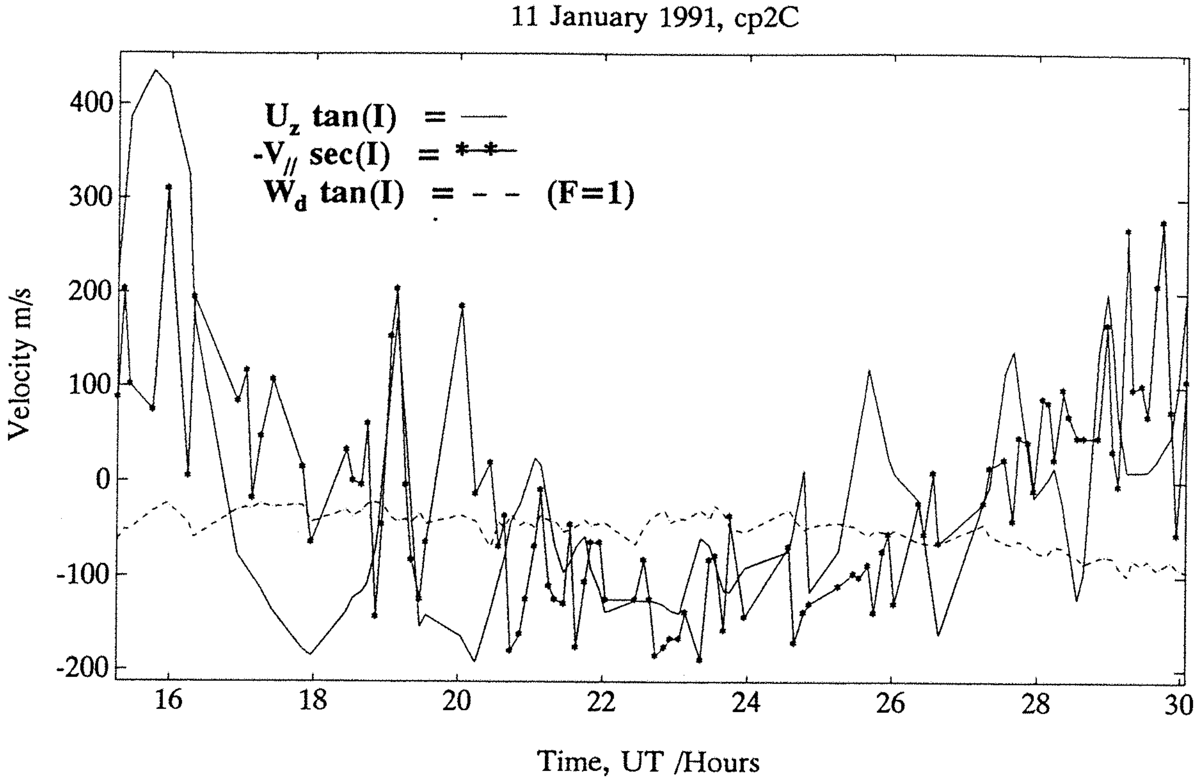
11 January 1991, cp2C
U_z tan(I) = —
$-V_{//}$ sec(I) = *-*-
W_d tan(I) = - - - (F=1)
Velocity m/s
400
300
200
100
0
-100
-200
16
18
20
22
24
26
28
30
Time, UT /Hours

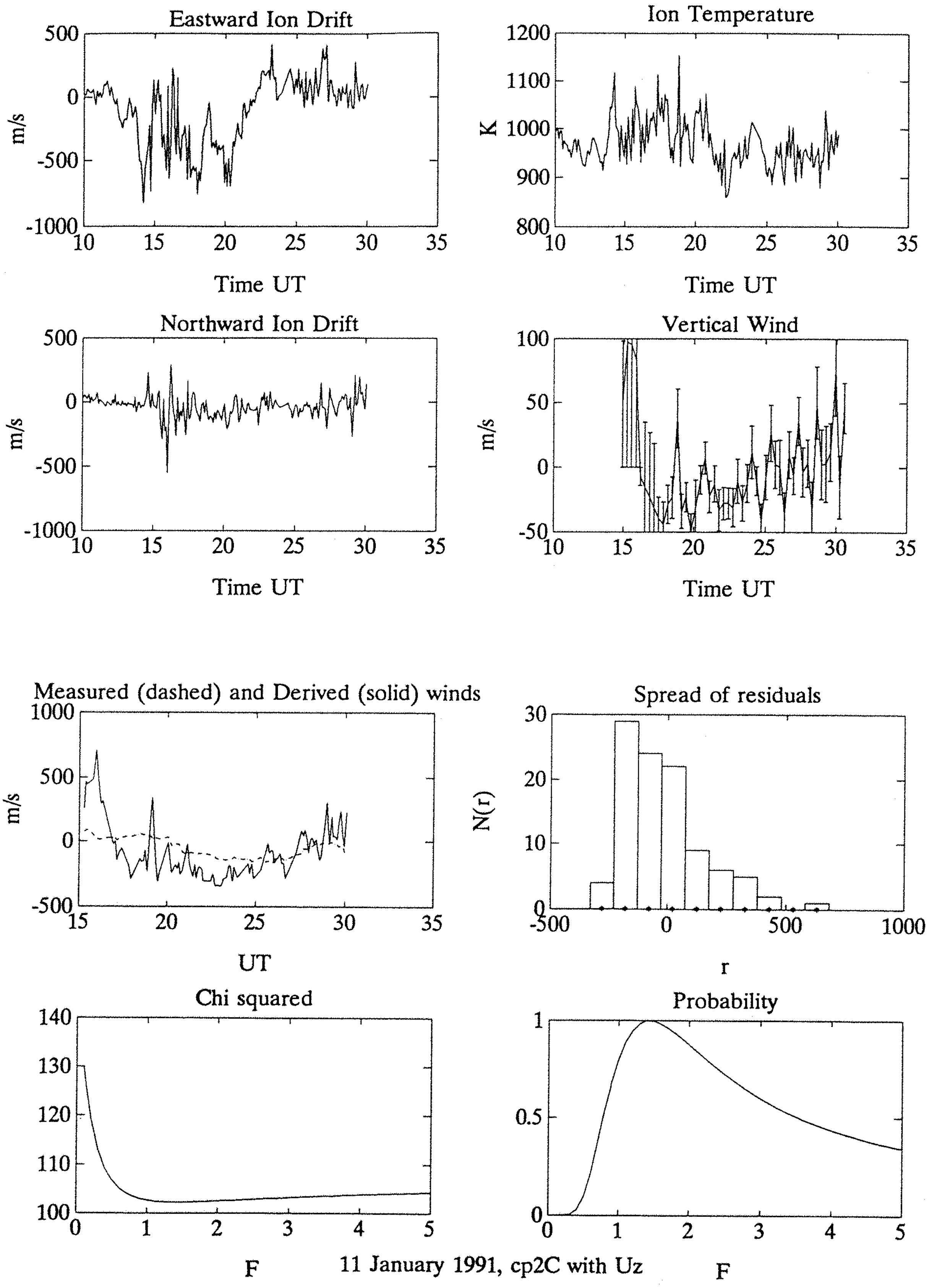

11 January 1991, cp2C with Uz

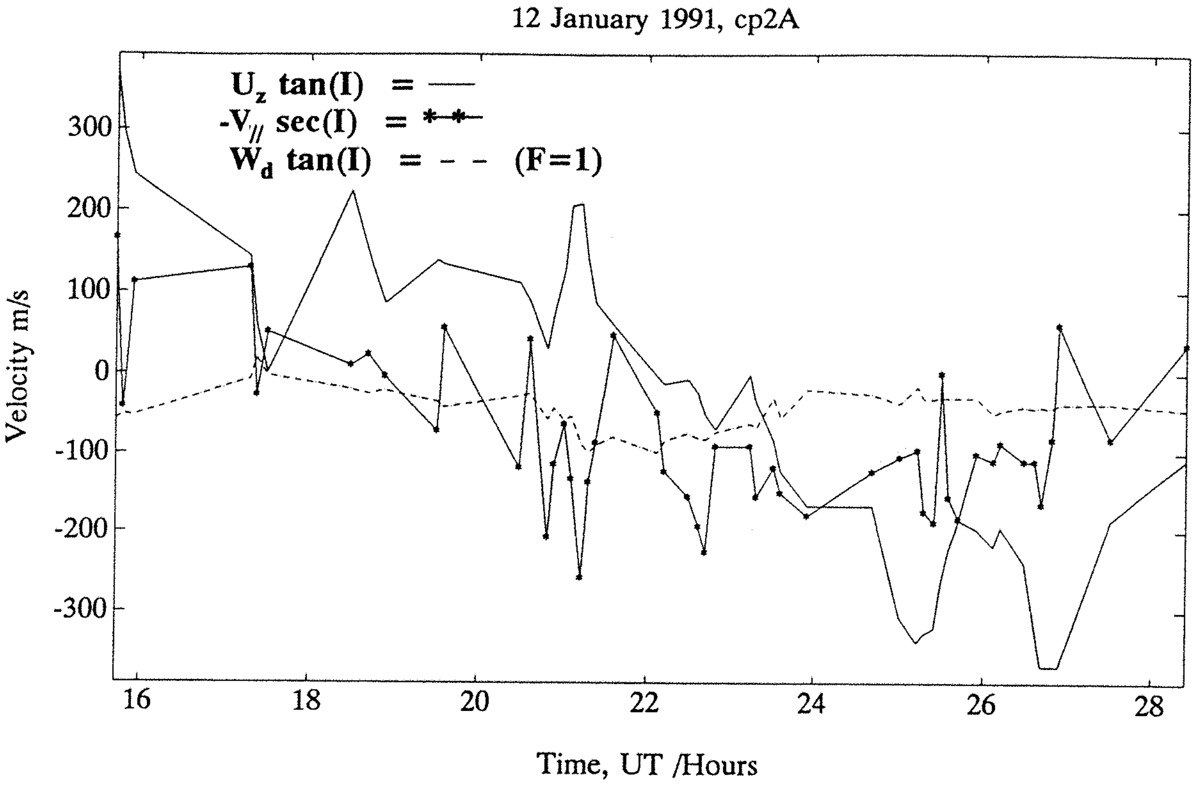
12 January 1991, cp2A
U_z tan(I) = —
-V_// sec(I) = *-*-
W_d tan(I) = - - - (F=1)
Velocity m/s
300
200
100
0
-100
-200
-300
16
18
20
22
24
26
28
Time, UT /Hours

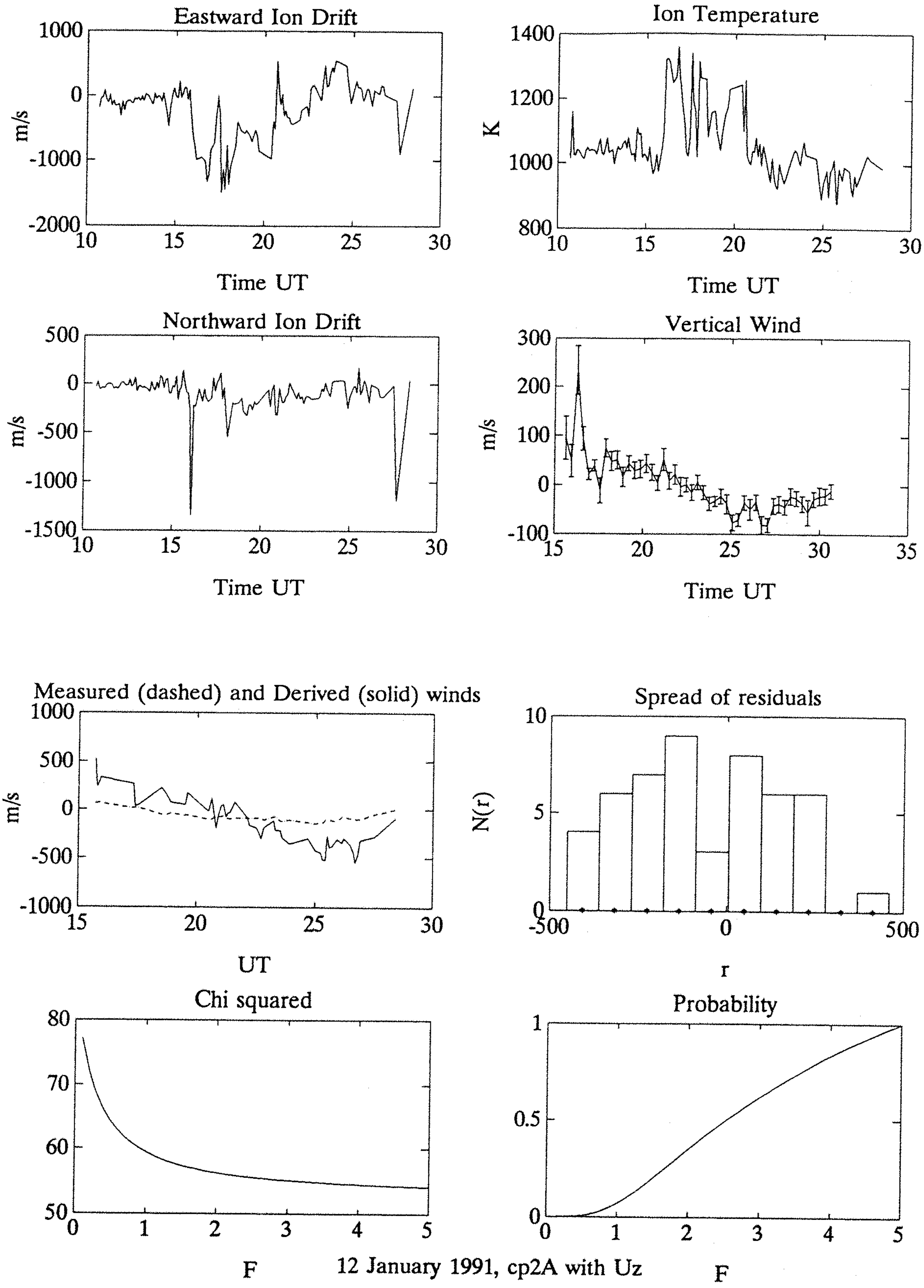

12 January 1991, cp2A with Uz

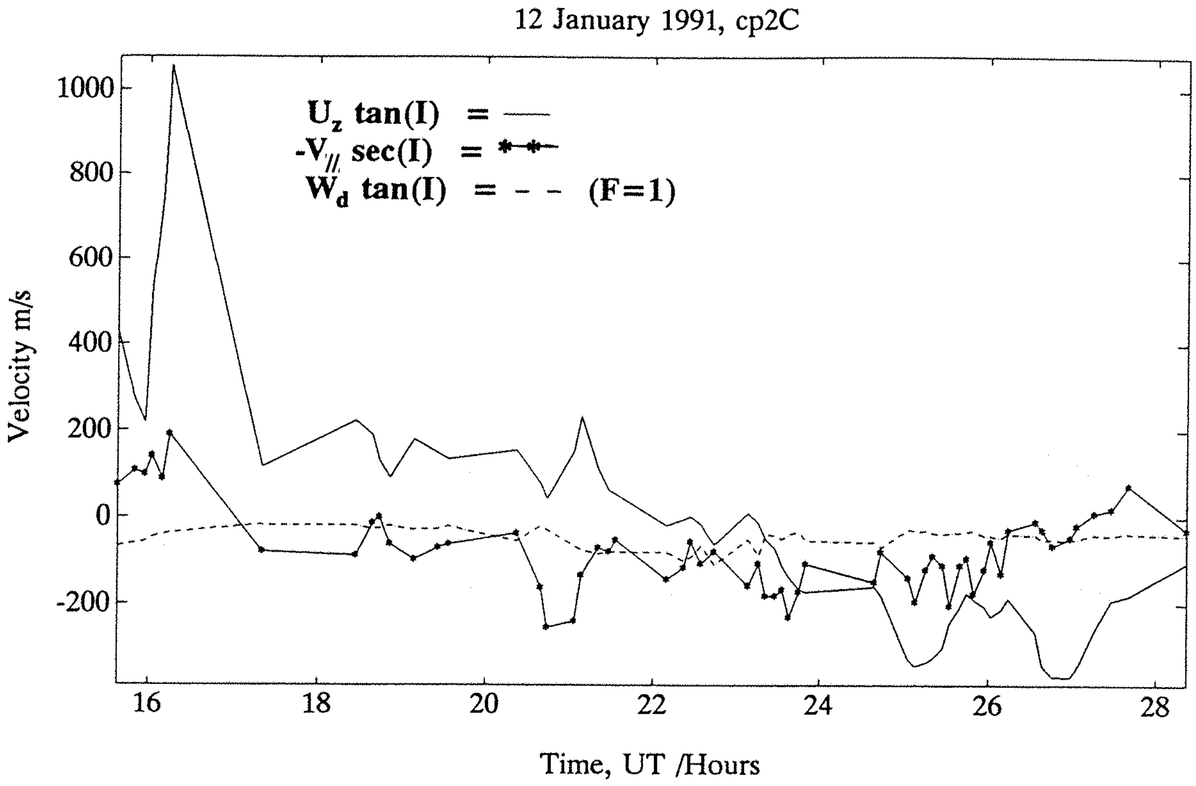
12 January 1991, cp2C
U_z tan(I) = —
$-V_{//}$ sec(I) = ✱✱
W_d tan(I) = - - - (F=1)
Velocity m/s
1000
800
600
400
200
0
-200
Time, UT /Hours
16
18
20
22
24
26
28

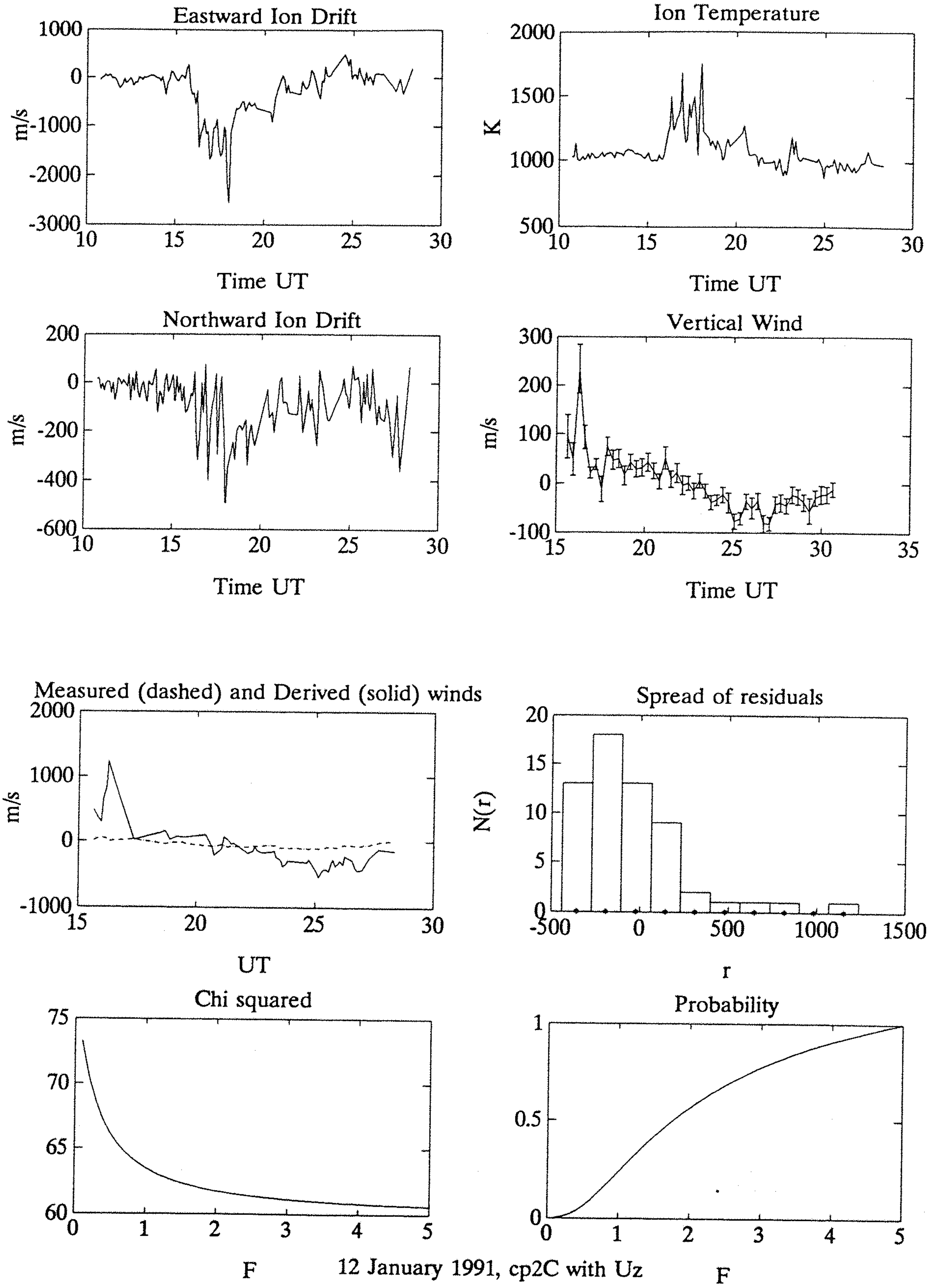

12 January 1991, cp2C with Uz

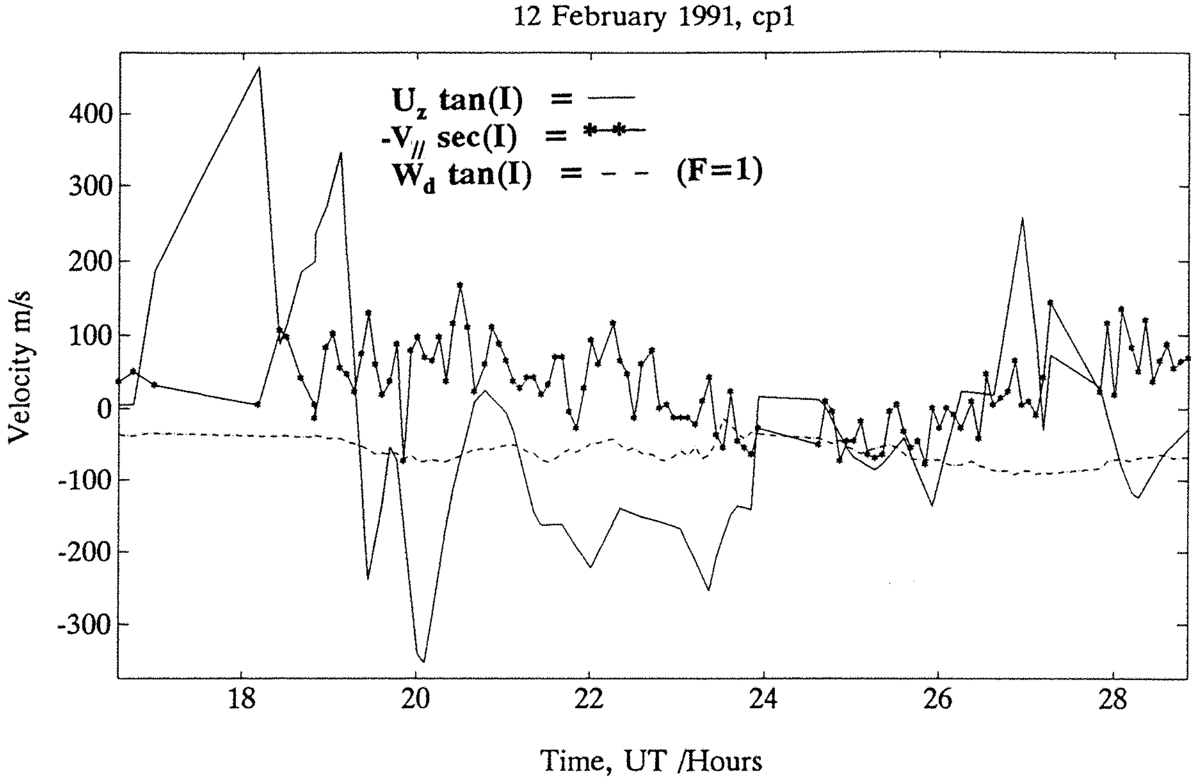

12 February 1991, cp1

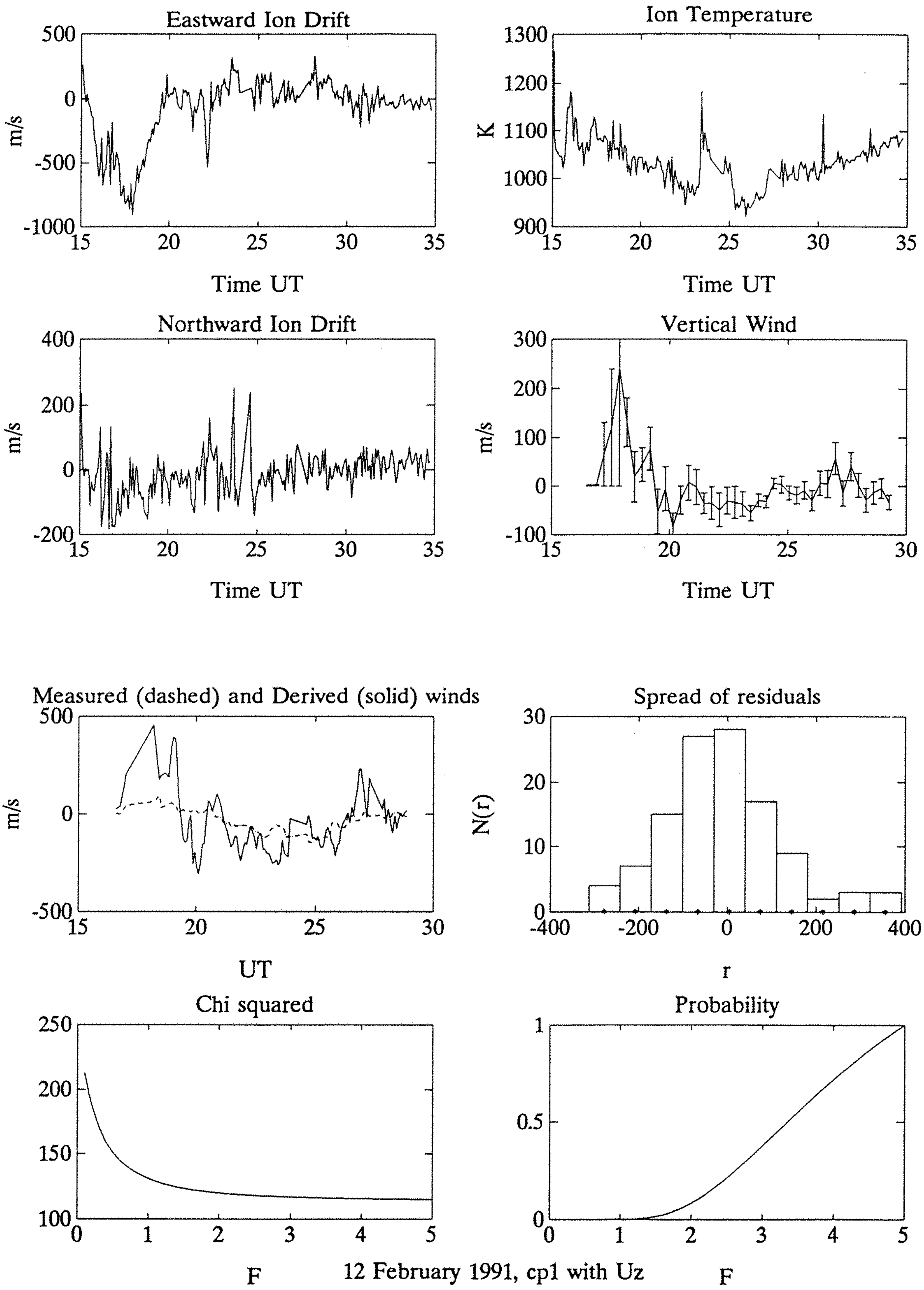

12 February 1991, cp1 with Uz

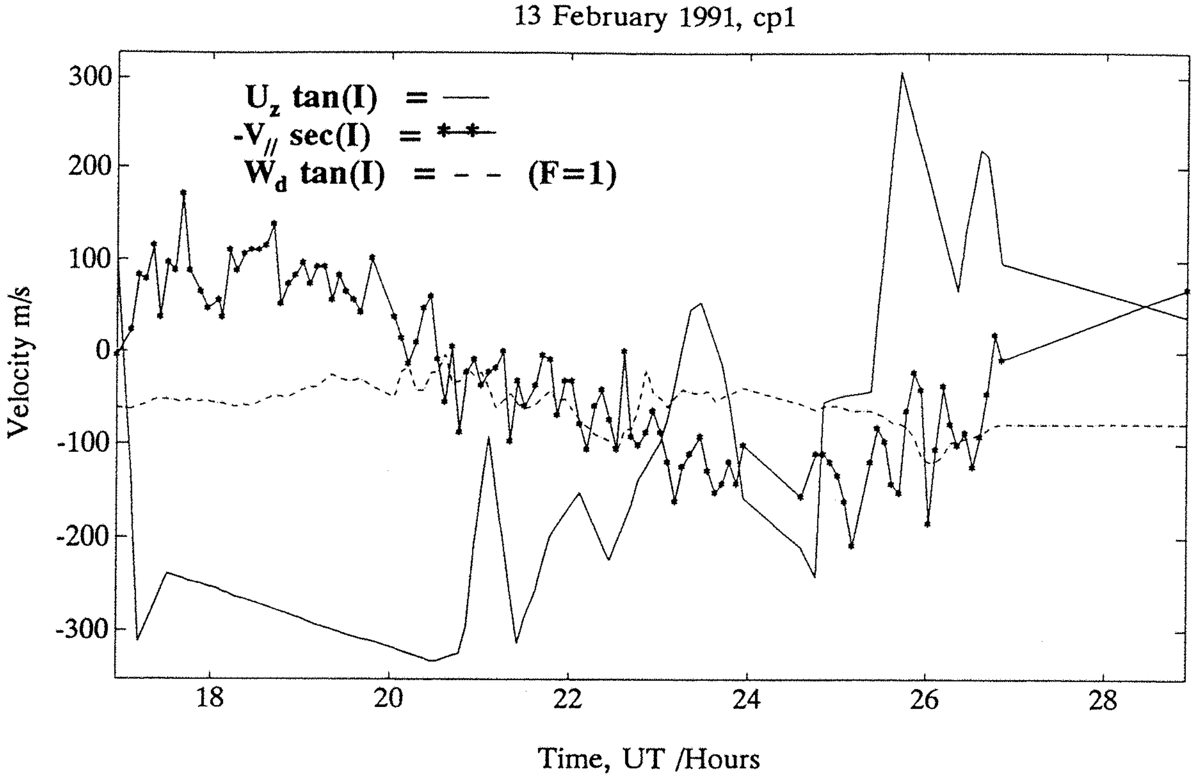
13 February 1991, cp1
U_z tan(I) = —
-V_// sec(I) = *-*
W_d tan(I) = - - - (F=1)
Velocity m/s
300
200
100
0
-100
-200
-300
18
20
22
24
26
28
Time, UT /Hours

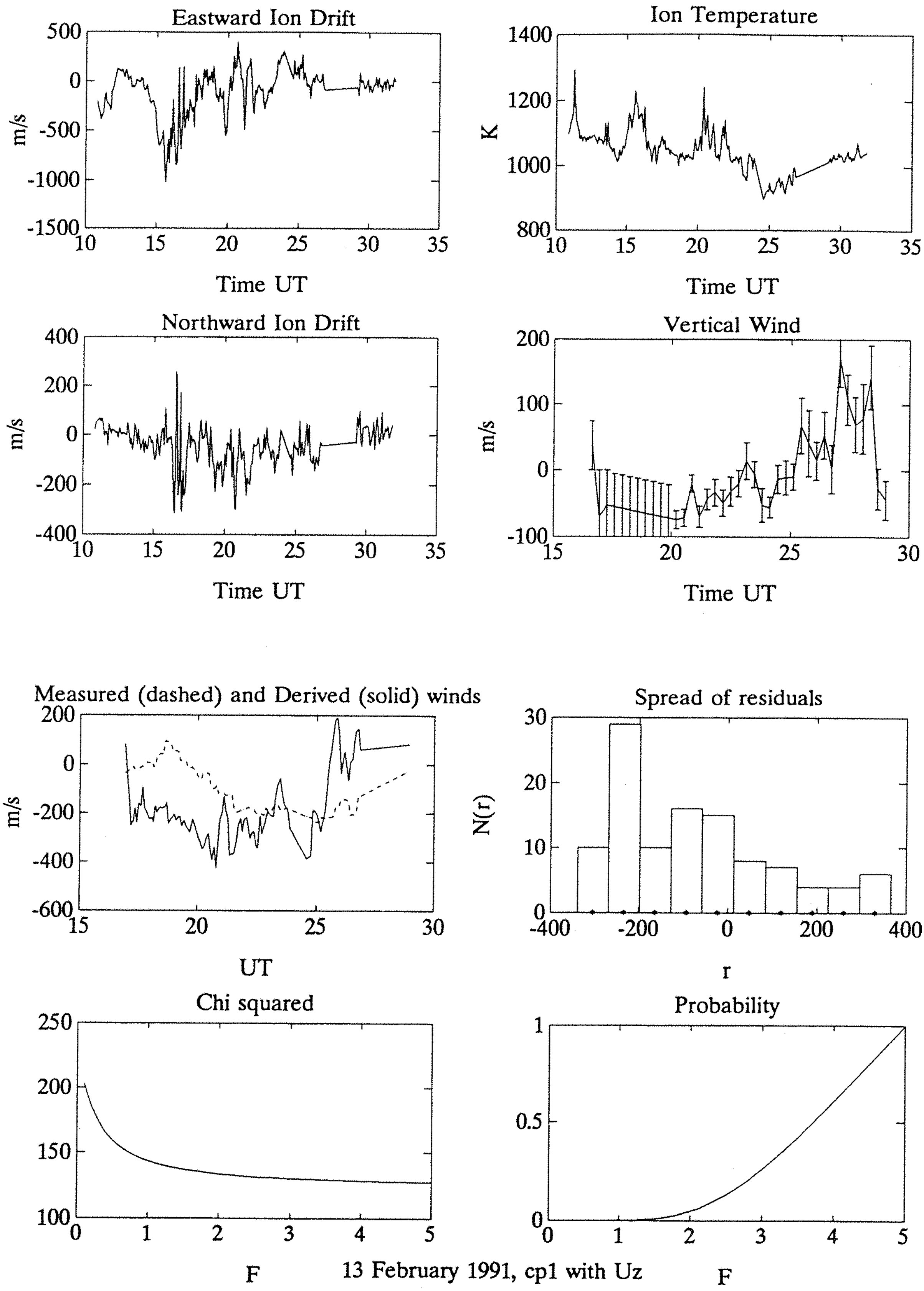

13 February 1991, cp1 with Uz

A. Aruliah, Thesis, University College London, Chapter 2, 1992.

P. Banks, Collision frequencies and energy transfer: ions, Planet. Space Sci. 14, 1105, 1966.

W. J. G. Beynon, P. J. S. Williams, Incoherent scatter of radio waves from the ionosphere, Rep. Prog. Phys., 41, 909, 1978.

A. R. Breen, P. J. S. Williams, Real and spurious anti-correlations between short-period variations of field-parallel and field perpendicular plasma velocities in EISCAT data, J. Atmos. Terr. Phys., 55, 675, 1993.

R. G. Burnside, F. A. Herrero, J. W. Meriwether, Jr., J. C. G. Walker, Optical observations of thermospheric dynamics at Arecibo, J. Geophys. Res., 86, 5532, 1981.

R. G. Burnside, R. A. Behnke, J. C. G. Walker, Meridional neutral winds in the thermosphere at Arecibo: Simultaneous incoherent scatter and airglow observations, J. Geophys. Res., 88, 3181, 1983.

R. G. Burnside, C. A. Tepley, V. B. Wickwar, The O^+-O collision cross-section: Can it be inferred from aeronomical measurements? Ann. Geophys. 5A, 343, 1987.

A. Dalgarno, The mobilities of ions in their parent gases, Phys. Trans. R. Soc., 250, 426, 1958.

J. V. Evans, Theory and practice of ionosphere study by Thomson scatter radar, Proc. IEEE, 57, 496, 1969.

A. D. Farmer, K. J. Winser, A. Aruliah, D. Rees, Ion-neutral dynamics: comparing Fabry-Perot measurements of neutral winds with those derived from radar observations, Adv. Space Res. 10, (6)281, 1990.

P. B. Hays, D. W. Rusch, R. G. Roble and J. C. G. Walker, The OI (6300 A) airglow, Rev. Geophys Space Phys., 16, 225, 1978.

S. L. Hess, Introduction to theoretical meteorology, Henry Holt and Company, New York, 1959.

T. L. Killeen, P. B. Hays and G. R. Carignan, Ion-neutral coupling in the high latitude F-region: Evaluation of ion heating terms from Dynamics Explorer 2, J. Geophys. Res., 89, 7495, 1984.

H. Knoff, E. A. Mason and J. T. Vanderslice, J. Chem. Phys., 40, 3548, 1964.

J. Lilensten, G. Thuillier, C. Lathuillere, W. Kofman, V. Fauliot, M. Hersé, Ann. Geophys., 10, 603, 1992

M. Lockwood, S. W. H. Cowley, M. P. Freeman, The excitation of plasma convection in the high-latitude ionosphere, J. Geophys. Res., 95, 7961, 1990.

M. Lockwood, I. W. McCrea G. H. Millward, R. J. Moffett, H. Rishbeth, EISCAT observations of ion composition and temperature anisotropy in the high-latitude F-region, J. Atmos. Terr. Phys., 55, 895, 1993.

R. J. Moffett, R. Selleck and G. J. Bailey, The influence of O^+-O collision frequency on ionospheric F-region behaviour, J. Atmos. Terr. Phys., 52, 125, 1990.

A. F. Nagy, R. J. Cicerone, P. B. Hays, K. D. McWatters, J. W. Meriwether, A. E. Belon and C. L. Rino, Simultaneous measurement of ion and neutral motions by radar and optical techniques, Radio Science, 9, 315, 1974.

D. Rees, N. Lloyd, P. J. Charleton, M. Carlson, J. Murdin, I. Häggström, Comparison of plasma flow and thermospheric circulation over northern Scandinavia using EISCAT and a Fabry-Perot interferometer, J. Atmos. Terr. Phys., 46, 545, 1984.

M. H. Rees, R. G. Roble, Excitation of $O(^1D)$ atoms in aurorae and emission of the [OI] 6300-Å line, Can. J. Phys., 64, 1608, 1986.

H. Rishbeth, O. K. Garriott, Introduction to ionospheric physics, Academic Press, 1969.

H. Rishbeth, S. Ganguly, J. C. G. Walker, Field aligned and field perpendicular velocities in the ionospheric F2-layer, J. Atmos. Terr. Phys. 40, 767, 1978.

H. Rishbeth, P. J. S. Williams, The EISCAT ionospheric radar: the system and its early results, Q. J. R. Astro. Soc. 26, 478, 1985.

R. W. Schunk and A. F. Nagy, Ionospheres of the terrestrial planets, Rev. Geophys. Space Sci. 18, 813, 1980.

D. P. Sipler, M. E. Hagan, M. E. Zipf and M. A. Biondi, Combined optical and radar wind measurements in the F-region over Millstone hill, J. Geophys. Res., 96, 255, 262, 1991.

W. M. Smart, Combination of observations, Camb. Univ. Press, 1958.

R. F. Stebbings, A. C. H. Smith and H. Ehrhardt, Charge transfer between oxygen atoms and O^+ and H^+ ions, J. Geophys. Res., 69, 11, 2349, 1964.

P. Stubbe, Frictional forces and collision frequencies between moving ion and neutral gases, J. Atmos. Terr. Phys. 30, 1965, 1968.

J. E. Titheridge, Mean Meridional winds in the ionosphere at 70°N, Planet. Space. Sci., 39, 657, 1991.

D. P. Thomas and P. J. S. Williams, J. Atmos. Terr. Phys. 37, 1271, 1975.

D. G. Torr and M. R. Torr, Chemistry of the thermosphere and ionosphere, J. Atmos. Terr. Phys., 41, 797, 1979.

G. Vasseur, Dynamics of the F-region observed with Thomson scatter - I Atmospheric circulation and neutral winds, J. Atmos. Terr Phys. 31, 397, 1969.

J. C. G. Walker, Correlation of wind and electric field in the nocturnal F-region, Geophys. J. R. astr. Soc., 60, 85, 1980.

V. B. Wickwar, J. W. Meriwether, Jr., P. B. Hays and A. F. Nagy, The meridional thermospheric neutral wind measured by radar and optical techniques in the auroral region, J. Geophys. Res., 89, 10, 987, 998, 1984.

K. J. Winser, A. D. Farmer, D. Rees and A. Aruliah, Ion neutral dynamics in the high latitude ionosphere : first results from the INDI experiment, J. Atmos. Terr. Phys. 50, 369, 1988.

K. J. Winser, M. Lockwood, G. O. L. Jones, H. Rishbeth, M. G. Ashford, Measuring ion temperatures and studying the ion energy balance in the high-latitude ionosphere, J. Atmos. Terr. Phys. 52, 501, 1990.